

Dissertation zur Erlangung des Doktorgrades  
der Fakultät für Chemie und Pharmazie  
der Ludwig-Maximilians-Universität München

**TWO-DIMENSIONAL BUILDING BLOCKS FOR THE  
SYNTHESIS OF LAYERED HYBRID MATERIALS**

Stephan Werner

aus

Wiesbaden, Deutschland

2014

## **Erklärung**

Diese Dissertation wurde im Sinne von § 7 der Promotionsordnung vom 28. November 2011 von Frau Prof. Dr. Bettina V. Lotsch betreut.

## **Eidesstattliche Versicherung**

Diese Dissertation wurde eigenständig und ohne unerlaubte Hilfe erarbeitet.

München, 23.06.2014

.....  
(Stephan Werner)

Dissertation eingereicht am 23.06.2014

1. Gutachter: Prof. Dr. Bettina V. Lotsch

2. Gutachter: Prof. Dr. Christina Scheu

Mündliche Prüfung am 14.07.2014

*Für Mama und Papa*

## ACKNOWLEDGEMENTS

First, I would like to express my gratitude to my supervisor Prof. Dr. Bettina V. Lotsch for giving me the opportunity to do research in her group. Throughout the entire time of work, I appreciated her expertise, the many helpful discussions and help at all times as well as the academic freedom in research.

For being the co-referee of my thesis, for many helpful discussions and for help in TEM questions, I thank Prof. Dr. Christina Scheu.

I want to thank Prof. Dr. Hans-Christian Böttcher, Prof. Dr. Konstantin Karaghiosoff, Prof. Dr. Dina Fattakhova-Rohlfing and Prof. Dr. Achim Hartschuh for being available as co-examiners in my viva voce.

Furthermore, I would like to thank the following colleagues:

- Prof. Hauke Clausen-Schaumann for his help and introduction into AFM theory and practice.
- Vincent Lau for electrochemical measurements and helpful discussions.
- Viola Duppel, Christian Ziegler and Kulpreet Viridi for TEM measurements and many helpful discussions upon interpretation of the results.
- Linus Stegbauer for his expertise and tips for improvement of organic syntheses.
- Claudia Kamella and Roland Eger for many solid state syntheses, helpful support and fun working days in Stuttgart.
- Hartmut Hartl and Marie-Luise Schreiber for ICP-AES measurements.
- Marion Sokoll for IR spectroscopy measurements.
- Eva Bruecher and Rainer Frankovsky for SQUID measurements.
- Christine Neumann and Peter Mayer for liquid NMR measurements.
- Christian Minke for his patience with my samples for SEM and solid-state NMR measurements.
- Thomas Bräuniger for many helpful suggestions in terms of interpreting solid state NMR data.
- Armin Schulz for Raman measurements.

- Mitsuharu Konuma for XPS measurements.
- Sophia Makowski for DTA-TG measurements.
- Wolfgang Wunschheim for any kind of support concerning computer and other hardware problems.

Special thanks go to “my” Bachelor students Katarina Marković, Matthias Wörsching and Philipp Ratza for their work and support in research and for fun evenings after work.

Thanks goes to my former and current lab mates of the “24/7 lab” D2.107: Christian Ziegler, Tanja Holzmann, Katharina Schwinghammer, Daniel Weber, Philipp Pust, Sebastian Schmiechen, Martin Mangstl, Sebastian Johansson, Jonas Häusler, Peter Wagatha and Philipp Strobel.

Moreover, I would like to thank all members of the Schnick, Johrendt, Hoch, Schmedt auf der Günne and Oeckler groups for a very pleasant working atmosphere, for helping me with any kind of problem I had, for fun group outings and evenings such as SingStar or carnival partys.

Big thanks go to the Lotsch group in Stuttgart: Jürgen Köhler, Jeanette Schüller-Knapp, Viola Duppel, Roland Eger, Xiuping Gao, Willi Hölle, Claudia Kamella, Friedrich Kögle, Marie-Luise Schreiber, Alexander Kuhn, Vincent Lau, Olalla Sánchez-Sobrado, Vijay Vyas, Pirmin Ganther, Frederik Haase, Tanja Holzmann, Katharina Schwinghammer, Brian Tuffy, Katalin Szendrei and Daniel Weber.

...and to the group in Munich: Christian Ziegler, Stephan Hug, Annekathrin Ranft, Erik Flügel, Linus Stegbauer, Ida Pavlichenko, Alberto von Mankowski, Claudia Lermer and the alumni Sebastian Junggeburth and Hongji Wang.

Thank you to the Skat group for exciting games and amusing breaks: Stebbo, Chris and Erik.

Chris, Sepp and Stebbo: Thank you for four unforgettable years. I do not think we did not do any kind of craziness in this time. We had fun evenings and nights in Munich and elsewhere; even though we might not remember all of what happend, it was a great time! I hope we stay in touch after our PhD time.

Thank you, Chris!

Particularly, I thank my parents, Mama and Papa, and my siblings, Julia and Sebastian. You made my academic career possible with your never ending support, pushing me forward and encouraging me even in the deepest valleys of motivation. Thank you for being the best family I could imagine!

Finally, I thank you from the bottom of my heart, Vanessa! You support me in any kind of circumstance and give me the power to overcome all of my problems. Thank you for just being you.

*Ich mach mein Ding,  
egal was die anderen sagen.*

*(Udo Lindenberg)*

## TABLE OF CONTENTS

<b>1. INTRODUCTION .....</b>	<b>1</b>
1.1 Two-Dimensional Materials.....	1
1.2 Layered Ionic Solids .....	5
1.2.1 Anionic 2D Materials .....	5
1.2.2 Cationic 2D materials .....	7
1.3 Siloxene.....	13
1.4 Layer-by-Layer Assembly .....	17
1.5 Objective .....	20
1.6 Bibliography.....	22
<b>2. CHARACTERIZATION METHODS.....</b>	<b>32</b>
2.1 X-ray Diffraction.....	32
2.2 Atomic Force Microscopy.....	33
2.3 Electron Microscopy .....	36
2.3.1 Scanning Electron Microscopy and Energy-dispersive X-ray Spectroscopy .....	36
2.3.2 Transmission Electron Microscopy .....	37
2.4 Vibrational Spectroscopy .....	40
2.4.1 Infrared spectroscopy .....	40
2.4.2 Raman spectroscopy .....	40
2.4.3 UV-Vis spectroscopy.....	41
2.5 Nuclear Magnetic Resonance Spectroscopy .....	41
2.5.1 Solution-State Nuclear Magnetic Resonance Spectroscopy.....	41
2.5.2 Solid-State Nuclear Magnetic Resonance Spectroscopy .....	42
2.6 X-ray Photoelectron spectroscopy .....	42
2.7 Magnetic measurements.....	43



2.8	Electrochemical Measurements .....	43
2.9	Elemental analysis.....	43
2.9.1	Inductively Coupled Plasma Atomic Emission Spectroscopy .....	43
2.9.2	CHNS Analysis .....	44
2.10	Light Scattering Experiments.....	44
2.11	Photoluminescence Measurements .....	44
2.12	Bibliography.....	45
<b>3.</b>	<b>LAYERED DOUBLE HYDROXIDES .....</b>	<b>46</b>
3.1	Exfoliation of $\text{Mn}^{\text{II}}\text{Al}^{\text{III}}$ Layered Double Hydroxide and Synthesis of LDH/Graphene Oxide Hybrid Material.....	47
3.1.1	Introduction .....	47
3.1.2	Experimental.....	50
3.1.3	Results and Discussion .....	54
3.1.4	Conclusion.....	65
3.1.5	Supporting Information .....	66
3.2	Layer-By-Layer Assembly of $\text{Mn}^{\text{II}}\text{Al}^{\text{III}}$ LDH and Graphene Oxide .....	72
3.2.1	Experimental.....	72
3.2.2	Results and Discussion .....	72
3.3	Exfoliation and Flocculation of $\text{Zn}^{\text{II}}\text{Cr}^{\text{III}}$ LDH and $\text{H}_x\text{Ti}_{2-x/4}\text{O}_4$ .....	76
3.3.1	Introduction .....	76
3.3.2	Results and Discussion .....	78
3.3.3	Experimental.....	83
3.4	Outlook.....	85
3.5	Bibliography.....	86

<b>4. LAYER-BY-LAYER ASSEMBLY OF OPPOSITELY CHARGED NANOSHEETS.....</b>	<b>90</b>
4.1 Artificial Solids by Design: Assembly and Electron Microscopy Study of Nanosheet-Derived Heterostructures.....	91
4.1.1 Introduction .....	92
4.1.2 Results and Discussion .....	94
4.1.3 Conclusion.....	107
4.1.4 Supporting Information .....	108
4.2 Bibliography.....	116
<b>5. SILOXENE .....</b>	<b>120</b>
5.1 Structure Investigations and Alkyl-modification of Siloxene.....	121
5.1.1 Introduction .....	121
4.1.2 Results and Discussion .....	124
5.1.3 Conclusion.....	140
5.1.4 Supporting Information .....	141
5.2 Bibliography.....	152
<b>6. SUMMARY.....</b>	<b>156</b>
6.1 Layered Double Hydroxides .....	156
6.2 Layer-by-Layer Assembly of Oppositely Charged Nanosheets.....	158
6.3 Siloxene.....	159
<b>7. CONCLUSION AND OUTLOOK .....</b>	<b>161</b>
<b>8. APPENDIX .....</b>	<b>164</b>
8.1 List of Publications .....	164
8.2 Curriculum Vitae.....	165

# 1. INTRODUCTION

## 1.1 TWO-DIMENSIONAL MATERIALS

Since the successful delamination of graphene by A. Geim and K. Novoselov in 2004,<sup>[1]</sup> the interest in the field of nanosheets has tremendously increased.<sup>[2-3]</sup> The two Russian researchers were awarded the Nobel Prize in Physics “for groundbreaking experiments regarding the two-dimensional material graphene” in 2010.<sup>[4]</sup> Graphene is “a flat monolayer of carbon atoms tightly packed into a 2D honeycomb lattice, and is a basic building block for graphitic materials of all other dimensionalities”.<sup>[5]</sup> Even though it was already Boehm et al. who reported on “*Dünnste Kohlenstoff-Folien*” in 1962,<sup>[6]</sup> Geim and Novoselov reopened up the field of nanosheet research with their achievement of isolating single graphene layers from the bulk compound graphite, thus confirming the existence of the first ultimate 2D material which they made amenable to nanoscale fabrication, even without a substrate. The main challenge in this research lies in the unambiguous characterization of the existence of monolayers, which was impossible to achieve in the early 1960s. However, with the help of electron microscopy, Boehm et al. show the existence of thin layers as depicted in Fig. 1.1. Since the delamination of graphene many other inorganic layered materials have been exfoliated into single layers. The interest in nanometer thick materials is due to their extraordinary properties and possible applications, especially in technological devices.<sup>[2-3,7-8]</sup> The exfoliation of two-dimensional (2D) bulk materials into monolayer nanosheets can schematically be seen in Fig 1.2. This chapter will give an overview over the state of the art of research conducted in the field of 2D materials with a focus on the delamination of different 2D materials into nanosheets and possible combinations of nanosheets to form hybrid compounds by layer-by-layer techniques, which is one of the objectives of this dissertation.

## 1 INTRODUCTION

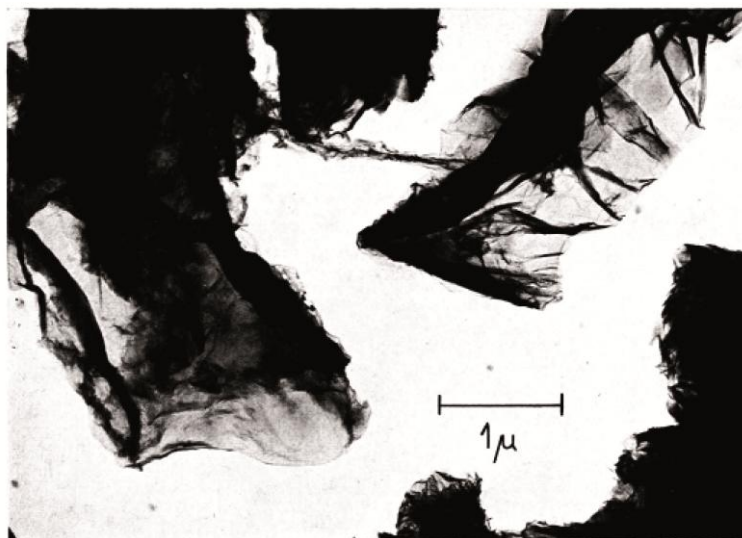


**Figure 1.1** Electron microscopy image showing thin foils of reduced graphene oxide flakes, obtained by H.P. Boehm and co-workers in 1962. Reprinted with permission from reference [6]. Copyright 1962 Zeitschrift für Naturforschung.

2D materials have been some of the most studied compounds in inorganic chemistry owing to their unusual physical phenomena that occur because of their anisotropic properties and pronounced size confinement.<sup>[2]</sup> In general, “quasi 2D materials” are layered organic, inorganic or hybrid compounds that exhibit similar atomic organization and bond strength along two dimensions and less strong bonding along the third dimension.<sup>[2]</sup> Nanosheets or 2D materials are the single layered building blocks from which layered (or “quasi 2D”) materials are made. They typically offer dimensions of several micrometers in lateral size and nanometer-sized thickness in the third dimension.

Graphene is the most prominent member of the family of delaminated 2D materials and exhibits exceptional optical, mechanical, electronic, and thermal properties.<sup>[5,9-12]</sup> The first calculations about the band structure of grapheme have already been undertaken by Wallace in 1947.<sup>[13]</sup> The properties of graphene differ significantly from those of the related bulk compound, graphite, and are caused by the anisotropy of the subnanometer thin sheet that is a material essentially only composed of surface, rather than bulk. However, graphene is only one compound of a large class of materials that are composed of single-atom or few-atom thick layers. In 1960, Walker<sup>[14]</sup> published his results on exfoliation of a phyllosilicate and six years later MoS<sub>2</sub> was synthesized as molecularly thin layer by Frindt.<sup>[15]</sup> Along with the publications by Boehm concerning the “*Dünnste Kohlenstoff-Folien*”,<sup>[6]</sup> which were the seminal attempts to delaminate graphite into single sheets, these were the first investigations

## 1 INTRODUCTION

to synthesize single layered materials. Along with the discovery of graphene, its oxidized analogue graphite oxide has been studied as well well.<sup>[6,16]</sup> Graphite oxide consists of graphene layers that are oxidized and carry hydroxyl, carboxyl, carbonyl and epoxide groups at the surface, yielding a non-stoichiometric compound with C:O ratios of 2.5-3.5.<sup>[17-19]</sup> Due to the oxidation and hydration of the layers, the layer distance between the planes rises from 3.35 Å in graphite to 6 Å in graphite oxide.<sup>[20]</sup> To date, graphene is commonly obtained by chemical reduction of graphite oxide. Mostly hydrazine hydrate is applied as reducing agent,<sup>[21-23]</sup> whereas reduction has also been shown with NaOH or KOH,<sup>[24]</sup> UV light,<sup>[25]</sup> or thermal<sup>[26]</sup> activation.

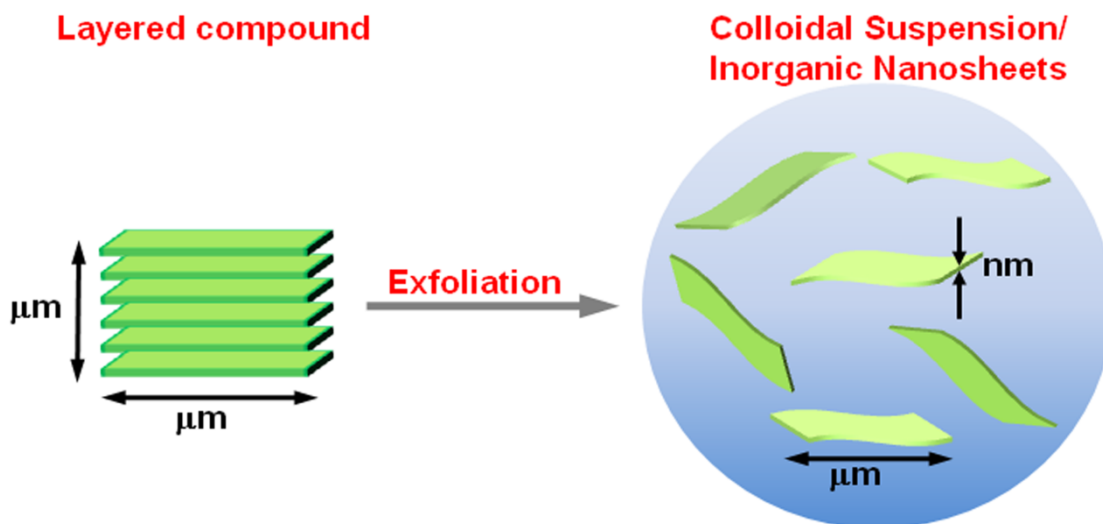


**Figure 1.2** Schematic illustration of exfoliation of a layered bulk compound into a colloidal suspension containing single layered nanosheets.

In general, 2D materials can be divided into two different classes: layered van der Waals solids and layered ionic solids. In layered van der Waals solids the crystal structure features neutral, single-atom or single-polyhedron thick layers with covalent or ionic bonding along two dimensions and weak dispersive interactions, i.e. van der Waals bonding along the third axis between adjacent layers.<sup>[2]</sup> Amongst the materials of this class that have already been successfully exfoliated are graphene,<sup>[1,6]</sup>  $\text{MoS}_2$ ,<sup>[15]</sup>  $\text{NbSe}_2$ ,<sup>[27-28]</sup> and many other metal dichalcogenides, which are one of the best studied families of van der Waals compounds. Especially early transition metal dichalcogenides with the stoichiometry  $\text{MX}_2$  ( $\text{M} = \text{Ti, Zr, Hf, V, Nb, Ta, Re}$  etc;  $\text{X} = \text{S, Se, Te}$ ) crystallize in trigonal prisms or octahedra that are connected by edge sharing to form infinite 2D layers.<sup>[29]</sup> In the following some metal

## 1 INTRODUCTION

chalcogenides that have been exfoliated are mentioned:  $\text{WS}_2$ ,<sup>[30]</sup>  $\text{TiSe}_2$ ,<sup>[31]</sup>  $\beta\text{-FeSe}$ ,<sup>[32]</sup>  $\text{ZnSe}$ ,<sup>[33]</sup>  $\text{Bi}_2\text{Se}_3$ ,<sup>[34]</sup> and  $\text{Bi}_2\text{Te}_3$ .<sup>[34-35]</sup> Other 2D van der Waals compounds that can be exfoliated are named in the following: hexagonal BN,<sup>[30,36]</sup>  $\text{Ti}_3\text{C}_2(\text{OH})_2$ , which is called “MXene” according to its graphene-like 2D morphology,<sup>[37]</sup>  $\text{Co}(\text{OH})_2$ <sup>[38]</sup> or the Zintl phases  $\text{CaSi}_2$  and  $\text{CaGe}_2$  to yield  $\text{Si}_6\text{H}_6$ ,<sup>[39-40]</sup>  $\text{Si}_6\text{H}_3(\text{OH})_3$ <sup>[41]</sup> or  $\text{Ge}_6\text{H}_6$ ,<sup>[42]</sup> respectively.

## 1.2 LAYERED IONIC SOLIDS

Layered ionic solids are the other large group of inorganic layered materials that can be delaminated into single sheets. The groups of Sasaki and Mallouk pioneered this field of research since they were among the first who realized the potential of these compounds, which include both the exfoliation of polyanionic and polycationic nanosheets derived from cation and anion exchangeable materials, respectively.<sup>[7-8,43-45]</sup> Figure 1.3 gives an overview of the crystal structures of different single layered nanosheets.

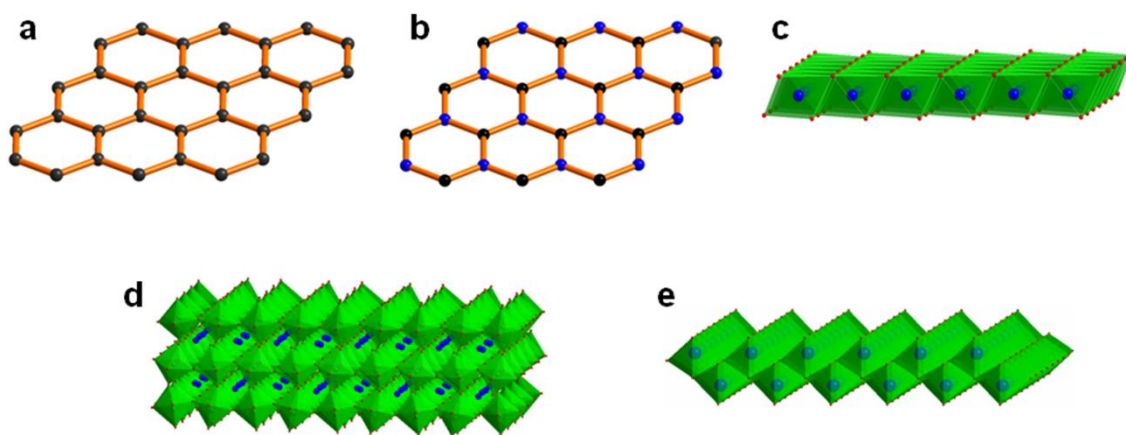


**Figure 1.3** Representations of single layers of different nanosheets materials: (a) graphene, (b) hexagonal-BN, (c)  $\text{Co}(\text{OH})_2$ , (d)  $\text{Ca}_2\text{Nb}_3\text{O}_{10}$  and (e)  $\text{Ti}_{1-x}\text{O}_2$ . The green polyhedra represent the different metal oxide octahedra.

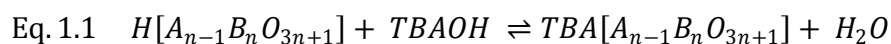
### 1.2.1 ANIONIC 2D MATERIALS

In this chapter the focus is on anionic nanosheets. Delamination of cation exchange materials to yield anionic nanosheets has been achieved for many different materials such as smectite clay minerals,<sup>[46-47]</sup> metal phosphates,<sup>[48-50]</sup> and metal oxides.<sup>[7,51]</sup> In particular, layered perovskites,<sup>[43,52-56]</sup> titanates,<sup>[57-60]</sup> and manganese oxides<sup>[61-64]</sup> sparked interest in metal oxide nanosheets due to their various functionalities.<sup>[65-67]</sup> In the following, layered perovskites are discussed in more detail, since later in this thesis the combination of positively and negatively charged nanosheets will become important, including perovskite nanosheets that serve as anionic layers.

Three-dimensional perovskites have the general formula  $\text{ABX}_3$ , whereas in most cases,  $\text{X} = \text{O}$ ,  $\text{A} = \text{s-, d-, f- block metals}$  and  $\text{B} = \text{small transition metal cations}$ . The larger A-site

## 1 INTRODUCTION

cations and the anions build a face-centered cubic (fcc) packing and the B-site ions occupy  $\frac{1}{4}$  of the octahedral voids, building a 3D crystal of corner-sharing octahedra. Layered perovskites, such as Dion-Jacobson (DJ), Ruddlesden-Popper (RP), and Aurivillius phases, consist of negatively charged perovskite slabs interleaved with metal cations or cationic metal oxide layers. DJ phases have the general formula  $A^+[A_{n-1}B_nO_{3n+1}]^-$  with negatively charged layers consisting of  $[A_{n-1}B_nO_{3n+1}]^-$  blocks and intercalated alkali, alkaline earth or rare earth metal ions ( $A'^+$ ) between the layers, thus compensating the negative layer charge. RP phases are structurally similar to DJ phases, whereas RP phases exhibit two interlayer cations per formula unit, thus exhibiting twice the interlayer charge in comparison to DJ phases.<sup>[54]</sup> In analogy with RP phases Aurivillius phases possess a charge density of 2 electrons per formula unit, while these compounds feature cationic  $Bi_2O_2^{2+}$  layers between the perovskite slabs.<sup>[54]</sup> Among layered perovskites, DJ phases are the first reported example with ion-exchange capability,<sup>[54]</sup> which makes them interesting and applicable for the synthesis of nanosheets. By replacing the interlayer cation ( $A'^+$ ) by soft chemical proton exchange, a proton containing perovskite with the sum formula  $H[A_{n-1}B_nO_{3n+1}]$  is generated. This compound can then be exfoliated with the help of bulky organic cations such as the tetrabutylammonium ion ( $TBA^+$ ), which is exchanged for the proton in a neutralization reaction between  $H^+$  and  $OH^-$ , thus separating the layers from each other.<sup>[43,52,57-58,68]</sup> Equation 1.1 describes the equilibrium reaction of cation-proton exchanged perovskite and  $TBA^+OH^-$ .



A prominent member of DJ perovskites is  $KCa_2Nb_3O_{10}$ , which was first synthesized by Dion et al.<sup>[69]</sup> and has been one of the first layered perovskites that have been exfoliated into single sheets.<sup>[52,56]</sup> Owing to its interesting properties such as superconductivity upon lithium intercalation into the bulk compound<sup>[70]</sup> or the ability of photochemical charge separation for photochemical water splitting for the hydrogen evolution reaction<sup>[71-73]</sup> upon exfoliation into  $TBACa_2Nb_3O_{10}$  nanosheets,  $KCa_2Nb_3O_{10}$  has been one of the best studied layered perovskites to date. A structural image of a single perovskite slab of the  $Ca_2Nb_3O_{10}^-$  nanosheet can be seen in Fig. 1.3 d.



## 1 INTRODUCTION

### 1.2.2 CATIONIC 2D MATERIALS

The group of cationic 2D materials predominantly comprises layered double hydroxides (LDH). The first known LDH, hydrotalcite, was discovered in Sweden in 1842. However, the accurate molecular formula  $[\text{Mg}_6\text{Al}_2(\text{OH})_{16}]\text{CO}_3 \cdot 4\text{H}_2\text{O}$  of the naturally occurring LDH was not published until 1915 by Manasse.<sup>[74]</sup> Being the first member of a large family of compounds, hydrotalcite subsequently gave its name to all naturally occurring LDHs. Since 1977, hydrotalcite is well known as the active pharmaceutical ingredient of the antacid Talcid<sup>®</sup> released from Bayer.<sup>[75]</sup> According to the large group of clay compounds that are able to exchange cations from their interlayer galleries, LDHs are often called “anionic clays” owing to their ability to exchange anions, which is rarely found in other materials. In 1942, renewed interest in LDHs arose – 100 years after their discovery – caused by a publication of Feitknecht reporting on *Doppelschichtstrukturen*.<sup>[76]</sup> Mistakenly, the structures were assigned to a layer of one metal hydroxide intercalated by a second layer of another metal hydroxide. It was not until the late 1960s that the correct structure of LDHs was revealed by Allmann and Taylor by X-ray diffraction.<sup>[77-78]</sup> Since then it has been known that both metal ions reside in the same hydroxide layer with edge-sharing  $\text{M}^{\text{II/III}}(\text{OH})_6$  octahedra forming a hexagonal Brucite-type layer analogous to  $\text{Mg}(\text{OH})_2$ . The Brucite layers are stacked in *c*-direction with anionic interlayer galleries forming either rhombohedral or hexagonal polymorphs, whereas most naturally occurring LDHs exist in the rhombohedral form.<sup>[79]</sup> The Brucite-type layers can be stacked in different ways, which gives rise to a variety of different polytype structures. If the hydroxyl groups of adjacent layers are located vertically above each other, a trigonal prismatic arrangement of the interlayer region results, whereas an octahedral arrangement forms when an offset of the  $\text{OH}^-$  groups exists. Hence, three different hexagonal two-layer polytypes exist, which are called  $2\text{H}_1$ ,  $2\text{H}_2$  and  $2\text{H}_3$ .<sup>[80]</sup> Moreover, in LDHs three-layer polytypes exist, whereof two have rhombohedral symmetry ( $3\text{R}_1$  and  $3\text{R}_2$ ) and the remaining seven polytypes ( $3\text{H}_1$  –  $3\text{H}_7$ ) have hexagonal symmetry. The reason for the arrangement in  $3\text{R}_1$  symmetry of most naturally occurring LDHs is that this structure allows the formation of hydrogen bonds of  $\text{OH}^-$  groups of both upper and lower layers with intercalated carbonate ions.<sup>[80-81]</sup> Figure 1.4 shows the structure of LDHs in a hexagonal and b rhombohedral symmetry respectively.

# 1 INTRODUCTION

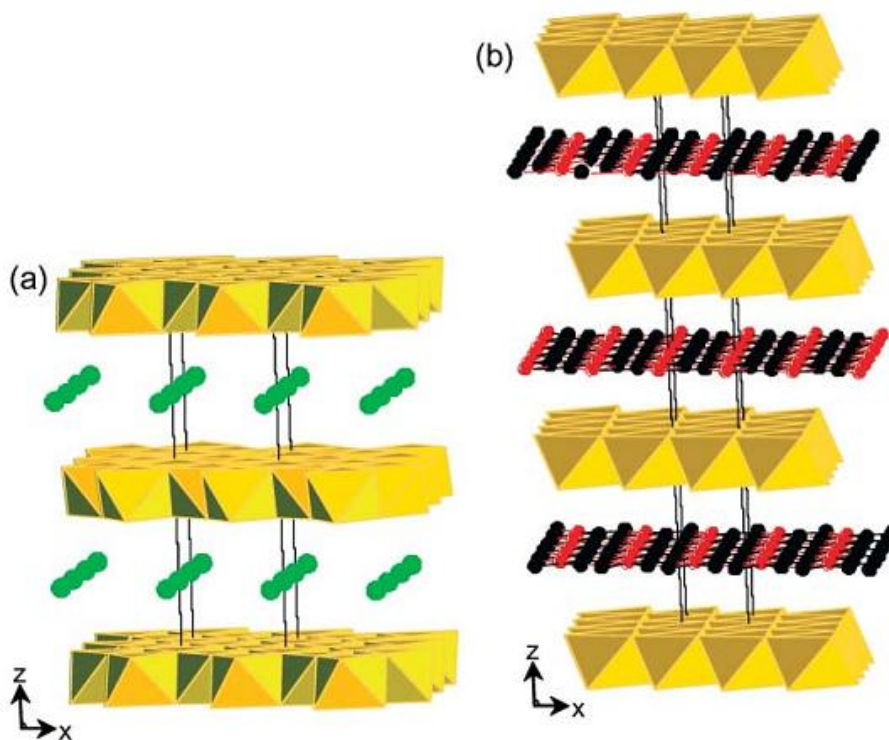


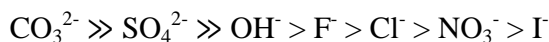
**Figure 1.4.** General structure of LDHs showing the Brucite-type layers consisting of edge-sharing octahedra (yellow) and the polymorphic stacking patterns: (a) hexagonal and (b) rhombohedral. Reproduced from reference [79] with permission from The Royal Society of Chemistry.

The generic formula of LDHs is described by:  $[M^{z+}_{1-x}M^{3+}_x(OH)_2]^{\zeta+}(X^{n-}_{\zeta/n}) \cdot mH_2O$ .<sup>[79]</sup> Usually  $z = 2$  and  $\zeta = x$ . Typical  $M^{2+}$  cations found in LDHs are  $Ca^{2+}$ ,  $Mg^{2+}$ ,  $Zn^{2+}$ ,  $Ni^{2+}$ ,  $Mn^{2+}$ ,  $Co^{2+}$  and  $Fe^{2+}$ , whereas typical  $M^{3+}$  cations are  $Al^{3+}$ ,  $Cr^{3+}$ ,  $Mn^{3+}$ ,  $Fe^{3+}$ ,  $Ga^{3+}$ ,  $Co^{3+}$  and  $Ni^{3+}$ . Pure phases of LDHs only exist in the range  $0.2 \leq x \leq 0.33$ , although it has been reported that LDHs exist in the range  $0.1 \leq x \leq 0.5$ .<sup>[82]</sup> Between the metal hydroxide layers, water molecules and anions are located. The anions compensate the positive charge of the Brucite layers, which is caused by the exchange of  $M^{2+}$  by  $M^{3+}$  cations.<sup>[83]</sup> The interlayer gallery space is disordered and the extended network of hydrogen bonds between the hydroxyl layers, anions and water is dynamically disordered. In addition, the stacking sequence is disordered and turbostratic disorder typically occurs in LDHs. All these phenomena make an accurate description of the structure extremely complex.<sup>[80]</sup> Furthermore, the forces between the layers are not yet fully understood and controversially discussed in the literature.<sup>[84-85]</sup> However, it has been shown that the synthesis of single crystals of LDHs can be achieved.<sup>[77,86]</sup> Intercalated anions often are halides,  $NO_3^-$ ,  $SO_4^{2-}$  or  $CO_3^{2-}$ , the latter being by far the most common intercalate in naturally occurring LDHs.

## 1 INTRODUCTION

However, also LDHs with other anions such as bulky organic molecules<sup>[87-88]</sup> have been successfully synthesized. Even silicates<sup>[89-90]</sup>, metal complexes<sup>[91]</sup> and polyoxometalates<sup>[92-93]</sup> have been incorporated into LDHs.

The synthesis of LDHs can be achieved in many different ways. The most prevalent routes are the coprecipitation method, the ion-exchange method and the “memory-effect”.<sup>[94]</sup> The coprecipitation method is a one-pot synthesis; aqueous solutions of  $M^{2+}$  and  $M^{3+}$  cations as well as a solution containing the interlayer anions are used as precursors. By adjusting the pH of the mixed solutions to a value of supersaturation of the metal cations yields coprecipitation, and phase separation of the metal cations can be avoided. Fritz Seel published a logarithmic diagram that displays pH precipitation curves of several metal hydroxides plotted against the concentration.<sup>[95]</sup> At pHs below the cross peaks of two different hydroxides only one metal hydroxide precipitates, whereas above the peaks phase segregation occurs. The synthesis of LDHs is mostly carried out under inert atmosphere since hydrotalcites have high affinity to carbonate. Generally, excess of the desired intercalated anion should be present in the reaction mixture to avoid co-intercalation of anions of the metal salts such as nitrates or halides. The following sequence of affinity of anion to LDH was established previously:<sup>[83]</sup>



This sequence is also of great importance for the anion exchange method, which is often applied when the desired intercalated anion is unstable in basic conditions and can thus not be intercalated by the coprecipitation method. Critical factors of this method are the above mentioned affinity of the incoming anion, the exchange medium, the pH value and the chemical composition of the host layers.<sup>[94]</sup>

The “memory-effect” of LDHs is a very interesting property of this class of materials. Calcining of LDHs leads to the removal of water and interlayer anions to yield mixed metal oxides. By rehydration of these oxides in water and the presence of anions, LDH structures form again in which the anions do not necessarily have to be the same as in the previous ones.<sup>[96]</sup> This phenomenon opens up another strategy for anion exchange reactions if coprecipitation and direct exchange are no viable possibilities.

According to their anion exchange ability, LDHs are used as anion exchangers for water treatments of inorganic<sup>[97-98]</sup> and organic contaminants,<sup>[99-100]</sup> nuclear waste management of fission products,<sup>[101-102]</sup> and  $CO_2$  as well as  $NO_x$  separation and capture.<sup>[103-104]</sup> Besides applications in adsorption and ion exchangers, LDHs can be used in various fields of

## 1 INTRODUCTION

medicine and biochemistry. As mentioned above,  $[\text{Mg}_6\text{Al}_2(\text{OH})_{16}]\text{CO}_3 \cdot 4\text{H}_2\text{O}$  is used as an antacid drug. Moreover, LDHs are suitable as controlled release formulations (CRFs), i.e. pharmaceuticals that release drugs in a retarded fashion, because of their little systemic effect to the human body.<sup>[105]</sup> Thus, drug delivery into bowels and retarded release of drugs and vitamins can be achieved by LDHs.<sup>[106-109]</sup> In addition to pharmaceutical applications, catalysis - mainly base catalysis - is a field of application for LDHs. For example flavonone has been synthesized using a LiAl LDH,<sup>[110]</sup> alcohols have been oxidized by gold nanoparticles supported on LDH,<sup>[111]</sup> benzene has been oxidized to phenol by Cu LDH<sup>[112]</sup> and MgAl  $\text{CO}_3$  LDH catalyzes luminol chemiluminescence with potential for sensor applications.<sup>[113]</sup>

Annealing of LDHs leads to controlled thermal decomposition of the materials and the formation of mixed metal oxides with high surface areas ranging between  $110 - 300 \text{ m}^2 \text{ g}^{-1}$ <sup>[114]</sup> compared to other metal oxides.<sup>[115-116]</sup> In the early 1970s BASF showed that such metal oxides prepared by calcining LDHs containing different metal cations (Mg, Zn, Ni, Cr, Co, Mn and Al) at  $473 - 723 \text{ K}$  and partial chlorination can be used as effective supports for Ziegler-catalysts in the polymerization of olefins.<sup>[117]</sup> Moreover, it has been shown very recently by the O'Hare group that a NiTi LDH can be used as photocatalyst for the oxygen evolution reaction (OER) in water using visible light.<sup>[118]</sup>

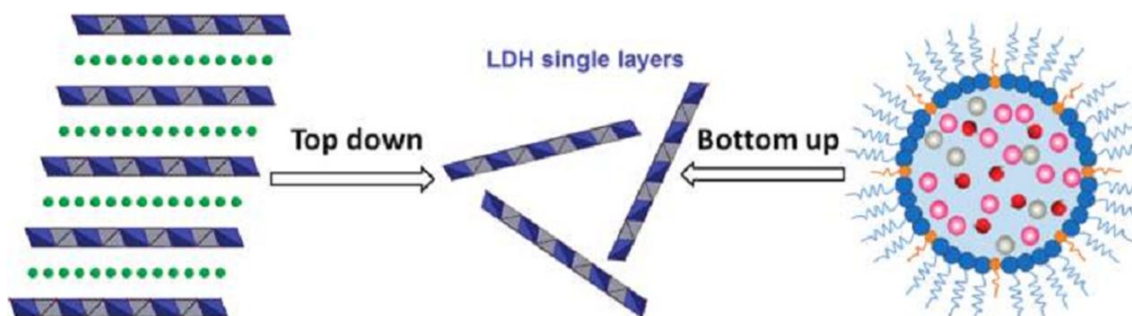


**Figure 1.5.** Scheme of top down and bottom up syntheses for LDH single layers. Reproduced from reference [119] with permission of The Royal Society of Chemistry.

Recently, a new field of applications has been opened up for LDHs. In 2000, Adachi-Pagano et al. were the first who reported on the successful delamination of a ZnAl LDH by refluxing the dodecyl sulfate intercalated LDH in butanol.<sup>[120]</sup> In general, exfoliation of LDHs into single layers can be achieved by two different synthetic routes. As shown in Fig. 1.5, top down and bottom up synthesis of LDH nanosheets is possible.<sup>[119]</sup> Whilst only

# 1 INTRODUCTION

a few LDH single layers have been successfully synthesized by bottom up synthesis in reverse microemulsion systems,<sup>[121-124]</sup> the top down method has been applied to many different hydrotalcites. The first top down synthesis has been achieved by refluxing in butanol; however, according to Hibino<sup>[125]</sup> formamide is predestined as solvent for exfoliation of LDHs. Owing to its ability to penetrate between the Brucite layers, the molecule breaks the hydrogen bonds in LDHs. In addition, the polar molecule can interact with the anions in the interlayer galleries and with the OH groups of the layers. Thus, the intercalant can be removed, which leads to exfoliation of the material.

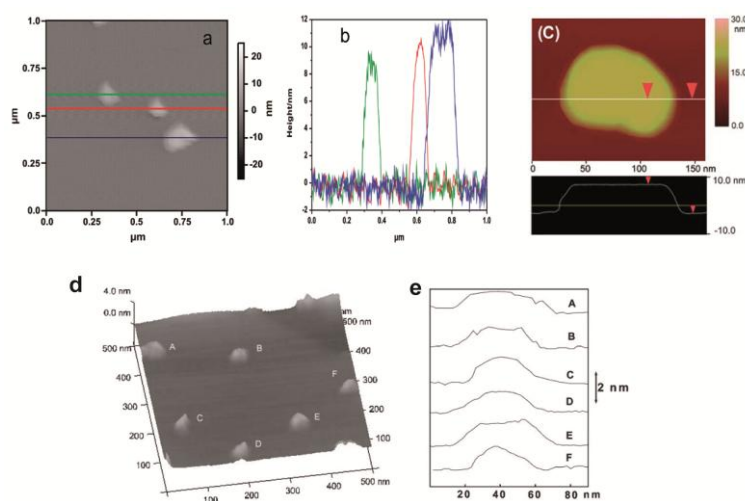


**Figure 1.6.** AFM images of different nanosheets with their corresponding height profiles: (a) and (b) “Top-down” exfoliated  $\text{Ni}^{\text{II}}\text{Al}^{\text{III}}$  LDH nanosheets. Reprinted with permission from reference [126]. Copyright (2010) American Chemical Society. (c) “top-down” exfoliated  $\text{Mg}^{\text{II}}\text{Al}^{\text{III}}$  LDH nanosheets. Reproduced from reference [127] with permission of The Royal Society of Chemistry. (d) and (e) bottom up exfoliated  $\text{M}^{\text{II}}\text{Al}^{\text{III}}$  nanosheets Reproduced from reference[121] with permission of The Royal Society of Chemistry.

The charge density of layered compounds is a critical factor that influences the feasibility of exfoliation. Since LDHs have significantly higher charge densities compared to other layered compounds, e.g. 0.040 electrons per  $\text{\AA}^2$  for  $\text{Zn}^{\text{II}}\text{Al}^{\text{III}}\text{NO}_3$  LDH<sup>[128]</sup> compared to 0.008-0.010 electrons per  $\text{\AA}^2$  for hectorite  $(\text{Na}_{0.3}(\text{Mg},\text{Li})_3(\text{Si}_4\text{O}_{10})(\text{F},\text{OH})_2)$ ,<sup>[119,129]</sup> it has been shown that the synthesis of LDH nanoplatelets is more difficult than exfoliation of other compounds.<sup>[96,119]</sup> However, several different LDHs such as  $\text{Mg}^{\text{II}}\text{Al}^{\text{III}}$ ,<sup>[130]</sup>  $\text{Co}^{\text{II}}\text{Al}^{\text{III}}$ ,<sup>[131]</sup>  $\text{Ni}^{\text{II}}\text{Al}^{\text{III}}$ ,<sup>[132]</sup>  $\text{Fe}^{\text{II}}\text{Al}^{\text{III}}$ ,<sup>[132]</sup>  $\text{Li}^{\text{I}}\text{Al}^{\text{III}}$ ,<sup>[133]</sup>  $\text{Co}^{\text{II}}\text{Fe}^{\text{III}}$ ,<sup>[134]</sup>  $\text{Co}^{\text{II}}\text{Co}^{\text{III}}$ ,<sup>[135]</sup> and  $\text{Co}^{\text{II}}\text{Ni}^{\text{II}}\text{Co}^{\text{III}}$  LDH<sup>[136]</sup> have been exfoliated by differently modified “top-down” techniques. Most publications

## 1 INTRODUCTION

about exfoliation of LDHs show the presence of thin films instead of delamination down to single layers. Simultaneously, the lateral particle size is mostly in the range of several hundreds of nanometers in comparison to several microns in other compounds. In Fig. 1.6 a,b nanosheets of  $\text{Ni}^{\text{II}}\text{Al}^{\text{III}}$  and  $\text{Mg}^{\text{II}}\text{Al}^{\text{III}}$  LDH (Fig. 1.6 c) are representatively shown to put the term “exfoliation of LDHs” into perspective compared to other materials. As can clearly be seen from these AFM images, the height of the sheets is between 10 and 2 nm and the shape of the particles in lateral as well as vertical direction is rather irregular. Taking the crystallographic thickness of Brucite layers of 0.48 nm into account, exfoliation down to single layers still remains a challenge. The “bottom-up” synthesis of LDH nanosheets that is carried out by coprecipitation in reverse microemulsions yields similar results as the top-down process. An AFM image of the nanosheets and the corresponding height profiles can be seen in Fig. 1.6 d and e. These results show the challenges of current research to produce well-defined cationically charged nanosheets delaminated down to single layers.

### 1.3 SILOXENE

Siloxene is a general term for layered silicon oxide-related compounds with a stoichiometry close to  $\text{Si}_6\text{H}_3(\text{OH})_3$ , which show structural differences as well as differences in the atomic connectivity of the silicon-based layers, namely Wöhler siloxene and Kautsky siloxene.

In 1863, Friedrich Wöhler synthesized the Zintl-phase compound  $\text{CaSi}_2$  from crystalline silicon, calcium chloride and sodium. He tested the obtained product for stability in different acids and claimed that its behavior in hydrochloric acid is the most “curious”.<sup>[137]</sup> He observed strong hydrogen evolution when  $\text{CaSi}_2$  was immersed in aqueous HCl and received a yellow-orange powder after completion of the reaction. He called the new product *Silicon*; later it was named Wöhler siloxene after its discoverer whereas its correct term regarding IUPAC nomenclature is 2-D-Poly[1,3,5-trihydroxyhexasilane].<sup>[138]</sup>  $\text{CaSi}_2$  is a Zintl-phase; these are composed of an electropositive ( $M$ ) and an electronegative ( $X$ ) metal and feature significant heteropolar binding character. Hence, the valence electrons of  $M$  can formally be transferred to  $X$ , yielding compounds with formal charges  $M^+X^-$ . Typically,  $M$  is an alkali, alkaline-earth metal or a lanthanide and  $X$  is a metal or semimetal of p-block elements of group III-V. The structure of the ionic compounds is dependent on the (8-N) rule.<sup>[139]</sup> Here, N is the number of valence electrons of the Zintl anions that are (8-N)-fold coordinated. In the case of  $(\text{Ca}^{2+})(\text{Si}^-)_2$ ,  $\text{Si}^-$  formally has five valence electrons and is thus  $(8-5) = 3$ -fold coordinated yielding a corrugated layered structure similar to the one of grey arsenic.<sup>[138,140]</sup>  $\text{Ca}^{2+}$  ions are intercalated between the silicon layers. By side and top view Figs. 1.7 a, b and c, d schematically show the layered structure of  $\text{CaSi}_2$  and Wöhler siloxene, respectively. As illustrated in Fig. 1.7 a and c, upon deintercalation of the  $\text{Ca}^{2+}$  ions and substitution by hydrogen as well as hydroxyl groups, the  $c$  spacing of the silicon backbone increases from 5.1 Å in  $\text{CaSi}_2$  to 5.4 – 6.2 Å in the resulting siloxene.<sup>[138,141-143]</sup> The synthesis of siloxene is achieved in a one step method.  $\text{CaSi}_2$  powder is immersed in ice-cooled concentrated HCl solution and stored in the dark for reaction for several hours until hydrogen evolution has stopped.<sup>[137,140]</sup> Similar to the synthesis and structure of Wöhler siloxene, another layered silicon structure without oxygen, polysilene, can be obtained. By carrying out the synthesis of Wöhler siloxene at  $-40^\circ\text{C}$  rather than at  $0 - 25^\circ\text{C}$ , hydrolysis of the silicon compound is largely avoided and thus polysilin ( $\text{Si}_6\text{H}_6$ ) is generated. Equation 1.2 describes the one-step synthesis of Wöhler siloxene. However, it can be split in two separate reaction steps. Firstly (Eq. 1.3), a topotactic reaction takes place removing the  $\text{Ca}^{2+}$  ions by solvation from the host lattice. During this process  $\text{Si}_6\text{H}_6$  and

## 1 INTRODUCTION

$\text{CaCl}_2(\text{aq})$  are formed. The second step (Eq. 1.4) describes the hydrolysis of polysilane that occurs only at temperatures at or above 0 °C.<sup>[138]</sup>

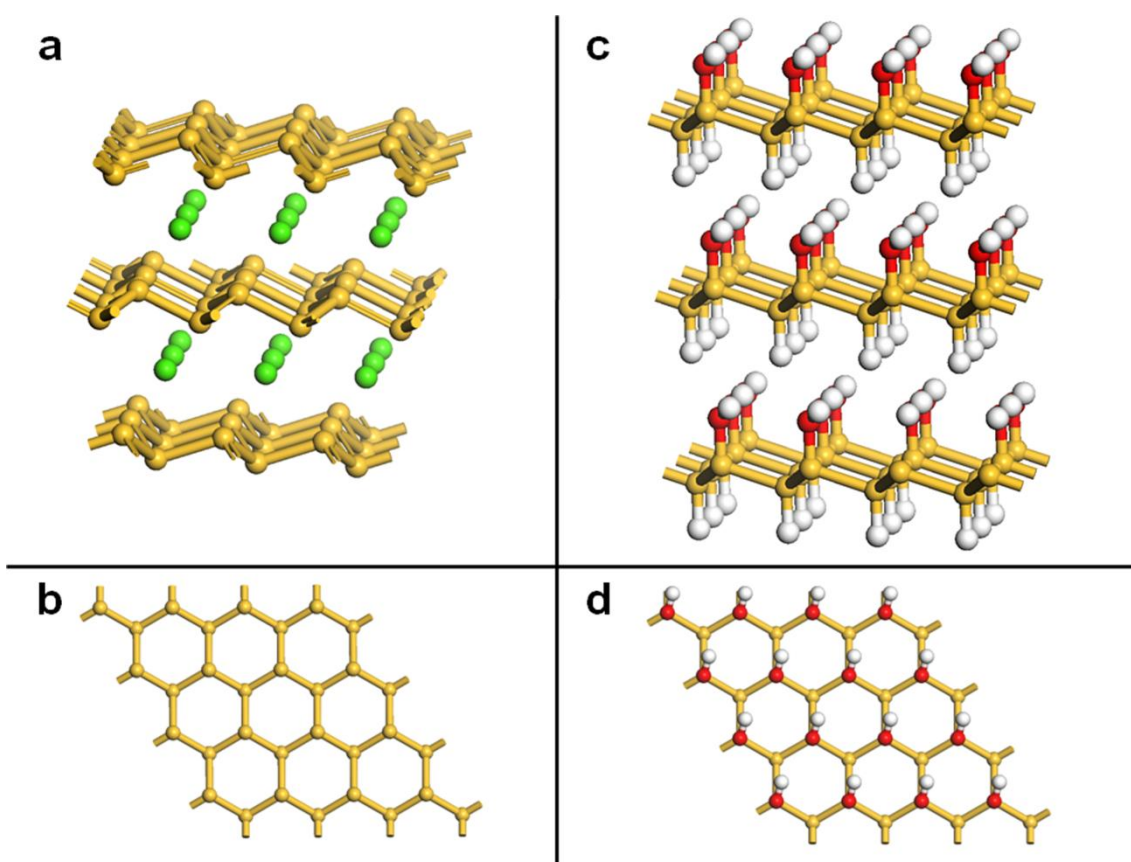
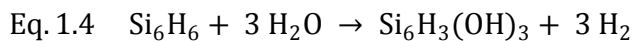
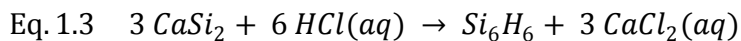
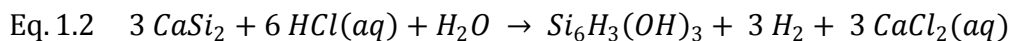


**Figure 1.7.** Crystallographic structure of  $\text{CaSi}_2$ : (a) side view and (b) top view onto a layer; Wöhler siloxene (c) side view and (d) top view onto a layer. (a) and (c) show the corrugated  $\text{Si}_6$ -rings forming the layered structure. Yellow, green, red and white spheres indicate silicon, calcium, oxygen and hydrogen atoms, respectively.

The synthesis of Wöhler siloxene is controversially discussed in the literature. Whilst Detlaff-Weglikowska et al.<sup>[140]</sup> claim that the reaction has to be carried out at 0 °C for three hours, Weiss et al. obtained single crystals of Wöhler siloxene at room temperature.<sup>[144]</sup> The



## 1 INTRODUCTION

latter mentioned that the oxygen content can be enriched in the product by higher temperatures and longer reaction times, leading to a sum formula of  $\text{Si}_6\text{H}_{3-x}(\text{OH})_{3+x}$  with  $x > 0$ .<sup>[138,144]</sup>

In addition to Wöhler siloxene a second modification, Kautsky siloxene, exists. In contrast to Wöhler siloxene the exact structure of this modification has not yet been determined. In 1921, Kautsky published his findings on the Wöhler compound that he obtained under “defined conditions”.<sup>[145]</sup> He synthesized the siloxene in an EtOH/H<sub>2</sub>O/conc. HCl solution and obtained a white-greenish powder, which he later called siloxene. He suggested the structure shown in Fig. 1.8 c based on elemental analysis and its chemical behavior against bromine and oxidizing agents, especially acids.<sup>[146-148]</sup>

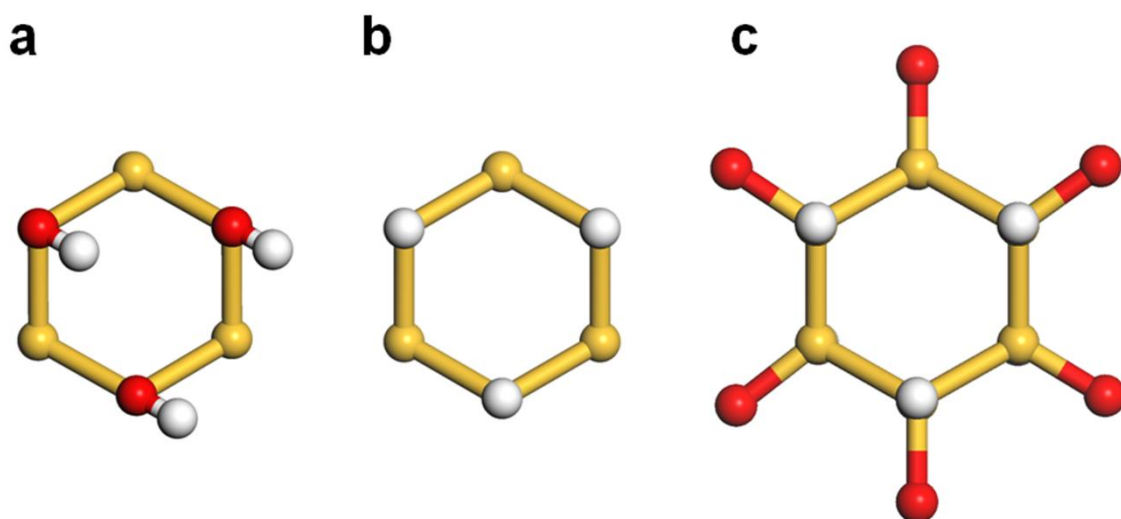


**Figure 1.8.** Smallest periodic 2D building block of (a) Wöhler siloxene, (b) polysilene and (c) Kautsky siloxene. Yellow, red and white spheres represent silicon, oxygen and hydrogen atoms, respectively. Note that half of the hydrogen atoms in (b) and (c) lie above and half lie below the Si plane.

In Kautsky siloxene the silicon forms six-rings but in contrast to the structure of Wöhler siloxene and polysilene (Fig. 1.8 a and b), the Si<sub>6</sub>-rings are interconnected by oxygen to form an infinite 2D network. The hydrogen is bound to the silicon atoms alternately above or below the layer. However, the accurate composition was not determined until 1999 by Kurmaev et al. based on Si L<sub>2,3</sub> x-ray emission spectroscopy (XES).<sup>[149]</sup> Hence, the Kautsky siloxene consists of 60.7% of the compound Kautsky proposed, 20.5% of H-Si-O<sub>3</sub> units and 18.8% of H-Si-(SiO<sub>2</sub>) units. The Si-O-Si bond angle of 180° in the idealized structure in Fig. 1.8 c is controversially discussed in the literature. According to Detlaff-Weglikowska

## 1 INTRODUCTION

et al. the energetically most favorable bond angle deviates from  $180^\circ$ , leading to a loss of the planar structure, whereas Gallo mentions that the  $180^\circ$  bond angle leads to ring strain that reduces the activation energy for rearrangement reactions.<sup>[138,140]</sup>

Little has yet been done on the elucidation of the siloxene structures by solid-state NMR spectroscopy. Only Brandt, Ready and Boyce reported on their results concerning  $^{29}\text{Si}$  nuclear magnetic resonance of luminescent silicon.<sup>[150]</sup> In their work they compare the peak positions of  $^{29}\text{Si}$  NMR of siloxene to those of crystalline, amorphous, and porous silicon as well as  $\text{SiO}_2$ , concluding that as-prepared Wöhler siloxene consists of a Si threefold coordinated planar structure and an additional oxide phase.

Due to their layered structure, siloxene and polysilene have attracted attention recently in the field of nanosheet research. Nakano et al. reported in 2005 on novel  $\text{Si}_6\text{H}_3(\text{OH})_3$  nanosheets exfoliated by using the organic surfactant dodecyl sulfate.<sup>[41]</sup> Thereby, they opened up a new field of research in silicon based nanosheets. In 2006, a Mg-doped  $\text{CaSi}_2$  ( $\text{CaSi}_{1.85}\text{Mg}_{0.15}$ ) was exfoliated in propylamine hydrochloride solution.<sup>[151]</sup> In order to obtain oxygen free nanosheets, subsequent research focused on the exfoliation of polysilene. Hence,  $\text{Si}_6\text{H}_6$  was exfoliated by reacting it with *n*-decylamine to form Si-N linkages and simultaneous exfoliation.<sup>[39]</sup> Later, polysilene nanosheets were obtained by forming a Si-C bond either by Grignard reaction or hydrosilylation.<sup>[40,152]</sup> Since the mentioned results are the only ones that were obtained for Si-based nanosheets, summing up it can be said that little has been undertaken in this area of research as yet.

### 1.4 LAYER-BY-LAYER ASSEMBLY

The design of solids with tailor-made properties is a key challenge and a major driving force of current research in chemistry and materials science. In classical solid-state chemistry mainly relying on high-temperature and high-pressure reaction protocols, the spectrum of products is typically limited due to the dependence of the synthesis on thermodynamic principles. In contrast, soft chemistry takes advantage of low reaction temperatures and hence kinetically controlled reactions, and thus opens up new synthetic routes based on preformed building blocks to create tailor-made artificial solids. Despite a lack of stability of many products synthesized by soft chemical protocols, especially the precise control over the composition of artificial solids is of great interest. This enables the design of materials that are inaccessible by conventional synthetic routes with combined properties of their constituent building blocks. The discovery of 2D nanosheets as preformed building blocks for hierarchical superlattices has taken up pace recently and was particularly developed by the pioneering work of Mallouk et al.<sup>[43-44,54,153-155]</sup> and Sasaki et al.<sup>[156-159]</sup> The broad scope of layered materials ranging from van der Waals solids such as graphene to ionic solids like metal oxides and hydroxides, the layer-by-layer method draws on a huge source of building blocks leading to a seemingly infinite variety of new multifunctional materials. In general, the combination of nanosheets to yield hybrid materials can be achieved by three different synthetic routes: flocculation, electrostatic layer-by-layer (LBL) deposition or by the Langmuir-Blodgett (LB) method. In Fig. 1.9 the three different synthetic routes are schematically depicted.

Flocculation yields randomly stacked, partially micro- and mesoporous nonaocomposites based on oppositely charged nanosheets. The hybrid compound is synthesized by mixing the colloidal suspensions of nanosheets. The negatively and positively charged nanosheets and counterions restack immediately upon mixing of the suspensions, building interstratified heterostructures which typically lack well-defined structures of the interlayer gallery as well as of the overall compound.<sup>[160]</sup> However, the flocculation method can be used to synthesize functional materials for electronic devices such as supercapacitors<sup>[161-163]</sup> or Li-ion batteries,<sup>[164]</sup> photoluminescent materials<sup>[165-166]</sup> and photocatalytically active compounds where pronounced structural order and a particular stoichiometry are less important.<sup>[167]</sup> In order to obtain hybrid compounds with defined structures, the electrostatic sequential assembly or Langmuir-Blodgett method are applied. Decher developed the electrostatic sequential deposition (ESD) technique to fabricate polymer films based on

## 1 INTRODUCTION

oppositely charged polyelectrolytes.<sup>[168]</sup> Later this method was extended to other materials such as proteins and colloidal nanoparticles.<sup>[160]</sup> This generic method relies on the electrostatic attraction and repulsion of the particles used and thus sequentially deposited single layers of different materials can be obtained on a predefined surface with a high level of control. As shown in Fig. 1.9 b the adsorption step of cationic and anionic particles is applied sequentially in order to obtain precise control over the nanoarchitecture. Nanosheets obtained from layered ionic solids are suited well for this technique because of their negative or positive layer charge. In this sense, charged nanosheets can be considered as “inorganic polyelectrolytes”. As described previously the ESD method was initially developed to assemble polyelectrolytes.<sup>[168]</sup> Subsequently, polyelectrolytes and nanosheets were assembled<sup>[155-157,169]</sup> before “nanosheet only” multilayer stacks were fabricated as will be discussed in more detail in chapter 4.<sup>[170-174]</sup>

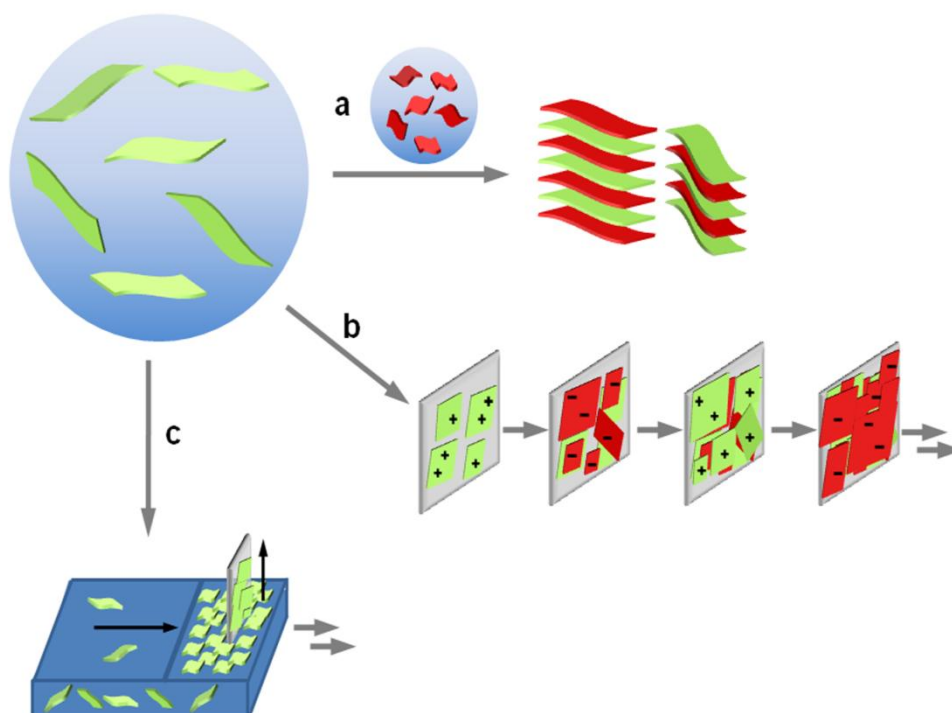


**Figure 1.9.** Illustration of different soft synthesis methods to obtain multilayer materials from nanosheet building blocks: (a) flocculation, (b) electrostatic sequential deposition (LBL) and (c) Langmuir-Blodgett method. Nanosheets are deposited on a substrate (grey rectangle) in methods (b) and (c).

In contrast to ESD, the LB method can in principle be applied to any kind of nanosheet and does not depend on the surface charge of the particles. This technique relies on the

## 1 INTRODUCTION

increasing particle concentration and simultaneous decrease of the surface area of the solvent. Therefore, an amphiphilic molecule is necessary, which is present in concentrations below the critical micellar concentration (CMC) to avoid the formation of micelles. However, it has been shown that LB deposition could be achieved without the use of amphiphiles.<sup>[175]</sup> As depicted in Fig. 1.9 c a colloidal suspension below CMC forms a monolayer of the particles at the solvent-air interface. By compressing the surface area with the help of a sliding barrier in a LB trough the monolayer at the surface becomes densely packed and can thus be transferred to a substrate that is vertically dipped into or lifted out of the suspension.<sup>[8]</sup> By repeated deposition of the same or different particle layers on top of each other multilayer assemblies can be achieved. Using the LB method different multilayer lattices composed of nanosheets have already been achieved yielding films with interesting properties such as photoconductivity,<sup>[176-177]</sup> high-k dielectric properties<sup>[178-179]</sup> or ferroelectricity.<sup>[180]</sup>

## 1 INTRODUCTION

### 1.5 OBJECTIVE

The synthesis of nanosheets and the formation of hybrid materials built of single layers has attracted much attention during the last years due to the expected versatile properties exhibited by nanosheets and their hybrid lattices, and the high level of control that is inherent to the nanoscale assembly process for the fabrication of complex solids. Especially in electronic devices small components are necessary in order to enhance the performance of these devices, and miniaturization is a key challenge which can be tackled by employing nanosheet rather than bulk materials. According to their anisotropy and thickness in the nanometer range, hybrid compounds synthesized from nanosheets are suited very well for application in such devices. A large variety of different nanosheets is indispensable for the extension of the nanosheet toolbox and their combination using layer-by-layer techniques. In addition, analysis of the parent bulk compounds of nanosheets and the structure of the hybrid materials is of high interest in order to understand the properties of the compounds and to optimize synthetic requirements. Therefore, this dissertation is divided into three main chapters that include the synthesis and identification of positively charged nanosheets, the formation of multilayer stacks including in-depth analysis as well as investigation and organic modification of the layered compound siloxene. In the following, the content of the chapters are discussed in more detail:

In nanosheet research positively charged nanosheets derived from layered double hydroxides are of particular interest since the fabrication of multilayer films by ESD requires anionic and cationic nanosheets. To date cationic nanosheets, precisely LDH nanosheets, are still scarce in comparison to their anionic counterparts. Hence, chapter 3 focuses on the exfoliation of MnAl LDH into nanosheets to extend the toolbox of cationic single layered materials. In addition, the LDH nanosheets were restacked with graphene oxide by flocculation to yield a hybrid compound that may be interesting for electronic applications.

In comparison to flocculation, which cannot be used to synthesize well-defined structures, chapter 4 is focused on ESD to yield ordered multilayer films composed of oppositely charged nanosheets. Therefore, MnAl LDH and  $\text{TBACa}_2\text{Nb}_3\text{O}_{10}$  nanosheets were sequentially assembled on a substrate to yield well-defined hybrid multilayer films. In this part the synthesis as well as the in-depth analysis of the formed compound is of interest. Analysis was achieved by transmission electron microscopy and electron energy loss

## 1 INTRODUCTION

spectroscopy of the prepared stacks to determine the exact structure of the multilayer stacks on the molecular level. Knowledge of the exact structure and composition of the compounds including voids and defects is important in order to understand the properties of the materials and to optimize the synthesis conditions for the design of future hybrid stacks.

The third goal of this thesis is the synthesis of nanosheets obtained from Zintl phase calcium disilicide and the analysis of the parent bulk compound siloxene, which is both discussed in chapter 5. Silicon is one of the most important semiconducting materials and little work has been done in the synthesis of single layered silicon based compounds as yet. By reacting  $\text{CaSi}_2$  with aqueous HCl the layered compound siloxene forms, which can be soft chemically exfoliated into alkyl modified single sheets. Nevertheless, since Wöhler siloxene rearranges into Kautsky siloxene under ambient atmosphere and in the presence of light, to date no detailed solid-state NMR investigation has been undertaken in order to elucidate the structure of these compounds or mixtures thereof, respectively. On that account a  $^{29}\text{Si}$  NMR study accompanied by IR and Raman spectroscopy is carried out to determine and study the composition of this compound. This is essential not only to understand the structure and composition of the bulk compound, but also the structure of the nanosheets derived from siloxene.

## 1.6 BIBLIOGRAPHY

- [1] K. S. Novoselov, A. K. Geim, S. V. Morozov, D. Jiang, Y. Zhang, S. V. Dubonos, I. V. Grigorieva, A. A. Firsov, *Science* **2004**, *306*, 666-669.
- [2] S. Z. Butler, S. M. Hollen, L. Cao, Y. Cui, J. A. Gupta, H. R. Gutiérrez, T. F. Heinz, S. S. Hong, J. Huang, A. F. Ismach, E. Johnston-Halperin, M. Kuno, V. V. Plashnitsa, R. D. Robinson, R. S. Ruoff, S. Salahuddin, J. Shan, L. Shi, M. G. Spencer, M. Terrones, W. Windl, J. E. Goldberger, *ACS Nano* **2013**, *7*, 2898-2926.
- [3] K. J. Koski, Y. Cui, *ACS Nano* **2013**, *7*, 3739-3743.
- [4] "The Nobel Prize in Physics 2010". *Nobelprize.org*. Nobel Media AB 2013. Web. 27 Mar 2014. <[http://www.nobelprize.org/nobel\\_prizes/physics/laureates/2010/](http://www.nobelprize.org/nobel_prizes/physics/laureates/2010/)>.
- [5] A. K. Geim, K. S. Novoselov, *Nat. Mater.* **2007**, *6*, 183-191.
- [6] H. P. Boehm, A. Clauss, Fischer, G.O., U. Hofmann, *Z. Naturforsch. B* **1962**, *17b*, 150-153.
- [7] M. Osada, T. Sasaki, *J. Mater. Chem.* **2009**, *19*, 2503-2511.
- [8] R. Ma, T. Sasaki, *Adv. Mater.* **2010**, *22*, 5082-5104.
- [9] M. Xu, T. Liang, M. Shi, H. Chen, *Chem. Rev.* **2013**, *113*, 3766-3798.
- [10] M. J. Allen, V. C. Tung, R. B. Kaner, *Chem. Rev.* **2009**, *110*, 132-145.
- [11] C. N. R. Rao, K. Biswas, K. S. Subrahmanyam, A. Govindaraj, *J. Mater. Chem.* **2009**, *19*, 2457-2469.
- [12] A. K. Geim, *Science* **2009**, *324*, 1530-1534.
- [13] P. R. Wallace, *Phys. Rev.* **1947**, *71*, 622-634.
- [14] G. F. Walker, *Nature* **1960**, *187*, 312-313.
- [15] R. F. Frindt, *J. Appl. Phys.* **1966**, *37*, 1928-1929.
- [16] H. P. Boehm, A. Clauss, G. O. Fischer, U. Hofmann, *Z. anorg. allg. Chem.* **1962**, *316*, 119-127.
- [17] U. Hofmann, A. Frenzel, E. Csalán, *Liebigs Ann. Chem.* **1934**, *510*, 1-41.
- [18] A. Clause, R. Plass, H. P. Boehm, U. Hofmann, *Z. anorg. allg. Chem.* **1957**, *291*, 205-220.
- [19] G. Ruess, *Monatsh. Chem. Verw. Tl.* **1947**, *76*, 381-417.



## 1 INTRODUCTION

- [20] U. Hofmann, E. König, *Z. anorg. allg. Chem.* **1937**, 234, 311-336.
- [21] S. Stankovich, R. D. Piner, X. Chen, N. Wu, S. T. Nguyen, R. S. Ruoff, *J. Mater. Chem.* **2006**, 16, 155-158.
- [22] D. Li, M. B. Muller, S. Gilje, R. B. Kaner, G. G. Wallace, *Nat. Nano* **2008**, 3, 101-105.
- [23] Y. Xu, H. Bai, G. Lu, C. Li, G. Shi, *J. Am. Chem. Soc.* **2008**, 130, 5856-5857.
- [24] X. Fan, W. Peng, Y. Li, X. Li, S. Wang, G. Zhang, F. Zhang, *Adv. Mater.* **2008**, 20, 4490-4493.
- [25] G. Williams, B. Seger, P. V. Kamat, *ACS Nano* **2008**, 2, 1487-1491.
- [26] H. C. Schniepp, J.-L. Li, M. J. McAllister, H. Sai, M. Herrera-Alonso, D. H. Adamson, R. K. Prud'homme, R. Car, D. A. Saville, I. A. Aksay, *J. Phys. Chem. B* **2006**, 110, 8535-8539.
- [27] F. Consadori, A. A. Fife, R. F. Frindt, S. Gygax, *Appl. Phys. Lett.* **1971**, 18, 233-235.
- [28] R. F. Frindt, *Phys. Rev. Lett.* **1972**, 28, 299-301.
- [29] J. A. Wilson, A. D. Yoffe, *Adv. Phys.* **1969**, 18, 193-335.
- [30] J. N. Coleman, M. Lotya, A. O'Neill, S. D. Bergin, P. J. King, U. Khan, K. Young, A. Gaucher, S. De, R. J. Smith, I. V. Shvets, S. K. Arora, G. Stanton, H.-Y. Kim, K. Lee, G. T. Kim, G. S. Duesberg, T. Hallam, J. J. Boland, J. J. Wang, J. F. Donegan, J. C. Grunlan, G. Moriarty, A. Shmeliov, R. J. Nicholls, J. M. Perkins, E. M. Grieveson, K. Theuwissen, D. W. McComb, P. D. Nellist, V. Nicolosi, *Science* **2011**, 331, 568-571.
- [31] P. Goli, J. Khan, D. Wickramaratne, R. K. Lake, A. A. Balandin, *Nano Lett.* **2012**, 12, 5941-5945.
- [32] D. Liu, W. Zhang, D. Mou, J. He, Y.-B. Ou, Q.-Y. Wang, Z. Li, L. Wang, L. Zhao, S. He, Y. Peng, X. Liu, C. Chen, L. Yu, G. Liu, X. Dong, J. Zhang, C. Chen, Z. Xu, J. Hu, X. Chen, X. Ma, Q. Xue, X. J. Zhou, *Nat. Commun* **2012**, 3, 931.
- [33] Y. Sun, Z. Sun, S. Gao, H. Cheng, Q. Liu, J. Piao, T. Yao, C. Wu, S. Hu, S. Wei, Y. Xie, *Nat. Commun.* **2012**, 3, 1057.
- [34] D. Kong, W. Dang, J. J. Cha, H. Li, S. Meister, H. Peng, Z. Liu, Y. Cui, *Nano Lett.* **2010**, 10, 2245-2250.

## 1 INTRODUCTION

- [35] K. M. F. Shahil, M. Z. Hossain, D. Teweldebrhan, A. A. Balandin, *Appl. Phys. Lett.* **2010**, 96, 153103.
- [36] K. K. Kim, A. Hsu, X. Jia, S. M. Kim, Y. Shi, M. Hofmann, D. Nezich, J. F. Rodriguez-Nieva, M. Dresselhaus, T. Palacios, J. Kong, *Nano Lett.* **2012**, 12, 161-166.
- [37] M. Naguib, M. Kurtoglu, V. Presser, J. Lu, J. Niu, M. Heon, L. Hultman, Y. Gogotsi, M. W. Barsoum, *Adv. Mater.* **2011**, 23, 4248-4253.
- [38] Z. Gao, W. Yang, Y. Yan, J. Wang, J. Ma, X. Zhang, B. Xing, L. Liu, *Eur. J. Inorg. Chem.* **2013**, 2013, 4832-4838.
- [39] H. Okamoto, Y. Kumai, Y. Sugiyama, T. Mitsuoka, K. Nakanishi, T. Ohta, H. Nozaki, S. Yamaguchi, S. Shirai, H. Nakano, *J. Am. Chem. Soc.* **2010**, 132, 2710-2718.
- [40] Y. Sugiyama, H. Okamoto, T. Mitsuoka, T. Morikawa, K. Nakanishi, T. Ohta, H. Nakano, *J. Am. Chem. Soc.* **2010**, 132, 5946-5947.
- [41] H. Nakano, M. Ishii, H. Nakamura, *Chem. Commun.* **2005**, 0, 2945-2947.
- [42] E. Bianco, S. Butler, S. Jiang, O. D. Restrepo, W. Windl, J. E. Goldberger, *ACS Nano* **2013**, 7, 4414-4421.
- [43] R. E. Schaak, T. E. Mallouk, *Chem. Mater.* **2000**, 12, 3427-3434.
- [44] R. E. Schaak, T. E. Mallouk, *Chem. Mater.* **2000**, 12, 2513-2516.
- [45] R. E. Schaak, T. E. Mallouk, *Chem. Commun.* **2002**, 706-707.
- [46] E. S. H. Leach, A. Hopkinson, K. Franklin, J. S. van Duijneveldt, *Langmuir* **2005**, 21, 3821-3830.
- [47] K. Norrish, *Discuss. Faraday Soc.* **1954**, 18, 120-134.
- [48] G. Alberti, M. Casciola, U. Costantino, *J. Colloid Interface Sci.* **1985**, 107, 256-263.
- [49] G. Alberti, C. Dionigi, E. Giontella, S. Murcia-MascarÃ³s, R. Vivani, *J. Colloid Interface Sci.* **1997**, 188, 27-31.
- [50] N. Yamamoto, T. Okuhara, T. Nakato, *J. Mater. Chem.* **2001**, 11, 1858-1863.
- [51] M. A. Bizeto, A. L. Shiguihara, V. R. L. Constantino, *J. Mater. Chem.* **2009**, 19, 2512-2525.
- [52] M. M. J. Treacy, S. B. Rice, A. J. Jacobson, J. T. Lewandowski, *Chem. Mater.* **1990**, 2, 279-286.

## 1 INTRODUCTION

- [53] K. S. Viridi, Y. Kauffmann, C. Ziegler, P. Ganter, B. V. Lotsch, W. D. Kaplan, P. Blaha, C. Scheu, *Phys. Rev. B* **2013**, *87*, 115108.
- [54] R. E. Schaak, T. E. Mallouk, *Chem. Mater.* **2002**, *14*, 1455-1471.
- [55] Y.-S. Han, I. Park, J.-H. Choy, *J. Mater. Chem.* **2001**, *11*, 1277-1282.
- [56] Y. Ebina, T. Sasaki, M. Watanabe, *Solid State Ionics* **2002**, *151*, 177-182.
- [57] T. Sasaki, M. Watanabe, H. Hashizume, H. Yamada, H. Nakazawa, *J. Am. Chem. Soc.* **1996**, *118*, 8329-8335.
- [58] T. Sasaki, M. Watanabe, *J. Am. Chem. Soc.* **1998**, *120*, 4682-4689.
- [59] W. Sugimoto, O. Terabayashi, Y. Murakami, Y. Takasu, *J. Mater. Chem.* **2002**, *12*, 3814-3818.
- [60] N. Miyamoto, K. Kuroda, M. Ogawa, *J. Mater. Chem.* **2004**, *14*, 165-170.
- [61] Z.-h. Liu, K. Ooi, H. Kanoh, W.-p. Tang, T. Tomida, *Langmuir* **2000**, *16*, 4154-4164.
- [62] Q. Gao, O. Giraldo, W. Tong, S. L. Suib, *Chem. Mater.* **2001**, *13*, 778-786.
- [63] Y. Omomo, T. Sasaki, Wang, M. Watanabe, *J. Am. Chem. Soc.* **2003**, *125*, 3568-3575.
- [64] X. Yang, Y. Makita, Z.-h. Liu, K. Sakane, K. Ooi, *Chem. Mater.* **2004**, *16*, 5581-5588.
- [65] A. Takagaki, T. Yoshida, D. Lu, J. N. Kondo, M. Hara, K. Domen, S. Hayashi, *J. Phys. Chem. B* **2004**, *108*, 11549-11555.
- [66] K. Fukuda, I. Nakai, Y. Ebina, R. Ma, T. Sasaki, *Inorg. Chem.* **2007**, *46*, 4787-4789.
- [67] K. Fukuda, K. Akatsuka, Y. Ebina, R. Ma, K. Takada, I. Nakai, T. Sasaki, *ACS Nano* **2008**, *2*, 1689-1695.
- [68] T. C. Ozawa, K. Fukuda, K. Akatsuka, Y. Ebina, T. Sasaki, K. Kurashima, K. Kosuda, *J. Phys. Chem. C* **2008**, *112*, 1312-1315.
- [69] M. Dion, M. Ganne, M. Tournoux, *Mater. Res. Bull.* **1981**, *16*, 1429-1435.
- [70] M. Kato, A. Inoue, I. Nagai, M. Kakihana, A. W. Sleight, Y. Koike, *Physica C* **2003**, *388-389*, 445-446.
- [71] O. C. Compton, F. E. Osterloh, *J. Phys. Chem. C* **2008**, *113*, 479-485.
- [72] K. Maeda, T. E. Mallouk, *J. Mater. Chem.* **2009**, *19*, 4813-4818.

## 1 INTRODUCTION

- [73] J. Zhao, F. E. Osterloh, *J. Phys. Chem. Lett.* **2014**, 5, 782-786.
- [74] E. Manasse, *Atti. Soc. Toscana Sci. Nat.* **1915**, 24, 92.
- [75] U. König, *Synthese, Charakterisierung und Eigenschaften von manganhaltigen Layered Double Hydroxides (LDHs)*, Halle, **2006**.
- [76] W. Feitknecht, M. Gerber, *Helv. Chim. Acta* **1942**, 25, 131-137.
- [77] R. Allmann, *Acta Crystallogr. B* **1968**, 24, 972-977.
- [78] H. F. W. Taylor, *Mineral. Mag.* **1969**, 37, 338-342.
- [79] A. I. Khan, D. O'Hare, *J. Mater. Chem.* **2002**, 12, 3191-3198.
- [80] M. R. Weir, J. Moore, R. A. Kydd, *Chem. Mater.* **1997**, 9, 1686-1690.
- [81] S. Carlino, *Solid State Ionics* **1997**, 98, 73-84.
- [82] D. G. Evans, X. Duan, *Struct. Bond.* **2005**, 119, 1.
- [83] K. Shinoda, N. Aikawa, *Phys. Chem. Miner.* **1998**, 25, 197-202.
- [84] M. Catti, G. Ferraris, S. Hull, A. Pavese, *Phys. Chem. Miner.* **1995**, 22, 200-206.
- [85] M. François, G. Renaudin, O. Evrard, *Acta Crystallogr. C* **1998**, 54, 1214-1217.
- [86] A. M. Fogg, J. S. Dunn, S.-G. Shyu, D. R. Cary, D. O'Hare, *Chem. Mater.* **1998**, 10, 351-355.
- [87] S. Werner, V. W.-h. Lau, S. Hug, V. Duppel, H. Clausen-Schaumann, B. V. Lotsch, *Langmuir* **2013**, 29, 9199-9207.
- [88] A. M. Fogg, J. S. Dunn, D. O'Hare, *Chem. Mater.* **1998**, 10, 356-360.
- [89] S. K. Yun, V. R. L. Constantino, T. J. Pinnavaia, *Clays Clay Miner.* **1995**, 43, 503-510.
- [90] A. S. Prakash, P. V. Kamath, M. S. Hegde, *Mater. Res. Bull.* **2000**, 35, 2189-2197.
- [91] J. D. Wang, G. Serrette, Y. Tian, A. Clearfield, *Appl. Clay Sci.* **1995**, 10, 103-115.
- [92] M. A. Drezdson, *Inorg. Chem.* **1988**, 27, 4628-4632.
- [93] J. He, M. Wei, B. Li, Y. Kang, D. Evans, X. Duan, X. Duan, *Preparation of Layered Double Hydroxides*, **2006**, pp. 89-119.
- [94] F. Seel, *Grundlagen der analytischen Chemie* **1976**, 176.
- [95] A. Vaccari, *Appl. Clay Sci.* **1999**, 14, 161-198.

## 1 INTRODUCTION

- [96] S. Radha, W. Milius, J. Breu, P. V. Kamath, *J. Solid State Chem.* **2013**, 204, 362-366.
- [97] G. V. Manohara, D. A. Kunz, P. V. Kamath, W. Milius, J. Breu, *Langmuir* **2010**, 26, 15586-15591.
- [98] L. Lv, J. He, M. Wei, D. G. Evans, X. Duan, *J. Hazard. Mater.* **2006**, 133, 119-128.
- [99] L. Lv, P. Sun, Z. Gu, H. Du, X. Pang, X. Tao, R. Xu, L. Xu, *J. Hazard. Mater.* **2009**, 161, 1444-1449.
- [100] F. Li, Y. Wang, Q. Yang, D. G. Evans, C. Forano, X. Duan, *J. Hazard. Mater.* **2005**, 125, 89-95.
- [101] M. Bouraada, M. Lafjah, M. S. Ouali, L. C. de Menorval, *J. Hazard. Mater.* **2008**, 153, 911-918.
- [102] L. Liang, L. Li, *J. Radioanal. Nucl. Chem.* **2007**, 273, 221-226.
- [103] Y. You, G. F. Vance, H. Zhao, *Appl. Clay Sci.* **2001**, 20, 13-25.
- [104] J. J. Yu, X. P. Wang, Y. X. Tao, Z. P. Hao, Z. P. Xu, *Ind. Eng. Chem. Res.* **2007**, 46, 5794-5797.
- [105] N. Hutson, B. Attwood, *Adsorption* **2008**, 14, 781-789.
- [106] S.-Y. Kwak, W. M. Kriven, M. A. Wallig, J.-H. Choy, *Biomaterials* **2004**, 25, 5995-6001.
- [107] A. I. Khan, L. Lei, A. J. Norquist, D. O'Hare, *Chem. Commun.* **2001**, 2342-2343.
- [108] L. L. Qin, M. Wang, R. R. Zhu, S. H. You, P. Zhou, S. L. Wang, *Int. J. Nanomed.* **2013**, 8, 2053-2064.
- [109] V. Bugatti, G. Gorrasi, F. Montanari, M. Nocchetti, L. Tammara, V. Vittoria, *Appl. Clay Sci.* **2011**, 52, 34-40.
- [110] J.-H. Choy, Y.-H. Son, *Bull. Korean Chem. Soc.* **2004**, 25, 122-126.
- [111] D. French, P. Schifano, J. Cortés-Concepción, S. Hargrove-Leak, *Catal. Commun.* **2010**, 12, 92-94.
- [112] L. Wang, X. Meng, F. Xiao, *Chinese J. Cat.* **2010**, 31, 943-947.
- [113] C. A. Antonyraj, S. Kannan, *Appl. Clay Sci.* **2011**, 53, 297-304.
- [114] Z. Wang, F. Liu, C. Lu, *Chem. Commun.* **2011**, 47, 5479-5481.
- [115] F. Li, X. Duan, *Struct. Bond.* **2006**, 119, 193-223.

## 1 INTRODUCTION

- [116] N.-K. Park, J. D. Lee, T. J. Lee, S. O. Ryu, C. H. Chang, *Fuel* **2005**, *84*, 2165-2171.
- [117] A. Nell, A. B. Getsoian, S. Werner, L. Kiwi-Minsker, A. T. Bell, *Langmuir* **2014**, *30*, 873-880.
- [118] H. D. Frielingsdorf, H. D. Mueller-Tamm, G. D. Schweier, L. Reuter, *Deutsches Patent*, **1973**.
- [119] Y. Zhao, B. Li, Q. Wang, W. Gao, C. J. Wang, M. Wei, D. G. Evans, X. Duan, D. O'Hare, *Chem. Sci.* **2014**.
- [120] Q. Wang, D. O'Hare, *Chem. Rev.* **2012**, *112*, 4124-4155.
- [121] M. Adachi-Pagano, C. Forano, J.-P. Besse, *Chem. Commun.* **2000**, 91-92.
- [122] G. Hu, N. Wang, D. O'Hare, J. Davis, *Chem. Commun.* **2006**, 287-289.
- [123] G. Hu, D. O'Hare, *J. Am. Chem. Soc.* **2005**, *127*, 17808-17813.
- [124] G. Hu, N. Wang, D. O'Hare, J. Davis, *J. Mater. Chem.* **2007**, *17*, 2257-2266.
- [125] M. E. Pérez-Bernal, R. J. Ruano-Casero, F. Benito, V. Rives, *J. Solid State Chem.* **2009**, *182*, 1593-1601.
- [126] T. Hibino, *Chem. Mater.* **2004**, *16*, 5482-5488.
- [127] M. Meyn, K. Beneke, G. Lagaly, *Inorg. Chem.* **1990**, *29*, 5201-5207.
- [128] A. R. Mermut, G. Lagaly, *Clays Clay Miner.* **2001**, *49*, 393-397.
- [129] T. Hibino, W. Jones, *J. Mater. Chem.* **2001**, *11*, 1321-1323.
- [130] Z. Liu, R. Ma, M. Osada, N. Iyi, Y. Ebina, K. Takada, T. Sasaki, *J. Am. Chem. Soc.* **2006**, *128*, 4872-4880.
- [131] Z. Liu, R. Ma, Y. Ebina, N. Iyi, K. Takada, T. Sasaki, *Langmuir* **2007**, *23*, 861-867.
- [132] M. Singh, M. I. Ogden, G. M. Parkinson, C. E. Buckley, J. Connolly, *J. Mater. Chem.* **2004**, *14*, 871-874.
- [133] R. Ma, Z. Liu, K. Takada, N. Iyi, Y. Bando, T. Sasaki, *J. Am. Chem. Soc.* **2007**, *129*, 5257-5263.
- [134] R. Ma, K. Takada, K. Fukuda, N. Iyi, Y. Bando, T. Sasaki, *Angew. Chem. Int. Ed.* **2008**, *47*, 86-89.
- [135] J. Liang, R. Ma, N. Iyi, Y. Ebina, K. Takada, T. Sasaki, *Chem. Mater.* **2010**, *22*, 371-378.
- [136] Y. Zhao, W. Yang, Y. Xue, X. Wang, T. Lin, *J. Mater. Chem.* **2011**, *21*, 4869-4874.

## 1 INTRODUCTION

- [137] F. Wöhler, *Liebigs Ann. Chem.* **1863**, 127, 257-274.
- [138] M. P. Gallo, *Zur Chemie von Siloxenen und zur Darstellung von Polysilinen und nanodimensionierten Siliciumteilchen*, Bielefeld, **2004**.
- [139] H. Schäfer, B. Eisenmann, W. Müller, *Angew. Chem. Int. Ed.* **1973**, 12, 694-712.
- [140] U. Dettlaff-Weglikowska, W. Hönle, A. Molassioti-Dohms, S. Finkbeiner, J. Weber, *Phys. Rev. B* **1997**, 56, 13132-13140.
- [141] J. Böhm, O. Hassel, *Z. anorg. allg. Chem* **1927**, 160, 152-164.
- [142] H. Ubara, T. Imura, A. Hiraki, I. Hirabayashi, K. Morigaki, *J. Non-Cryst. Solids* **1983**, 59-60, Part I, 641-644.
- [143] J. R. Dahn, B. M. Way, E. Fuller, J. S. Tse, *Phys. Rev. B* **1993**, 48, 17872-17877.
- [144] A. Weiss, G. Beil, H. Meyer, *Z. Naturforsch. B* **1979**, 34b, 25-30.
- [145] H. Kautsky, *Z. anorg. allg. Chem.* **1921**, 117, 209-242.
- [146] E. Hengge, *Silicon Chemistry II, Vol. 51*, Springer Berlin Heidelberg, **1974**, 1-127.
- [147] E. Hengge, *Silicium-Chemie, Vol. 9/1*, Springer Berlin Heidelberg, **1967**, 145-164.
- [148] H. Kautsky, *Z. Naturforsch. B* **1952**, 174.
- [149] E. Z. Kurmaev, S. N. Shamin, D. L. Ederer, U. Dettlaff-Weglikowska, J. r. Weber, *J. Mater. Res.* **1999**, 14, 1235-1237.
- [150] M. S. Brandt, S. E. Ready, J. B. Boyce, *Appl. Phys. Lett.* **1997**, 70, 188-190.
- [151] H. Nakano, T. Mitsuoka, M. Harada, K. Horibuchi, H. Nozaki, N. Takahashi, T. Nonaka, Y. Seno, H. Nakamura, *Angew. Chem. Int. Ed.* **2006**, 45, 6303-6306.
- [152] H. Nakano, M. Nakano, K. Nakanishi, D. Tanaka, Y. Sugiyama, T. Ikuno, H. Okamoto, T. Ohta, *J. Am. Chem. Soc.* **2012**, 134, 5452-5455.
- [153] S. W. Keller, H.-N. Kim, T. E. Mallouk, *J. Am. Chem. Soc.* **1994**, 116, 8817-8818.
- [154] H.-N. Kim, S. W. Keller, T. E. Mallouk, J. Schmitt, G. Decher, *Chem. Mater.* **1997**, 9, 1414-1421.
- [155] M. Fang, C. H. Kim, G. B. Saupe, H.-N. Kim, C. C. Waraksa, T. Miwa, A. Fujishima, T. E. Mallouk, *Chem. Mater.* **1999**, 11, 1526-1532.
- [156] T. Sasaki, Y. Ebina, M. Watanabe, G. Decher, *Chem. Commun.* **2000**, 2163-2164.
- [157] T. Sasaki, Y. Ebina, T. Tanaka, M. Harada, M. Watanabe, G. Decher, *Chem. Mater.* **2001**, 13, 4661-4667.

## 1 INTRODUCTION

- [158] T. Tanaka, K. Fukuda, Y. Ebina, K. Takada, T. Sasaki, *Adv. Mater.* **2004**, *16*, 872-875.
- [159] M. Osada, Y. Ebina, K. Takada, T. Sasaki, *Adv. Mater.* **2006**, *18*, 295-299.
- [160] T. Sasaki, *J. Ceram. Soc. Jpn.* **2007**, *115*, 9-16.
- [161] Z. Gao, J. Wang, Z. Li, W. Yang, B. Wang, M. Hou, Y. He, Q. Liu, T. Mann, P. Yang, M. Zhang, L. Liu, *Chem. Mater.* **2011**, *23*, 3509-3516.
- [162] S. Chen, J. Zhu, X. Wu, Q. Han, X. Wang, *ACS Nano* **2010**, *4*, 2822-2830.
- [163] L. Wang, D. Wang, X. Y. Dong, Z. J. Zhang, X. F. Pei, X. J. Chen, B. Chen, J. Jin, *Chem. Commun.* **2011**, *47*, 3556-3558.
- [164] B. Li, H. Cao, J. Shao, H. Zheng, Y. Lu, J. Yin, M. Qu, *Chem. Commun.* **2011**, *47*, 3159-3161.
- [165] B.-I. Lee, S.-H. Byeon, *Chem. Commun.* **2011**, *47*, 4093-4095.
- [166] H. Xin, R. Ma, L. Wang, Y. Ebina, K. Takada, T. Sasaki, *Appl. Phys. Lett.* **2004**, *85*, 4187-4189.
- [167] J. L. Gunjekar, T. W. Kim, H. N. Kim, I. Y. Kim, S.-J. Hwang, *J. Am. Chem. Soc.* **2011**, *133*, 14998-15007.
- [168] G. Decher, *Science* **1997**, *277*, 1232-1237.
- [169] Wang, Y. Omomo, N. Sakai, K. Fukuda, I. Nakai, Y. Ebina, K. Takada, M. Watanabe, T. Sasaki, *Chem. Mater.* **2003**, *15*, 2873-2878.
- [170] L. Li, R. Ma, Y. Ebina, K. Fukuda, K. Takada, T. Sasaki, *J. Am. Chem. Soc.* **2007**, *129*, 8000-8007.
- [171] H. Li, L. Deng, G. Zhu, L. Kang, Z.-H. Liu, *Mat. Sci. Eng. B* **2012**, *177*, 8-13.
- [172] X. Zhang, Y. Wang, X. Chen, W. Yang, *Mater. Lett.* **2008**, *62*, 1613-1616.
- [173] E. Coronado, C. Mart  -Gastaldo, E. n. Navarro-Moratalla, A. Ribera, S. J. Blundell, P. J. Baker, *Nat. Chem.* **2010**, *2*, 1031-1036.
- [174] R. Chalasani, A. Gupta, S. Vasudevan, *Sci. Rep.* **2013**, *3*.
- [175] M. Muramatsu, K. Akatsuka, Y. Ebina, K. Wang, T. Sasaki, T. Ishida, K. Miyake, M.-a. Haga, *Langmuir* **2005**, *21*, 6590-6595.
- [176] K. Saruwatari, H. Sato, J. Kameda, A. Yamagishi, K. Domen, *Chem. Commun.* **2005**, 1999-2001.



## 1 INTRODUCTION

- [177] K. Saruwatari, H. Sato, T. Idei, J. Kameda, A. Yamagishi, A. Takagaki, K. Domen, *J. Phys. Chem. B* **2005**, *109*, 12410-12416.
- [178] M. Osada, K. Akatsuka, Y. Ebina, H. Funakubo, K. Ono, K. Takada, T. Sasaki, *ACS Nano* **2010**, *4*, 5225-5232.
- [179] K. Akatsuka, M.-a. Haga, Y. Ebina, M. Osada, K. Fukuda, T. Sasaki, *ACS Nano* **2009**, *3*, 1097-1106.
- [180] B.-W. Li, M. Osada, T. C. Ozawa, Y. Ebina, K. Akatsuka, R. Ma, H. Funakubo, T. Sasaki, *ACS Nano* **2010**, *4*, 6673-6680.

## 2. CHARACTERIZATION METHODS

### 2.1 X-RAY DIFFRACTION

X-ray diffraction (XRD) is a method that enables the characterization of samples with regards to their phase purity, crystallinity, particle size, symmetry and structure. The incident X-rays are scattered by sets of crystal lattice planes, which is geometrically described by the Bragg law:<sup>[1]</sup>

$$\text{Eq. 2.1} \quad n\lambda = 2d\sin\theta$$

Here,  $n$  is the diffraction order,  $\lambda$  is the wavelength of the incident X-rays,  $d$  is the distance of the lattice planes and  $\theta$  is the Bragg angle at which constructive interference occurs. Figure 2.1 schematically outlines the Bragg diffraction of incident X-rays from parallel lattice planes.

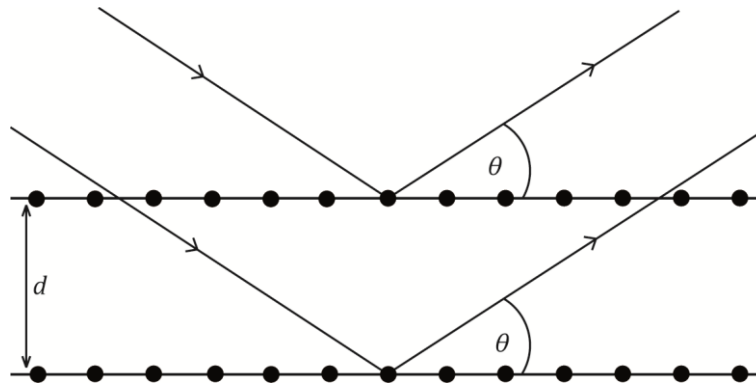


**Figure 2.1.** Schematic representation of Bragg diffraction.

## 2 CHARACTERIZATION METHODS

X-ray diffraction of layered materials is of particular interest since these exhibit characteristic (00*l*) reflections corresponding to the basal *d*-spacing of the lattice planes resulting from the stacked layers. In addition, small angle XRD can be operated in order to analyze the periodicity of restacked 2D materials and multilayer heterostructures with large *d*-spacings. In contrast to layered bulk compounds, true 2D materials show three main differences in the XRD pattern: a) only (*hk*0) reflections occur, b) the shape of the Bragg reflections is asymmetrical (so-called Warren-type peak profiles) and c) the locations of the peaks are slightly displaced from those of the bulk compound.<sup>[2-3]</sup> The reason for a) is obvious, since no periodicity in *c* direction exists, while b) and c) result from anisotropic effects of the nanosheets.<sup>[3]</sup> With the help of XRD, 2D nanosheets can be distinguished from their bulk material on the one hand, and from restacked nanosheets on the other.

X-ray diffraction experiments were performed on the following diffractometers (in this work CuK<sub>α1</sub> radiation with  $\lambda = 1.540562 \text{ \AA}$  was used for all measurements): Huber G670 (Huber, Rimsting; Ge(111)-monochromator, external standard SiO<sub>2</sub>) Guinier Imaging Plate diffractometer; Bruker D8 Avance diffractometer (Bruker AXS, Madison) in Bragg Brentano geometry; STOE diffractometers (Stadi P and Stadi P Combi, both in transmission geometry).

### 2.2 ATOMIC FORCE MICROSCOPY

Atomic force microscopy (AFM) is a method that has been developed to characterize surfaces of materials. The AFM scans the surface of a compound with a scanning probe, which is attached to a cantilever and brought into proximity with the sample. The forces that occur between surface and tip lead to a deflection of the cantilever according to Hooke's law:

$$\text{Eq. 2.2} \quad F = -kx$$

*k* is the spring constant of the cantilever and *x* the deflection. The deflection of the cantilever that distorts in *z*-direction is measured by a photodiode. By converting this signal,

## 2 CHARACTERIZATION METHODS

a topographic image of the surface is generated. An AFM can be run in three different modes: contact-mode, intermittent-contact-mode and non-contact-mode.

Figure 2.2 shows a Lennard-Jones potential, which describes the interactions between the sample and the scanning probe in more detail. The forces that occur are essentially van der Waals forces that are attractive and contact forces that are repulsive. Schematically the areas of interest are sketched when measured in contact- and intermittent-contact-mode. Upon approaching the sample probe to the surface attractive forces occur, which lead to a snap on of the cantilever to the surface of the sample at the minimum of energy. Upon further decrease of the distance, repulsive contact forces surmount the attractive forces. The contact-mode of AFMs is carried out in the labeled area in Fig. 2.2 from the snap on to smaller distances, whereas intermittent-contact-mode is run at the opposite side of the snap on point. Non-contact-mode is also conducted in the area from snap on to higher distances between sample and tip, whereas in this mode no snap on occurs. In the following, the different modes are explained in more detail:

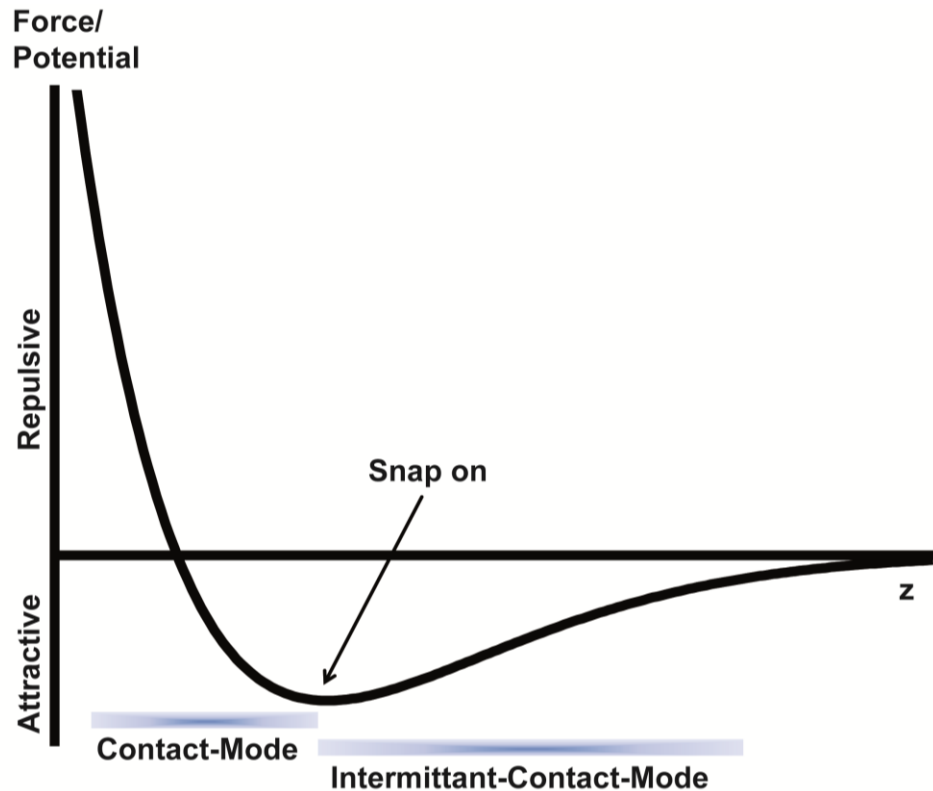


**Figure 2.2.** Lennard-Jones potential showing the force/potential vs. distance curve between sample surface and scanning probe. Labeled areas are representative for contact- and intermittent-contact-mode.

## 2 CHARACTERIZATION METHODS

*Contact-mode:* In contact-mode the sample probe is always in direct contact to the sample surface. This mode can be divided into constant height and constant force mode. The former is characterized by the constant height of the cantilever during the measurement. Since the cantilever is fixed, different absolute values of forces occur during the scan and hence different bending of the cantilever appears. The signal of the different forces is then detected and a topographic image is produced. The second mode is the constant force mode, i.e. the force of the cantilever is fixed and hence the sample probe is lifted by the  $z$ -piezo in a way that the no bending of the cantilever occurs. In this case the topographic image is generated by converting the  $z$ -piezo signal of the cantilever. Contact-mode was the first developed mode for AFM and is applicable for rather flat and non-adhesive surfaces since in other cases the tip suffers from scratching at the surface.

*Non-contact-mode:* In this mode the cantilever is not in contact with the surface but the occurring attractive forces are detected. Furthermore, this is a dynamic AFM mode, i.e. the cantilever is oscillated at its resonance frequency. During scanning of the sample the oscillating cantilever interacts with the surface and hence the oscillating frequency as well as the amplitude change, which is both detected and transferred to produce a topographic image.

*Intermittent-contact-mode:* Similarly to non-contact-mode, this mode is a dynamic operating mode. The cantilever is oscillated near its resonance frequency and scanned across the sample. In most cases the exciting frequency is slightly below the resonance frequency because upon approach of the sample probe to the surface, the amplitude of the cantilever decreases and thus the oscillating frequency increases and shifts towards the resonance frequency. However, in contrast to non-contact-mode, the tip is intermittently in contact with the surface (see Fig. 2.2 snap on). The topographic image is generated by imaging the variation of the oscillating frequency and thus the forces applied to the cantilever.

All measurements in this thesis were performed in intermittent-contact-mode using OMCL-AC160TS (Olympus Co., Tokyo) cantilevers. Measurements were conducted either on a MFP-3D AFM (Asylum Research, Santa Barbara) or on a Nano Wizard AFM (JPK, Berlin).

## 2.3 ELECTRON MICROSCOPY

Electron microscopy (EM) relies on the same physical principles as visible light microscopy (VLM). However, according to the shorter wavelength of electrons compared to visible light, the resolution of EM reaches down to  $< 1 \text{ \AA}^{[4]}$  compared to a minimum resolution of ca. 200 nm in VLM. Similar to VLM, in EM the incident beam is focused by different condenser lenses and apertures.

An electron beam impinges on the sample and thus the electrons interact with the specimen. EM is carried out under ultra high vacuum (UHV) conditions in order to avoid interactions between the electrons and gas molecules. Fig. 2.3 schematically shows the possible processes that can occur during electron beam-specimen interaction.

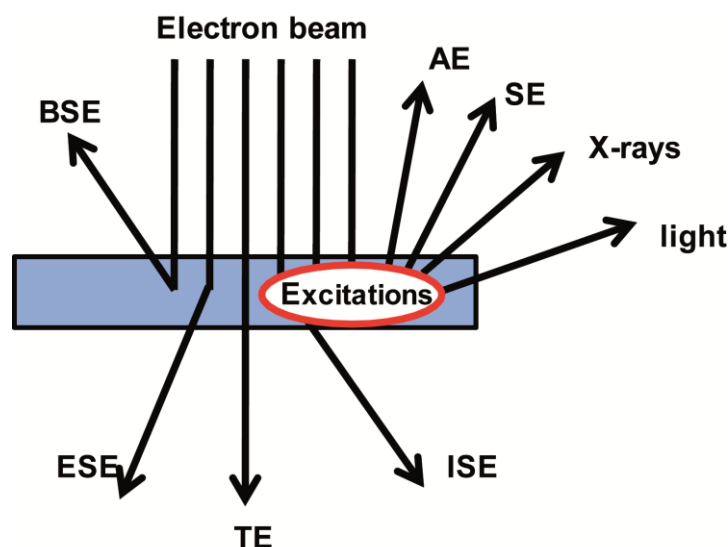


**Figure 2.3.** Schematic drawing of the signals in electron microscopy resulting from electron beam-sample interactions. BSE : backscattered electrons; ESE : elastically scattered electrons; TE : transmitted electrons from the primary beam; ISE : inelastically scattered electrons; AE : Auger electrons; SE : secondary electrons.

### 2.3.1 SCANNING ELECTRON MICROSCOPY AND ENERGY-DISPERSIVE X-RAY SPECTROSCOPY

Scanning electron microscopy (SEM) and energy-dispersive X-ray spectroscopy (EDX) were applied in order to elucidate the morphology and composition of the samples. In SEM an electron beam, typically accelerated by voltages between 1 and 30 keV, is scanned over

## 2 CHARACTERIZATION METHODS

the sample. Secondary electrons (SE) and backscattered electrons (BSE) are detected. The BSE yield elemental contrast information and the SE produce a topographic image of the sample. An EDX detector can be coupled to a SEM in order to elucidate the local chemical composition of the sample. With EDX X-rays, generated in the sample from the incident electron beam, are detected. The energies of the detected X-rays are specific for every element due to the different atomic shells.

All measurements were performed on a JEOL 6500F microscope (JEOL, Tokyo), which is equipped with an EDX detector (Model 7418, Oxford Instruments, Abingdon) and exhibits a maximum acceleration voltage of 40 kV.

### 2.3.2 TRANSMISSION ELECTRON MICROSCOPY

Transmission electron microscopy (TEM) obeys the same principles as SEM, whereas in TEM acceleration voltages between 80 and 300 keV are used and not just SE and BSE can be detected. Samples that are measured by TEM are prepared to be not thicker than ca. 100 nm so that transmitted electrons (TE) from the primary beam, elastically scattered electrons (ESE), and inelastically scattered electrons (ISE) can be detected in transmission mode. These electrons are focused and separated by several lenses and apertures between the sample and the detector. The schematic structure of a TEM is depicted in Figure 2.4. In the back focal plane of the objective lens the diffraction pattern is obtained, which is then enlarged by intermediate and projector lens. According to the different electrons that are generated in TEM, this technique offers various modes to measure the electrons and thus to get diverse information about the sample. These modes include bright-field (BF) and dark-field (DF) TEM, high resolution (HR)TEM, scanning (S)TEM and high-angle annular dark field (HAADF) STEM, which are discussed in the following:

*BF:* In this mode any scattered electron is blocked by apertures and only TE are detected. Thus, areas that exhibit higher scattering than others appear dark in the resulting image because the scattered electrons are captured. This effect is called thickness contrast. Another effect also plays a crucial role in imaging modes: Elements with higher atomic number,  $Z$ , than others lead to stronger scattering and thus appear darker in BF mode.

*DF:* This imaging mode is inverted compared to BF imaging. Hence, the TE are blocked by an aperture and only scattered electrons are used for imaging. Therefore, thicker regions of the sample and elements with high  $Z$  appear bright in this mode.

## 2 CHARACTERIZATION METHODS

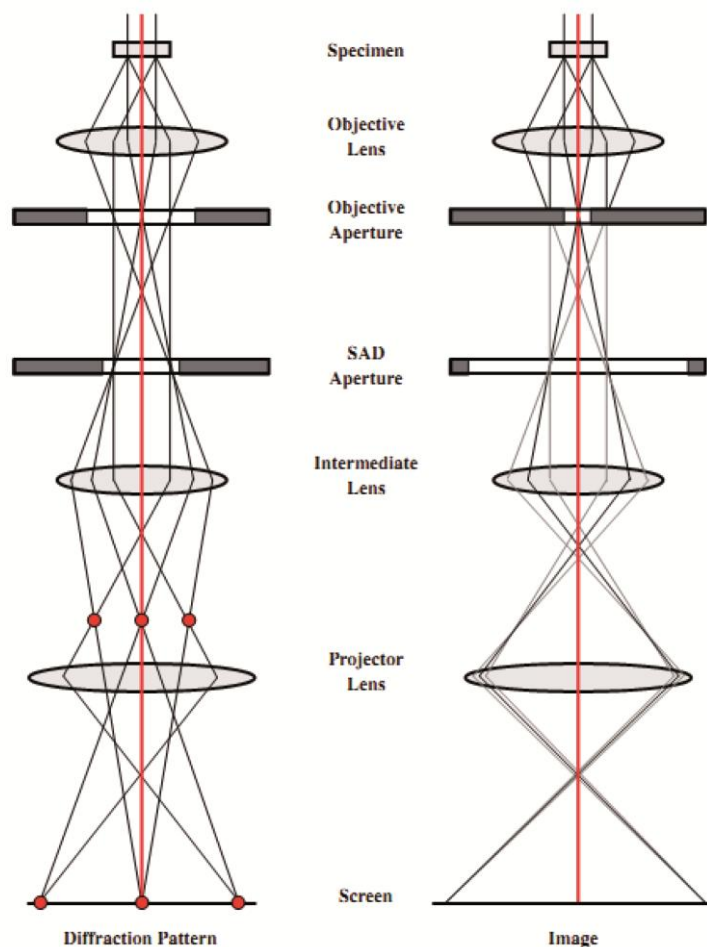


**Figure 2.4.** Schematic depiction of the components of a TEM including the electron beam path in diffraction (left) and imaging (right) mode. Reprinted with permission from reference [5]. Copyright 2008 John Wiley & Sons.

*HRTEM:* With the help of HRTEM samples can be investigated with feature sizes down to the atomic scale with a resolution of  $< 0.1 \text{ nm}$ .<sup>[6-7]</sup> This mode operates without apertures so that both, scattered and unscattered electrons are detected and contribute to the image. By tilting the specimen in zone axis the lattice planes of the sample can be made visible.

*STEM:* In this mode a convergent beam is scanned across the sample and only TE are detected. Depending on the angle of the scattered electrons a BF, DF or an HAADF detector is used. The latter allows the determination of different elements since the intensity of the signal at high angles is proportional to the square of the atomic number  $Z$ .

In addition to the imaging modes, analytical techniques such as EDX and electron energy loss spectroscopy (EELS) were performed with TEM. EDX has been discussed in chapter 2.3.1. With EELS transmitted inelastically scattered electrons and their energy losses are



## 2 CHARACTERIZATION METHODS

detected with a spectrometer yielding high spatial and energy resolution. Figure 2.5 shows an exemplary EEL spectrum, which can be classified into three main regions: zero-loss peak (ZLP), low energy loss and high energy loss region. The ZLP occurs at 0 eV in all spectra and mainly consists of unscattered electrons, which did not undergo energy loss processes. In addition, phonons resulting from quasi-elastically scattered electrons contribute to the ZLP. The low loss region is located between 0 – 50 eV and is dominated by oscillating electrons (plasmons) of the solid. The third region occurs at energy losses higher than 50 eV and is called high-energy loss or core loss region. This region is used to determine the inner-shell electrons that are excited to higher energy levels and are characteristic for every element. The resulting edges from energy losses are used to identify the local elemental composition of the sample.

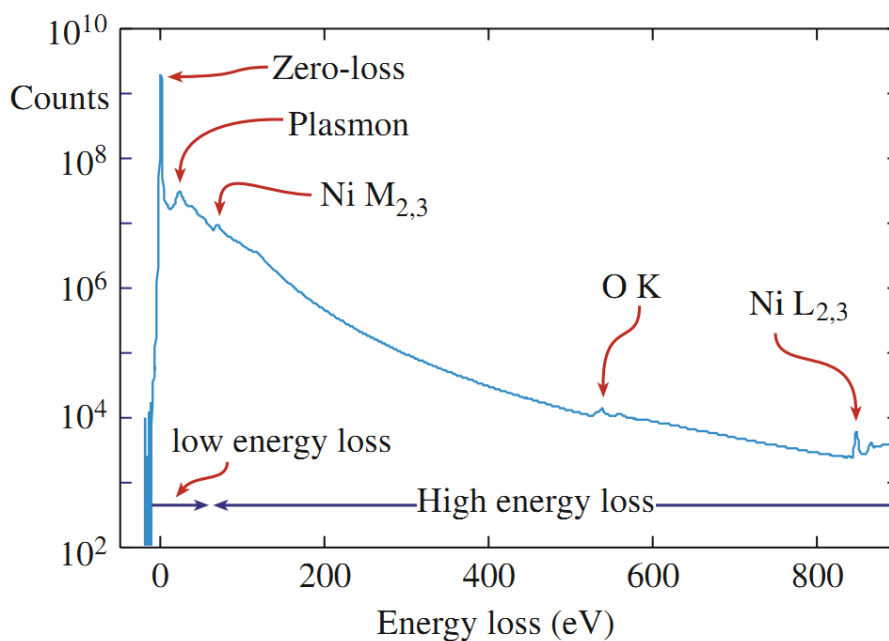


**Figure 2.5.** EEL spectrum showing the three main regions: ZLP, low energy loss and high energy loss region as well as some exemplary edges. Reprinted with permission from reference [8]. Copyright 2009 Springer Science+Business Media.

## 2 CHARACTERIZATION METHODS

In this work, TEM was applied in BF, DF, HAADF-STEM mode coupled with EDX and EELS. Therefore, different microscopes were used as listed in Table 2.1.

**Table 2.1.** Instrument data for the transmission electron microscopes used in this thesis.

Microscope	Parameter
Philips CM30 ST (Philips, Amsterdam)	LaB <sub>6</sub> cathode, 300 keV
JEOL 2011 (JEOL, Tokyo)	LaB <sub>6</sub> cathode, 200 keV
FEI Titan 80-300 (S)TEM (FEI, Hillsboro)	Field emission gun (FEG), 300 keV EDAX Sapphire (Si(Li) detector (EDAX) Mahwah) HAADF-detector (FISCHIONE INSTRUMENTS (Model 3000)); Tridiem energy filter (GATAN)
FEI Titan 80-300 Cubed (S)TEM (FEI, Hillsboro)	High-brightness X-FEG, 300 keV, two aberrations for the probe and image forming lenses, Gatan GIF (model 866) spectrometer

## 2.4 VIBRATIONAL SPECTROSCOPY

### 2.4.1 INFRARED SPECTROSCOPY

Infrared (IR) spectroscopy was carried out either on a Spectrum BXII FT-IR (Perkin Elmer, Waltham) or on a IFS 66v/S (Bruker, Madison) spectrometer. On the latter spectrometer the samples were measured in form of KBr pellets. Therefore, 300 mg KBr and 3 mg of the sample were thoroughly pestled and pressurized using a hand press with a press capacity of 10 kN.

### 2.4.2 RAMAN SPECTROSCOPY

Raman spectroscopy was performed on a Jobin Yvon Typ V 010 labram single grating spectrometer (Horiba, Singapore), equipped with a double super razor edge filter and a peltier cooled CCD camera. Spectra are recorded in quasi-backscattering geometry using the linearly polarized 632.817 nm line of a He/Ne gas laser with power less than 1 mW, focused on a 10  $\mu$ m spot through a 50x microscope objective on to the top surface of the sample.

## 2 CHARACTERIZATION METHODS

### 2.4.3 UV-VIS SPECTROSCOPY

UV-Vis spectroscopy was carried out on a Cary 500 spectrophotometer (Varian, Palo Alto) in order to obtain the absorption spectra of the samples. To calculate the optical band gaps of the samples the spectra were recorded in absorbance mode and converted into the diffuse reflectance (R) that was obtained by Kubelka-Munk function:

$$\text{Eq. 2.3} \quad F(R) = \frac{(1 - R)^2}{2R}$$

F(R) was plotted against the photon energy. By applying a linear fit to the absorption edge the band gap was obtained.

## 2.5 NUCLEAR MAGNETIC RESONANCE SPECTROSCOPY

Nuclear magnetic resonance (NMR) spectroscopy is an analytical method that investigates the local structure of compounds. All nuclei with a spin that deviates from zero have an intrinsic magnetic moment and can therefore be used for NMR spectroscopy. By applying an external magnetic field to a nuclide, an interaction between the two appears leading to a resonance frequency, which is dependent on both, the external field and the intrinsic magnetic properties of the nucleus. This resonance frequency is called Larmor frequency ( $\nu_L$ ), which is described by the following equation:

$$\text{Eq. 2.4} \quad \nu_L = -\gamma \cdot B_0$$

$\gamma$  : gyromagnetic ratio;  $B_0$  : magnitude of the magnetic field.

### 2.5.1 SOLUTION-STATE NUCLEAR MAGNETIC RESONANCE SPECTROSCOPY

In solution-state NMR Brownian motion of the dissolved molecules occurs. This motion averages out anisotropic properties of the samples.  $^1\text{H}$  and  $^{13}\text{C}$  solution state NMR were recorded as single pulse measurements in  $\text{CDCl}_3$  on a JEOL DELTA NMR (JEOL, Tokyo) with respect to TMS as external standard.

## 2 CHARACTERIZATION METHODS

### 2.5.2 SOLID-STATE NUCLEAR MAGNETIC RESONANCE SPECTROSCOPY

Since in solid-state (ss) NMR anisotropic effects such as the orientation of an isotope with respect to the external magnetic field cannot be averaged out by Brownian motion, line broadening of the signals occurs. The orientation of the nuclei to the external magnetic field is described as dipolar coupling by the following equation:

$$\text{Eq. 2.5} \quad \Delta B = \frac{\mu_0}{4\pi} (3 \cos^2 \theta - 1) \mu r^{-3}$$

$\Delta B$ : variation in the local magnetic field,  $\mu_0$ : permeability of free space,  $\mu$ : magnetic moment of the nucleus,  $r$ : distance vector and  $\theta$ : angle between  $r$  and the direction of the external magnetic field.

In solid-state NMR magic angle spinning (MAS) is applied to average out the dipolar coupling and anisotropic interactions. The angle  $\theta = 54.74^\circ$  complies with the condition  $3\cos^2\theta - 1 = 0$  and, hence, the dipolar interactions are averaged out and disappear from the recorded spectrum. The dipolar coupling in ss NMR can be divided in homo- and heteronuclear dipolar coupling. Other factors that influence the line broadening in ss NMR are chemical shift anisotropy (CSA) and quadrupolar coupling. The second order quadrupolar interaction can be minimized by spectrometers with high induction and thus high Larmor frequency, since the quadrupolar coupling is inversely proportional to  $\nu_L$ .<sup>[9]</sup>

In addition, in some measurements cross-polarization (CP) was used to increase the signal intensity of isotopes with low abundance and/or low gyromagnetic ratio (e.g.  $^{29}\text{Si}$ ). In this technique the polarization of a more abundant isotope (mostly  $^1\text{H}$  is used) is transferred to the rare nucleus leading to an intensity increase.

$^1\text{H}$  and  $^{29}\text{Si}$  ss MAS NMR spectroscopy was carried out on a BRUKER DSX500 Avance spectrometer (Bruker, Madison) with a proton resonance frequency of 500 MHz using a 4 mm MAS-rotor ( $\text{ZrO}_2$ ) in a 11.75 T magnet field with a spinning frequency of 6 kHz.

## 2.6 X-RAY PHOTOELECTRON SPECTROSCOPY

X-ray photoelectron spectroscopy (XPS) was used to identify surface compositions of samples, the chemical environment and hybridization/oxidation states of the elements contained in the sample. The measurements were performed on an Axis Ultra (Kratos Analytical, Manchester) X-ray photoelectron spectrometer.

### 2.7 MAGNETIC MEASUREMENTS

Magnetic measurements were carried in order to elucidate magnetic susceptibilities of the samples. The measurements were done on a SQUID magnetometer type MPMS 7.0 (Quantum Design, San Diego).

### 2.8 ELECTROCHEMICAL MEASUREMENTS

To explore the electrochemical behavior of the samples, cyclic voltammograms (CV) and galvanostatic charge/discharge curves were collected. For the measurements, the analyte was pestled with a few drops of ethanol, acetylene black and poly(tetrafluoroethylene) in a mortar. The obtained paste was transferred onto a Ti foil and dried at 60 °C in a vacuum oven. The measurements were then carried out in a flat cell using Pt as counter electrode and a saturated calomel electrode (SCE) as reference. CV measurements were carried out at scan speeds of 2 to 200 mVs<sup>-1</sup> with up to 500 cycles. Potentiostatic and galvanostatic experiments were conducted using a Solartron SI 1287 Electrochemical Interface (Solartron Analytical, Kingston on Thames) or a Princeton Applied Research VersaSTAT electrochemical workstation (Princeton Applied Research, Princeton).

### 2.9 ELEMENTAL ANALYSIS

Elemental analysis (EA) was applied to elucidate the chemical composition of the materials.

#### 2.9.1 INDUCTIVELY COUPLED PLASMA ATOMIC EMISSION SPECTROSCOPY

Inductively coupled plasma atomic emission spectroscopy (ICP-AES) was carried out on a VISTA RL CCD simultaneous ICP-AES analyzer system (Agilent Technologies, Waldbronn). Therefore, the analyte was dissolved in oxidizing acids and the solutions were applied to the instrument. By inductively coupled plasma, the solution was then fragmented into its components and analyzed by atomic emission spectroscopy.

## 2 CHARACTERIZATION METHODS

### 2.9.2 CHNS ANALYSIS

C/H/N/S EA was performed on an Elementar vario EL (Elementar Analysensysteme, Hanau).

### 2.10 LIGHT SCATTERING EXPERIMENTS

Dynamic light scattering (DLS) and zeta potential measurements were performed to reveal particle sizes and the surface potential of colloidal particles. The measurements were carried out on a Malvern Nano ZS Zetasizer (Malvern, Worcestershire). The zeta potential measurements were analyzed using the Henry equation:

$$\text{Eq. 2.6} \quad U_E = \frac{2\varepsilon z f(Ka)}{3\eta}$$

$\varepsilon$  : dielectric constant;  $z$  : zeta potential;  $f(Ka)$  : Henry's function;  $\eta$  : viscosity.

In aqueous medium Henry's equation equals 1.5 according to the Smoluchowski approximation and 1.0 in organic solvents according to the Hückel approximation.

### 2.11 PHOTOLUMINESCENCE MEASUREMENTS

Photoluminescence measurements were carried to determine emission maxima of the samples. The samples were measured as powders in reflection mode with an excitation wavelength of 360 nm. The measurements were run on an USB 4000 spectrometer (Ocean Optics, Dunedin) using an excitation wavelength of 360 nm.

### 2.12 BIBLIOGRAPHY

- [1] W. H. Bragg, W. L. Bragg, *Proc. R. Soc. London, A* **1913**, 88, 428-438.
- [2] R. A. Gordon, D. Yang, E. D. Crozier, D. T. Jiang, R. F. Frindt, *Phys. Rev. B* **2002**, 65, 125407.
- [3] D. Yang, R. F. Frindt, *J. Mater. Res.* **1996**, 11, 1733-1738.
- [4] M. Haider, S. Uhlemann, J. Zach, *Ultramicroscopy* **2000**, 81, 163-175.
- [5] D. Brandon, W. D. Kaplan, in *Microstructural Characterization of Materials*, **2008**, pp. 179-260.
- [6] P. C. Tiemeijer, M. Bischoff, B. Freitag, C. Kisielowski, *Ultramicroscopy* **2012**, 118, 35-43.
- [7] P. C. Tiemeijer, M. Bischoff, B. Freitag, C. Kisielowski, *Ultramicroscopy* **2012**, 114, 72-81.
- [8] D. B. Williams, C. B. Carter, *Transmission Electron Microscopy* **2009**, 680.
- [9] M. A. Fichera, *Festkörper – NMR – Untersuchungen an thermischen Abbauprodukten von flammgeschützten Polymeren*, Berlin **2008**.

## 3. LAYERED DOUBLE HYDROXIDES

This chapter deals with the synthesis, exfoliation, restacking and layer-by-layer behavior of  $\text{Mn}^{\text{II}}\text{Al}^{\text{III}}$  LDH and  $\text{Zn}^{\text{II}}\text{Cr}^{\text{III}}$  LDH with graphene oxide (GO) and  $\text{Ti}_{2-x/4}\text{O}_4^{x-}$ , respectively.

Besides exfoliation of the LDHs to increase the toolbox of cationic 2D materials and proof of concept experiments to demonstrate the feasibility of flocculation and layer-by-layer assembly of cationic LDHs with other layered inorganic materials, the objective of this part of the thesis was the design of new functional hybrid materials for electrochemical and photochemical applications. Especially the composite material  $\text{GO}/\text{Mn}^{\text{II}}\text{Al}^{\text{III}}$  LDH is promising as electrode material in pseudocapacitive energy storage schemes, as it shows enhanced specific capacities over those of the separate components.



## 3.1 EXFOLIATION OF $\text{Mn}^{\text{II}}\text{Al}^{\text{III}}$ LAYERED DOUBLE HYDROXIDE AND SYNTHESIS OF LDH/GRAPHENE OXIDE HYBRID MATERIAL

Stephan Werner, Vincent Wing-hei Lau, Stephan Hug, Viola Duppel, Hauke Clausen-Schaumann and Bettina V. Lotsch

Published in: *Langmuir* **2013**, 29, 9199.

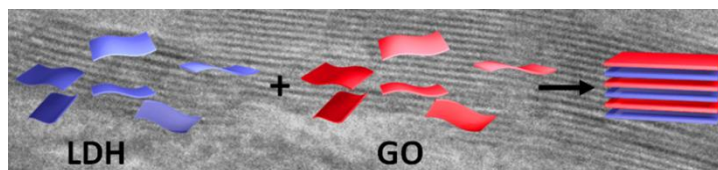
DOI: 10.1021/la400846w

Copyright © 2013 American Chemical Society

<http://pubs.acs.org/doi/abs/10.1021/la400846w>

### ABSTRACT

We report on the synthesis and exfoliation of  $\text{Mn}^{\text{II}}\text{Al}^{\text{III}}$  sulfonate and sulfate layered double hydroxides (LDHs) and their



combination with graphene oxide by charge-directed self-assembly. The synthesis of the LDH compounds has been accomplished either directly by coprecipitation of the respective hydroxides with sulfonate anions or by ion-exchange of the chloride-containing LDH with sodium dodecylsulfate. Exfoliation of the bulk material in formamide yields colloidal suspensions of positively charged nanosheets with lateral dimensions of tens to hundreds of nanometers and thicknesses down to 1.3 nm, ascertained by TEM and AFM. Flocculation of the LDH nanosheets with an aqueous graphene oxide suspension yields a hybrid material that can be converted to a reduced graphene oxide/LDH composite by hydrazine reduction. The hybrid materials were tested for pseudocapacitive electrochemical storage capacity and electrocatalytic oxygen evolution reactions and showed significant increases compared to the pristine materials.

### 3.1.1 INTRODUCTION

The discovery of graphene<sup>[1]</sup> has sparked tremendous interest in two-dimensional (2D) materials during the last years. Owing to their morphology and unique properties relevant to

### 3 LAYERED DOUBLE HYDROXIDES

fields ranging from electronics to catalysis, research has intensified especially in the field of metal oxide and hydroxide nanosheet materials.<sup>[2-3]</sup> Layered titanates,<sup>[4]</sup> metal chalcogenides<sup>[5]</sup> and phosphates,<sup>[6]</sup> perovskites<sup>[7]</sup> as well as metal hydroxides<sup>[8-9]</sup> are amongst those materials that already have been successfully exfoliated into nanosheets. Typically, the thickness of nanosheets is on the order of a few nanometers and their lateral size ranges from several hundred nanometers to a few microns. The small thickness and high anisotropy of nanosheet materials significantly alter their properties compared to the corresponding bulk material, in part as a result of quantum size confinement effects operating in this size regime. Furthermore, stacking of 2D nanosheet materials by flocculation, Langmuir-Blodgett (LB) or Layer-by-Layer (LbL) techniques opens up new avenues to tailor-made, multifunctional hybrid materials featuring properties that are distinct from those of the individual nanosheets.<sup>[10-11]</sup>

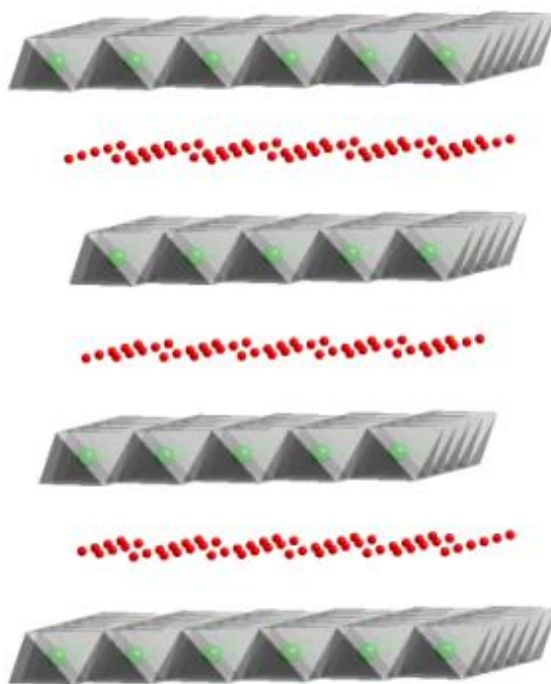


**Figure 3.1.** Structure of a generic LDH showing the Brucite-type layers (grey octahedra) and the intercalating anions (red spheres). The green spheres indicate di- and trivalent metal ions forming the centers of the octahedra.

LDHs are hydrotalcite-like clay compounds that are built-up by cationic Brucite-type ( $\text{Mg}(\text{OH})_2$ ) metal hydroxide layers composed of edge-sharing  $\text{M}^{\text{II/III}}(\text{OH})_6$  octahedra and anionic counterions located between the layers. The composition of a LDH is generally

### 3 LAYERED DOUBLE HYDROXIDES

described by the formula:  $[M^{II}_{1-x}M^{III}_x(OH)_2](X^{n-}_{x/n}) \cdot mH_2O$ . Their straightforward synthesis, stability and non-toxic nature entails possible applications of LDHs ranging from catalysis<sup>[12]</sup> to antireflection coatings<sup>[13]</sup> and drug delivery<sup>[14]</sup>. Furthermore, their magnetic<sup>[15]</sup> and photocatalytic<sup>[16]</sup> properties have attracted attention recently. A generic layered structure of a LDH is shown in Fig. 3.1. Typical divalent cations are  $Mg^{2+}$ ,  $Zn^{2+}$ ,  $Co^{2+}$ ,  $Ca^{2+}$ ,  $Cu^{2+}$ , etc, while trivalent cations imparting the positive charge to the metal hydroxide layers are e.g.  $Al^{3+}$ ,  $Cr^{3+}$ ,  $Fe^{3+}$ ,  $Co^{3+}$  and  $Mn^{3+}$ .

Owing to the positive layer charge, exfoliation of LDHs yields colloidal suspensions of positively charged nanosheets.<sup>[17]</sup> Delamination of LDHs can be accomplished using different intercalation schemes and solvents. The best known route is exfoliation in formamide with the help of ultrasonication or mechanical shaking. Exfoliation in other solvents such as butanol, acrylates and toluene has also been reported.<sup>[18-19]</sup> LDHs that have been successfully exfoliated include  $Mg^{II}Al^{III}$  LDH,<sup>[17-19]</sup>  $Co^{II}Al^{III}$  LDH,<sup>[19-20]</sup>  $Zn^{II}Al^{III}$  LDH,<sup>[20-21]</sup>  $Zn^{II}Co^{II}Al^{III}$  LDH,<sup>[21]</sup>  $Ni^{II}Al^{III}$  LDH,<sup>[20-21]</sup>  $Co^{II}Co^{III}$  LDH,<sup>[9]</sup>  $Co^{II}Fe^{III}$  LDH,<sup>[15]</sup>  $Co^{II}Ni^{III}$  LDH<sup>[22]</sup> and  $Li^IAl^{III}$  LDH.<sup>[23]</sup> Restacking of LDH nanosheets together with negatively charged sheets<sup>[24-25]</sup> or nanoparticles<sup>[26]</sup> to construct functional hybrid materials has come into focus of research lately. Owing to its negative surface charge and conductivity, graphene oxide (GO) is an ideal material for the combination with LDHs to form supercapacitors. The conductivity of GO can be enhanced by reduction to reduced graphene oxide (RGO). Fig. 3.2 schematically shows the combination of exfoliated LDH and GO and subsequent reduction to RGO. Combination of GO and RGO with other nanosheet materials such as  $Ni^{II}Al^{III}$  LDH,<sup>[27-29]</sup>  $Ni^{II}Fe^{III}$  LDH,<sup>[30-31]</sup>  $Ni^{II}Mn^{II}$  LDH,<sup>[32-33]</sup>  $Ni(OH)_2$ ,<sup>[34-36]</sup>  $Co^{II}Al^{III}$  LDH<sup>[37-38]</sup> and  $MnO_2$ <sup>[39-41]</sup> has been shown to furnish interesting hybrid materials for applications in electronic devices such as supercapacitors and Li-ion batteries. To our knowledge, very little work has been done on the synthesis and investigation of  $Mn^{II}Al^{III}$  LDHs<sup>[42-45]</sup> for electrode materials and the exfoliation and combination of this material with graphene-derivatives has not been undertaken as yet. Besides the possible relevance of  $Mn^{II}Al^{III}$  LDHs in combination with graphene as energy storage materials, further applications of  $Mn^{II}Al^{III}$  LDHs that may be envisioned are as cation exchangers and catalysts for the decomposition of toxic organic compounds.<sup>[43]</sup> Furthermore, manganese oxide compounds are known to support oxygen evolution reactions (OER), whereas to our knowledge manganese hydroxides have not yet been tested for such applications.<sup>[46]</sup>

### 3 LAYERED DOUBLE HYDROXIDES

In this work we present the synthesis and first successful exfoliation of a  $\text{Mn}^{\text{II}}\text{Al}^{\text{III}}$  based LDH with different sulfonic acids and organic sulfates as charge compensating anions. Furthermore, a simple route to produce composite materials containing exfoliated graphene oxide (GO/LDH) and reduced graphene oxide (RGO/LDH) is introduced. The LDHs, including bulk material and nanosheets, as well as the hybrid materials made thereof were comprehensively characterized by X-ray diffraction (XRD), scanning electron microscopy (SEM), elemental analysis (combustion analysis and ICP), transmission electron microscopy (TEM) and atomic force microscopy (AFM). In addition, electrochemical experiments were conducted to evaluate these materials as potential electrodes in energy storage devices and electrocatalysis.

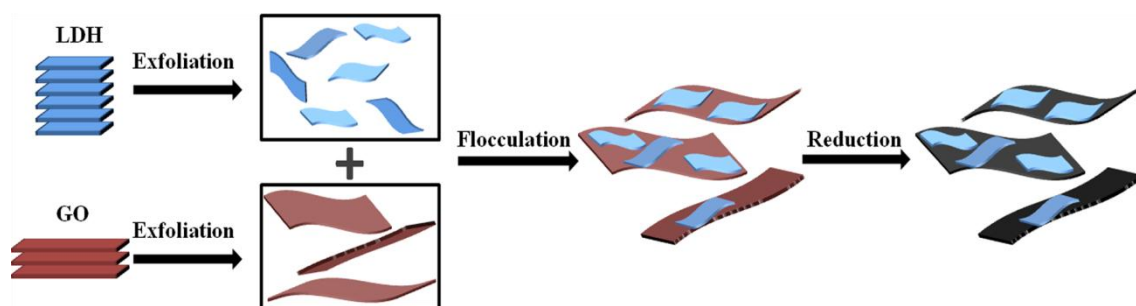


**Figure 3.2.** Reaction scheme of the three-step protocol for the synthesis of graphene-derivatized LDH hybrid materials, starting from the respective bulk materials, followed by exfoliation, flocculation and reduction.

#### 3.1.2 EXPERIMENTAL

All chemicals and solvents were purchased from commercial suppliers and used without further purification: Sodium dodecyl sulfate (Merck KGaA, 90%), 2-naphthalenesulfonic acid (Molekula, 98%), 4-ethylbenzenesulfonic acid (Sigma-Aldrich, 95%), toluenesulfonic acid (Fluka, 99%), manganese nitrate ( $\text{Mn}(\text{NO}_3)_2 \cdot 4\text{H}_2\text{O}$ , Sigma-Aldrich, 97%), aluminum nitrate ( $\text{Al}(\text{NO}_3)_3 \cdot 9\text{H}_2\text{O}$ , Fluka, 99%), sodium hydroxide (AppliChem, 97%), formamide (Fluka, 98%), sulfuric acid (Brenntag, 95-98%), potassium persulfate (Grüssing, 99%), phosphorous pentoxide (VWR International, 99.3%), sodium nitrate (Applichem, 98%), potassium permanganate (Applichem, 99%), hydrogen peroxide (Brenntag, 30%), hydrochloric acid (Brenntag, 30%), graphite flakes (NGS Naturgraphit, 99.8%), ammonia (Merck, 32%), hydrazinium hydrate (Merck, 80%).

### 3 LAYERED DOUBLE HYDROXIDES

**Synthesis of the LDHs.** The sulfonate intercalated LDHs were obtained by the coprecipitation method.  $\text{Mn}(\text{NO}_3)_2 \cdot 4\text{H}_2\text{O}$  (3.33 mmol, 836 mg) and  $\text{Al}(\text{NO}_3)_3 \cdot 9\text{H}_2\text{O}$  (1.67 mmol, 627 mg) were dissolved in 100 mL deionized water. An aqueous solution of sulfonic acid (1 mM, 100 mL) was added to the metal salt solution. All further synthesis steps were carried out under argon atmosphere. The solution pH was adjusted to pH 9 by slowly adding aqueous NaOH (1 M) yielding a brown precipitate, which was then aged overnight in the mother liquor at room temperature without stirring. The product was recovered by filtration and washed several times with water and acetone and dried under vacuum overnight to completely remove the solvent.

The  $\text{Mn}^{\text{II}}\text{Al}^{\text{III}}$  dodecylsulfate LDH was synthesized in a two step synthesis followed by an anion exchange reaction of the LDH. First,  $\text{Mn}^{\text{II}}\text{Al}^{\text{III}}$  chloride LDH was synthesized according to Aisawa *et al.*<sup>[43]</sup> In the second step 100 mg of the obtained LDH was dispersed in a solution of 10 mmol sodium dodecylsulfate (2.88 g) in 60 mL deionized water. The sodium dodecylsulfate was kept in 2.5 fold excess to completely exchange all anions. To isolate the brownish product the precipitate was filtered and washed several times with water and acetone, before it was dried under vacuum overnight.

**Exfoliation of the bulk material.** Exfoliation of the  $\text{Mn}^{\text{II}}\text{Al}^{\text{III}}$  dodecylsulfate LDH into positively charged nanosheets was accomplished in two different ways. In the first route 10 mg LDH were dispersed in 10 mL formamide and further ultrasonicated for 30 minutes. The second route was carried out by dispersing 10 mg LDH in 10 mL formamide and shaking the suspension at 200 rpm for 28 days using a GFL 3005 shaker (Gesellschaft für Labortechnik, Burgwedel). To remove any non-exfoliated particles the suspension was subjected to 15 min of centrifugation

at 5,000 rpm using a Sigma 3-30K centrifuge (Sigma, Osterode).

**Synthesis and exfoliation of graphene oxide.** Graphene oxide was synthesized from natural Madagascar graphite flakes in a modified Hummers method.<sup>[47]</sup> A solution of 30 mL conc.  $\text{H}_2\text{SO}_4$ , 3.61 mmol (976 mg)  $\text{K}_2\text{S}_2\text{O}_8$  and 3.52 mmol (500 mg)  $\text{P}_2\text{O}_5$  was stirred and heated to 80 °C. Graphite (167 mmol, 2.0 g) was added and the suspension was stirred at 80 °C for an additional hour. Subsequently the reaction mixture was cooled down to room temperature overnight, diluted with 100 mL of water, filtered and washed with copious amounts of water until the pH was neutral. The black product was dried overnight and subjected to the Hummers method. Thus, the pre-oxidized powder was dispersed in 70 mL cooled  $\text{H}_2\text{SO}_4$  (0 °C). 1.5 g  $\text{NaNO}_3$  and 10 g  $\text{KMnO}_4$  (63.3 mmol) were added and the

### 3 LAYERED DOUBLE HYDROXIDES

mixture was stirred at 35 °C for two hours. Then 100 mL water were added and the temperature was allowed to rise to 95-98 °C. After further 15 min of stirring 250 mL of water and 10 mL of H<sub>2</sub>O<sub>2</sub> (30% in H<sub>2</sub>O) were added. The reaction mixture was then filtered and washed with 250 mL HCl (1M). The obtained brownish product was dispersed in water and subjected to dialysis to completely remove all metal ions and acids. The gel-like product was then diluted in water and exfoliation was carried out by ultrasonic treatment (30 minutes, 550 W).

**Synthesis of the GO/LDH and RGO/LDH composite materials.** 10 mL of the LDH nanosheet suspension (1 g L<sup>-1</sup> formamide) was mixed with 10 mL of GO suspension (0.5 g L<sup>-1</sup> water). The composite material immediately started to flocculate. The mixture was allowed to stay overnight and aggregation was complete after 24 hours. The product was centrifuged at 15,000 rpm for 30 min, the supernatant solvents were removed and the solid product was dried under vacuum. To obtain the RGO/LDH composite material GO/LDH was subjected to hydrazine reduction according to Wallace and co-workers.<sup>[48]</sup> 50 mg of the starting material was dispersed in 10 mL of water, then 40 µL ammonia (32% in water) were added to keep the suspension under basic conditions. Subsequently, 2 µL of hydrazine hydrate (80% in water) were added, the mixture was heated to 95 °C and stirred for two hours. The precipitate was centrifuged at 15,000 rpm for 30 min, the solvents were removed and the powder was dried under vacuum.

Characterization. X-ray powder diffraction (XRD) data were collected with a Huber G670 Guinier Imaging Plate diffractometer (Huber, Rimsting; Cu Kα1-radiation, λ = 154.051 pm, Ge(111)-monochromator, external standard SiO<sub>2</sub>) at room temperature.

Transmission electron microscopy (TEM) of exfoliated nanosheets was carried out on a Philips CM30 ST instrument (Philips, Eindhoven) equipped with a thermal LaB<sub>6</sub> cathode operating at 300 kV. To generate the samples for TEM, a nanosheet suspension in formamide was drop coated on a lacey carbon grid and dried under vacuum due to the low vapor pressure of formamide.

Scanning electron microscopy (SEM) was carried out on a JSM-6500F electron microscope (JEOL Ltd., Tokyo) for morphology analysis of the LDH compounds. The elemental composition of the material was determined by energy dispersive X-ray analysis (EDX) and inductively coupled plasma atomic emission spectroscopy (ICP-AES) using a VISTA RL CCD simultaneous ICP-AES analyzer system (Agilent Technologies, Waldbronn). C/H/N

### 3 LAYERED DOUBLE HYDROXIDES

elemental analysis (EA) was carried out with an Elementar vario EL (Elementar Analysensysteme, Hanau).

FTIR measurements were performed with an IFS 66v/S (Bruker, Madison) spectrometer.

Atomic force microscopy (AFM) measurements were carried out with a Nano Wizard atomic force microscope (JPK Instruments, Berlin) using OMCL-AC160TS micro-cantilevers (Olympus Co., Tokyo) for AC mode imaging. Nanosheet suspensions ( $0.5 \text{ g L}^{-1}$ ) were deposited on freshly cleaved mica sheets and the solvent was evaporated. The images were recorded in intermittent contact mode with  $512 \times 512$  pixel resolution and line rates of 0.5-0.8 Hz. For data analysis Gwyddion SPM analysis software (version 2.23) was used.

Zeta potential of the colloidal suspensions was determined by a Malvern Nano ZS Zetasizer (Malvern, Worcestershire) at  $20^\circ\text{C}$  in formamide using the Hückel-method.

X-ray photoelectron spectroscopy (XPS) was done on an Axis Ultra (Kratos Analytical, Manchester) X-ray photoelectron spectrometer.

Magnetic susceptibility measurements were carried out on a MPMS 7.0 (Quantum Design, San Diego).

Nitrogen adsorption measurements were performed at  $-196^\circ\text{C}$  with an Autosorb iQ instrument (Quantachrome Instruments, Boynton Beach). Samples were outgassed in vacuum at  $150^\circ\text{C}$  for 12 h to remove all physisorbed species. The analysis station was equipped with high-precision pressure transducers and a turbo molecular pump. For Brunauer-Emmett-Teller (BET) calculations pressure ranges were chosen with the help of the BET Assistant in the ASiQwin software (version 2.0). In accordance with the ISO recommendations multipoint BET tags equal to or below the maximum in  $V \cdot (1 - P/P_0)$  were chosen.

To explore the electrochemical behavior of these materials, cyclic voltammograms (CV) and galvanostatic charge/discharge curves were collected. The working electrode was prepared as follows. The analyte (GO/LDH and RGO/LDH), acetylene black (Alfa Aesar) and poly(tetrafluoroethylene) (Aldrich) in a mass ratio of 80:15:5 were mixed together with a few drops of ethanol in an agate mortar and pestle until a homogenous paste was obtained. The paste was then applied with a spatula onto titanium foil (Alfa Aesar, 99.7%) at loading between 4 and 6 mg. The foil with the deposited sample was dried overnight at  $60^\circ\text{C}$  in a vacuum oven.

The foil with the deposited sample was then assembled into a flat cell, using a platinum foil as the counter electrode and a saturated calomel electrode (SCE) as the reference electrode.

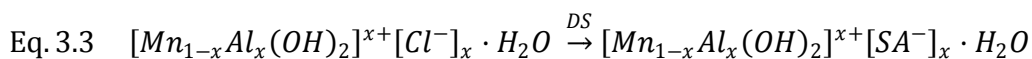
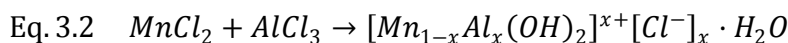
### 3 LAYERED DOUBLE HYDROXIDES

All potential values quoted are versus the SCE. An aqueous solution of sodium nitrate (0.5 M) was used as the electrolyte. Potentiostatic and galvanostatic experiments were conducted using a Solartron SI 1287 Electrochemical Interface or a Princeton Applied Research VersaSTAT electrochemical workstation.

Cyclic voltammograms were collected between -200 and 800 mV at the specified scan rate for at least five cycles. For galvanic charge/discharge experiments, the working electrode was charged to 800 mV and discharged to -200 mV at the specified current for at least ten cycles.

#### 3.1.3 RESULTS AND DISCUSSION

The sulfonate intercalated LDHs were synthesized in one step by direct ion-exchange intercalation of the sulfonate into the LDH. Synthesis of the  $Mn^{II}Al^{III}$  dodecylsulfate LDH proceeds in two steps by anion exchange reaction of  $Mn^{II}Al^{III}$  chloride LDH, synthesized according to Aisawa et al.<sup>[43]</sup>, with a 2.5 fold excess of the organic sulfate. The reaction of the direct intercalation and the two-step synthesis are described by the following equations:



*SA: sulfonic acid; DS: dodecyl sulfate*

Fig. 3.3 shows the XRD patterns of  $Mn^{II}Al^{III}$  ethylbenzenesulfonate LDH (1),  $Mn^{II}Al^{III}$  toluenesulfonate LDH (2),  $Mn^{II}Al^{III}$  naphthalenesulfonate LDH (3),  $Mn^{II}Al^{III}$  dodecylsulfate LDH (4) and  $Mn^{II}Al^{III}$  chloride LDH (5). The series of 00 $l$  reflections that occur up to the 5<sup>th</sup> order in the layered structures suggest a certain degree of order along the layer stacking direction, whereas  $hk0$  reflections ( $d = 2.73 \text{ \AA}$ ;  $d = 1.57 \text{ \AA}$ ) are hardly visible. Successful intercalation is evidenced by the shift of the 00 $l$  reflections towards smaller angles (Table 1), corresponding to the incorporation of the bulky anions and subsequent widening of the interlayer space compared to the material containing small inorganic anions (sample 5).



### 3 LAYERED DOUBLE HYDROXIDES

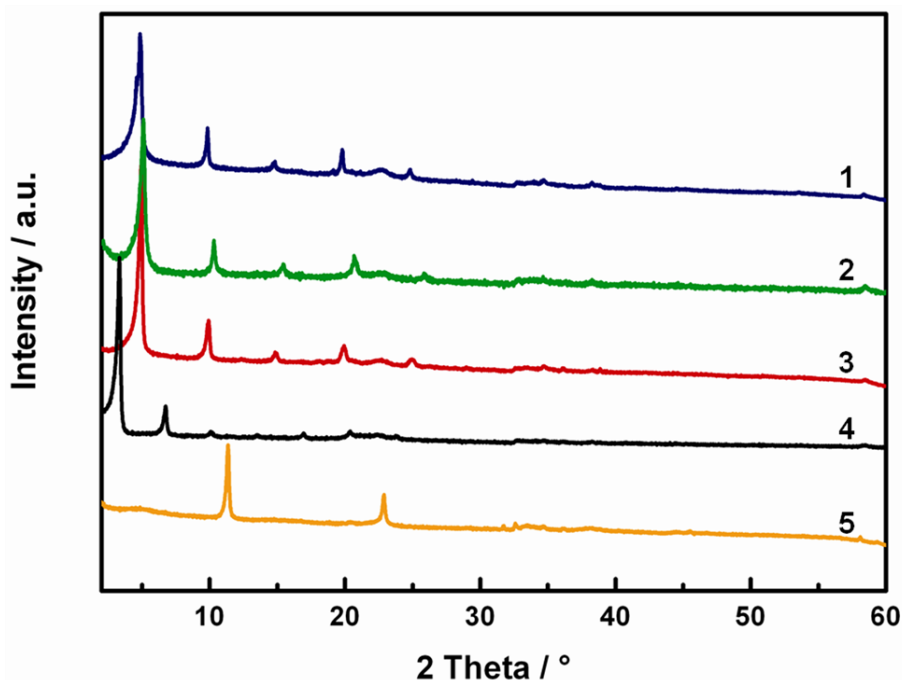


**Figure 3.3.** XRD pattern of **1**  $\text{Mn}^{\text{II}}\text{Al}^{\text{III}}$  ethylbenzenesulfonate, **2**  $\text{Mn}^{\text{II}}\text{Al}^{\text{III}}$  toluenesulfonate LDH, **3**  $\text{Mn}^{\text{II}}\text{Al}^{\text{III}}$  naphthalenesulfonate LDH, **4**  $\text{Mn}^{\text{II}}\text{Al}^{\text{III}}$  dodecylsulfate LDH and **5**  $\text{Mn}^{\text{II}}\text{Al}^{\text{III}}$  chloride LDH.

The FTIR spectra (Fig. 3.4 a) of the SA-LDHs show typical bands of sulfonic acids around  $1170\text{ cm}^{-1}$ ,  $1030\text{ cm}^{-1}$  and  $680\text{ cm}^{-1}$ , as well as bands for Mn-O stretching around  $419\text{ cm}^{-1}$  and Al-O stretching at  $600\text{ cm}^{-1}$ .<sup>[49]</sup> The broad absorption band between  $3700\text{ cm}^{-1}$  and  $2800\text{ cm}^{-1}$  is assigned to the O-H stretching modes of hydrogen-bonded interlayer water molecules and hydroxyl groups. The sharp bands between  $2800\text{ cm}^{-1}$  and  $3000\text{ cm}^{-1}$  are attributed to the C-H stretching modes of the organic anions and are strongest in the case of DS, in line with its large aliphatic carbon backbone. The absence of bands at  $1400\text{ cm}^{-1}$  and  $790\text{ cm}^{-1}$  (Fig. 3.4 b and c, area marked in yellow) points to the absence carbonate for all compounds. SEM analysis (S1) including energy-dispersive X-ray spectroscopy (EDX) was carried out to confirm the results and to assure the homogeneity of the samples. The elemental formulas and the  $d$  values of the LDHs, extracted from ICP-AES and powder XRD data, respectively, are given in Table 1. In order to confirm the oxidation state of Mn magnetic susceptibility measurements were carried out in an applied field of 50,000 Oe to determine the Bohr magneton. According to the literature<sup>[50]</sup>  $\text{Mn}^{2+}$  exhibits values for the Bohr magneton of 5.7-6.1  $\mu\text{B}$ , whereas the values 4.9-5.0  $\mu\text{B}$  and 3.8-4.0  $\mu\text{B}$  are characteristic for  $\text{Mn}^{3+}$  and  $\text{Mn}^{4+}$ , respectively. Fig. S3.2 shows the inverse susceptibilities plotted against the temperature yielding values of the Bohr magneton for the dodecylsulfate

### 3 LAYERED DOUBLE HYDROXIDES

LDH of 5.7  $\mu\text{B}$ , for the ethylbenzenesulfonate LDH of 5.7  $\mu\text{B}$ , for the toluenesulfonate LDH of 6.0  $\mu\text{B}$  and for the naphthalenesulfonate LDH of 5.7  $\mu\text{B}$ , thus evidencing the retention of  $\text{Mn}^{2+}$  in the LDH intercalation compounds.

**Table 3.1.** Intercalating anions, empirical formulas,  $d$  values and Mn/Al ratios for the different LDHs.

	Intercalant	Formula	$d$ value/ $\text{\AA}$	Mn/Al ratio
1	Ethylbenzenesulfonate (ES)	$[\text{Mn}_{0.67}\text{Al}_{0.31}(\text{OH})_2]$ $[\text{ES}_{0.31} \cdot 0.42 \text{H}_2\text{O}]$	18.25	2.16
2	Toluenesulfonate (TS)	$[\text{Mn}_{0.67}\text{Al}_{0.32}(\text{OH})_2]$ $[\text{TS}_{0.29} \cdot 0.78 \text{H}_2\text{O}]$	17.26	2.16
3	Naphthalenesulfonate (NS)	$[\text{Mn}_{0.67}\text{Al}_{0.35}(\text{OH})_2]$ $[\text{NS}_{0.34} \cdot 0.30 \text{H}_2\text{O}]$	17.89	1.91
4	Dodecylsulfate (DS)	$[\text{Mn}_{0.67}\text{Al}_{0.31}(\text{OH})_2]$ $[\text{DS}_{0.24} \cdot 0.78 \text{H}_2\text{O}]$	26.58	2.16
5	Chloride	$[\text{Mn}_{0.67}\text{Al}_{0.31}(\text{OH})_2]$ $[\text{Cl}_{0.31} \cdot 0.47 \text{H}_2\text{O}]$	7.80	2.16

Exfoliation of  $\text{Mn}^{\text{II}}\text{Al}^{\text{III}}$  LDHs. Exfoliation of all compounds was carried out by ultrasonic treatment of the LDHs in formamide or mechanical shaking for  $> 20$  days in formamide. According to Hibino<sup>[20]</sup> formamide is predestined for the exfoliation of LDHs due to its capability to penetrate between the Brucite-type layers, interact with the interlayer anions and thus remove these molecules. Exfoliation of the LDHs yielded brownish colloidal suspensions. The presence of nanoparticles in the suspensions is evidenced by the Tyndall effect shown in Fig. 3.5 c.

The zeta potentials of the colloidal suspensions are +35.5 mV for the dodecylsulfate LDH, +46.1 mV for the ethylbenzenesulfonate LDH, +48.8 mV for the toluenesulfonate LDH and +35.8 mV for the naphthalenesulfonate LDH, indicating that the nanosheets are positively charged and the suspensions are stable. A representative TEM image along with a related selected area electron diffraction (SAED) pattern of a nanosheet (Figs. 3.5 a and b) confirms the hexagonal crystal structure of the LDHs and suggests the existence of very thin layers. The reflections corresponding to  $d$  values of 1.53  $\text{\AA}$  and 2.66  $\text{\AA}$  as seen by

### 3 LAYERED DOUBLE HYDROXIDES

SAED match well with the XRD patterns. The AFM tapping mode images in Figs. 3.5 d and S3.3 show exfoliated  $\text{Mn}^{\text{II}}\text{Al}^{\text{III}}$  LDHs with lateral dimensions of about 50-400 nm.

Different exfoliation protocols have shown that ultrasonication does not significantly reduce the lateral size of the nanosheets. Nevertheless, it can clearly be seen that the nanosheet edges are typically rough and irregular in shape, which may be rationalized by sheet damage during the exfoliation step. The height of the exfoliated nanosheets ranges from a minimum of 1.29 nm up to about 5.00 nm. Considering the known thickness of the Brucite-type layers of around 0.5 nm,<sup>[51]</sup> we conclude that exfoliation was successful down to two or three layers. This estimation, however, is rather conservative, as the nanosheets are surrounded by an organic ligand and hydration shell and likely restack as they are deposited on the substrate. Hence, the observed nanosheet thicknesses can be considered as an upper limit to their actual thickness in the suspension.

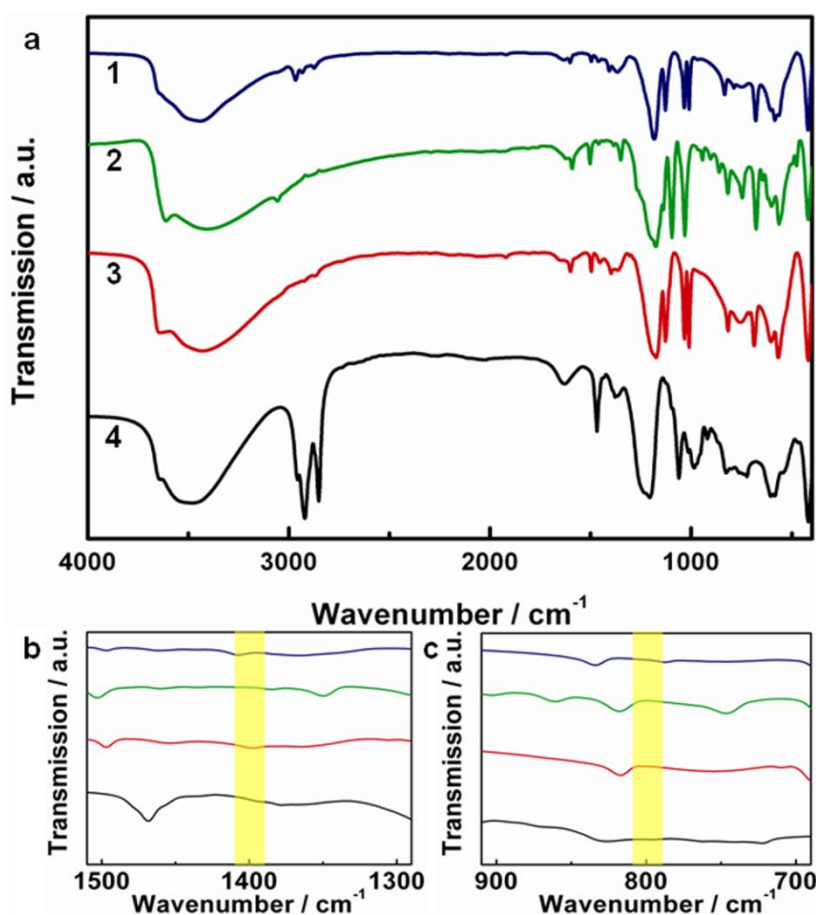


**Figure 3.4.** FTIR spectra of **1**  $\text{Mn}^{\text{II}}\text{Al}^{\text{III}}$  ethylbenzenesulfonate, **2**  $\text{Mn}^{\text{II}}\text{Al}^{\text{III}}$  toluenesulfonate LDH, **3**  $\text{Mn}^{\text{II}}\text{Al}^{\text{III}}$  naphthalenesulfonate LDH and **4**  $\text{Mn}^{\text{II}}\text{Al}^{\text{III}}$  dodecylsulfate LDH.

### 3 LAYERED DOUBLE HYDROXIDES

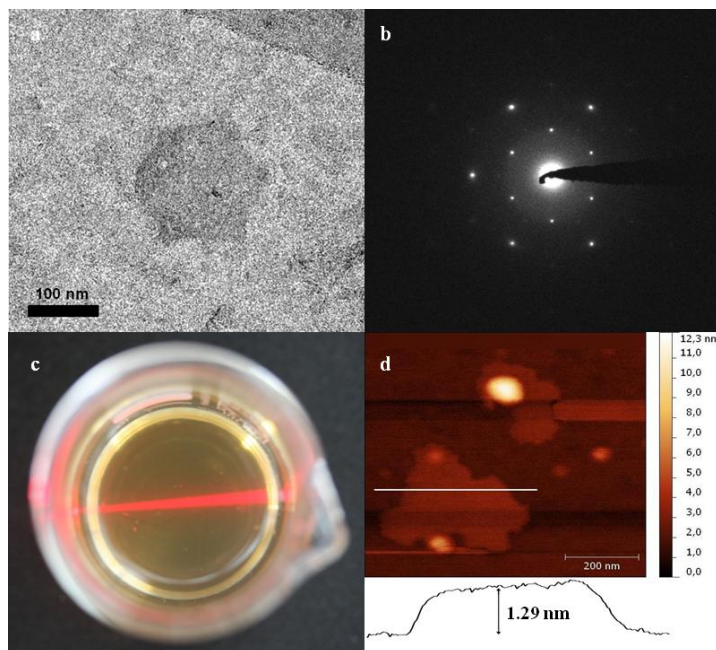


**Figure 3.5.** (a) TEM image of a  $\text{Mn}^{\text{II}}\text{Al}^{\text{III}}$  dodecylsulfate LDH nanosheet and (b) a related SAED pattern. (c) Cuvette containing the nanosheet suspension through which the beam of a laser pointer is passed. The clearly visible Tyndall effect confirms the existence of colloidal particles in the suspension. (d) AFM image and height profile of an aggregate of nanosheets.

Flocculation of GO/LDH and reduction to RGO/LDH. Owing to its negative surface charge graphite oxide, GO, is an excellent candidate for the fabrication of electrostatically assembled LDH/GO nanostructures to yield functional hybrid materials that are constructed with a high degree of interfacial contacts between the two components and, hence, efficient phase separation on the nanometer scale.

GO was synthesized according to Kovtyukhova *et al.*<sup>[47]</sup> For elemental analysis, FTIR and powder XRD measurements the nanosheets were freeze-dried. Fig. S3.4 shows the XRD pattern of the as-synthesized powder. The peak at  $11.6^\circ$   $2\theta$  is assigned to the (001) lattice plane corresponding to the interlayer distance  $d = 7.6 \text{ \AA}$ .<sup>[52]</sup> According to the literature<sup>[53]</sup> the interlayer distance of dry GO is  $6.35 \text{ \AA}$  and  $7.7 \text{ \AA}$  for GO stored in an atmosphere with 50 % relative humidity. The peak at  $22.6^\circ$  is usually associated with high amounts of adsorbed water,<sup>[54]</sup> and the reflections at  $34.8^\circ$  and  $42.2^\circ$  are assigned as 110 and 101, respectively.<sup>[55]</sup> The FTIR spectrum and band assignments of the freeze-dried GO is shown in Fig. S3.5 and Table S1. The result of the elemental analysis (Table S2) is in good agreement with the literature.<sup>[56]</sup>

### 3 LAYERED DOUBLE HYDROXIDES

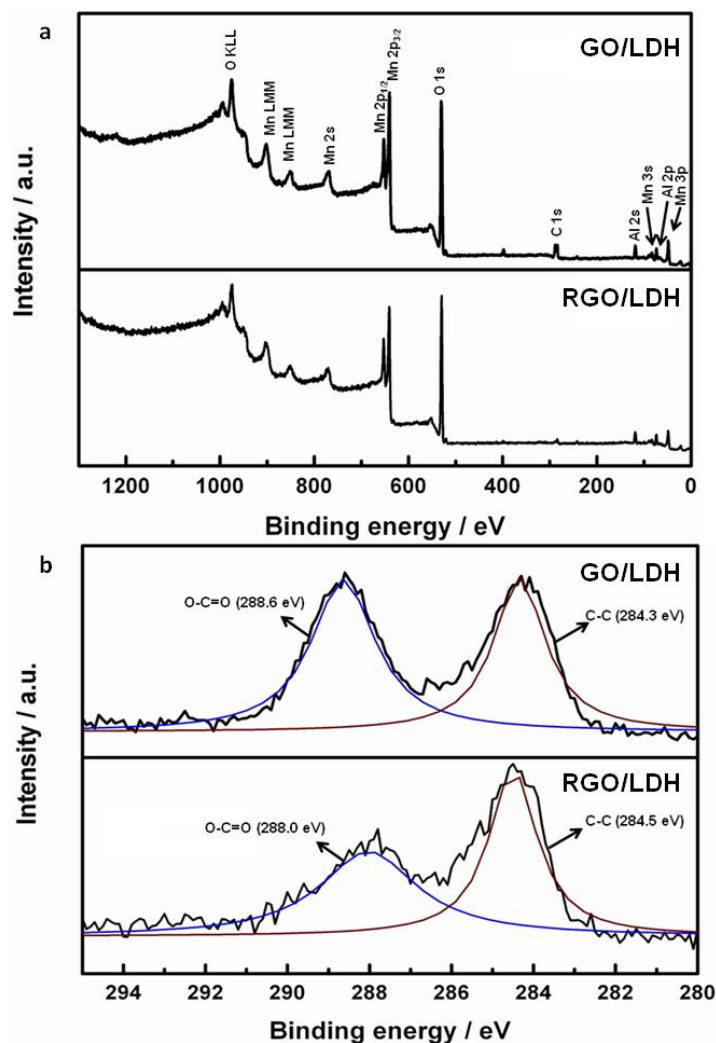


**Figure 3.6.** XPS (a) survey and (b) C1s spectra of GO/LDH and RGO/LDH samples.

Directed assembly of GO and LDH nanosheets was accomplished by flocculation of GO and LDH. Subsequently, a reduced graphene oxide (RGO)/LDH hybrid material was obtained by hydrazine reduction of the as-synthesized GO/LDH. It should be noted that the pristine LDH, when subjected to the same reduction reaction, did not show any noticeable chemical or spectroscopic changes. Figs. 3.6 a and b outline the survey and C1s XPS spectra of the two materials. The survey spectra demonstrate that both GO and LDH are present in the flocculated sample. The peaks at 640.5 eV, 652.0 eV and 769.5 eV corresponding to Mn2p<sub>3/2</sub>, Mn2p<sub>1/2</sub> and Mn2s as well as the peaks at 73.5 eV and 118.5 eV originating from Al2p and Al2s confirm the presence of the Mn<sup>II</sup>Al<sup>III</sup> LDH. The absence of the S2p<sub>3/2</sub> peak at 164.0 eV evidences that the sulfonate anions are essentially removed from the composite material. The C1s spectra (Fig. 3.6 b) give information about the degree of

### 3 LAYERED DOUBLE HYDROXIDES

oxidation of the graphitic species. The peak at 288.6 eV resulting from carboxylate groups (O-C=O) strongly decreases in the reduced sample in comparison to the pristine GO/LDH by a factor of 3.3.<sup>[57]</sup> This indicates a partial reduction of the GO/LDH compound, which is consistent with previous studies in the literature.<sup>[30]</sup> The ratio of Mn:Al in the GO/LDH and RGO/LDH material were determined as 2.2:1 and 2.4:1, respectively. The ratio of Mn:C in the GO/LDH and RGO/LDH sample amounts to 1:1 and 2.6:1, respectively. The significantly decreased carbon content in the reduced sample may tentatively be attributed to less beneficial interactions between the hydrophilic LDH and the hydrophobic carbon matrix.

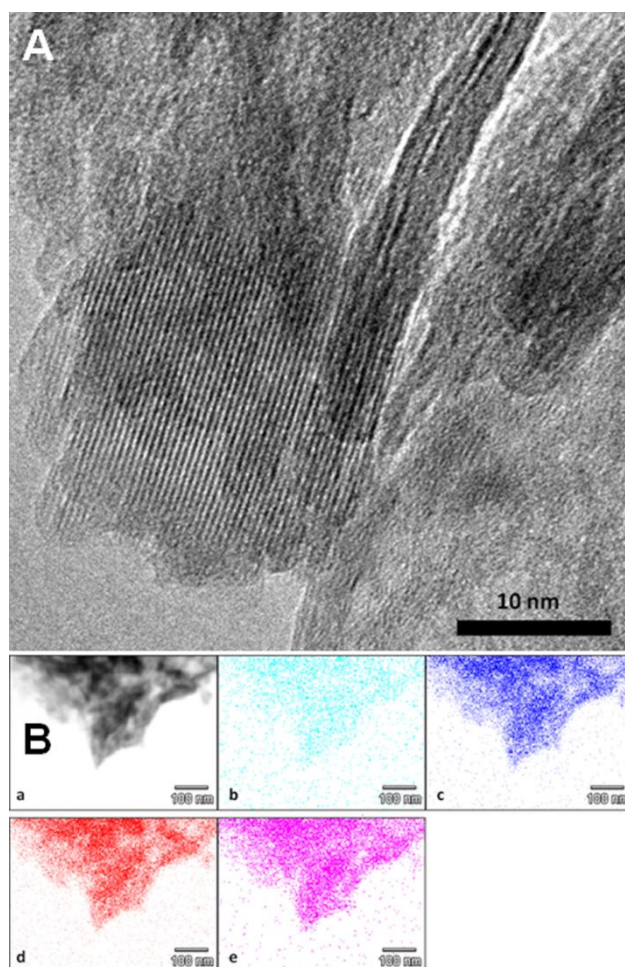


**Figure 3.7.** A) TEM image of RGO/LDH hybrid material. The lattice fringes correspond to  $d$  values of 4.6 Å, thus indicating the reduction of GO to graphene. B) (a) TEM image of the RGO/LDH composite and related EDX mapping of the (b) C-K, (c) O-K, (d) Mn-K and (e) Al-K edges, demonstrating the homogeneous distribution of all elements across the observed region.



### 3 LAYERED DOUBLE HYDROXIDES

The BET surface areas of GO/LDH and RGO/LDH are  $178 \text{ m}^2\text{g}^{-1}$  and  $148 \text{ m}^2\text{g}^{-1}$ , respectively, which is fairly high compared to other LDH-based hybrids, for example LDH/titanate with a maximal BET surface area of  $104 \text{ m}^2\text{g}^{-1}$ .<sup>[25]</sup> The reduction of GO decreases the surface area of the hybrid material due to the removal of carboxylate groups and the resulting capability of the layers to align and stack more efficiently. Accordingly, partial order of the hybrid compound is retained as ascertained by TEM analysis (Fig. 3.7 A). Lattice planes with a distance of  $4.6 \text{ \AA}$  point to regions of GO reduced to graphene. In Fig. 3.7 B an EDX mapping of the RGO/LDH underlines the homogeneous distribution of C, O, Mn and Al in the sample.

The manganese centres available in these hybrid materials provide redox-active sites for potential applications in electrochemistry, which include pseudocapacitive energy storage components (as shown previously for other GO/LDH and RGO/LDH material).<sup>[27-41,57]</sup> We thus characterized the electrochemical properties of these hybrid materials to evaluate their feasibility for these applications. To test these materials as supercapacitors, we have conducted small scale galvanostatic and potentiostatic experiments based on literature protocols.  $\text{Na}_2\text{SO}_4$  was employed as the electrolyte, as opposed to the more common NaOH or KOH electrolyte, due to excessive oxygen evolution from oxidation of the hydroxide when an alkaline solution was used. This was not unexpected, since oxo-compounds or oxides of manganese are known to be electrocatalysts for the oxygen evolution reaction.<sup>[46]</sup> However, the application of manganese hydroxide as OER electrocatalyst has not been explored and will be elaborated in the subsequent section. CVs in aqueous  $0.5 \text{ M Na}_2\text{SO}_4$  solution (Fig. 3.8 a-b) of the two hybrid compounds were collected at different scan rates between  $2$  and  $100 \text{ mV s}^{-1}$ . The voltammograms obtained at a scan rate of  $5 \text{ mV s}^{-1}$  for GO/LDH, RGO/LDH and pristine LDH are also shown together in Figure 3.8c. For the GO/LDH material and the pristine LDH, the voltammograms at slow scan rates showed a reduction at around  $470 \text{ mV}$  and an oxidation in the  $200\text{-}300 \text{ mV}$  range, which we attribute to the redox cycle between  $\text{Mn}^{2+}$  and its higher oxidation states. For the RGO/LDH, the manganese redox peaks are barely observable, indicating that the current is largely capacitive with a near-zero faradaic contribution. The absence of the redox event for this material may be due to compaction of the layered structure after reduction, resulting in a loss of surface area and reduced exposure of the manganese centres.

Repeated cyclic voltammetry measurements for 500 cycles at  $100 \text{ mV s}^{-1}$  (Figure 3.8e) showed minor decrease in the capacitive and/or faradaic currents for the two materials, demonstrating their general stability in a broad electrochemical potential window. Galvanic

### 3 LAYERED DOUBLE HYDROXIDES

charge/discharge cycles for the three materials are shown in Figure 3.8 d. All materials showed a fast potential drop in the initial stage of discharge, corresponding to internal resistance, followed by a slow potential decay attributed to the pseudocapacitance of the electroactive materials. The specific capacitance  $C_{SP}$  was calculated using the following equation<sup>[27]</sup>:

$$\text{Eq. 3.4} \quad C_{SP} = i \cdot \Delta t \cdot m^{-1} \cdot \Delta v^{-1}$$

where  $i$  is the galvanic current,  $\Delta t$  the discharge time,  $m$  the mass of the electroactive material and  $\Delta v$  the total potential change. At a galvanic discharge current of 0.5 mA, the specific capacitance values of GO/LDH, RGO/LDH and LDH are 20, 13 and 11 F g<sup>-1</sup>, respectively.

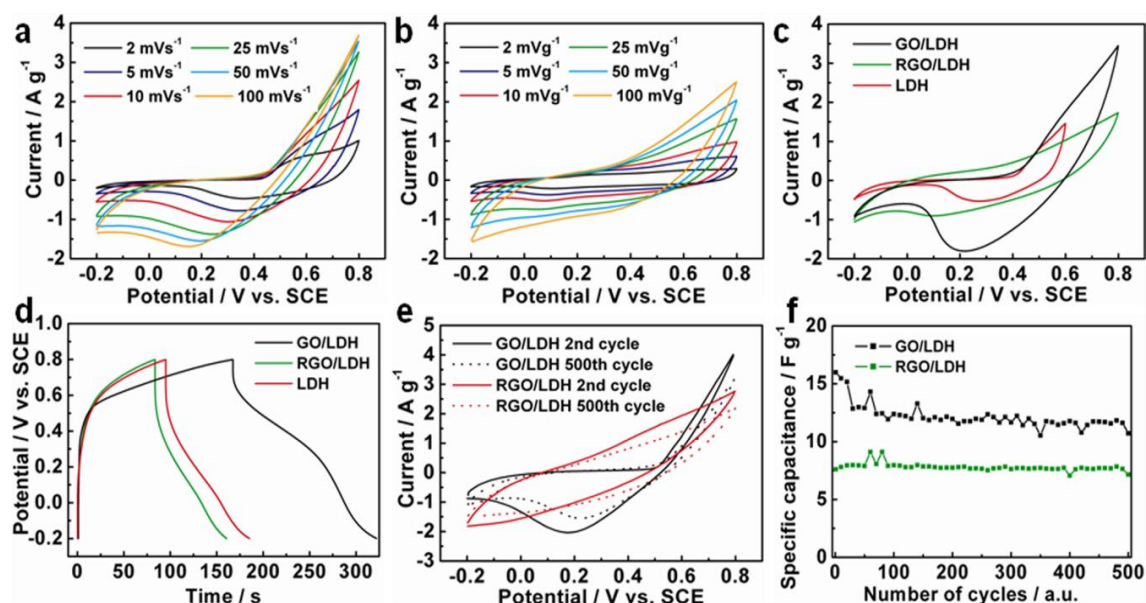


**Figure 3.8.** Cyclic voltammograms of (a) GO/LDH, (b) RGO/LDH and (c) comparison of cyclic voltammograms of GO/LDH, RGO/LDH and LDH at a scan rate of 5 mV·s<sup>-1</sup>, (d) charge/discharge curves of GO/LDH, RGO/LDH and LDH at a galvanostatic current of 0.5 mA. (e) Cyclic voltammograms of GO/LDH and RGO/LDH of the 2<sup>nd</sup> and 500<sup>th</sup> cycle, (f) cyclic stability curves of GO/LDH and RGO/LDH at 10 mA.



### 3 LAYERED DOUBLE HYDROXIDES

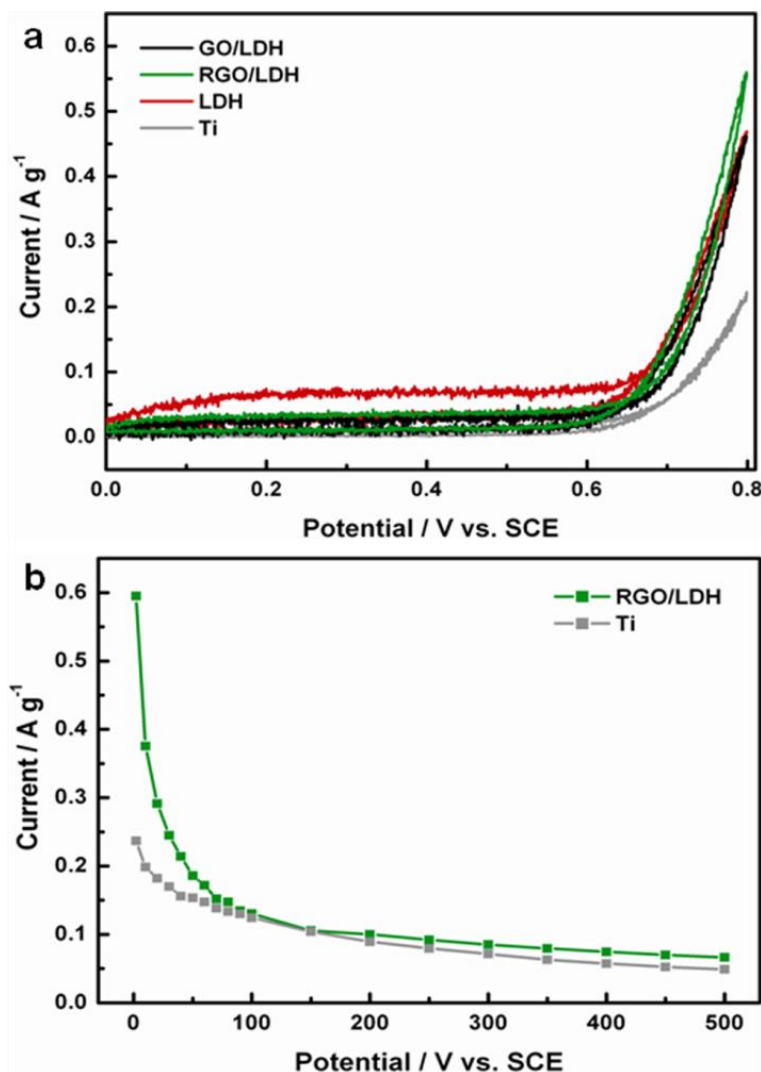


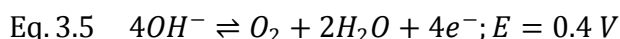
**Figure 3.9.** a) Cyclic voltammograms of GO/LDH, RGO/LDH, LDH and Ti-foil at a scan rate of  $1 \text{ mV}\cdot\text{s}^{-1}$  in  $1 \text{ M NaOH}$  solution. b) Cyclic stability curves of RGO/LDH and Ti-foil at  $200 \text{ mV}\cdot\text{s}^{-1}$  in  $1 \text{ M NaOH}$  solution.

The contribution from chemically reduced graphene oxide can be excluded, as its specific capacitance has been determined to be  $1.14 \text{ F g}^{-1}$ .<sup>[58]</sup> The enhancement of capacitance of GO/LDH over the RGO/LDH material is attributed to the pseudocapacitive behavior resulting from the redox cycle of the manganese centers. As mentioned above, we rationalized the low capacitance of RGO/LDH to be due to the reduced availability of the manganese redox centres, as evidenced by the CV, as a result of the partial compaction of the layered structure, thus decreasing the pseudocapacitance contribution. Furthermore, compositing of the LDH with GO led to a capacitance increase over the pristine LDH, an enhancement that we attribute to electronic coupling between the GO and the redox active

### 3 LAYERED DOUBLE HYDROXIDES

manganese centers in the LDH, thus illustrating the advantage of nanoscale hybridisation of layered materials. The electrochemical stability of the hybrid materials was tested by galvanostatic charge/discharge at a current of 10 mA and, in agreement with results from the cyclic voltammetry experiments these materials showed general stability for 500 cycles (Fig. 3.8 f). Their electrochemical stability and redox properties highlight the potential applicability of these materials as nanoscale electronic devices.

As mentioned above, the pristine LDH and hybrid materials were observed to evolve oxygen under an applied anodic potential in alkaline electrolyte and were thus also explored for their electrocatalytic OER activity. CVs (Fig. 3.9 a) were conducted between 0 and 800 mV in NaOH solution (1 M). A slow scan rate ( $1 \text{ mV s}^{-1}$ ) was used to simulate quasi-equilibrium conditions, such that diffusion limitation was avoided and capacitive current was minimized. These hybrid materials started evolving oxygen at slightly above 600 mV ( $\sim 840 \text{ mV vs SHE}$ ), which represents a required overpotential of  $\sim 440 \text{ mV}$  for hydroxide oxidation:



The OER currents for LDH, GO/LDH and RGO/LDH, at loading of approximately  $200 \mu\text{g}$  on the titanium foil, are more than twice as high as the unmodified foil at a potential of 800 mV. We emphasize that, on a per manganese site basis, the electrocatalytic activity of the two hybrid samples are underestimated, since the same mass loading was used in all experiments for both the pure LDH and the LDH composite. As it is possible for oxygen to evolve through the oxidation of the coordinating hydroxide we conducted repeated cycling at  $200 \text{ mV s}^{-1}$  for 500 cycles to test for electrochemical stability in RGO/LDH. A plot of the cycle number *versus* peak current in Figure 3.9 b shows that, for the initial 100 cycles, the OER peak current dropped quickly, before plateauing in the onward cycles. Thus, the instability of the anodic current is attributed to oxidation of the coordinating hydroxide, which is not replenished by the hydroxide from the solution as necessary in a catalytic cycle. Although these materials cannot yet be considered as an effective electrocatalyst, their ability to evolve oxygen illustrates the possibility of using Mn-LDH centres as the core in the design of an OER electrocatalyst, in addition to the oxo-manganese species that are well-studied in the literature.<sup>[46,59]</sup> Further studies in this area addressing their stability issue (e.g. by improving the surface area and thus facilitate the access of hydroxide to replenish

### 3 LAYERED DOUBLE HYDROXIDES

the oxidized ligand at the manganese centre) will be conducted in future work and will provide a better evaluation of these materials for electrocatalytic applications.

#### 3.1.4 CONCLUSION

In this work we presented the synthesis of  $\text{Mn}^{\text{II}}\text{Al}^{\text{III}}$  sulfonate and dodecylsulfate LDHs by coprecipitation and anion exchange, respectively, and their exfoliation in formamide to yield colloidal suspensions of positively charged nanosheets. The 2D sheets were comprehensively characterized by AFM, zeta potential measurements and TEM, demonstrating the retention of the hexagonal structure of the parent Brucite-type layers. Furthermore, we demonstrated the facile flocculation of the positively charged LDH nanosheets with an aqueous graphene oxide (GO) suspension to yield an intimately mixed nanocomposite with high surface area. This material was partially reduced with hydrazine to RGO/LDH. Both GO/LDH and RGO/LDH exhibited electrochemical stability over a wide potential window as well as over repeated charge/discharge cycles. GO/LDH displayed improved capacitance over pristine LDH and the RGO/LDH, an enhancement attributed to the Faradic contribution and electronic coupling of the LDH with GO.<sup>[24,27]</sup> Furthermore the LDH and the hybrid compounds were tested as electrocatalyst for the OER and exhibited oxygen evolution under an anodic potential. Although their electrochemical stability remains an issue, these results illustrate the possibility of using a hydroxyl-manganese centre in the bottom-up design of OER electrocatalyst. Finally, this work can be seen as a first step towards obtaining positively charged  $\text{Mn}^{2+}$ -containing nanosheets, which may become relevant as nanoscale building blocks in the emerging field of nanoarchitectonics based on magnetic nanostructures, and for the rational synthesis of nanoscale hybrid materials for supercapacitors, batteries and electrocatalysis.

### 3 LAYERED DOUBLE HYDROXIDES

#### 3.1.5 SUPPORTING INFORMATION

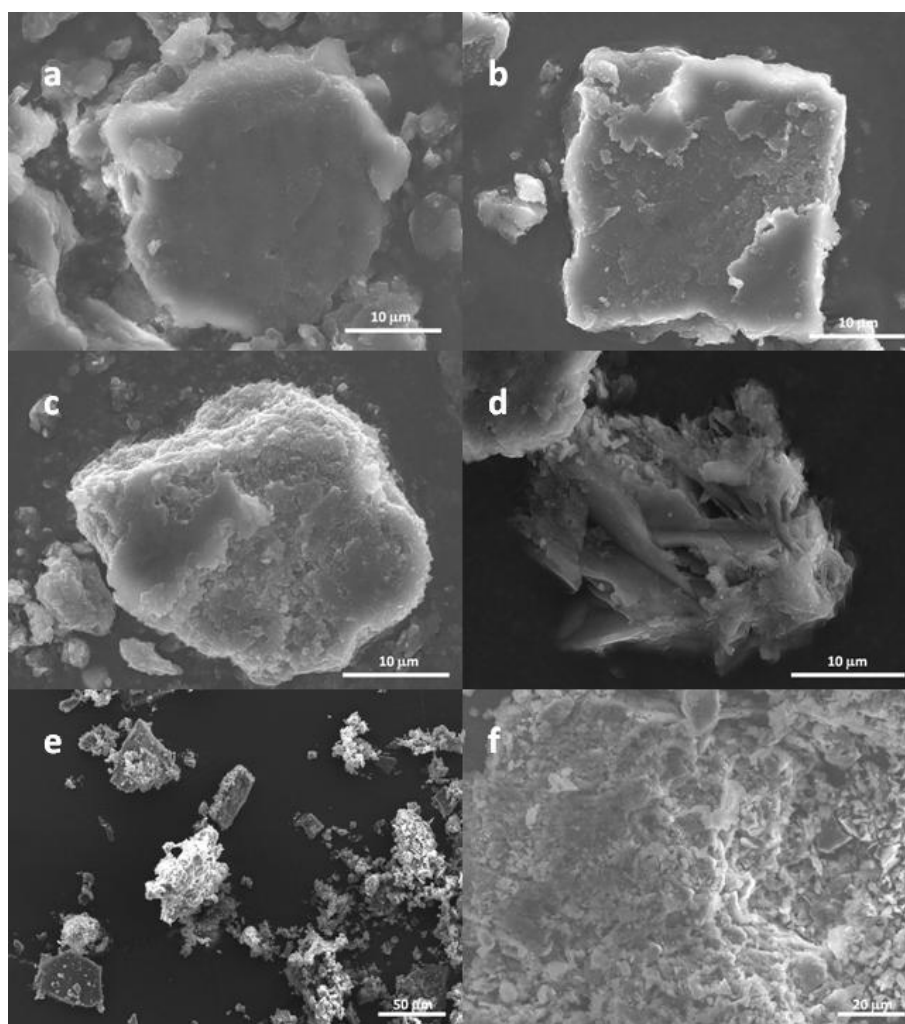


**Fig. S3.1.** SEM images of (a) Mn<sup>II</sup>Al<sup>III</sup> dodecylsulfate LDH, (b) Mn<sup>II</sup>Al<sup>III</sup> ethylbenzenesulfonate LDH, (c) Mn<sup>II</sup>Al<sup>III</sup> toluenesulfonate LDH, (d) Mn<sup>II</sup>Al<sup>III</sup> naphthalenesulfonate, (e) GO/LDH and (f) GNS/LDH.

### 3 LAYERED DOUBLE HYDROXIDES

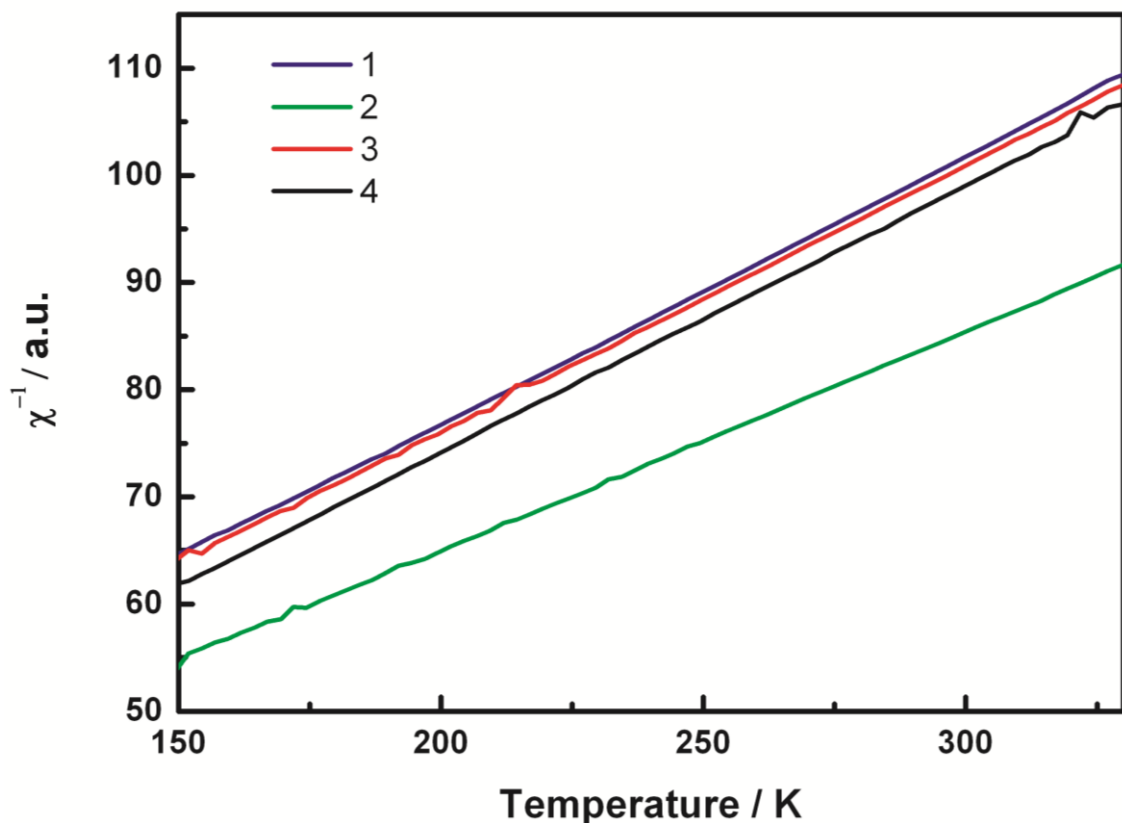


**Fig. S3.2.** Inverse susceptibilities plotted versus the temperature of **1**  $\text{Mn}^{\text{II}}\text{Al}^{\text{III}}$  ethylbenzenesulfonate, **2**  $\text{Mn}^{\text{II}}\text{Al}^{\text{III}}$  toluenesulfonate LDH, **3**  $\text{Mn}^{\text{II}}\text{Al}^{\text{III}}$  naphthalenesulfonate LDH, **4**  $\text{Mn}^{\text{II}}\text{Al}^{\text{III}}$  dodecylsulfate LDH.

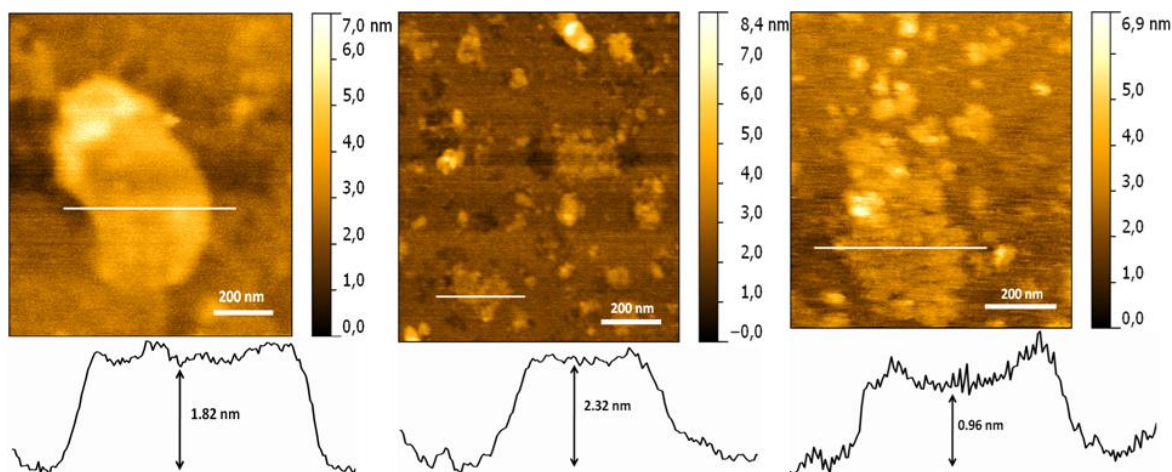


**Fig. S3.3.** AFM images of exfoliated (a)  $\text{Mn}^{\text{II}}\text{Al}^{\text{III}}$  ethylbenzenesulfonate LDH, (b)  $\text{Mn}^{\text{II}}\text{Al}^{\text{III}}$  toluenesulfonate LDH and (c)  $\text{Mn}^{\text{II}}\text{Al}^{\text{III}}$  naphthalenesulfonate.

### 3 LAYERED DOUBLE HYDROXIDES

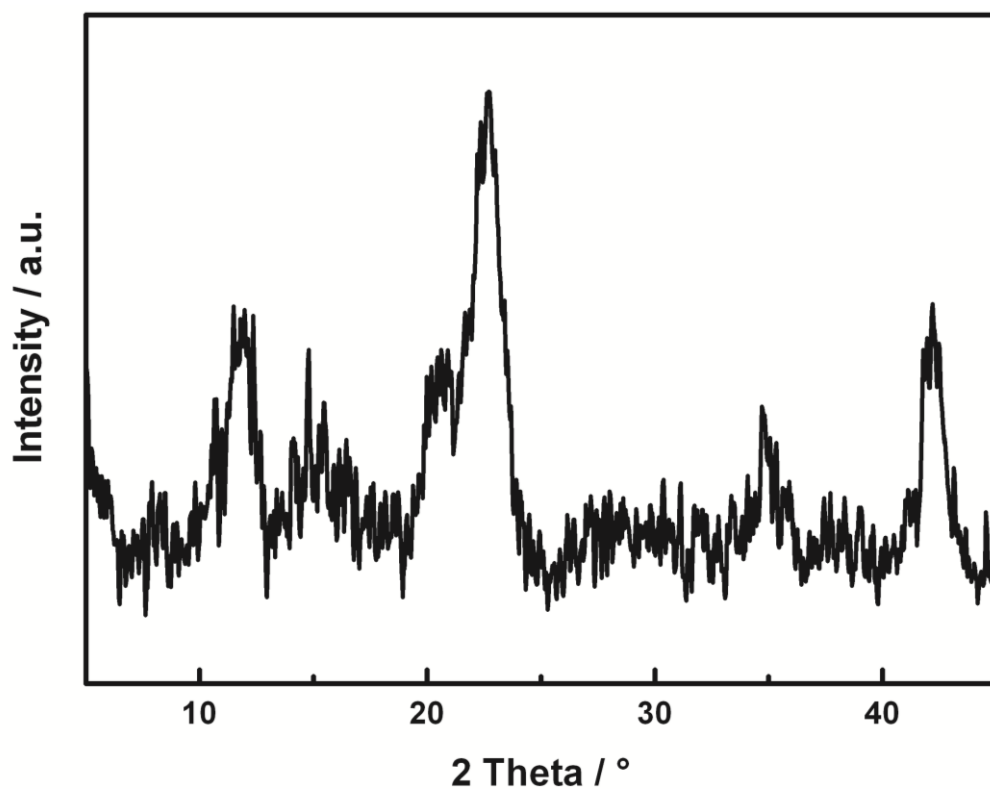


Fig. S3.4. XRD pattern of freeze-dried GO.

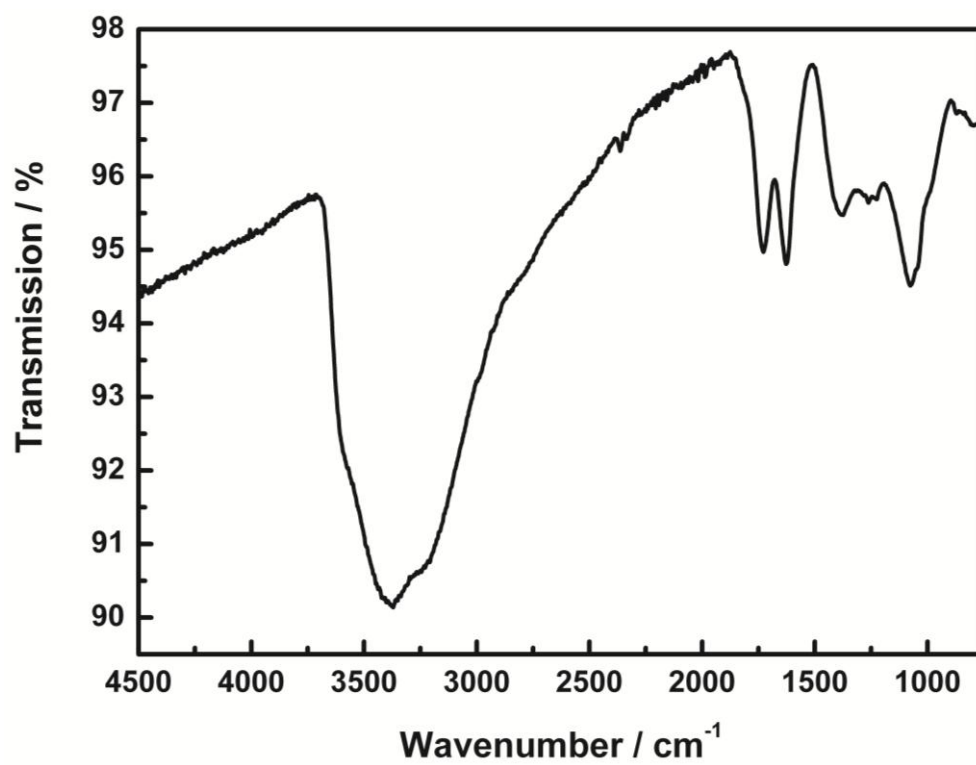


Fig. S3.5. FTIR spectrum of freeze-dried GO.

### 3 LAYERED DOUBLE HYDROXIDES

**Table S1.** Assignment of the vibrational modes of GO.

Modes/ $\text{cm}^{-1}$	Assignment
3376	$\nu(\text{OH})$ water, alcohol
1730	$\nu(\text{C}=\text{O})$
1622	$\delta(\text{OH})$ water
1382	$\delta(\text{OH})$ alcohol
1256	$\nu(\text{C}-\text{O})$
1080	$\nu(\text{C}-\text{OH})$

**Table S2.** Elemental analysis of GO. The values are given in weight-%, the amount of oxygen was calculated from the difference to 100 %.

C	H	O	S	C/O
46.09%	2.20%	50.40%	1.31%	1.22

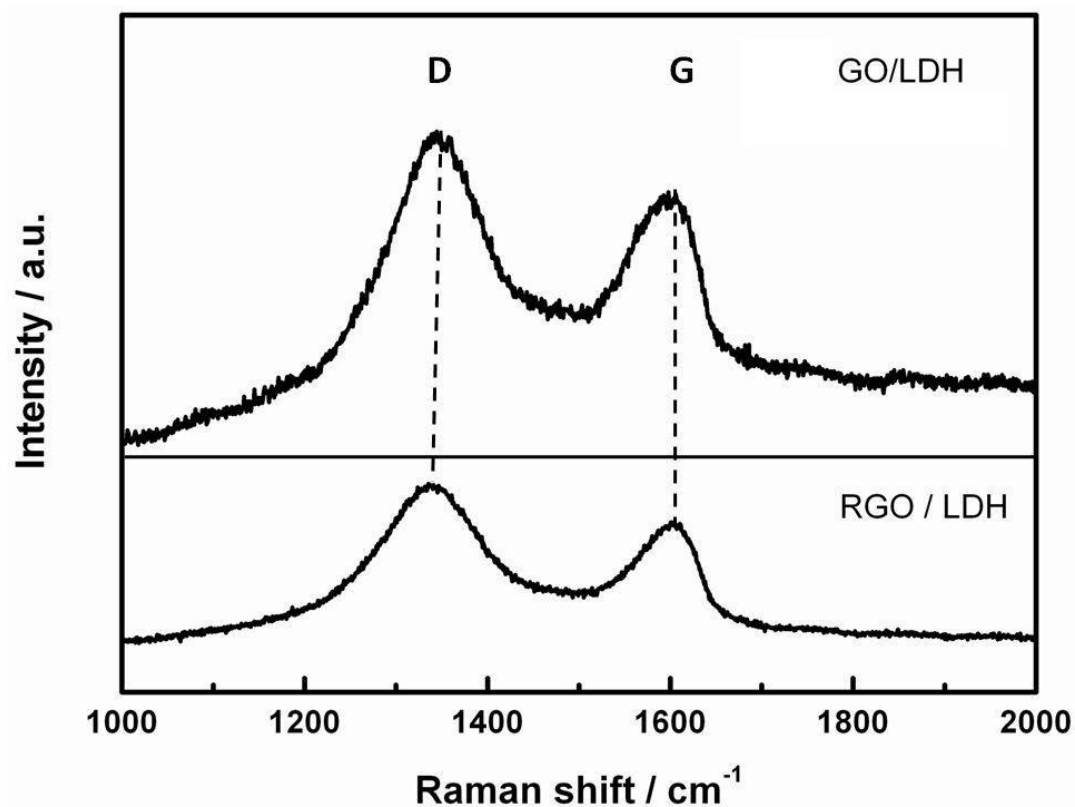


**Fig. S3.6.** Raman spectra of GO/LDH and RGO/LDH.

### 3 LAYERED DOUBLE HYDROXIDES

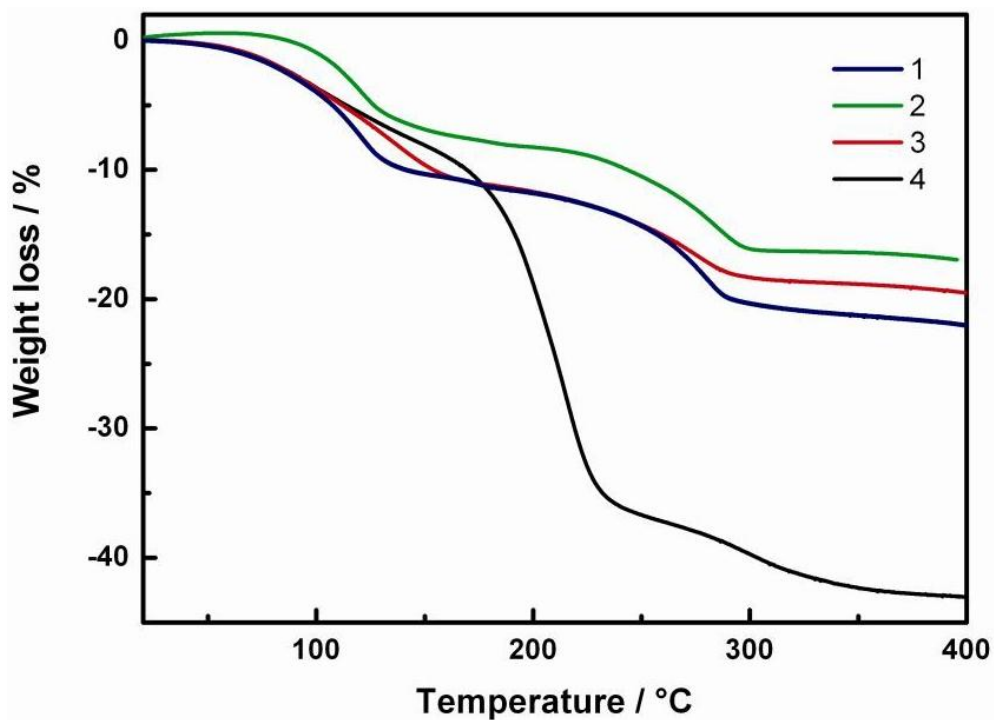


**Fig. S3.7.** DTA-TG curves of **1**  $\text{Mn}^{\text{II}}\text{Al}^{\text{III}}$  ethylbenzenesulfonate LDH, **2**  $\text{Mn}^{\text{II}}\text{Al}^{\text{III}}$  toluenesulfonate LDH, **3**  $\text{Mn}^{\text{II}}\text{Al}^{\text{III}}$  naphthalenesulfonate LDH and **4**  $\text{Mn}^{\text{II}}\text{Al}^{\text{III}}$  dodecylsulfate LDH.

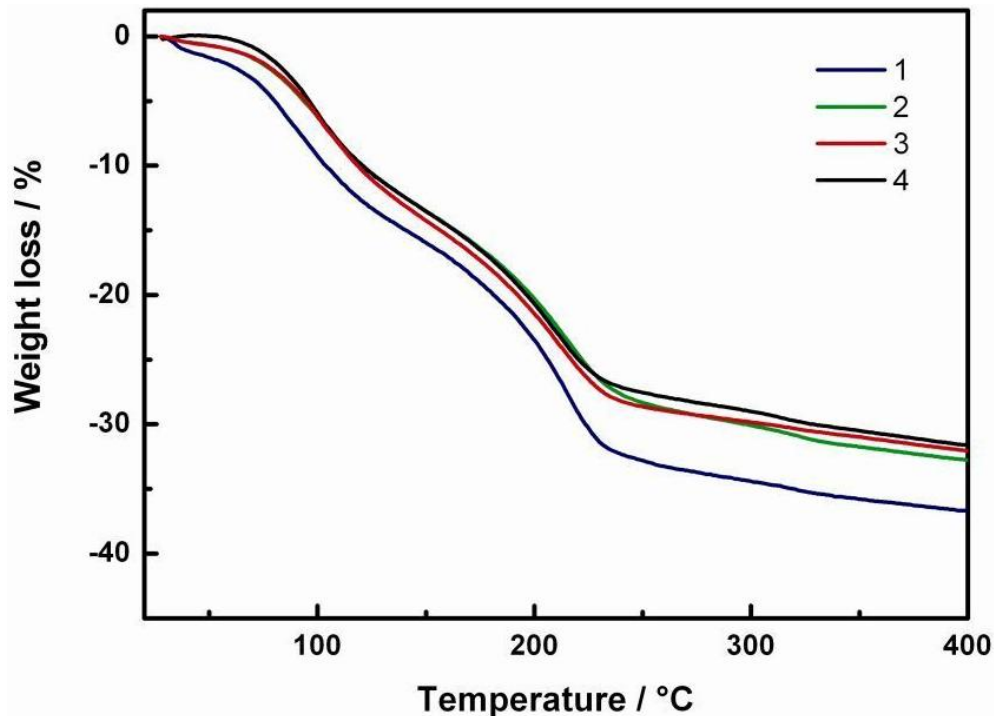


**Fig. S3.8.** DTA-TG curves of exfoliated samples of **1**  $\text{Mn}^{\text{II}}\text{Al}^{\text{III}}$  ethylbenzenesulfonate LDH, **2**  $\text{Mn}^{\text{II}}\text{Al}^{\text{III}}$  toluenesulfonate LDH, **3**  $\text{Mn}^{\text{II}}\text{Al}^{\text{III}}$  naphthalenesulfonate LDH and **4**  $\text{Mn}^{\text{II}}\text{Al}^{\text{III}}$  dodecylsulfate LDH. The weight loss steps are less pronounced and the overall thermal stability of the nanosheets is lower.



### **3 LAYERED DOUBLE HYDROXIDES**

#### **FUNDING SOURCES**

This work was supported by the Max Planck Society, the cluster of excellence Nanosystems Initiative Munich (NIM), the Fonds der Chemischen Industrie (FCI) and the Center for Nanoscience (CeNS).

#### **ACKNOWLEDGMENT**

We thank Kulpreet S. Viridi for TEM measurements, Christian Minke for SEM measurements, Dr. M. Konuma for XPS measurements, Dr. Reinhard Kremer and Eva Brücher for magnetic susceptibility measurements, Armin Schulz for Raman measurements and Helmut Hartl and Marie-Luise Schreiber for ICP-AES analysis.

## 3.2 LAYER-BY-LAYER ASSEMBLY OF $\text{Mn}^{\text{II}}\text{Al}^{\text{III}}$ LDH AND GRAPHENE OXIDE

In addition to the flocculation experiments of GO with  $\text{Mn}^{\text{II}}\text{Al}^{\text{III}}$  LDH, the two compounds have been assembled in an electrostatic layer-by-layer fashion. The scope of this chapter is the proof of concept of custom-made 3D hybrid materials consistent with oppositely charged two dimensional nanosheets, as well as the in-depth analysis of the hybrid lattice.

### 3.2.1 EXPERIMENTAL

$\text{Mn}^{\text{II}}\text{Al}^{\text{III}}$  LDH and GO nanosheets were synthesized as described in chapter 3.1. The multilayer films composed of GO and LDH were then assembled using a StratoSequence 6 LBL robot (nanoStrata Inc., Tallahassee). After exfoliation, a Si (100) wafer terminated with a native  $\text{SiO}_2$  layer (Si/ $\text{SiO}_2$ ) was first immersed into the LDH nanosheet suspension in formamide for 15 min, then rinsed in water for 1.5 min, immersed in the GO nanosheet suspension in water for 15 min and rinsed in water again for 1.5 min. This procedure was repeated  $n$  times in order to obtain multilayer films. The washed film was dried under  $\text{N}_2$  gas flow for 1 min after each cycle.

### 3.2.2 RESULTS AND DISCUSSION

Besides flocculation of LDH with GO and its subsequent reduction, which naturally results in rather disordered lamellar assemblies, exfoliated LDH nanosheets have also been used for the sequential electrostatic layer-by-layer assembly with GO nanosheets. Here, the objective was the synthesis of well-defined hybrid heterostructures with strictly alternating layer sequences.<sup>[60]</sup> Therefore, positively charged LDH nanosheets and negatively charged GO sheets were used for electrostatic LBL assembly. Figure 10 shows a plot of the average thickness of a GO/LDH film measured by AFM.

The plot shows a linear progression of the average thickness of the films compared to the number of double layers (dl). The regression yields  $f(x) = 1.007 \cdot x$ . Taking the crystallographic thicknesses of LDH Brucite layers (0.48 nm)<sup>[51]</sup> and GO (0.69 nm)<sup>[61]</sup> into account, the experimentally obtained data fits to the theoretical values if the sequential adsorption of one nanosheet LDH and GO per cycle is assumed. The film thickness of 100 dl is 114.6 nm on average, while the theoretically expected thickness is 117.0 nm.

### 3 LAYERED DOUBLE HYDROXIDES

Films with less than 5 dl were not considered owing to the high inhomogeneity of the films. It was observed that several layers have to be deposited on the silicon wafers until homogeneous films were obtained. This is in accordance with the fact that the first adsorbed layer – LDH – covered the Si wafers by roughly 30%. The corresponding AFM images and height profiles of the films are shown in Fig. 3.11.

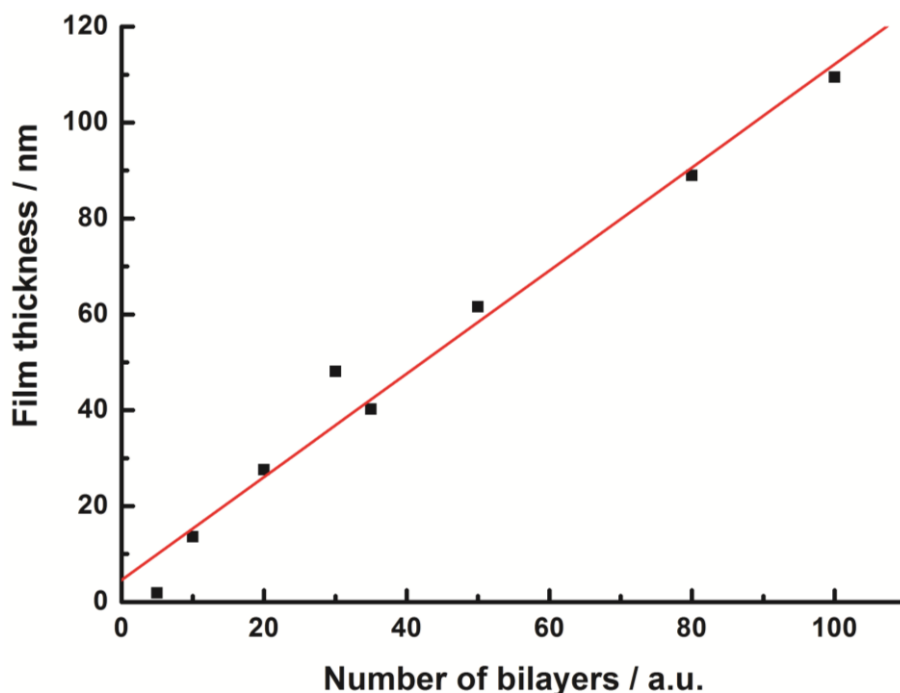


**Figure 10.** Film thickness versus number of bilayers in the GO/LDH film. The red line shows the linear regression through zero.

The successful deposition of the GO/LDH double layers is supported by TEM cross-section analysis. Figure 3.12 a shows the layered structure of the films and in Fig. 3.12 b the lattice parameter 0.48 nm was found, pointing to LDH layers. However, the shown region seems to be solely restacked LDH as the lattice parameter of a LDH/GO double layer, 1.17 nm) cannot be found in the cross section images. An explanation therefore is the rapid decomposition of the multilayer stack upon beam irradiation and possible destruction of the film during the cross section preparation. EDX analysis could not be performed on the cross section samples due to their sensitivity to the electron beam. Likewise, decomposition of the film can be seen in Fig. 3.12 c-e, which show the rapid decay of the layered structure at  $t = 0$  s,  $t = 30$  s and  $t = 120$  s.

### 3 LAYERED DOUBLE HYDROXIDES

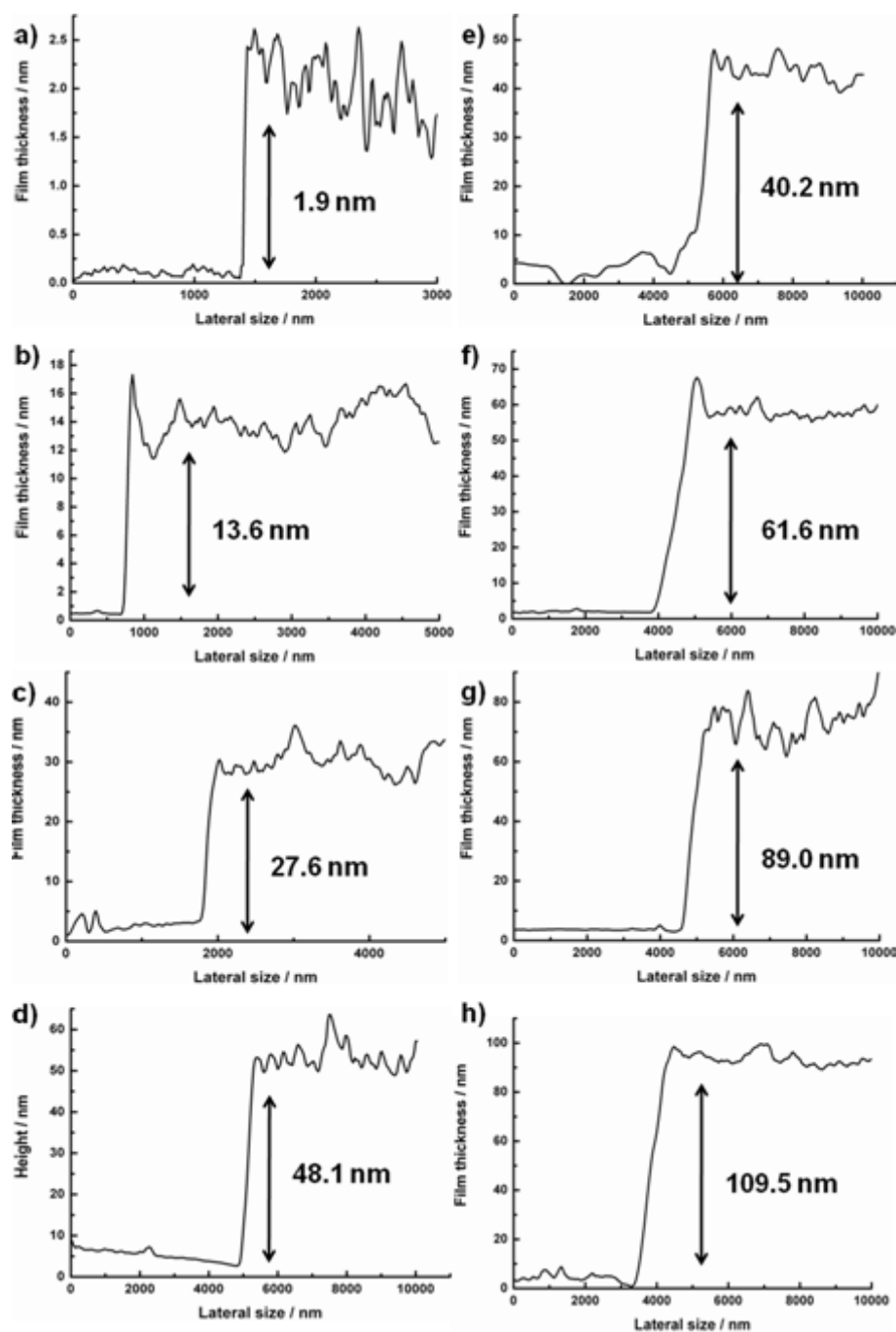


**Fig. 3.11.** Height profiles of the (a) 5 dl, (b) 10 dl, (c) 20 dl, (d) 30 dl, (e) 35 dl, (f) 50 dl, (g) 80 dl and (h) 100 dl films.

### 3 LAYERED DOUBLE HYDROXIDES

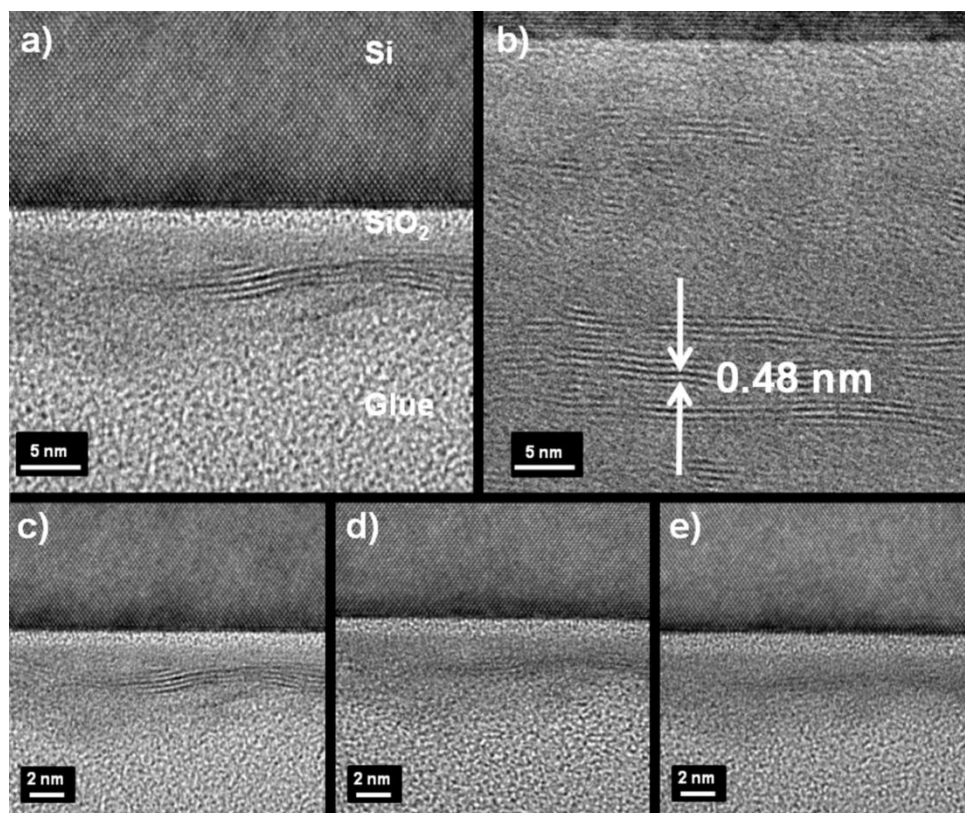


**Figure 3.12.** (a) TEM cross section image of a GO/LDH film, (b) crystallographic thickness of restacked LDH layers, (c), (d) and (e) show the decomposition of a GO/LDH film at  $t = 0$  s,  $t = 30$  s and  $t = 120$  s, respectively.

### 3.3 EXFOLIATION AND FLOCCULATION OF $\text{Zn}^{\text{II}}\text{Cr}^{\text{III}}$ LDH AND $\text{H}_x\text{Ti}_{2-x/4}\text{O}_4$

#### 3.3.1 INTRODUCTION

Due to the continuously increasing demand for renewable energy sources the search for materials, which are suitable for photocatalysis, is ongoing. Especially compounds that are capable of full water splitting, i.e. both oxygen and hydrogen evolution, are highly desired. The following equation is the basis for the water splitting reaction:<sup>[62]</sup>

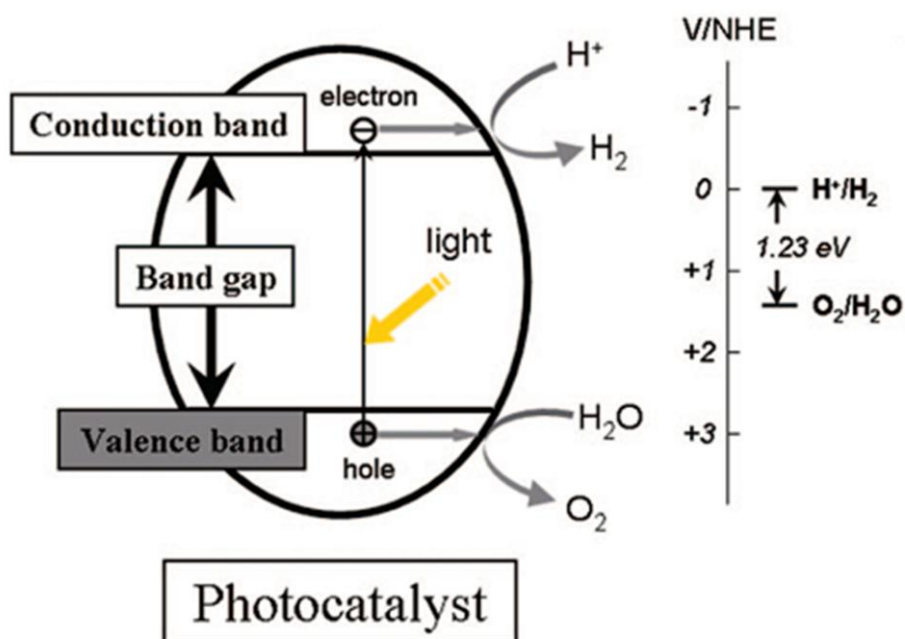
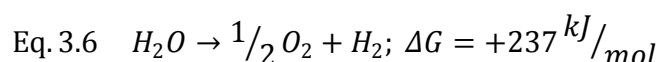


**Figure 3.13.** Principle of semiconductor-based photocatalytic water splitting. Reprinted with permission from reference [63]. Copyright (2010) American Chemical Society

Figure 3.13 shows schematically the principle of semiconductor based photocatalysis. By light irradiation electron-hole pairs are generated in the photocatalytically active compound, which then oxidizes and/or reduces the water. For the hydrogen evolution reaction (HER) the bottom of the conduction band has to be more negative than the hydrogen reduction

### 3 LAYERED DOUBLE HYDROXIDES

potential in order to transfer the electron from the photocatalyst to the electrolyte and thus to reduce  $H^+$ . Generally the potentials are normalized versus the standard hydrogen electrode (SHE). For the OER, the valence band has to be more positive than the water oxidation potential to be able to accept electrons from water. To date effective photocatalysts for HER and OER are still scarce and hence, a possible solution to fill this gap is the synthesis of hybrid compounds consisting of building blocks that are suitable for either HER or OER. Previously it has been shown that  $CrO_6$  octahedra in a hydrotalcite matrix are suitable for the OER,<sup>[64]</sup> especially  $Zn^{II}Cr^{III}$  carbonate LDH showed exceptionally high efficiency.<sup>[16]</sup> In addition, it is well known that many titanates can be applied for the HER.<sup>[62-63]</sup> In light of this, electrostatic LBL method offers an excellent opportunity to combine different photocatalytically active compounds and especially the layered LDH and titanate into one single photocatalytically active platform for water splitting. Although the precisely engineered band alignment between the two types of layers as well as their electronic coupling, for example by using the so-called Z-scheme approach relying on suitable electrolytes, is the key for the design of layered catalyst systems for overall water splitting,<sup>[65]</sup> the combination of two photoactive layers in a bulk heterojunction-type fashion is a first step towards enhanced charge separation between the two types of layers. In addition surface plays an important role in catalysis. Since nanoparticles in general and thus also nanosheets exhibit exceptional high surface areas compared to the parent bulk compounds, the catalytic activity of nanosheets is expected to be enhanced over bulk compounds in terms of photocatalysis.

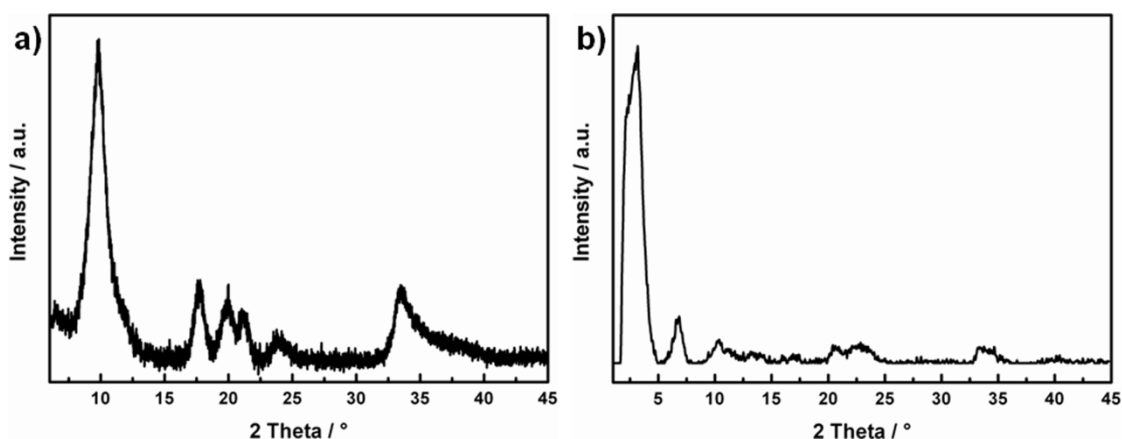
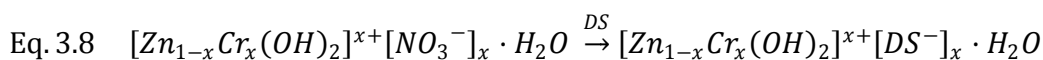
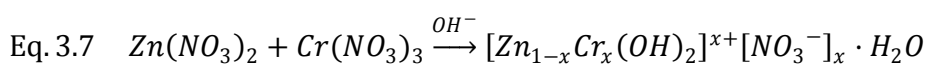
Therefore, positively charged  $Zn^{II}Cr^{III}$  LDH and negatively charged titanate nanosheets were electrostatically assembled using the soft chemical flocculation method. According to the literature, both components are expected to exhibit higher photocatalytic activity when exfoliated into single sheets and subsequently restacked to yield hybrid compounds because of a more effective charge separation of electron hole pairs due to an electron transfer from  $Zn^{II}Cr^{III}$  LDH conduction band to the conduction band of the titanate.<sup>[25]</sup>  $Zn^{II}Cr^{III}$  nitrate LDH consists of Brucite-type layers containing  $Zn^{2+}$  and  $Cr^{3+}$  as metal centers, whereas nitrate and  $H_2O$  are intercalated between the layers in order to compensate the positive charge. The intercalated anions can then be exchanged by DS to increase the interlayer space and thus to facilitate exfoliation of the compound. On the other hand the HER active compound  $Cs_xTi_{2-x/4}O_4$  used as layered anionic building block was cation-exchanged by repeated acid leaching to yield  $H_xTi_{2-x/4}O_4 \cdot H_2O$ .<sup>[66-67]</sup> This compound consists of non-stoichiometric  $TiO_x$  layers, which are intercalated by  $H^+$  cations as well as  $H_2O$  for charge

### 3 LAYERED DOUBLE HYDROXIDES

compensation. Exfoliation of the layered protonic titanate was achieved by osmotic swelling of the compound in aqueous tetrabutylammonium hydroxide (TBAOH) solution. Subsequently, the oppositely charged nanosheets were flocculated and tested for photocatalytic activity.

#### 3.3.2 RESULTS AND DISCUSSION

Exfoliation of  $\text{Zn}^{\text{II}}\text{Cr}^{\text{III}}$  LDH was achieved in a three-step synthesis. First, a  $\text{Zn}^{\text{II}}\text{Cr}^{\text{III}} \text{NO}_3$  LDH was synthesized by co-precipitation in a way analogous to a  $\text{Zn}^{\text{II}}\text{Cr}^{\text{III}} \text{CO}_3$  LDH described in the literature, using  $\text{Zn}(\text{NO}_3)_2$  and  $\text{Cr}(\text{NO}_3)_3$  as precursors.<sup>[16]</sup> The nitrate anions were then exchanged for dodecyl sulfate anions (see equation below), followed by exfoliation of the compound in formamide.



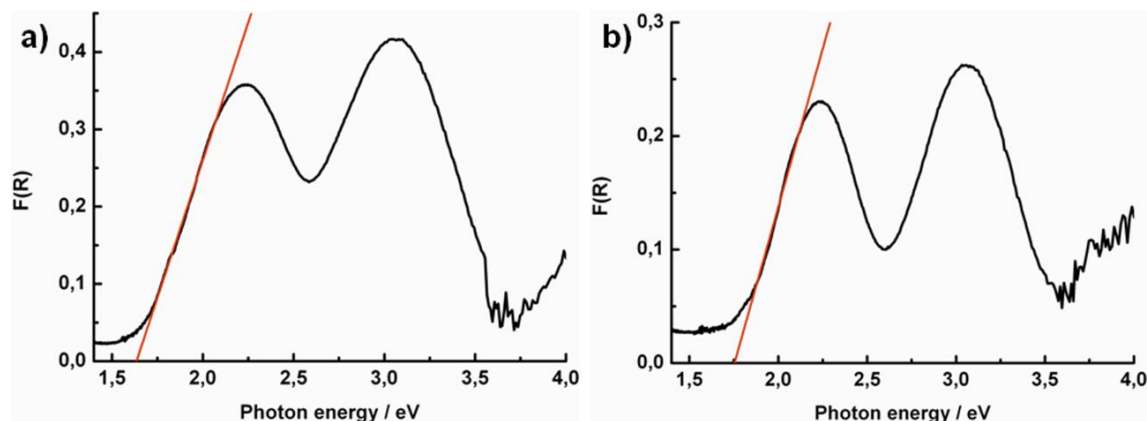
**Figure 3.13.** XRD patterns of (a)  $\text{Zn}^{\text{II}}\text{Cr}^{\text{III}} \text{NO}_3$  LDH and (b)  $\text{Zn}^{\text{II}}\text{Cr}^{\text{III}} \text{DS}$  LDH.

Figure 3.13 a and b shows the XRD patterns of the nitrate and dodecyl sulfate LDHs. The  $d_{003}$ -values of the compounds obtained from these data are 8.9 Å and 27.7 Å, respectively, which is in agreement with the published values of similar LDHs.<sup>[68-69]</sup> The empirical formula of the dodecyl sulfate LDH was determined as  $[\text{Zn}_{1.9}\text{Cr}(\text{OH})_6][\text{DS}_{0.9}] \cdot \text{H}_2\text{O}$ . Nitrogen was not found in the sample, suggesting the full exchange of the nitrate for dodecyl sulfate. However, according to the broad reflections we assume that different



### 3 LAYERED DOUBLE HYDROXIDES

stacking patterns are present in the sample, i.e. that although nitrate is fully exchange by DS, it is possible that the arrangement of the DS in the interlayer galleries is not uniform. The angle between DS and the Brucite-type layers may vary and hence a distribution of the interlayer gallery distances occurs.



**Figure 3.14.** (a) and (b) Kubelka-Munk plots of  $\text{Zn}^{\text{II}}\text{Cr}^{\text{III}} \text{NO}_3$  LDH and  $\text{Zn}^{\text{II}}\text{Cr}^{\text{III}}$  DS LDH, respectively. The red line shows the linear regression to extrapolate the optical band gaps.

For a  $\text{Zn}^{\text{II}}\text{Cr}^{\text{III}} \text{CO}_3$  LDH the diffuse reflectance spectrum was published previously, showing two absorption maxima at 410 and 570 nm.<sup>[16]</sup> To probe the absorption properties of the  $\text{Zn}^{\text{II}}\text{Cr}^{\text{III}} \text{NO}_3$  and DS LDHs, the materials were tested for UV-Vis activity by diffuse reflectance measurements. The UV-Vis spectra of the  $\text{Zn}^{\text{II}}\text{Cr}^{\text{III}} \text{NO}_3$  LDH and  $\text{Zn}^{\text{II}}\text{Cr}^{\text{III}}$  DS LDH, plotted as Kubelka-Munk function (chapter 2.4.3), can be found in Fig. 3.14 a and b, respectively. In agreement with the literature, both LDHs show two absorption bands: The nitrate species shows the two maxima at 407 and 556 nm, and the dodecyl sulfate compound at 409 and 557 nm. Linear regression of the plots yields optical “band gaps” of 1.63 eV for the nitrate species and 1.75 eV for the dodecyl sulfate LDH. These optical band gaps can be assigned to *d-d* transitions of the  $\text{Cr}^{3+}$  ion in the LDH,<sup>[64]</sup> i.e. to the  $^4\text{A}_{2g} \rightarrow ^4\text{T}_{2g}$  transition.

Exfoliation of the  $\text{Zn}^{\text{II}}\text{Cr}^{\text{III}}$  DS LDH was achieved by 30 min sonication in formamide. The colloidal suspension showed the Tyndall effect and an AFM image of the nanosheets with the corresponding height profiles is outlined in Fig. 3.15 a and b.

### 3 LAYERED DOUBLE HYDROXIDES

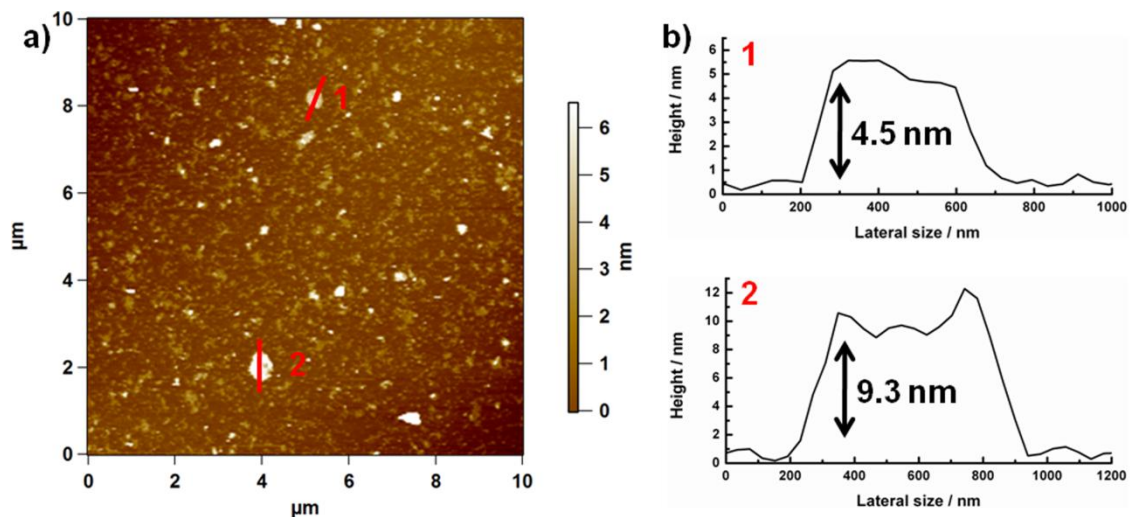


**Figure 3.15.** (a) AFM image of  $\text{Zn}_2\text{Cr}(\text{OH})_6^+$  nanosheets and (b) corresponding height profiles of **1** and **2**.

According to the crystallographic thickness of the LDH ( $\sim 0.5$  nm), of the physisorbed organic surfactant ( $\sim 1.7$  nm) on the surface and the obtained minimum height of 4.49 nm, exfoliation down to approximately two layers was successful. However, it has to be mentioned that the nanosheets are quite small in lateral size and the shape of the sheets is rather irregular due to the exfoliation process driven by sonication in formamide. This might also be because the compound may not consist of equally arranged interlayer galleries, which then causes different stages of exfoliation.

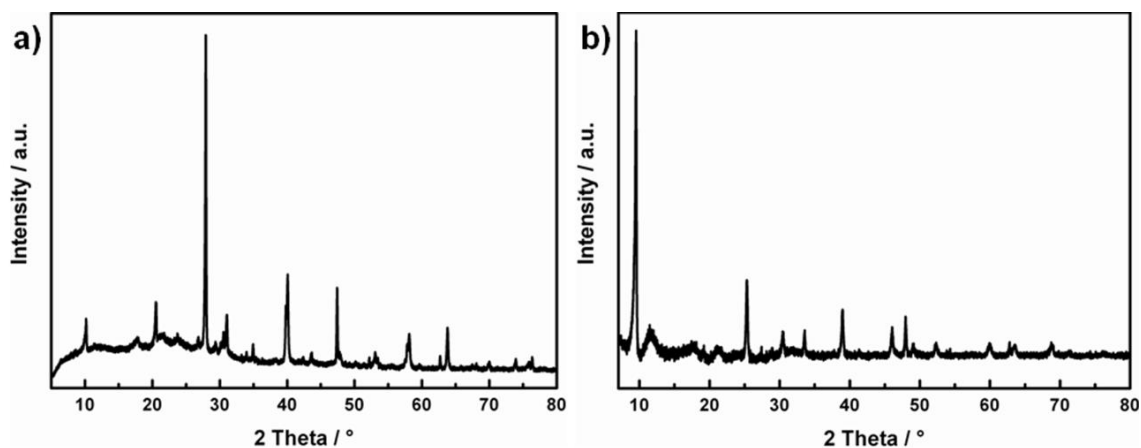


**Figure 3.16.** XRD pattern of (a)  $\text{Cs}_x\text{Ti}_{2-x/4}\text{O}_4$  and (b)  $\text{H}_x\text{Ti}_{2-x/4}\text{O}_4$ .

$\text{Ti}_{2-x/4}\text{O}_4^{x-}$  nanosheets were obtained by first synthesizing the layered cesium titanate  $\text{Cs}_x\text{Ti}_{2-x/4}\text{O}_4$  in a typical solid-state reaction, followed by wet-chemical cation-proton exchange and

### 3 LAYERED DOUBLE HYDROXIDES

exfoliation using TBAOH as organic surfactant. The reaction of TBAOH and  $H^+$  from the layered titanate is a neutralization reaction yielding  $H_2O$  and  $TBA^+$  attached to the titanate (Eq. 3.8). Figure 3.16 a and b show the XRD patterns of the  $Cs_xTi_{2-x/4}O_4$  and  $H_xTi_{2-x/4}O_4$  with the corresponding reference patterns, respectively.<sup>[70-71]</sup> Elemental analysis of the layered titanates yielded the following compositions:  $Cs_{0.4}TiO_{2.2}$  and  $H_{0.38}Cs_{0.02}TiO_{2.2}$ . The protonated species of the titanate was then exfoliated by shaking  $H_{0.38}Cs_{0.02}TiO_{2.8}$  in an aqueous TBAOH solution resulting in a turbid colloidal suspension of nanosheets. An AFM image with the corresponding height profile is shown in Fig. 3.17 a and b.

Flocculation of the two oppositely charged nanosheets yielded a turquoise powder, whereas the individual components  $Zn^{II}Cr^{III}$  DS LDH and  $H_xTi_{2-x/4}O_4$  are purple and colorless powders, respectively (Fig. 3.18). This points to a shift of the absorption maxima of the constituent building blocks (see below). Elemental analysis was carried out in order to ascertain the composition of the hybrid sample. Thus, the metal ratio  $Ti : Zn : Cr$  in the hybrid is 11 : 2 : 1. Even though the starting molar ratio of  $H_xTi_{2-x/4}O_4 : Zn^{II}Cr^{III}$  DS LDH was 3:1, the experimentally obtained ratio of 11 : 1 differs substantially from the theoretical one. An explanation for the observed discrepancy may be the equilibrium reaction of  $H_xTi_{2-x/4}O_4$  and TBAOH:

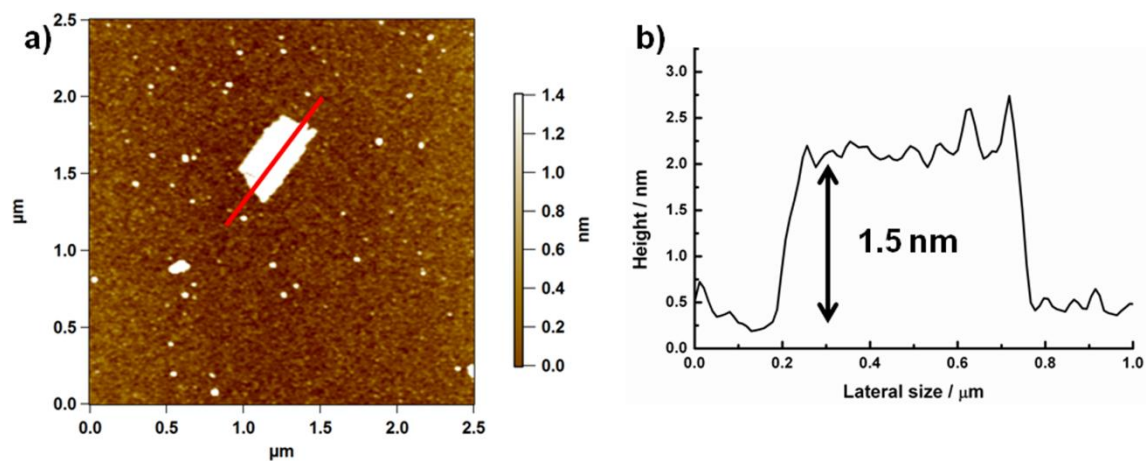
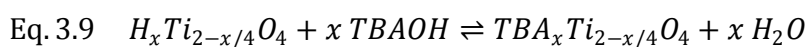


**Figure 3.17.** (a) AFM image of a  $Ti_{2-x/4}O_4^{x-}$  nanosheet and (b) the corresponding height profile taken along the red bar.



### 3 LAYERED DOUBLE HYDROXIDES

According to the literature<sup>[72]</sup>, a maximum coverage of 84% of  $\text{TBA}^+$  on the surface of the  $\text{Ca}_2\text{Nb}_3\text{O}_{10}^-$  nanosheets discussed above can be achieved. Hence, less LDH will be adsorbed at the surface since the residual  $\text{H}^+$  cannot be exchanged by LDH (see chapter 4). On the other hand, parts of the LDH were not exfoliated and thus removed upon centrifugation of the nanosheet suspension. Decomposition of the LDH is not a likely explanation for the mismatch, since there was no indication that the LDH might have been dissolved under the present reaction conditions.

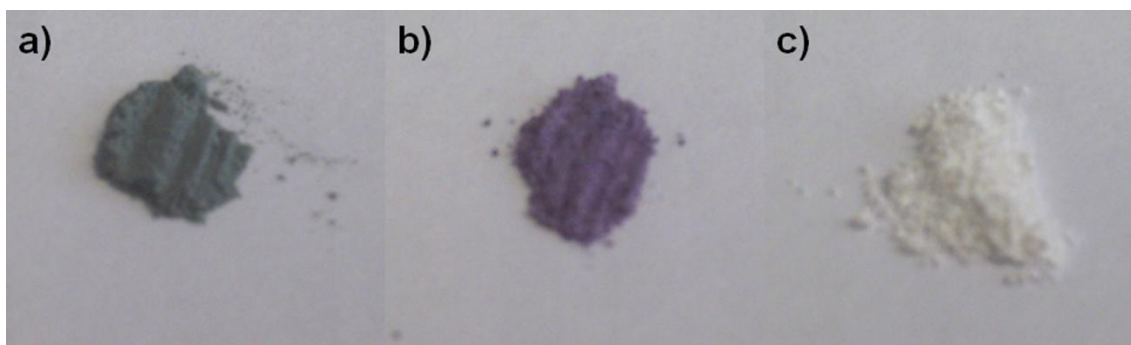


**Figure 3.18.** Photographs of (a) flocculated sample, (b)  $\text{Zn}^{\text{II}}\text{Cr}^{\text{III}}$  DS LDH and (c)  $\text{H}_x\text{Ti}_{2-x/4}\text{O}_4$ .

As mentioned before, the color change of the hybrid material indicates a shift of the absorption spectra of the pristine materials. Figure 3.18 a shows the absorption spectra of the hybrid material, the pristine LDH and the titanate. The spectrum of the pristine titanate shows an absorption band in the UV region with a maximum at 312 nm. As mentioned earlier, the pristine LDH exhibits two absorption bands in the visible region at 409 and 557 nm. The hybrid compound, however, shows a red shift of the two absorption bands that result from the LDH. The band at 409 nm is shifted by 25 nm to 434 nm and the band at 557 nm is shifted by 45 nm to 602 nm. The result of this shift is a reduction of the optical band gap to 1.58 eV, obtained by linear regression of the Kubelka-Munk plot shown in Fig. 3.19 b. In order to test the catalytic performance of the hybrid compound, activity for both HER and OER were investigated. However, no photocatalytic activity could be determined. Nevertheless, these results show that the combination of different compounds does not necessarily result in hybrids with the combined properties of the building blocks, but can also yield materials with new features. Especially the shift of the absorption maxima is of interest since no exchange of the Cr-ligands (OH) and thus no change in the  $d-d$  transitions of the  $\text{Cr}^{3+}$  ion is expected. However, a possible explanation for this effect is that the  $\text{OH}^-$  ligands still have been partially replaced by another ligand – such as water or

### 3 LAYERED DOUBLE HYDROXIDES

titanate— causing a weaker splitting of the octahedral ligand field during the exfoliation process. Caused by the sonication process during exfoliation the Brucite-type layers might have suffered in stability and hence a ligand exchange seems possible. This would also explain the splitted maxima in the absorption spectra in Figure 3.19, which might result from different ligands at the  $\text{Cr}^{3+}$  centers.

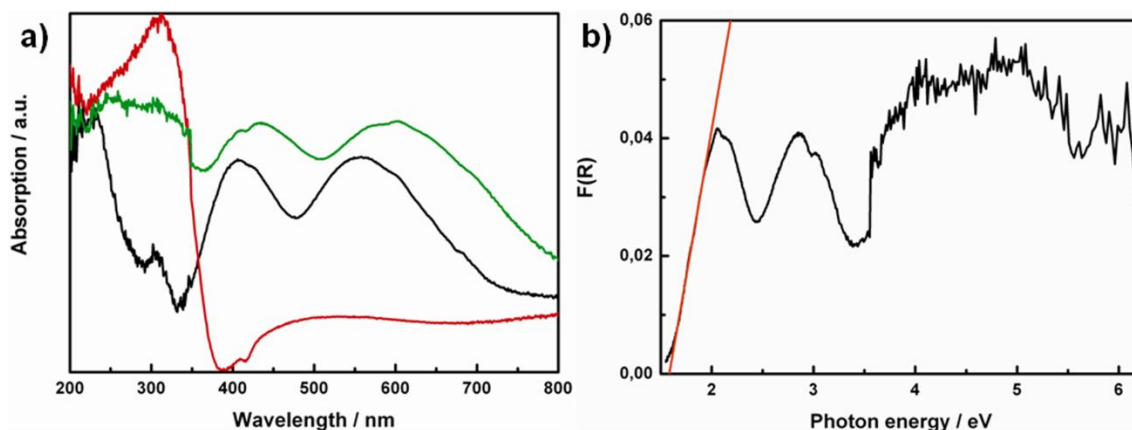


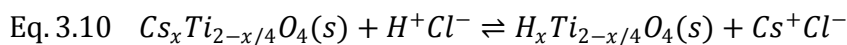
**Figure 3.19.** (a) UV-Vis absorption spectra of  $[\text{Ti}_{2-x/4}\text{O}_4]_6[\text{Zn}_2\text{Cr}(\text{OH})_6]$  hybrid material (green),  $\text{Zn}^{\text{II}}\text{Cr}^{\text{III}}$  DS LDH (black) and  $\text{Cs}_x\text{Ti}_{2-x/4}\text{O}_4$  (red).  $x = 0.7$ . (b) Kubelka-Munk plot with linear regression of the hybrid material.

#### 3.3.3 EXPERIMENTAL

**$\text{Zn}_2\text{Cr}(\text{OH})_6^+$  synthesis.**  $\text{Zn}^{\text{II}}\text{Cr}^{\text{III}}$   $\text{NO}_3$  LDH was synthesized by the coprecipitation method. 2.97 g (10.0 mmol)  $\text{Zn}(\text{NO}_3)_2 \cdot 6\text{H}_2\text{O}$  and 2.00 g (5.0 mmol)  $\text{Cr}(\text{NO}_3)_3 \cdot 9\text{H}_2\text{O}$  were dissolved in 30 mL deionized and degassed water. The further synthesis was then carried out under argon atmosphere. 1M NaOH was added until pH 9 was reached. The thick precipitate was allowed to crystallize at 60 °C for 24 h. Then the precipitate was filtrated, washed with water and acetone and dried at 60 °C under vacuum overnight. To obtain the  $\text{Zn}^{\text{II}}\text{Cr}^{\text{III}}$  DS LDH, 2.88 g (100.0 mmol) of sodium dodecylsulfate was dissolved in 100 mL deionized water and 0.2 g of the nitrate LDH was dispersed in this solution. The resulting suspension was shaken for 5 d on a mechanical shaker. The mixture was then filtrated and washed with water. The solid residue was dried at 60 °C under vacuum overnight. To exfoliate the  $\text{Zn}^{\text{II}}\text{Cr}^{\text{III}}$  DS LDH, 0.1 g of the purple powder was dispersed in 100 mL formamide and sonicated for 30 min. To remove non-exfoliated particles the suspension was centrifuged at 5,000 rpm. The resulting supernatant was used for the flocculation experiments.

### 3 LAYERED DOUBLE HYDROXIDES

**Ti<sub>2-x/4</sub>O<sub>4</sub><sup>x-</sup> synthesis.** The layered cesium titanate Cs<sub>x</sub>Ti<sub>2-x/4</sub>O<sub>4</sub> was prepared in a typical solid state reaction. 0.65 g (2.0 mmol) Cs<sub>2</sub>CO<sub>3</sub> and 0.85 g (10.6 mmol) TiO<sub>2</sub> were thoroughly grinded and mixed in a crucible. The mixture was heated to 800 °C and held at this temperature for 20 h. After cooling to room temperature, grinding and heating of the mixture with the same temperature program was applied. Anion exchange of the cesium titanate was achieved by dispersing 0.2 g of the powder in 40 mL 1M aqueous HCl and shaking the suspension at room temperature for three days. The HCl was replaced once a day to increase the H<sup>+</sup> concentration, remove released Cs<sup>+</sup> and thus shift the equilibrium to the right side of the following equation:



The resulting powder was filtrated, washed with copious amounts of water and dried at 60 °C under vacuum. Exfoliation of the protonated titanate was then carried out by dispersing 0.1 g of the bulk material in 100 mL 0.2M aqueous TBAOH solution and shaking the suspension for 10 d. To remove non-exfoliated particles, the suspension was centrifuged with 15,000 rpm for 15 min. The supernatant was decanted, showed the Tyndall effect and was used for flocculation experiments.

**Flocculation of Zn<sub>2</sub>Cr(OH)<sub>6</sub><sup>+</sup> and Ti<sub>2-x/4</sub>O<sub>4</sub><sup>x-</sup>.** The flocculated heterostructure of Zn<sub>2</sub>Cr(OH)<sub>6</sub><sup>+</sup>/Ti<sub>2-x/4</sub>O<sub>4</sub><sup>x-</sup> was synthesized by slowly mixing the colloidal suspensions of 100 mL 1 g/L Zn<sub>2</sub>Cr(OH)<sub>6</sub><sup>+</sup> in formamide and 50 mL 1 g/L Ti<sub>2-x/4</sub>O<sub>4</sub><sup>x-</sup> in H<sub>2</sub>O. Flocculation of the oppositely charged nanosheets occurred immediately. However, the suspension was stirred for 1 d to yield complete flocculation and was then centrifuged at 25,000 rpm for 15 min. The supernatant was a clear solution and removed and the precipitate was dried at 60 °C under vacuum for 5 d to remove any solvent.

## 3.4 OUTLOOK

In this chapter, it was demonstrated that LDHs can be exfoliated into their cationically charged two-dimensional Brucite-type layers by soft chemical approaches. Furthermore, the combination of these nanosheets with other inorganic materials such as graphene oxide or titanate nanosheets yields new hybrid materials that are inaccessible by conventional synthetic routes. Both flocculation, leading to random restacking without control of the exact structure, as well as layer-by-layer deposition with a precise control of the synthesized structure have been applied and yielded hybrid structures. Especially the properties of the new materials are of interest as they can combine or differ from those of the constituent compounds. This fact makes hybrid structures of high interest for future research. Taking the diversity of LDHs with their different compositions and properties as well as the variety of inorganic 2D compounds that can be separated into negatively charged nanosheets into account, the diversity of possible building blocks is almost exhaustless, i.e. the number of conceivable combinations to build new structures seems infinite. The design of new heterostructures can therefore contribute to numerous electronic, optical, catalytic and biological applications and yield new materials such as electrode materials for super- and pseudocapacitors, semiconductors, magnetic materials and materials for drug delivery.

## 3.5 BIBLIOGRAPHY

- [1] K. S. Novoselov, A. K. Geim, S. V. Morozov, D. Jiang, Y. Zhang, S. V. Dubonos, I. V. Grigorieva, A. A. Firsov, *Science* **2004**, *306*, 666-669.
- [2] R. Ma, T. Sasaki, *Adv. Mater.* **2010**, *22*, 5082-5104.
- [3] M. Osada, T. Sasaki, *J. Mater. Chem.* **2009**, *19*, 2503-2511.
- [4] N. Miyamoto, K. Kuroda, M. Ogawa, *J. Mater. Chem.* **2004**, *14*, 165-170.
- [5] H. S. S. Ramakrishna Matte, A. Gomathi, A. K. Manna, D. J. Late, R. Datta, S. K. Pati, C. N. R. Rao, *Angew. Chem. Int. Ed.* **2010**, *49*, 4059-4062.
- [6] G. Alberti, M. Casciola, U. Costantino, *J. Colloid Interf. Sci.* **1985**, *107*, 256-263.
- [7] S. Ida, C. Ogata, M. Eguchi, W. J. Youngblood, T. E. Mallouk, Y. Matsumoto, *J. Am. Chem. Soc.* **2008**, *130*, 7052-7059.
- [8] T. Hibino, M. Kobayashi, *J. Mater. Chem.* **2005**, *15*, 653-656.
- [9] R. Ma, K. Takada, K. Fukuda, N. Iyi, Y. Bando, T. Sasaki, *Angew. Chem. Int. Ed.* **2008**, *47*, 86-89.
- [10] S. W. Keller, H.-N. Kim, T. E. Mallouk, *J. Am. Chem. Soc.* **1994**, *116*, 8817-8818.
- [11] L. Li, R. Ma, Y. Ebina, K. Fukuda, K. Takada, T. Sasaki, *J. Am. Chem. Soc.* **2007**, *129*, 8000-8007.
- [12] B. Sels, D. D. Vos, M. Buntinx, F. Pierard, A. Kirsch-De Mesmaeker, P. Jacobs, *Nature* **1999**, *400*, 855-857.
- [13] J. Han, Y. Dou, M. Wei, D. G. Evans, X. Duan, *Angew. Chem. Int. Ed.* **2010**, *49*, 2171-2174.
- [14] J.-H. Choy, S.-Y. Kwak, J.-S. Park, Y.-J. Jeong, J. Portier, *J. Am. Chem. Soc.* **1999**, *121*, 1399-1400.
- [15] M. Shao, M. Wei, D. G. Evans, X. Duan, *Chem. Commun.* **2011**, *47*, 3171-3173.
- [16] C. G. Silva, Y. Bouizi, V. Fornes, H. Garcia, *J. Am. Chem. Soc.* **2009**, *131*, 13833-13839.
- [17] L. Li, R. Ma, Y. Ebina, N. Iyi, T. Sasaki, *Chem. Mater.* **2005**, *17*, 4386-4391.
- [18] S. O'Leary, D. O'Hare, G. Seeley, *Chem. Commun.* **2002**, 1506-1507.
- [19] V. V. Naik, T. N. Ramesh, S. Vasudevan, *J. Phys. Chem. Lett.* **2011**, *2*, 1193-1198.



### 3 LAYERED DOUBLE HYDROXIDES

- [20] T. Hibino, *Chem. Mater.* **2004**, *16*, 5482-5488.
- [21] Z. Liu, R. Ma, Y. Ebina, N. Iyi, K. Takada, T. Sasaki, *Langmuir* **2007**, *23*, 861-867.
- [22] J. Liang, R. Ma, N. Iyi, Y. Ebina, K. Takada, T. Sasaki, *Chem. Mater.* **2010**, *22*, 371-378.
- [23] M. Singh, M. I. Ogden, G. M. Parkinson, C. E. Buckley, J. Connolly, *J. Mater. Chem.* **2004**, *14*, 871-874.
- [24] L. Wang, D. Wang, X. Y. Dong, Z. J. Zhang, X. F. Pei, X. J. Chen, B. Chen, J. Jin, *Chem. Commun.* **2011**, *47*, 3556-3558.
- [25] J. L. Gunjekar, T. W. Kim, H. N. Kim, I. Y. Kim, S.-J. Hwang, *J. Am. Chem. Soc.* **2011**, *133*, 14998-15007.
- [26] J. Zhao, X. Kong, W. Shi, M. Shao, J. Han, M. Wei, D. G. Evans, X. Duan, *J. Mater. Chem.* **2011**, *21*, 13926-13933.
- [27] Z. Gao, J. Wang, Z. Li, W. Yang, B. Wang, M. Hou, Y. He, Q. Liu, T. Mann, P. Yang, M. Zhang, L. Liu, *Chem. Mater.* **2011**, *23*, 3509-3516.
- [28] Y. Lin, L. Ruiyi, L. Zaijun, L. Junkang, F. Yinjun, W. Guangli, G. Zhiguo, *Electrochim. Acta* **2013**, *95*, 146-154.
- [29] N. Yulian, L. Ruiyi, L. Zaijun, F. Yinjun, L. Junkang, *Electrochim. Acta* **2013**, *94*, 360-366.
- [30] H. Li, G. Zhu, Z.-H. Liu, Z. Yang, Z. Wang, *Carbon* **2010**, *48*, 4391-4396.
- [31] G. Abellán, E. Coronado, C. Marti-Gastaldo, E. Pinilla-Cienfuegos, A. Ribera, *J. Mater. Chem.* **2010**, *20*, 7451-7455.
- [32] G. Abellán, M. Latorre-Sanchez, V. Fornés, A. Ribera, H. García, *Chem. Commun.* **2012**, *48*, 11416-11418.
- [33] M. Latorre-Sanchez, P. Atienzar, G. Abellán, M. Puche, V. Fornés, A. Ribera, H. García, *Carbon* **2012**, *50*, 518-525.
- [34] C. Nethravathi, M. Rajamathi, N. Ravishankar, L. Basit, C. Felser, *Carbon* **2010**, *48*, 4343-4350.
- [35] B. Li, H. Cao, J. Shao, H. Zheng, Y. Lu, J. Yin, M. Qu, *Chem. Commun.* **2011**, *47*, 3159-3161.
- [36] J. Chang, H. Xu, J. Sun, L. Gao, *J. Mater. Chem.* **2012**, *22*, 11146-11150.
- [37] X. Dong, L. Wang, D. Wang, C. Li, J. Jin, *Langmuir* **2012**, *28*, 293-298.

### 3 LAYERED DOUBLE HYDROXIDES

- [38] J. Fang, M. Li, Q. Li, W. Zhang, Q. Shou, F. Liu, X. Zhang, J. Cheng, *Electrochim. Acta* **2012**, *85*, 248-255.
- [39] Q. Cheng, J. Tang, J. Ma, H. Zhang, N. Shinya, L.-C. Qin, *Carbon* **2011**, *49*, 2917-2925.
- [40] S. Chen, J. Zhu, X. Wu, Q. Han, X. Wang, *ACS Nano* **2010**, *4*, 2822-2830.
- [41] W. Yang, Z. Gao, J. Wang, B. Wang, Q. Liu, Z. Li, T. Mann, P. Yang, M. Zhang, L. Liu, *Electrochim. Acta* **2012**, *69*, 112-119.
- [42] F. Malherbe, C. Forano, J. P. Besse, *J. Mater. Sci. Lett.* **1999**, *18*, 1217-1219.
- [43] S. Aisawa, H. Hirahara, H. Uchiyama, S. Takahashi, E. Narita, *J. Solid State Chem.* **2002**, *167*, 152-159.
- [44] Z. P. Xu, L. Li, C.-Y. Cheng, R. Ding, C. Zhou, *Appl. Clay Sci.* **2012**, *74*, 102-108.
- [45] C. Obayashi, M. Ishizaka, T. Konishi, H. Yamada, K. Katakura, *Electrochemistry* **2012**, *80*, 879-882.
- [46] D. M. Robinson, Y. B. Go, M. Mui, G. Gardner, Z. Zhang, D. Mastrogiovanni, E. Garfunkel, J. Li, M. Greenblatt, G. C. Dismukes, *J. Am. Chem. Soc.* **2013**, *135*, 3494-3501.
- [47] N. I. Kovtyukhova, P. J. Ollivier, B. R. Martin, T. E. Mallouk, S. A. Chizhik, E. V. Buzaneva, A. D. Gorchinskiy, *Chem. Mater.* **1999**, *11*, 771-778.
- [48] D. Li, M. B. Muller, S. Gilje, R. B. Kaner, G. G. Wallace, *Nat. Nanotechnol.* **2008**, *3*, 101-105.
- [49] U. König, *Synthese, Charakterisierung und Eigenschaften von manganhaltigen Layered Double Hydroxides (LDHs)*, Halle, **2006**.
- [50] A. Weiss, H. Witte, *Magnetochemie* **1973**, 136.
- [51] M. J. Hudson, S. Carlino, D. C. Apperley, *J. Mater. Chem.* **1995**, *5*, 323-329.
- [52] H.-J. Shin, K. K. Kim, A. Benayad, S.-M. Yoon, H. K. Park, I.-S. Jung, M. H. Jin, H.-K. Jeong, J. M. Kim, J.-Y. Choi, Y. H. Lee, *Adv. Funct. Mater.* **2009**, *19*, 1987-1992.
- [53] A. C. H.P. Boehm, G.O. Fischer, U. Hofmann, *Z. Naturforsch. B* **1962**, *17*, 150.
- [54] S. Cervený, F. Barroso-Bujans, Á. Alegría, J. Colmenero, *J. Phys. Chem. C* **2010**, *114*, 2604-2612.

### 3 LAYERED DOUBLE HYDROXIDES

- [55] A. V. Talyzin, V. L. Solozhenko, O. O. Kurakevych, T. Szabó, I. Dékány, A. Kurnosov, V. Dmitriev, *Angew. Chem. Int. Ed.* **2008**, *47*, 8268-8271.
- [56] W. S. Hummers, R. E. Offeman, *J. Am. Chem. Soc.* **1958**, *80*, 1339-1339.
- [57] X. Yan, J. Chen, J. Yang, Q. Xue, P. Miele, *ACS Appl. Mater. Interfaces* **2010**, *2*, 2521-2529.
- [58] L. Buglione, E. L. K. Chng, A. Ambrosi, Z. Sofer, M. Pumera, *Electrochem. Commun.* **2012**, *14*, 5-8.
- [59] J.-S. Lee, G. S. Park, H. I. Lee, S. T. Kim, R. Cao, M. Liu, J. Cho, *Nano Lett.* **2011**, *11*, 5362-5366.
- [60] K. Markovic, *Synthesis, Exfoliation and Layer-by-Layer Assembly of Layered Double Hydroxides with Graphene Oxide and  $Ti_{2-x/4}O_4^{x-}$* , München **2012**.
- [61] T. Nakajima, A. Mabuchi, R. Hagiwara, *Carbon* **1988**, *26*, 357-361.
- [62] F. E. Osterloh, *Chem. Mater.* **2007**, *20*, 35-54.
- [63] X. Chen, S. Shen, L. Guo, S. S. Mao, *Chem. Rev.* **2010**, *110*, 6503-6570.
- [64] Y. Zhao, S. Zhang, B. Li, H. Yan, S. He, L. Tian, W. Shi, J. Ma, M. Wei, D. G. Evans, X. Duan, *Chem. Eur. J.* **2011**, *17*, 13175-13181.
- [65] K. Maeda, *ACS Catalysis* **2013**, *3*, 1486-1503.
- [66] J.-H. Choy, H.-C. Lee, H. Jung, S.-J. Hwang, *J. Mater. Chem.* **2001**, *11*, 2232-2234.
- [67] T. Sasaki, M. Watanabe, *J. Am. Chem. Soc.* **1998**, *120*, 4682-4689.
- [68] M. Meyn, K. Beneke, G. Lagaly, *Inorg. Chem.* **1990**, *29*, 5201-5207.
- [69] S. Werner, V. W.-h. Lau, S. Hug, V. Duppel, H. Clausen-Schaumann, B. V. Lotsch, *Langmuir* **2013**, *29*, 9199-9207.
- [70] I. E. Grey, C. Li, I. C. Madsen, J. A. Watts, *J. Solid State Chem.* **1987**, *66*, 7-19.
- [71] T. Sasaki, M. Watanabe, Y. Michiue, Y. Komatsu, F. Izumi, S. Takenouchi, *Chem. Mater.* **1995**, *7*, 1001-1007.
- [72] C. Ziegler, S. Werner, M. Bugnet, M. Wörsching, V. Duppel, G. A. Botton, C. Scheu, B. V. Lotsch, *Chem. Mater.* **2013**, *25*, 4892-4900.

### 4. LAYER-BY-LAYER ASSEMBLY OF OPPOSITELY CHARGED NANOSHEETS

The rational design of artificial solids made up of oppositely charged nanosheets is the subject matter of this chapter. Therefore, positively charged  $\text{Mn}^{\text{II}}\text{Al}^{\text{III}}$  LDH and negatively charged perovskite sheets were sequentially stacked utilizing electrostatic forces in a soft chemical approach to form new tailor-made hybrid materials. The artificial compounds were studied in depth by electron microscopy methods such as high-resolution transmission electron microscopy (HRTEM), scanning transmission electron microscopy (STEM) and electron energy loss spectroscopy (EELS) to obtain atomic resolution. In addition to these insights into the materials, it could be shown that the choice of the dispersing solvent of the constituent nanosheets affects the resulting structure of the hybrid lattices.

## 4.1 ARTIFICIAL SOLIDS BY DESIGN: ASSEMBLY AND ELECTRON MICROSCOPY STUDY OF NANOSHEET-DERIVED HETEROSTRUCTURES

Christian Ziegler,<sup>†</sup> Stephan Werner,<sup>†</sup> Matthieu Bugnet, Matthias Wörsching, Viola Duppel, Gianluigi A. Botton, Christina Scheu, Bettina V. Lotsch

Published in: *Chem. Mater.*, **2013**, 25, 4892.

DOI: 10.1021/cm402950b

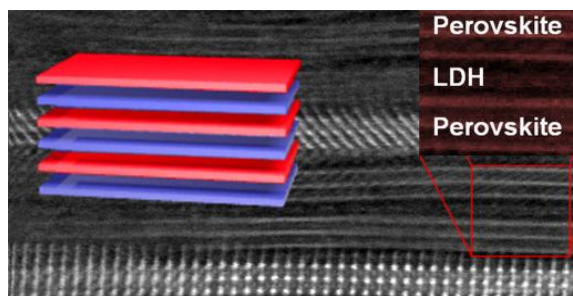
Copyright © 2013 American Chemical Society

<http://pubs.acs.org/doi/abs/10.1021/cm402950b>

*2D materials, heterostructures, layer-by-layer assembly, perovskite, electron microscopy, EELS*

### ABSTRACT

Two-dimensional materials do not only attract interest owing to their anisotropic properties and quantum confinement effects, but also lend themselves as well-defined building blocks for the rational design of 3D materials with custom-made



structures and, hence, properties. Here, we present the bottom-up fabrication of an artificial superlattice derived from positively charged layered double hydroxide (LDH) and negatively charged perovskite layers sequentially assembled by electrostatic layer-by-layer deposition. In contrast to previously employed bulk methods averaging out the elemental distribution within such stacks, we use a combination of HRTEM, STEM and EEL spectroscopy to elucidate the structure and composition of the multilayer stack with a high spatial resolution on the subnanometer scale. Atomic column resolved STEM coupled with EELS line-scans confirms the periodic arrangement of individual nanosheets by evaluation of the Ca-L<sub>2,3</sub> and Mn-L<sub>2,3</sub> edges. Furthermore, HRTEM confirms the formation of up to 100 double layer thick films, thus demonstrating the transition from ultrathin nanosheet assemblies to artificial bulk solids with engineered structures and, hence, property profiles.

## 4 LAYER-BY-LAYER ASSEMBLY OF OPPOSITELY CHARGED NANOSHEETS

We ascertain the formation of densely packed stacks with a well-ordered layered morphology, while non-idealities such as lack of in-plane layer registry, layer terminations, sheet bending and contamination by residual ligands are side effects of the solution-based deposition process. In addition, we demonstrate that the packing density of the multilayer system can be tuned by changing the LDH dispersing agent from formamide to water, resulting in porous stacks containing about eight-times less LDH and featuring significantly increased interlayer distances.

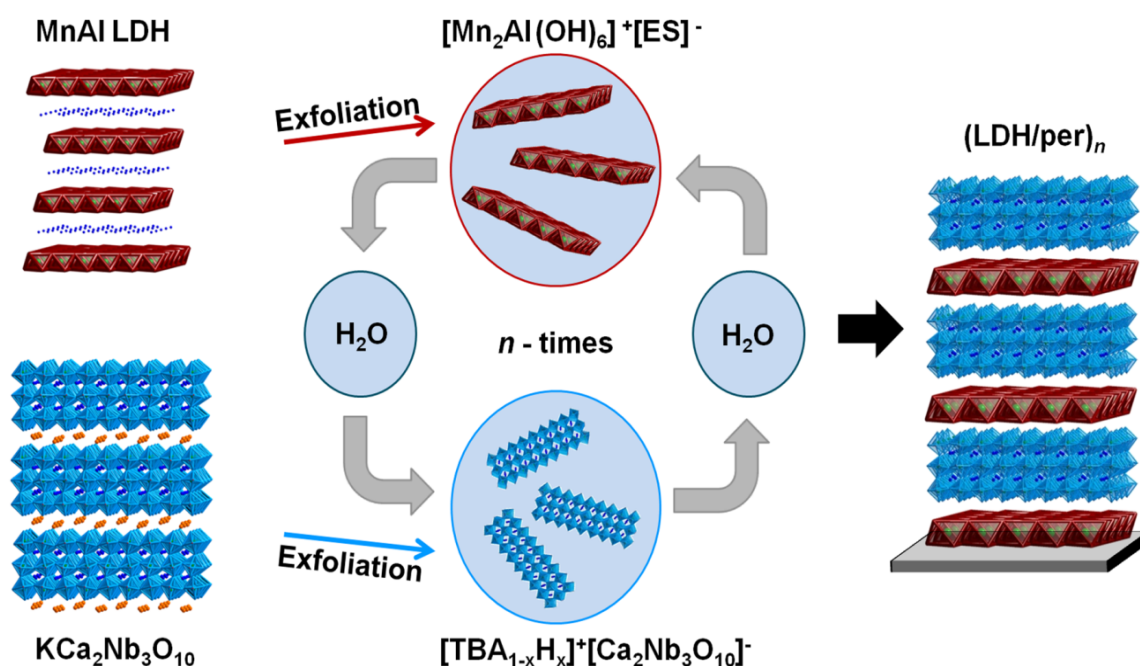


**Figure 4.1.** Schematic drawing of the liquid-phase process, employed to construct hybrid superlattices. Exfoliation of the layered bulk materials into  $\text{Mn}_2\text{Al}(\text{OH})_6^+$  and  $\text{Ca}_2\text{Nb}_3\text{O}_{10}^-$  nanosheets is followed by electrostatic LBL assembly with intermediate washing steps in order to achieve 3D (LDH/per)<sub>n</sub> heterostructures immobilized on a substrate.

### 4.1.1 INTRODUCTION

The rational design of solids with tailor-made properties has been a hallmark of soft chemistry and a major driving force of modern materials science. In principle, high temperature solid-state synthesis is governed by thermodynamic principles and is therefore inherently constrained with respect to the compositions and structures that can be realized. In contrast, kinetically controlled soft chemistry protocols, relying on the use of pre-formed

#### 4 LAYER-BY-LAYER ASSEMBLY OF OPPOSITELY CHARGED NANOSHEETS

building blocks and operating at low temperatures, open up pathways to unconventional solids with large compositional scope, albeit often at the expense of stability. Driven by the rise of nanochemistry and the ability to sculpture well-defined nanoscale building blocks such as two-dimensional (2D) nanosheets, the modular assembly of preformed nano-objects into hierarchical superlattices has taken shape in recent years, based on the pioneering work by Mallouk<sup>[1-6]</sup> and by Sasaki<sup>[7-10]</sup>. As a prerequisite for designing complex solids from nanosheet building blocks, the successful isolation of graphene, along with the identification of its unique properties, has sparked the quest for inorganic 2D materials with extraordinary physical characteristics.<sup>[11-17]</sup> Given the rapidly increasing number of nanosheets such as LDHs,<sup>[18]</sup> transition metal oxides,<sup>[19]</sup> metal disulfides<sup>[20]</sup> and other layered materials<sup>[21]</sup> at hand, we envision the rational synthesis of complex, multifunctional solids by combining different types of nanosheets into precisely arranged heterostructures with unique property profiles. The design of artificial solids with custom-made properties, which are otherwise inaccessible due to thermodynamic constraints under high temperature conditions, will be useful in a range of applications, including spintronics, optoelectronics and catalysis.<sup>[1, 4, 7, 8, 22]</sup> For example, vertical heterojunctions composed of photoactive layers may be engineered to optimize charge separation and transport, and miniaturized versions of photocatalytic donor-acceptor systems are accessible using the 2D building block approach. To achieve maximum control over the layer sequence, we use an electrostatic layer-by-layer (LBL) procedure (also known as electrostatic self-assembly deposition, ESD). Alternative deposition protocols that have been employed by other groups include the Langmuir-Blodgett (LB) method<sup>[23-29]</sup> or flocculation<sup>[30-35]</sup> of oppositely charged nanosheets, although the former lacks scalability and the latter typically yields disordered assemblies. In LBL, multilayer films form due to electrostatic and hydrophobic forces between positively and negatively charged nanosheets in a self-limiting fashion, thus allowing for a high level of control over the layer sequence at the (sub)nanoscale.<sup>[6]</sup> In previous works, anionic inorganic nanosheets were stacked with cationic polymers such as poly(diallyldimethylammonium chloride) (PDDA),<sup>[4, 7, 8, 36]</sup> whereas cationic inorganic nanosheets can be assembled with anionic polymers such as poly(sodium styrene-4-sulfonate) (PSS).<sup>[37]</sup> Recent approaches have delineated routes to obtain polymer-free films after ultraviolet-visible (UV) irradiation of the hybrid films, leading to the photoinduced decomposition of the polycations forming the organic substructure.<sup>[23-26]</sup> In contrast, only very few studies have been dedicated to the direct combination of positively and negatively charged inorganic nanosheets. An important advantage of using charged nanosheets to

## 4 LAYER-BY-LAYER ASSEMBLY OF OPPOSITELY CHARGED NANOSHEETS

assemble multilayer structures instead of organic polyelectrolytes is that sequentially grown layers do not necessarily interpenetrate, thus giving rise to more rigid, structurally well-defined superlattices.<sup>[38]</sup> Li *et al.* reported a successful LBL assembly of anionic  $\text{Ti}_{0.91}\text{O}_2^{0.36-}$  or  $\text{Ca}_2\text{Nb}_3\text{O}_{10}^-$  with cationic  $\text{Mg}_{0.67}\text{Al}_{0.33}(\text{OH})_2^{0.33+}$  nanosheets with up to 10 bilayers.<sup>[39]</sup> Other examples are  $\text{Ni}_{0.8}\text{Fe}_{0.2}(\text{OH})_2/\text{MnO}_2$ ,<sup>[40]</sup>  $\text{Mg}_{0.67}\text{Al}_{0.33}(\text{OH})_2/\text{MnO}_2$ ,<sup>[41]</sup>  $\text{Co}_{0.67}\text{Al}_{0.33}(\text{OH})_2/\text{montmorillonite}$ ,<sup>[42]</sup>  $\text{Co}_{0.67}\text{Al}_{0.33}(\text{OH})_2/\text{polyvinyl alcohol/graphene oxide}$ <sup>[43]</sup> and  $\text{Ni}_{0.66}\text{Al}_{0.33}(\text{OH})_2/\text{TaS}_2$ ,<sup>[44]</sup> which were assembled into hybrid thin films by exfoliation-restacking experiments. Ida *et al.* developed a synergistic LBL system exhibiting a drastic change in photoluminescence, using  $\text{Ti}_{1.81}\text{O}_4$  as an ‘antenna’ for UV-light harvesting and  $\text{Eu}(\text{OH})_{3-x}$  as an emissive layer in  $\text{Eu}(\text{OH})_{3-x}/\text{Ti}_{1.81}\text{O}_4$  nanocomposites. This system, similar to the others, was only composed of 1-4 layers.<sup>[45]</sup>

All of these studies, however, monitor the assembly process only indirectly, implicitly assuming the alternate stacking of oppositely charged and fully delaminated monolayers. Thus, ultimate evidence of the alternate layer stacking by means of high-resolution analytical techniques is still elusive. Furthermore, the transition from ultrathin films to artificial solids with bulk dimensions has yet to be demonstrated.

To fill this gap, we present a locally resolved, precise elemental and structural analysis of a novel artificial solid composed of perovskite and layered double hydroxide nanosheets. We use high-resolution TEM (HRTEM) as well as scanning TEM (STEM) combined with energy-dispersive X-ray spectroscopy (EDX) and electron energy loss spectroscopy (EELS) to elucidate both the composition and structure of the hybrid system with ultrahigh resolution to yield insights into the interfacial quality, real structure and morphology of the stack. The thickness of the 200-layer system approaches the bulk level, thus demonstrating the feasibility of the modular, rational synthesis of new solids from 2D building blocks by soft chemistry. In addition, our analysis adds to the understanding and improvement of the colloidal interactions and interfacial integrity determining the overall quality of the resulting superlattices.

### 4.1.2 RESULTS AND DISCUSSION

We assembled a multilayer film composed of nanosheet building blocks by sequentially adsorbing cationically charged  $[\text{Mn}_2\text{Al}(\text{OH})_6]^+[\text{ES}]^-$  nanosheets (abbreviated as  $\text{Mn}_2\text{Al}(\text{OH})_6^+$  in the following;  $\text{ES}^-$ : ethylbenzenesulfonate) suspended in either formamide or water and anionically charged  $[(\text{TBA})_{1-x}\text{H}_x]^+[\text{Ca}_2\text{Nb}_3\text{O}_{10}]^-$  nanosheets (abbreviated as



#### 4 LAYER-BY-LAYER ASSEMBLY OF OPPOSITELY CHARGED NANOSHEETS

$\text{Ca}_2\text{Nb}_3\text{O}_{10}^-$  in the following;  $\text{TBA}^+$ : tetra-*n*-butylammonium) suspended in water on a planar Si/SiO<sub>2</sub> substrate. Before we consider the multilayer stacks, the building blocks -  $\text{Mn}_2\text{Al}(\text{OH})_6^+$  and  $\text{Ca}_2\text{Nb}_3\text{O}_{10}^-$  nanosheets – will be briefly discussed in the following. LDHs are described by the general formula  $[\text{M}^{\text{II}}_{1-x}\text{M}^{\text{III}}_x(\text{OH})_2][\text{A}^{n-}_{x/n} \cdot m \text{H}_2\text{O}]$ , where  $\text{M}^{\text{II}}$  and  $\text{M}^{\text{III}}$  represent di- and trivalent metal ions within the Brucite-like layers (here  $\text{Mn}^{\text{II}}$  and  $\text{Al}^{\text{III}}$ ), and  $\text{A}^{n-}$  is an organic or inorganic interlayer anion (e.g. ES).<sup>[46]</sup> The structure of a LDH is depicted in Figure 4.1 (red). Attractive electrostatic forces between the cationic layers and the interlayer anions stabilize the structure. To overcome these forces and exfoliate the layered structure, the LDH is typically swollen with formamide and exfoliated by ultrasonication, yielding positively charged nanosheets.<sup>[47]</sup> The empirical formula of the synthesized LDH was determined to be  $[\text{Mn}_{2.1}\text{Al}(\text{OH})_6][\text{ES} \cdot 1.3 \text{H}_2\text{O}]$  by ICP-AES and elemental analysis.

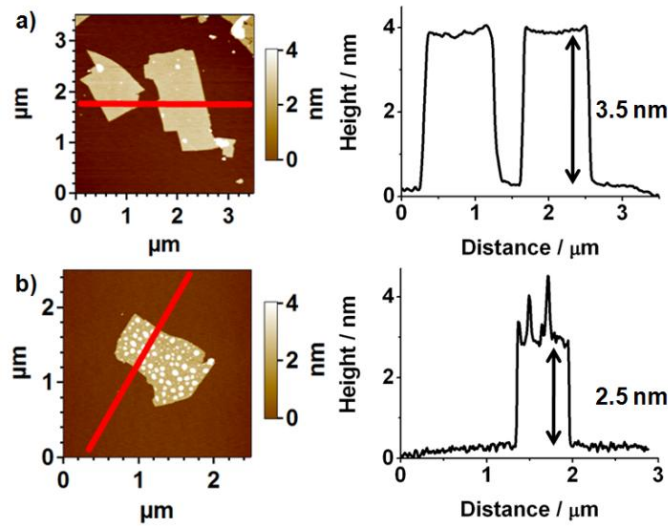


**Figure 4.2.** AFM images and corresponding height profiles of  $\text{Ca}_2\text{Nb}_3\text{O}_{10}^-$  nanosheets after (a) synthesis and (b) 1:2 dilution of the sample shown in (a) with water.

Dion-Jacobson-type layered perovskites can be described by the general formula  $\text{M}[\text{A}_{n-1}\text{B}_n\text{O}_{3n+1}]$  ( $\text{A} = \text{Ca}, \text{Sr}, \text{La}$  etc.  $\text{B} = \text{Ti}, \text{Nb}, \text{Ta}$  etc.), where the negatively charged  $[\text{A}_{n-1}\text{B}_n\text{O}_{3n+1}]^-$  layers composed of blocks of  $n$  corner-sharing  $\text{BO}_6$  octahedra are interleaved with exchangeable monovalent cations  $\text{M}^+$  ( $\text{M} = \text{H}, \text{K}, \text{Rb}$  etc.).<sup>[6]</sup> In the monoclinic structure of  $\text{KCa}_2\text{Nb}_3\text{O}_{10}$  the corner sharing  $\text{BO}_6$  octahedra are distorted from the ideal cubic structure as shown in Figure 1 (blue).

#### 4 LAYER-BY-LAYER ASSEMBLY OF OPPOSITELY CHARGED NANOSHEETS

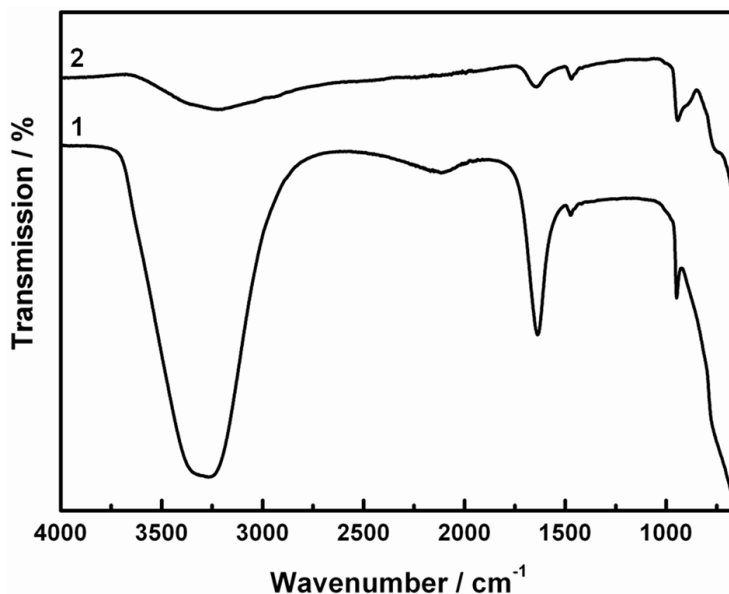


**Figure 4.3.** IR spectra of  $\text{TBA}_{0.84}\text{H}_{0.14}\text{Ca}_2\text{Nb}_3\text{O}_{10}$  before **1** and after **2** dilution with water.

Both types of nanosheets were synthesized by intercalation – exfoliation protocols according to established procedures, which are detailed in the Supporting Information.<sup>[48-50]</sup> Atomic force microscopy (AFM) typically reveals  $\text{Mn}_2\text{Al}(\text{OH})_6^+$  nanosheets with a height around 1.5-1.7 nm and lateral dimensions of several hundreds of nanometers (Figure S4.3,S4.4), when exfoliated in formamide or water, respectively.  $\text{Ca}_2\text{Nb}_3\text{O}_{10}^-$  nanosheets were determined with a typical height of 3.5 nm and lateral sizes around 1-2  $\mu\text{m}$  (Figure 4.2a). Note that the nanosheet thicknesses are higher than the crystallographic thicknesses or those determined experimentally under ultra-high vacuum conditions (0.48 nm<sup>[51]</sup> to 0.81 nm<sup>[18]</sup> for  $\text{Mn}_2\text{Al}(\text{OH})_6^+$  and 1.44 nm<sup>[39]</sup> to 1.80 nm<sup>[28]</sup> for  $\text{Ca}_2\text{Nb}_3\text{O}_{10}^-$ ), which is rationalized by the presence of the ligand shell and adsorption of water, as AFM measurements were carried out under ambient rather than vacuum conditions.<sup>[52]</sup> To prove this hypothesis, the contribution of the  $\text{TBA}^+$  ligand shell to the overall height of the  $\text{Ca}_2\text{Nb}_3\text{O}_{10}^-$  nanosheets was established. First, the amount of  $\text{TBA}^+$  in  $[(\text{TBA})_{1-x}\text{H}_x]^+[\text{Ca}_2\text{Nb}_3\text{O}_{10}]^-$  was determined to be 0.84 ( $x = 0.16$ ) by elemental analysis (see Table S4.1) In the second step, the nanosheet suspension was subjected to a 1:2 dilution with water, since the comparatively high amount of  $\text{TBA}^+$  suggests a relatively dense packing of  $\text{TBA}^+$  on the nanosheet surface.<sup>[4]</sup> Figure 4.2 displays AFM measurements of the undiluted (top) and diluted samples (bottom) with the corresponding height profiles. The undiluted sample shows an almost flat surface of the nanosheet with an initial height of 3.5 nm, whereas the diluted sample exhibits the formation of spots on the surface, along with a decrease of the initial height to around 2.5 nm. With higher dilution the spots vanish

#### 4 LAYER-BY-LAYER ASSEMBLY OF OPPOSITELY CHARGED NANOSHEETS

almost completely. We attribute these observations to the reversible proton – TBA<sup>+</sup> exchange between [(TBA)<sub>1-x</sub>H<sub>x</sub>]<sup>+</sup>[Ca<sub>2</sub>Nb<sub>3</sub>O<sub>10</sub>]<sup>-</sup> and water:

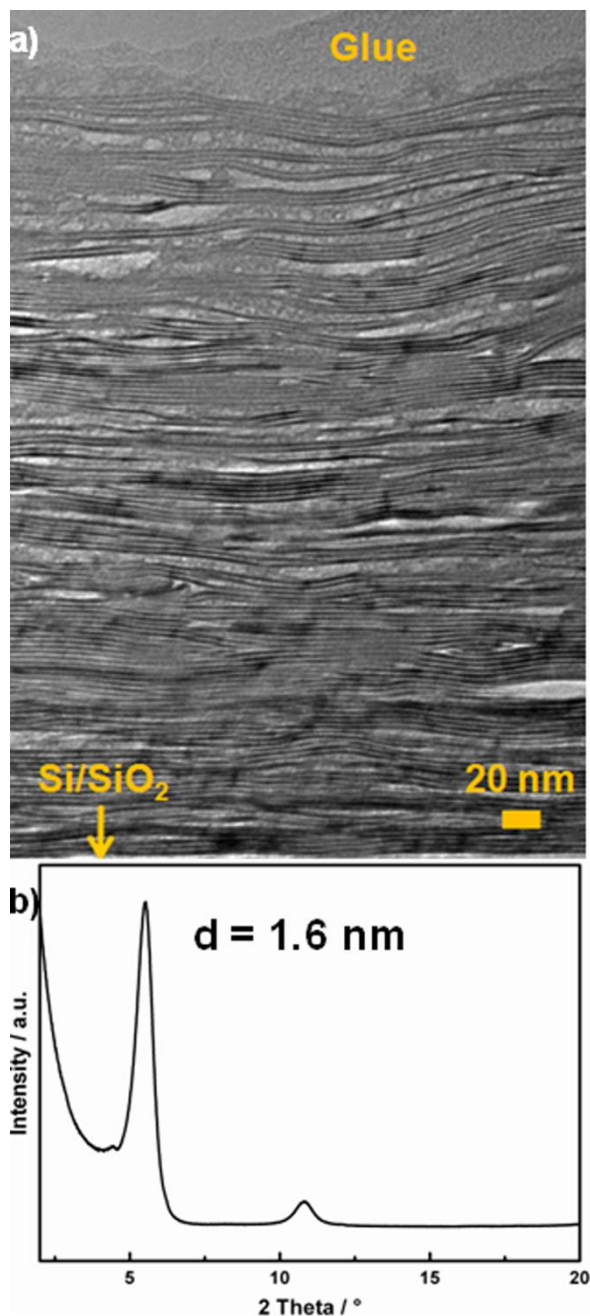
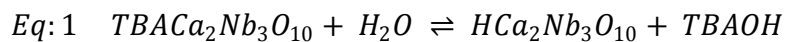


**Figure 4.4.** (a) Bright field HRTEM micrograph of the cross-section of a 100 bilayer (LDH<sub>fa</sub>/per)<sub>100</sub> film obtained by electrostatic LBL assembly. (b) XRD pattern of (LDH/per)<sub>80</sub> measured in reflection mode.

#### 4 LAYER-BY-LAYER ASSEMBLY OF OPPOSITELY CHARGED NANOSHEETS

Our assumption that  $\text{TBA}^+$  is washed away by diluting with water was further confirmed by IR spectroscopy (Fig. 4.3). While the spectrum of  $\text{TBA}_{0.84}\text{H}_{0.16}\text{Ca}_2\text{Nb}_3\text{O}_{10}$  shows strong absorption bands due to the organic ligand, the intensity of these bands at  $3300$  and  $1638\text{ cm}^{-1}$  are strongly decreased compared to the Nb-O stretching band just below  $1000\text{ cm}^{-1}$  in the spectrum of the nanosheets diluted with water. Therefore, taking into account the thickness calculated from crystallographic data of one perovskite block in the  $\text{KCa}_2\text{Nb}_3\text{O}_{10}$  bulk material ( $1.44\text{ nm}$ ) and the coverage of the nanosheets with  $\text{TBA}^+$  (top and bottom,  $\approx 2 \cdot 0.2\text{ nm}^{[28]}$ ), as well as the presence of surface-adsorbed water, we can ascertain the formation of single  $\text{Ca}_2\text{Nb}_3\text{O}_{10}^-$  nanosheets.<sup>[39]</sup>

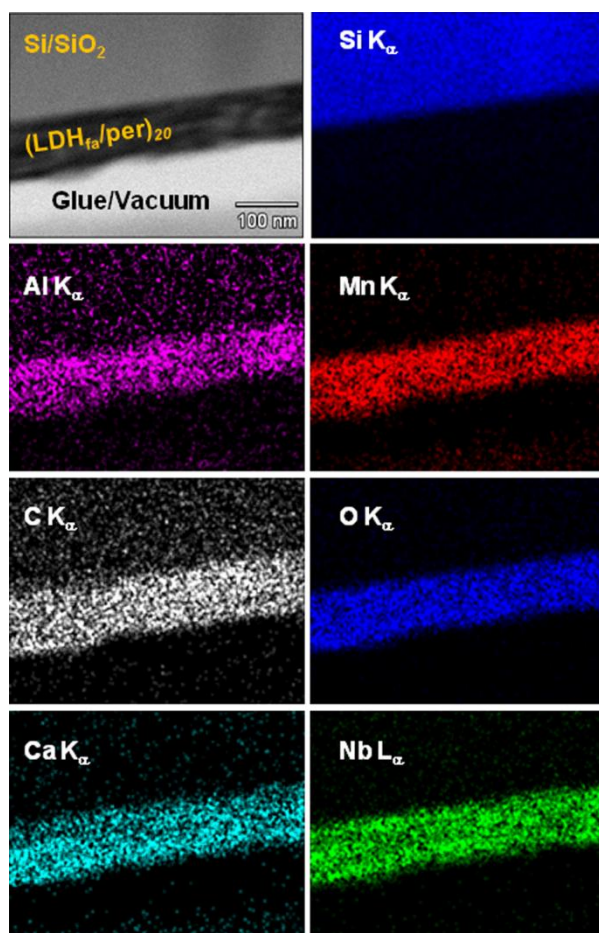


**Figure 4.5.** EDX mapping of a  $(\text{LDH}_{\text{fa}}/\text{per})_{20}$  stack on Si showing homogeneous distribution of all elements. Si  $\text{K}_\alpha$ , C  $\text{K}_\alpha$ , O  $\text{K}_\alpha$ , Al  $\text{K}_\alpha$ , Mn  $\text{K}_\alpha$ , Ca  $\text{K}_\alpha$  and Nb  $\text{L}_\alpha$  signals were measured.

Figure 4.1 schematically depicts the formation of  $(\text{LDH}_{\text{fa/aq}}/\text{per})_n$  multilayer films (fa = LDH exfoliated in formamide, aq = LDH exfoliated in water,  $n$  = number of bilayers).

#### 4 LAYER-BY-LAYER ASSEMBLY OF OPPOSITELY CHARGED NANOSHEETS

$\text{Mn}_2\text{Al}(\text{OH})_6^+$  and  $\text{Ca}_2\text{Nb}_3\text{O}_{10}^-$  are alternately adsorbed on a Si/SiO<sub>2</sub> substrate with washing steps in between to remove excess material and avoid flocculation of the colloidal suspensions. All protocols in the literature relying on positively charged LDH nanosheets use sheets suspended in formamide in order to avoid contamination with carbonate dissolved in water through contact with air. This measure accounts for the fact that the cationic LDH layers have a high affinity to divalent carbonate anions, which are difficult to exchange for monovalent anions and could therefore influence the LBL assembly.<sup>[39]</sup> In the present study  $\text{Ca}_2\text{Nb}_3\text{O}_{10}^-$  was dispersed in water rather than formamide, since no signs of agglomeration of  $\text{Mn}_2\text{Al}(\text{OH})_6^+$  during the LBL process was observed.

Figure 4.4a shows an overview HRTEM image of a cross-section sample of a multilayer (LDH<sub>fa</sub>/per)<sub>100</sub> film. The layers are grown in an ordered fashion on the Si/SiO<sub>2</sub> substrate, yet “real structure” effects as opposed to an ideally ordered structure composed of infinitely extended sheets are clearly visible. The layers show a significant degree of flexibility and bending around defects such as sheet terminations, which leads to voids and overlaps in the assembly. Hence, displacements and small holes are visible in the cross-section sample, which can also arise from mechanical forces acting on the sample during the TEM cross-section preparation. Accordingly, the XRD pattern of a (LDH/per) multilayer stack shows two (00 $l$ ) reflections around 5.5 and 11.0° 2 theta, pointing to a double layer thickness of  $\approx 1.6$  nm (Figure 4.4b). The reflections are broadened due to sheet bending and different layer packing densities as seen in the TEM cross-section images of the stack. The number of counted bilayers (100 $\pm$ 5) and the effective thickness of the stack (250 nm) roughly correspond to that expected for a 100 bilayer film (100 • (1.44 nm + 0.48 nm) = 192 nm), taking holes and irregularities into account. A plot of the number of bilayers, determined by AFM, vs. thickness of the stack shows a linear progression of the layer thickness (Fig. S4.5). The presence of both components –  $\text{Mn}_2\text{Al}(\text{OH})_6^+$  and  $\text{Ca}_2\text{Nb}_3\text{O}_{10}^-$  – in the assembly was verified based on an EDX mapping of the LDH- and perovskite-specific elements, respectively (Figure 4.5). The signal of the Al K $\alpha$ , Mn K $\alpha$ , Ca K $\alpha$ , Nb L $\alpha$ , and O-K $\alpha$  peaks from EDX maps shows evidence of a homogeneous distribution throughout the multilayer, thus confirming the formation of a hybrid nanostructure featuring layered components intimately mixed at the nanoscale. The observed carbon signal either arises from the remaining organic counterions (TBA<sup>+</sup> and ES<sup>-</sup>) or from the glue used for TEM sample preparation. EDX quantification confirms that the amount of  $\text{Ca}_2\text{Nb}_3\text{O}_{10}^-$  is 2-3 times higher than that of  $\text{Mn}_2\text{Al}(\text{OH})_6^+$ . Individual spectra and related quantification data are shown in Figure S4.7 and Table S4.3. In order to draw further conclusions on the local structure of the

#### 4 LAYER-BY-LAYER ASSEMBLY OF OPPOSITELY CHARGED NANOSHEETS

stack and to ascertain the sequential assembly of nanosheets (rather than the formation of a disordered nanocomposite as obtained by flocculation), atomic column resolved high-angle annular dark field (HAADF)-STEM measurements were performed.

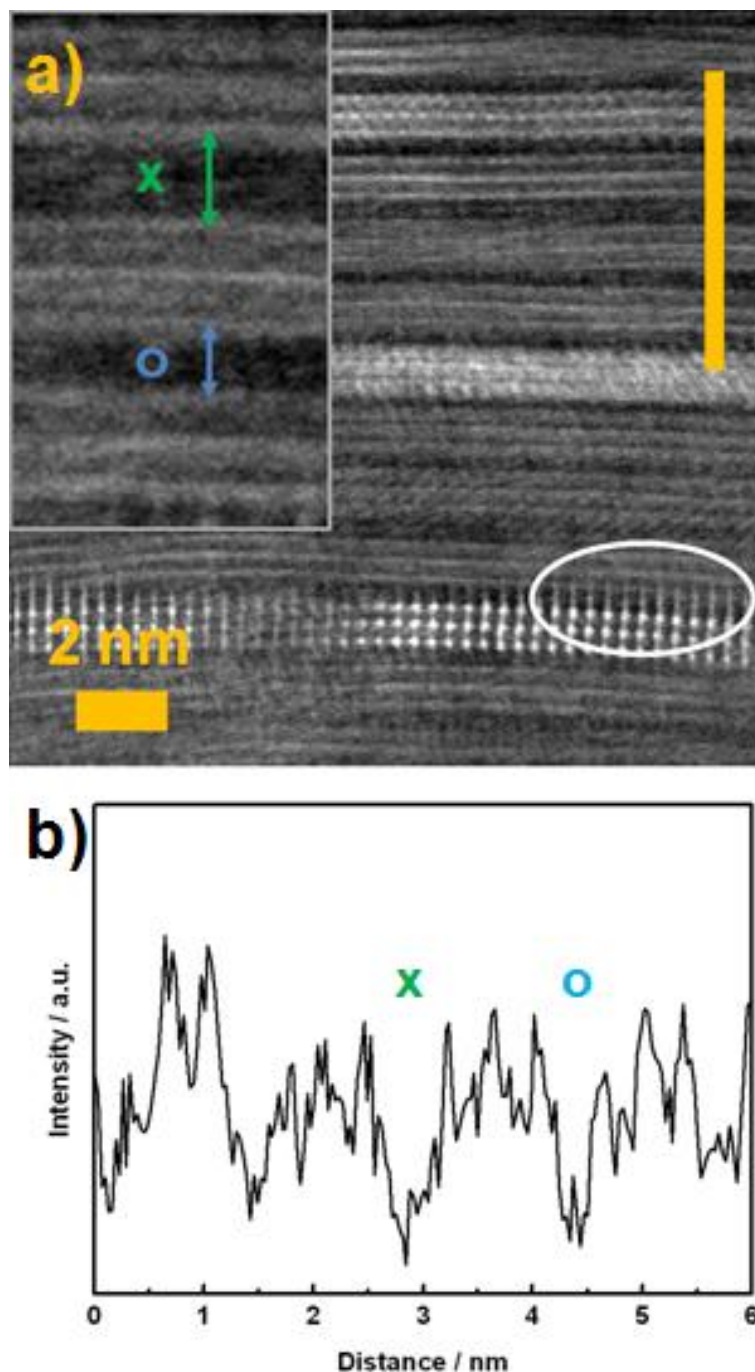


**Figure 4.6.** (a) High-resolution HAADF-STEM image of a  $(\text{LDH}_{\text{fa}}/\text{per})_{100}$  film and (b) intensity profile taken along the orange bar with the green cross marking a large and the blue circle a smaller distance between individual perovskite layers, as shown in the inset. The white ellipse highlights a region where additional columns are visible due to a projection effect.

#### 4 LAYER-BY-LAYER ASSEMBLY OF OPPOSITELY CHARGED NANOSHEETS

The HAADF image (Figure 4.6a) shows an alternating sequence of three bright columns/planes with one broad dark layer in between. Given the sensitivity to the atomic number in HAADF imaging, we attribute the dark slabs to the LDH as will be discussed below. Nevertheless, STEM measurements reveal rapid disintegration under the electron beam, which might explain why no crystalline signature was obtained in these regions. The bright columns/planes arranged in regular “triplets” originate from the heavy niobium atoms and hence can be related to the perovskite layer composed of three edge-sharing  $\text{NbO}_6$  octahedra as fundamental structural motif. These layers are not always oriented along the zone axis as expected for the bulk material, but tilted with respect to each other within the plane of the sheets (i.e. by rotation around a common axis perpendicular to the substrate); thus, the atomic columns can appear as lines in the off-axis orientation. This is clear evidence of the presence of individual delaminated perovskite sheets rather than non-exfoliated bulk material. Some of the perovskite sheets are brighter than others; this is likely related to their orientation with respect to the electron beam. Indeed, it can be observed that brighter layers are atomically resolved, whereas the darker layers are not.

Besides the stacking disorder due to sheet terminations and corrugations owing to varying amounts of adsorbed LDH between the perovskite layers, another observation should be pointed out: In Figure 4.6a the white ellipse marks an area where additional niobium columns seem to be present. This can result from inhomogeneous adsorption of LDH and, hence, formation of wedges causing a tilting of the perovskite layers in the projection of the TEM foil. Figure 4.6b shows the corresponding intensity profile taken along the orange bar (Fig. 4.6a). This intensity profile yields Nb-Nb distances inside a perovskite layer of 3.6-4.2 Å and shows Nb-Nb distances between two different layers starting from 6-9 Å. Figure 4.7a shows the atomic distances of Nb-Nb and Ca-Ca within a perovskite layer in horizontal and vertical directions. In Table S4.4 these distances are listed and compared to the values obtained from the perovskite layer in the bulk materials  $\text{KCa}_2\text{Nb}_3\text{O}_{10}$  (monoclinic, space group  $P2_1/m$ ) and  $\text{HCa}_2\text{Nb}_3\text{O}_{10} \cdot 0.5 \text{H}_2\text{O}$  (tetragonal, space group  $P4/mbm$ ). The values are significantly different and can therefore not be considered an imaging artifact. All experimental values are in agreement with the distances found in the bulk materials. The inset of Figure 4.6b displays a smaller distance marked with a blue circle next to a larger distance marked with a green cross between two perovskite layers, which is also highlighted in the intensity profile. This observation confirms that the distances between the perovskite layers are not constant due to different amounts of adsorbed LDH. The smaller distance is close to the distances found between two perovskite

#### 4 LAYER-BY-LAYER ASSEMBLY OF OPPOSITELY CHARGED NANOSHEETS

layers in the  $\text{HCa}_2\text{Nb}_3\text{O}_{10} \cdot 0.5 \text{H}_2\text{O}$  bulk material and might suggest deposition of multiple layers of  $\text{HCa}_2\text{Nb}_3\text{O}_{10}$  upon partial  $\text{TBA}^+$  – proton exchange during the LBL process. To test this possibility and its impact on the multilayer formation, we attempted to assemble  $\text{Ca}_2\text{Nb}_3\text{O}_{10}^-$  without  $\text{Mn}_2\text{Al}(\text{OH})_6^+$  under otherwise identical experimental conditions and found that this leads to a random accumulation of sheets without a defined multilayer structure. Similarly, the addition of  $\text{Mn}^{2+}$  and  $\text{Al}^{3+}$  ions in solution does not lead to multilayer structures but rather to the deposition of a few layers of  $\text{Ca}_2\text{Nb}_3\text{O}_{10}^-$  on the substrate (Fig. S4.6).

Hence, as expected and in line with the TEM results, oppositely charged nanosheets are crucial for the fabrication of such heterostructures and multilayer stacking of  $\text{HCa}_2\text{Nb}_3\text{O}_{10}$  without the presence of LDH can be excluded. Figure 4.7a shows a HR-STEM image where an EELS line-scan was performed along the orange line. 128 EEL spectra were taken along a distance of 16.3 nm with a dispersion of 0.5 eV/channel. In the range from 169 to 1193 eV most major ionization edges of interest are visible: the Nb- $\text{M}_{4,5}$  with an onset at 205 eV and a delayed maximum, the Ca- $\text{L}_{2,3}$  with two white-lines at 346 eV and 350 eV, the Nb- $\text{M}_{2,3}$  at 363 eV and 378 eV with a sharp threshold peak, the O-K at 532 eV, and the Mn- $\text{L}_{2,3}$  at 640 eV and 651 eV. Figure 4.6b depicts all EEL spectra integrated over the full set of data with the energy scale calibrated based on the Ca- $\text{L}_3$  edge in the dataset. The Mn- $\text{L}_{2,3}$  edge is only visible in the dark layer, whereas the Ca- $\text{L}_{2,3}$  is always present, but with significantly decreased intensity in the dark layer. This is different to measurements known from literature performed on  $(\text{LaNb}_2\text{O}_7/\text{Ca}_2\text{Nb}_3\text{O}_{10})_n$  multilayer stacks, where the perovskite layers are less sensitive to electron irradiation and the signals can clearly be distinguished.<sup>[28]</sup>

Another factor already evident from the EDX data is that less  $\text{Mn}_2\text{Al}(\text{OH})_6^+$  than  $\text{Ca}_2\text{Nb}_3\text{O}_{10}^-$  is present throughout the sample. Hence, the signal for the Mn- $\text{L}_{2,3}$  edge is weak. In addition, elements tend to have a low inelastic scattering cross-section at high energy losses. Figure 4.7c shows enlarged the extracted and normalized signal of Ca- $\text{L}_{2,3}$  and Nb- $\text{M}_{2,3}$ , whereas the Mn- $\text{L}_{2,3}$  and the O-K edge are depicted in Figure 4.7d with the individual spectra of the bright perovskite layer (blue line) and the dark LDH layer (red line), respectively. Note that the signal of the Ca- $\text{L}_{2,3}$  and Nb- $\text{M}_{2,3}$  edges decreases, but does not totally vanish. This can be explained by a slight tilt of the measured multilayer region with respect to the incident beam and the finite resolution of the experimental technique, giving rise to signal contributions from layer regions deeper in the stack. Furthermore, a change of the O-K near-edge fine structures is visible, indicating a change of the



#### 4 LAYER-BY-LAYER ASSEMBLY OF OPPOSITELY CHARGED NANOSHEETS

environment of the oxygen atoms when comparing the pristine perovskite with the hybrid superlattice. An intensity profile of the extracted Ca-L<sub>2,3</sub>, Mn-L<sub>2,3</sub> and O-K edges is shown in Figure 4.7e (for details see Supporting Information). The maximum of the Mn-L<sub>2,3</sub> signal consistently lies in the minimum of the Ca-L<sub>2,3</sub> signal, thus proving the alternate stacking of individual Mn<sub>2</sub>Al(OH)<sub>6</sub><sup>+</sup> nanosheets with Ca<sub>2</sub>Nb<sub>3</sub>O<sub>10</sub><sup>-</sup> nanosheets at the nanometer scale. Notably, this finding implies full delamination of the LDH and perovskite sheets in solution or upon interaction with the respective oppositely charged top nanosheet layer.

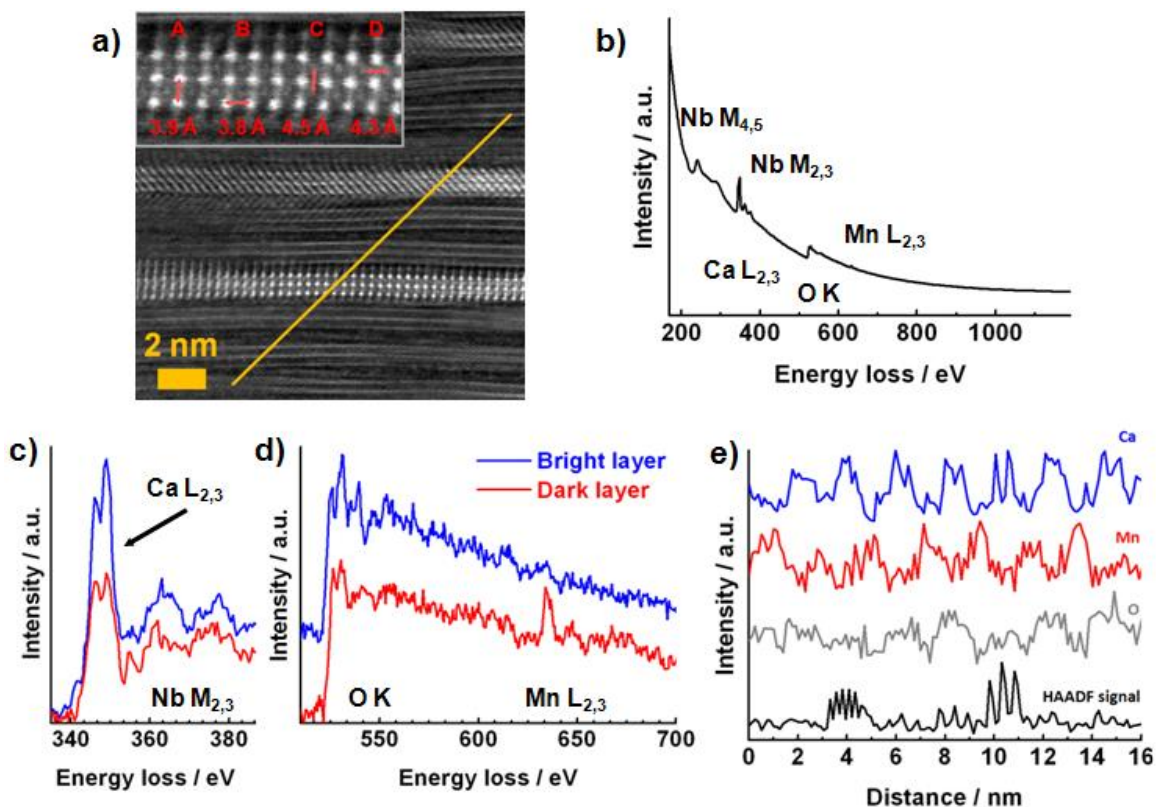


**Figure 4.7.** (a) STEM cross-section image of a (LDH<sub>fa</sub>/per)<sub>100</sub> film. The inset shows the vertical (vert) and horizontal (horiz) distances between A) Nb-Nb<sub>horiz</sub>, B) Nb-Nb<sub>vert</sub>, C) Ca-Ca<sub>vert</sub>, D) Ca-Ca<sub>horiz</sub>. The orange line corresponds to an EELS line-scan, where (b) shows the corresponding summed up EEL spectra, (c) the individual EEL spectra of the Ca-L<sub>2,3</sub> and Nb-M<sub>2,3</sub> edges without shift and (d) the individual EEL spectra of the O-K and Mn-L<sub>2,3</sub> edge with a vertical shift of the blue spectra. In (c) and (d) the spectra from the bright layer (perovskite) are shown in blue, those from the dark layer (LDH) in red. e) Extracted intensity profiles of Ca-L<sub>2,3</sub>, Mn-L<sub>2,3</sub>, O-K, and the HAADF signal taken along the orange line in (a).

#### 4 LAYER-BY-LAYER ASSEMBLY OF OPPOSITELY CHARGED NANOSHEETS

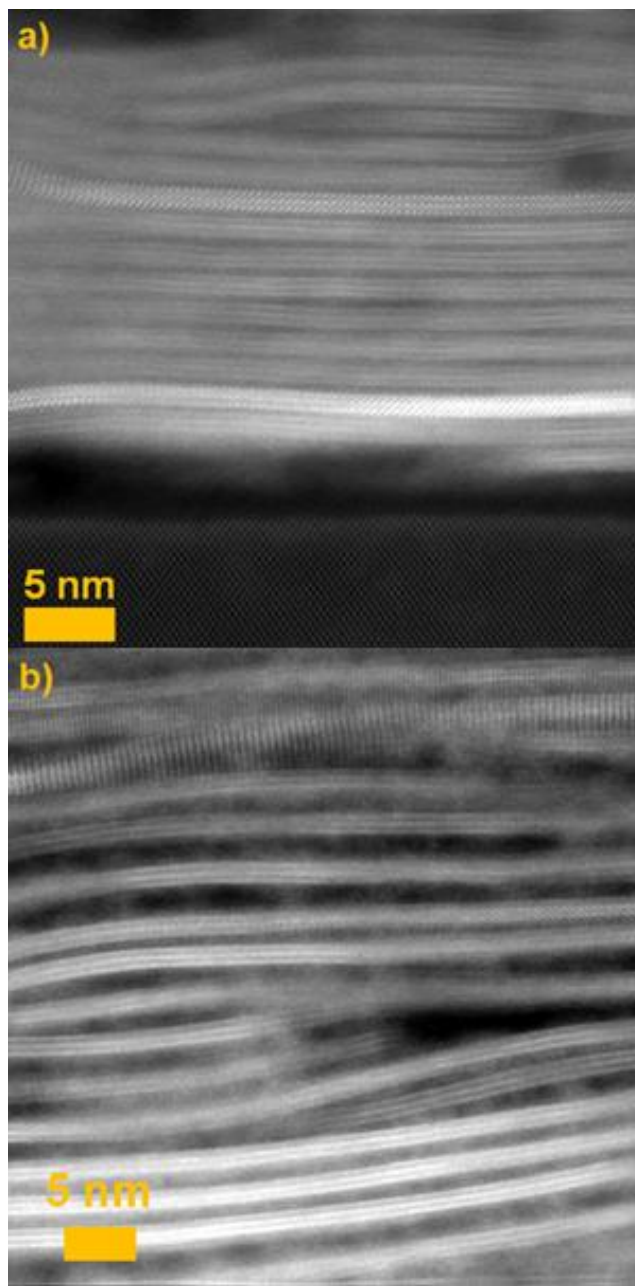


**Figure 4.8.** Comparison of STEM cross-section images taken from a  $(\text{LDH}_{\text{fa}}/\text{per})_{100}$  film assembled with the LDH being dispersed in formamide (a), and a  $(\text{LDH}_{\text{aq}}/\text{per})_{90}$  film with the LDH dispersed in water (b).

The O-K signal is more dominant in the perovskite region, but less pronounced than the Ca- $\text{L}_{2,3}$  signal showing the additional existence of oxygen atoms between the layers, which can be attributed to the  $\text{Mn}_2\text{Al}(\text{OH})_6^+$  layers. The Al- $\text{L}_{2,3}$  edge (73 eV) is influenced by the rising background from the Nb- $\text{N}_{2,3}$  (34 eV), Ca- $\text{M}_{2,3}$  (25 eV) and Mn- $\text{M}_{2,3}$  (49 eV) edges. In addition, the amount of aluminum present in the sample is low, which makes the detection of the Al- $\text{L}_{2,3}$  edge difficult. Also, the Al-K edge is located at much higher energy-losses ( $\sim 1560$  eV) and hence shows a weaker signal for the same acquisition time. However, an

#### 4 LAYER-BY-LAYER ASSEMBLY OF OPPOSITELY CHARGED NANOSHEETS

increased exposure time quickly leads to contamination and therefore to an enhanced background of the C-K edge, which renders the detection of the Al-K edge challenging and rather unreliable under the present conditions and nature of the sample.

The above analysis yields insights into the structure and morphology of the multilayer stack both on the atomic and nanoscale. In line with the solution-based stepwise “growth” process, epitaxial layer stacking is neither expected nor observed.

Nevertheless, the adsorption process generates densely packed regions with little defects next to regions with major stacking faults and locally aggregated organic residues, which likely stem from residual, non-exchanged ligands.

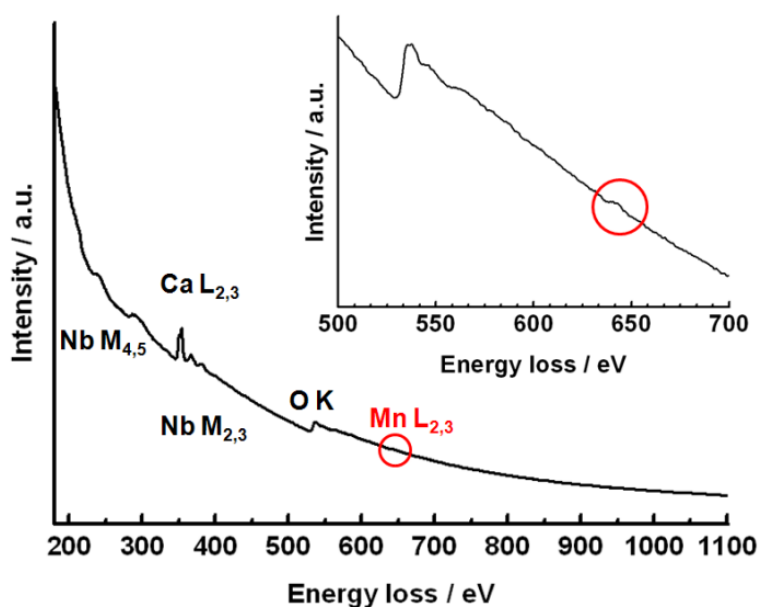


**Figure 4.9.** EELS line-scan of a  $(\text{LDH}_{\text{aq}}/\text{per})_{90}$  film showing all spectra summed in black and the O-K and Mn- $\text{L}_{2,3}$  edge (marked in red) enlarged in the inset.

Along these lines, it is instructive to probe the influence of the assembly conditions on the structure and interfacial quality of the resulting heterostructures. Therefore, in addition to the  $(\text{LDH}_{\text{fa}}/\text{per})_{100}$  multilayer film assembled with formamide as dispersing solvent for the LDH, a  $(\text{LDH}_{\text{aq}}/\text{per})_{90}$  stack using aqueous suspensions throughout was synthesized. Accordingly, exfoliation of the LDH was carried out in  $\text{H}_2\text{O}$  rather than formamide. A low-resolution cross-sectional STEM image of both samples is shown in Figure 4.8 for comparison. In contrast to the  $(\text{LDH}_{\text{fa}}/\text{per})_{100}$  film, the  $(\text{LDH}_{\text{aq}}/\text{per})_{90}$  film is less densely stacked and apparently exhibits larger distances between the perovskite layers. The amount

#### 4 LAYER-BY-LAYER ASSEMBLY OF OPPOSITELY CHARGED NANOSHEETS

of LDH attached to the perovskite sheets appears to be less than in the  $(\text{LDH}_{\text{fa}}/\text{per})_{100}$  stack and the space between the perovskite layers is not as homogeneously filled. EDX analysis suggests that approximately ten times less  $\text{Mn}_2\text{Al}(\text{OH})_6^+$  is present in the  $(\text{LDH}_{\text{aq}}/\text{per})_{90}$  stack than in the  $(\text{LDH}_{\text{fa}}/\text{per})_{100}$  film. In agreement with its porous and less ordered structure, the  $(\text{LDH}_{\text{aq}}/\text{per})_{90}$  film is less stable under the electron beam, making EELS line-scans unfeasible under the given circumstances. Figure 4.9 displays an overall EEL spectrum for the  $(\text{LDH}_{\text{aq}}/\text{per})_{90}$  stack, similar to the one shown for  $(\text{LDH}_{\text{fa}}/\text{per})_{100}$ . All edges are less pronounced and the signal for the Mn-L<sub>2,3</sub> edge is further decreased, with only a small peak visible as shown in the inset (marked with a red circle). We attribute the lower amount of LDH in the water-based sample to the equilibrium reaction described above (eq. 1), which is visualized schematically in Fig. 4.10. During the LDH deposition, the outer  $[(\text{TBA})_{1-x}\text{H}_x]^+[\text{Ca}_2\text{Nb}_3\text{O}_{10}]^-$  layer of the stack is exposed to water.

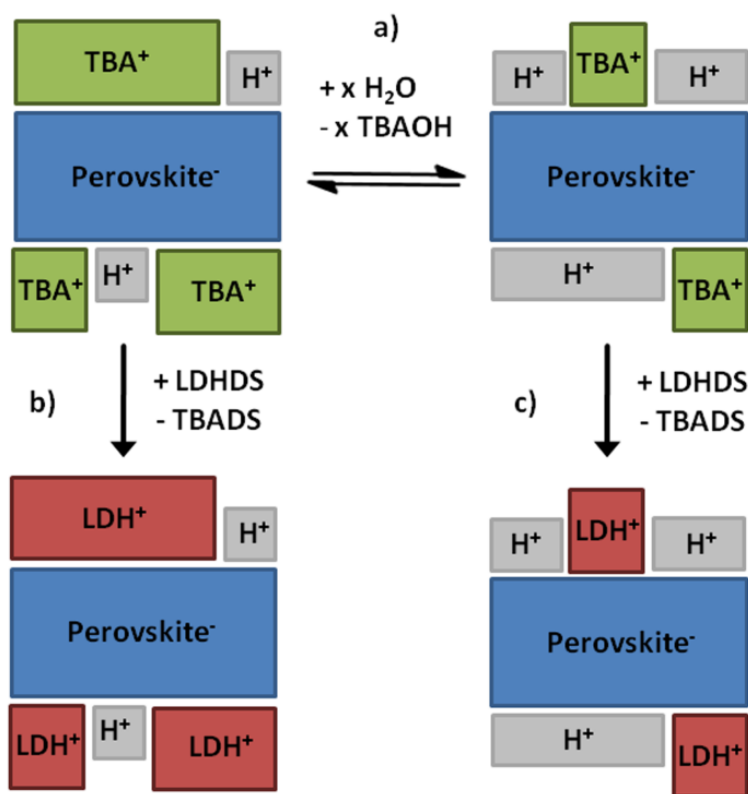


**Figure 4.10.** Scheme depicting the proposed formation mechanism of a  $(\text{LDH}/\text{per})_n$  film as a function of the equilibrium reaction (a). Densely packed  $(\text{LDH}_{\text{fa}}/\text{per})_n$  films are obtained in step (b), while in step (c) less dense  $(\text{LDH}_{\text{aq}}/\text{per})_n$  films are generated due to a shift of the equilibrium reaction of TBAOH and water.

## 4 LAYER-BY-LAYER ASSEMBLY OF OPPOSITELY CHARGED NANOSHEETS

According to eq. 1, the equilibrium is shifted to the right, thus increasing the degree of protonation (larger  $x$ ) for the  $[(\text{TBA})_{1-x}\text{H}_x]^+[\text{Ca}_2\text{Nb}_3\text{O}_{10}]^-$  nanosheets whilst diluting the suspension with water. Hence, less  $\text{TBA}^+$  is present on the nanosheets, thus reducing the apparent layer charge density on the nanosheet surface when assuming only minimal dissociation of the protons in contrast to  $\text{TBA}^+$ . Therefore, the fraction of cations at the nanosheet surface exchangeable with LDH is reduced, giving rise to an overall higher amount of protons along with a lower amount of LDH in the final heterostructure. This is further substantiated by monitoring the pH whilst adding HCl to an aqueous  $\text{TBA}_{0.84}\text{H}_{0.16}\text{Ca}_2\text{Nb}_3\text{O}_{10}$  suspension. Figure S4.8 shows the pH plotted versus the molar fraction of  $\text{TBA}^+$  in  $\text{TBA}_x\text{H}_{1-x}\text{Ca}_2\text{Nb}_3\text{O}_{10}$ . Similar to the titration of  $\text{TBA}_x\text{H}_{1-x}\text{TiNbO}_5$  with  $\text{HCl}^{[3]}$  two equivalent points were found.

The relevant one for the LbL assembly is the equivalent point at pH 8.7. Above this pH a single phase unilamellar colloid exists, which is necessary for a successful LbL deposition. Just below pH 5.5 solid  $\text{TBA}_x\text{H}_{1-x}\text{Ca}_2\text{Nb}_3\text{O}_{10}$  with a proton fraction of more than 50% starts precipitating. We infer from these results that the change of solvents employed for the dispersion of the nanosheets apparently has a major impact on the structure and composition of the resulting superlattices. Although the choice of solvent is limited by the limited dispersability of the nanosheets in many solvents, this finding nevertheless points out an important design criterion in the assembly of nanosheets, which is governed by colloidal stability, ionic strength, composition of the Helmholtz double layer and solution equilibria influenced by the pH.

### 4.1.3 CONCLUSION

We have demonstrated the rational synthesis of a complex two-component solid composed of  $\text{Mn}_2\text{Al}(\text{OH})_6^+$  and  $\text{Ca}_2\text{Nb}_3\text{O}_{10}^-$  nanosheets by means of electrostatic layer-by-layer assembly, which highlights the feasibility of the “rational design” of complex solids through judicious combination of nanosheet building blocks. For the first time, we have been able to map out the structure and elemental distribution within the stacks locally resolved by HRTEM, STEM and EELS analysis, and ascertained the presence of alternating, compositionally distinct LDH and perovskite layers of consistent and reproducible minimum thickness, i.e. single sheets. While the perovskite layers are highly crystalline and stable, no crystalline signature of the LDH layers was obtained owing to their rapid damage under the electron beam. The morphology of the multilayer films can be modified by

## 4 LAYER-BY-LAYER ASSEMBLY OF OPPOSITELY CHARGED NANOSHEETS

selection of different nanosheet dispersing solvents, which was demonstrated by fabricating dense stacks from LDH dispersed in formamide, whilst suspension in water leads to less dense stacks containing a smaller overall amount of LDH. This feature will be helpful as a future design criterion to tune the composition and porosity of the stacks.

In addition, we demonstrated that multilayer films composed of 100 double layers (and possibly more) can easily be obtained by ESD, which is a first step towards the synthesis of tailor-made bulk solids rather than ultrathin films from individual 2D building blocks. Finally, with this study we add evidence to the notion that solids can in fact be “designed” in a rational way by taking advantage of soft chemistry routes to new solids, rather than relying on traditional explorative solid-state synthesis which is largely driven by thermodynamic principles.

### 4.1.4 SUPPORTING INFORMATION

#### Experimental procedures

**Chemicals.** All chemicals and solvents were purchased from commercial suppliers and used without further purification: 4-ethylbenzenesulfonic acid (Sigma-Aldrich, 95%), manganese nitrate ( $\text{Mn}(\text{NO}_3)_2 \cdot 4 \text{H}_2\text{O}$ , Sigma-Aldrich, 97%), aluminum nitrate ( $\text{Al}(\text{NO}_3)_3 \cdot 9 \text{H}_2\text{O}$ , Fluka, 99%), sodium hydroxide (NaOH, AppliChem, 97%), formamide (Fluka, 98%), potassium carbonate ( $\text{K}_2\text{CO}_3$ , Merck KGaA, 99%), calcium carbonate ( $\text{CaCO}_3$ , Grüssing, 99%), niobium pentoxide ( $\text{Nb}_2\text{O}_5$ , Alfa Aesar, 99.5%), tetra-*n*-butylammonium hydroxide 30-hydrate (Sigma-Aldrich, 98%). Deionized water was used throughout all procedures.

**$\text{Mn}_2\text{Al}(\text{OH})_6^+$  Synthesis.** The LDH bulk compounds were synthesized by a typical coprecipitation method according to the literature.<sup>[48]</sup>  $\text{Mn}(\text{NO}_3)_2 \cdot 4 \text{H}_2\text{O}$  (3.33 mmol, 835 mg) and  $\text{Al}(\text{NO}_3)_3 \cdot 9 \text{H}_2\text{O}$  (1.67 mmol, 626 mg) were dissolved in 100 mL water. An aqueous solution of 4-ethylbenzenesulfonic acid (1 mM, 100 mL) was added to the metal nitrate solution. Under Argon atmosphere (to avoid absorption of ambient  $\text{CO}_2$ ) 1 M NaOH was added dropwise to the solution to adjust the pH to 9.0. The brown precipitate was recovered by filtration, washed with water and acetone and dried under vacuum for 24 h. Exfoliation of MnAl ethylbenzenesulfonate (ES) LDH in formamide was carried out by dispersing 25 mg of the bulk material in 50 mL formamide and subsequent sonication for 30 min. The resulting colloidal suspensions were centrifuged at 1,000 rpm for 10 min to

#### 4 LAYER-BY-LAYER ASSEMBLY OF OPPOSITELY CHARGED NANOSHEETS

remove possible non-exfoliated particles. The supernatant was used for further synthesis. Exfoliation of the LDH in water was done by dispersing 25 mg bulk LDH in 50 mL water and subsequent sonication for 5 min.

**Ca<sub>2</sub>Nb<sub>3</sub>O<sub>10</sub><sup>-</sup> Synthesis.** KCa<sub>2</sub>Nb<sub>3</sub>O<sub>10</sub> was synthesized in a modified procedure according to Dion *et al.*<sup>[49]</sup> K<sub>2</sub>CO<sub>3</sub>, CaCO<sub>3</sub> and Nb<sub>2</sub>O<sub>5</sub> were mixed and thoroughly grinded in the molar ratio 1.2 : 4 : 3. The mixture was then fired up to a temperature of 1200 °C for 60 h. 1 g of the as-synthesized powder was stirred in 40 mL 5M HNO<sub>3</sub> for 5 d to achieve cation-proton exchange. The acid was replaced every day.<sup>[53]</sup> For exfoliation 0.2 g of the proton-exchanged form HCa<sub>2</sub>Nb<sub>3</sub>O<sub>10</sub>·0.5 H<sub>2</sub>O were dispersed with tetra-*n*-butylammonium hydroxide 30-hydrate (TBAOH) at a molar ratio of 1:1 in 50 mL aqueous solution. The suspension was shaken for 4 weeks and non-exfoliated particles were removed by centrifugation at 3,000 rpm for 30 min. The supernatant with a nanosheet concentration of ~2mg/mL was used for further synthesis.

**Multilayer assembly.** The multilayer films composed of Mn<sub>2</sub>Al(OH)<sub>6</sub><sup>+</sup> and Ca<sub>2</sub>Nb<sub>3</sub>O<sub>10</sub><sup>-</sup> were assembled using a StratoSequence 6 LBL robot (nanoStrata Inc., Tallahassee). After exfoliation, a Si (100) wafer terminated with a native SiO<sub>2</sub> layer (Si/SiO<sub>2</sub>) was first immersed into the LDH nanosheet suspension in formamide for 10 min, then rinsed in water for 1 min, immersed in the perovskite nanosheet suspension in water for 10 min and rinsed in water again for 1 min. This procedure was repeated *n* times in order to obtain multilayer films depicted as (LDH<sub>fa</sub>/per)<sub>*n*</sub>. The washed film was dried under N<sub>2</sub> gas flow for 1 min after each cycle. Multilayer films based on LDH suspended in water instead of formamide were assembled in the same way and are labelled as (LDH<sub>aq</sub>/per)<sub>*n*</sub>.

**Cross-section preparation.** For transmission electron microscopy (TEM) characterizations a sandwich structure was prepared by gluing two Si/SiO<sub>2</sub> wafers together on the side of the multilayers and subsequently cutting the sandwich structure into discs. The discs were grinded, dimpled and ion-thinned.

**Characterization.** X-ray diffraction (XRD) analysis, scanning electron microscopy (SEM) coupled with energy-dispersive X-ray (EDX) analysis, inductively coupled plasma atomic emission spectroscopy (ICP-AES), elemental analysis, atomic force microscopy (AFM) and transmission electron microscopy (TEM) were used to monitor starting and intermediate compounds as well as the obtained nanosheets. XRD data of powders were collected using a Huber G670 (Huber, Rimsting; Cu K<sub>α1</sub>-radiation, λ = 154.051 pm, Ge(111)-monochromator, external standard SiO<sub>2</sub>) Guinier Imaging Plate diffractometer. XRD of

#### 4 LAYER-BY-LAYER ASSEMBLY OF OPPOSITELY CHARGED NANOSHEETS

multilayer stacks was performed on a Bruker D8 Advance diffractometer (Bruker, Billerica, Cu  $K_{\alpha 1}$ -radiation,  $\lambda = 154.051$  pm). SEM was conducted on a JSM-6500F electron microscope (JEOL Ltd., Tokyo). The microscope was equipped with a 7418 EDX detector (Oxford Instruments, Abingdon). ICP-AES was done using a VISTA RL CCD and ICP-AES analyzer system (Agilent Technologies, Waldbronn). An Elementar vario EL (Elementar Analysensysteme, Hanau) was employed for elemental analysis (EA). To this end, nanosheets were isolated by centrifugation and the carbon, hydrogen and nitrogen mass fraction measured. The excess hydrogen content not attached to the TBA<sup>+</sup> was calculated and used for the determination of x. AFM measurements were performed on a MFP-3D Stand alone AFM (Asylum Research, Santa Barbara). Tapping-mode was applied using OMCL-AC160TS-R3 (Olympus, Tokio) cantilevers with a resonant frequency of 300 kHz. A Philips CM30 ST microscope (300 kV, LaB<sub>6</sub> cathode, CS = 1.15 mm, Royal Philips Electronics, Amsterdam) was used for EDX mapping. The HAADF STEM imaging, and STEM-EDX/EELS investigations were performed in a FEI Titan 80-300 Cubed (S)TEM (FEI, Hillsboro) operated at 300 kV, equipped with a high brightness X-FEG, two aberration correctors for the probe and the image forming lenses, and a Gatan GIF (model 866) spectrometer. The EELS line-scan was performed taking 128 spectra along a distance of 16.3 nm with a dispersion of 0.5 eV/channel. Exposure time was 0.4 s. Energy-windows of 353.0-366 eV for Ca-L<sub>2,3</sub>, 533.0-581 eV for O-K and 640.0-652 eV for Mn-L<sub>2,3</sub> were used for the signal extraction along the measured distance.



#### 4 LAYER-BY-LAYER ASSEMBLY OF OPPOSITELY CHARGED NANOSHEETS

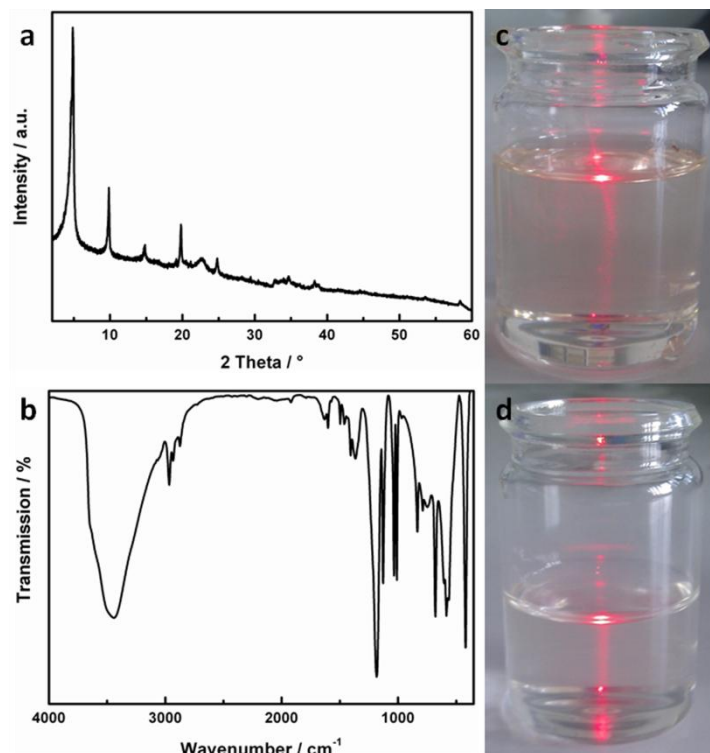


**Figure S4.1.** (a) XRD and (b) IR of MnAl ES LDH, (c) and (d) photographs of  $\text{Mn}_2\text{Al}(\text{OH})_6^+$  nanosheets suspended in formamide and water, respectively.

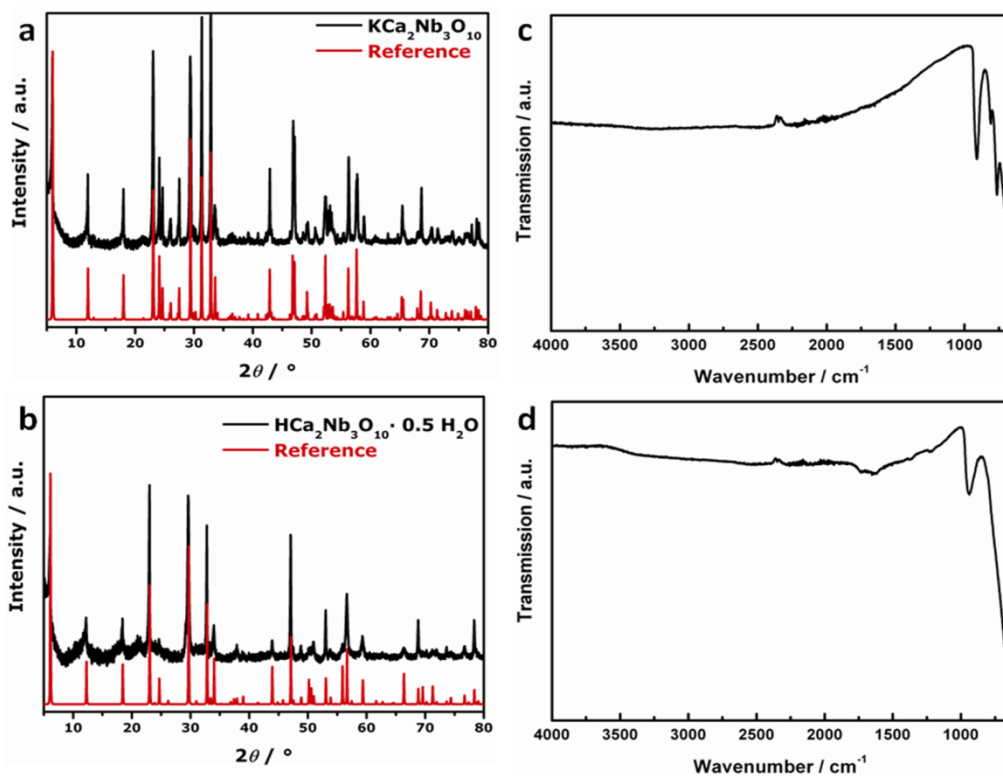


**Figure S4.2.** Left: XRD patterns of (a)  $\text{KCa}_2\text{Nb}_3\text{O}_{10}$ , (b)  $\text{HCa}_2\text{Nb}_3\text{O}_{10} \cdot 0.5 \text{H}_2\text{O}$  with the respective simulated patterns<sup>[54, 55]</sup> taken from the ICSD data base; right: IR of (c)  $\text{KCa}_2\text{Nb}_3\text{O}_{10}$  and (d)  $\text{HCa}_2\text{Nb}_3\text{O}_{10}$ .

#### 4 LAYER-BY-LAYER ASSEMBLY OF OPPOSITELY CHARGED NANOSHEETS

**Table S4.1.** EDX quantification data for  $\text{KCa}_2\text{Nb}_3\text{O}_{10}$ ,  $\text{HCa}_2\text{Nb}_3\text{O}_{10} \times 0.5 \text{H}_2\text{O}$  and  $\text{Ca}_2\text{Nb}_3\text{O}_{10}^-$ .

Element (atomic%) Compound	K $K_\alpha$	Ca $K_\alpha$	Nb $L_\alpha$	O $K_\alpha$
$\text{KCa}_2\text{Nb}_3\text{O}_{10}$	5.7	11.0	19.0	64.4
$\text{HCa}_2\text{Nb}_3\text{O}_{10}^*$	-	11.7	20.6	67.8
$\text{Ca}_2\text{Nb}_3\text{O}_{10}^-$	-	12.2	19.0	67.4

\*ICP-AES yielded  $\text{HCa}_{2.2}\text{Nb}_3\text{O}_{10} \times n \text{H}_2\text{O}$  without traces of K.

**Table S4.2.** Elemental analysis (C, H, N) of  $\text{Ca}_2\text{Nb}_3\text{O}_{10}^-$ . The values are given in weight-%.

N	C	H	Formula
0.79 %	10.05 %	2.18 %	$\text{TBA}_{0.84}\text{H}_{0.16}\text{Ca}_2\text{Nb}_3\text{O}_{10}$

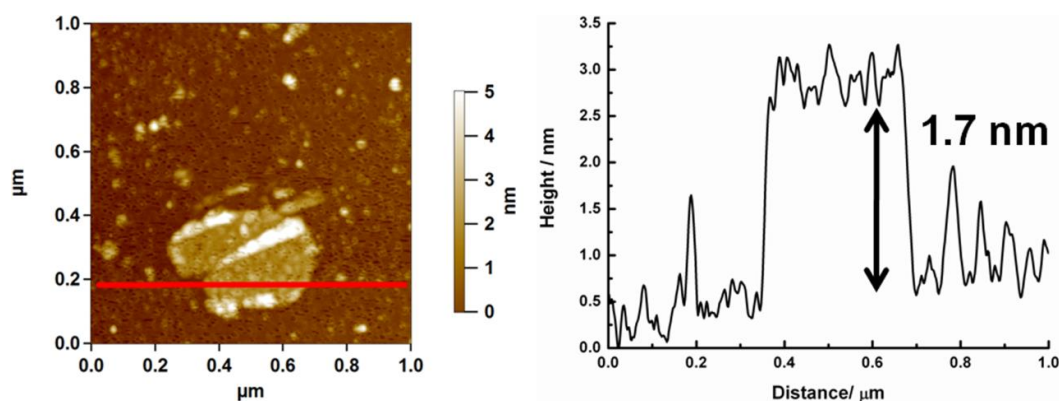


**Figure S4.3.** AFM image and corresponding height profile of a  $[\text{Mn}_{0.67}\text{Al}_{0.33}(\text{OH})_2]^{0.33+}[\text{ES}_{0.33}]^{0.33-}$  (ES: ethylbenzenesulfonate) nanosheet exfoliated in formamide.

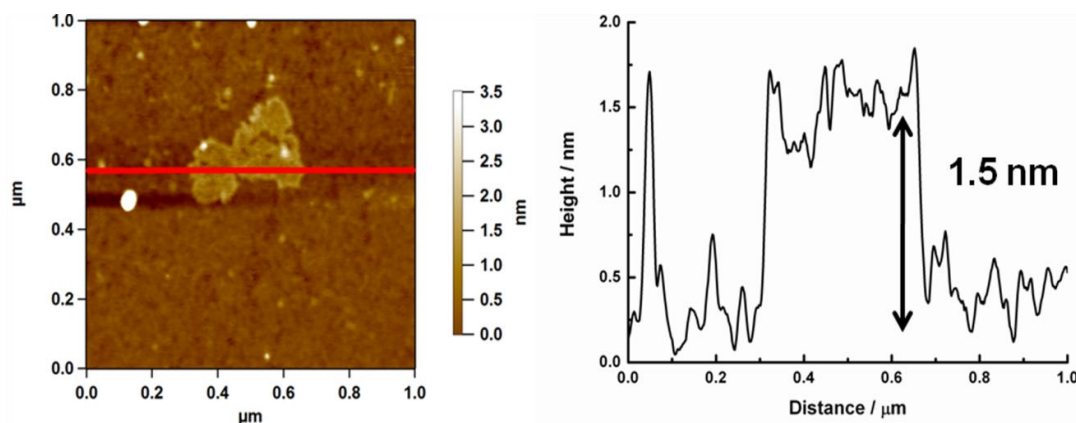


**Figure S4.4.** AFM image and corresponding height profile of a  $[\text{Mn}_{0.67}\text{Al}_{0.33}(\text{OH})_2]^{0.33+}[\text{ES}_{0.33}]^{0.33-}$  (ES: ethylbenzenesulfonate) nanosheet exfoliated in water.

#### 4 LAYER-BY-LAYER ASSEMBLY OF OPPOSITELY CHARGED NANOSHEETS

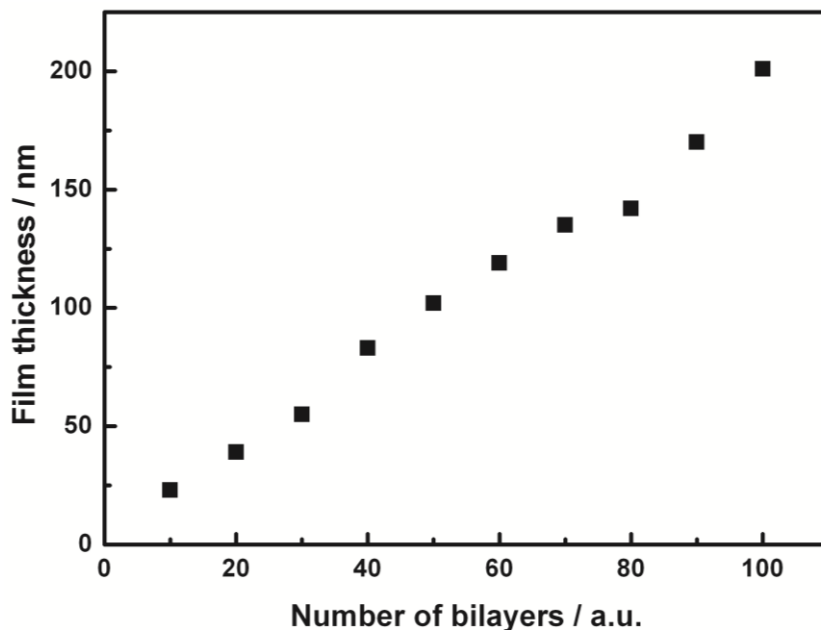


**Figure S4.5.** Number of bilayers vs. film thickness.

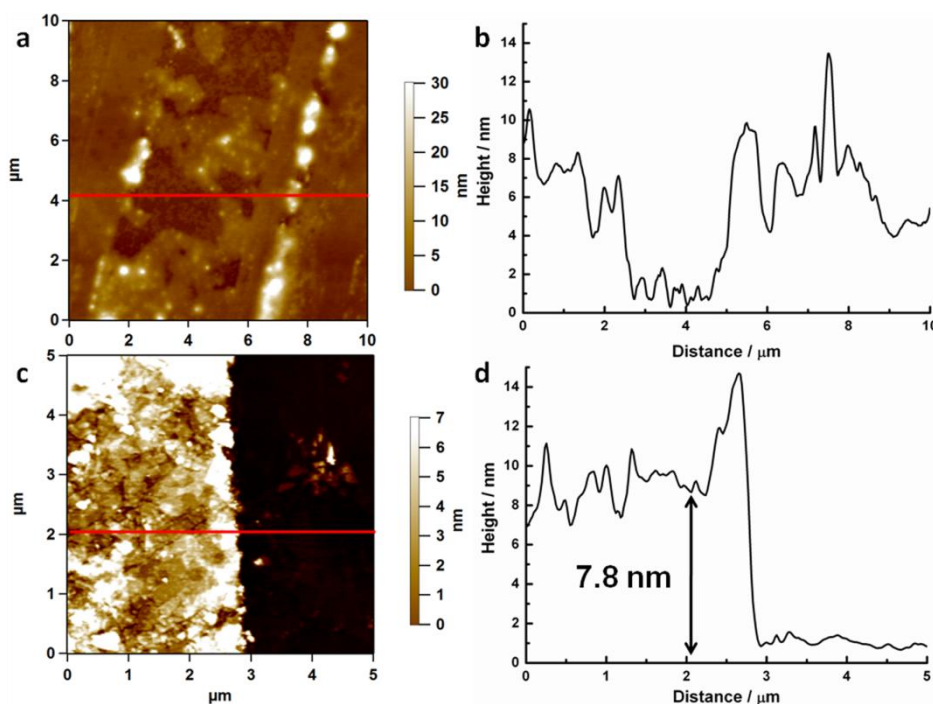


**Figure S4.6.** (a) AFM image of 100 layers of  $\text{Ca}_2\text{Nb}_3\text{O}_{10}^-$  nanosheets and (b) its corresponding height profile. (c) AFM image of 60 layers of  $\text{Ca}_2\text{Nb}_3\text{O}_{10}^-$  nanosheets and  $\text{MnCl}_2/\text{AlCl}_3$  dissolved in formamide. The images show that perovskite nanosheets stacked without positively charged counterparts and perovskite nanosheets stacked with  $\text{Mn}^{2+}$  and  $\text{Al}^{3+}$  ions do not form thick multilayer films.

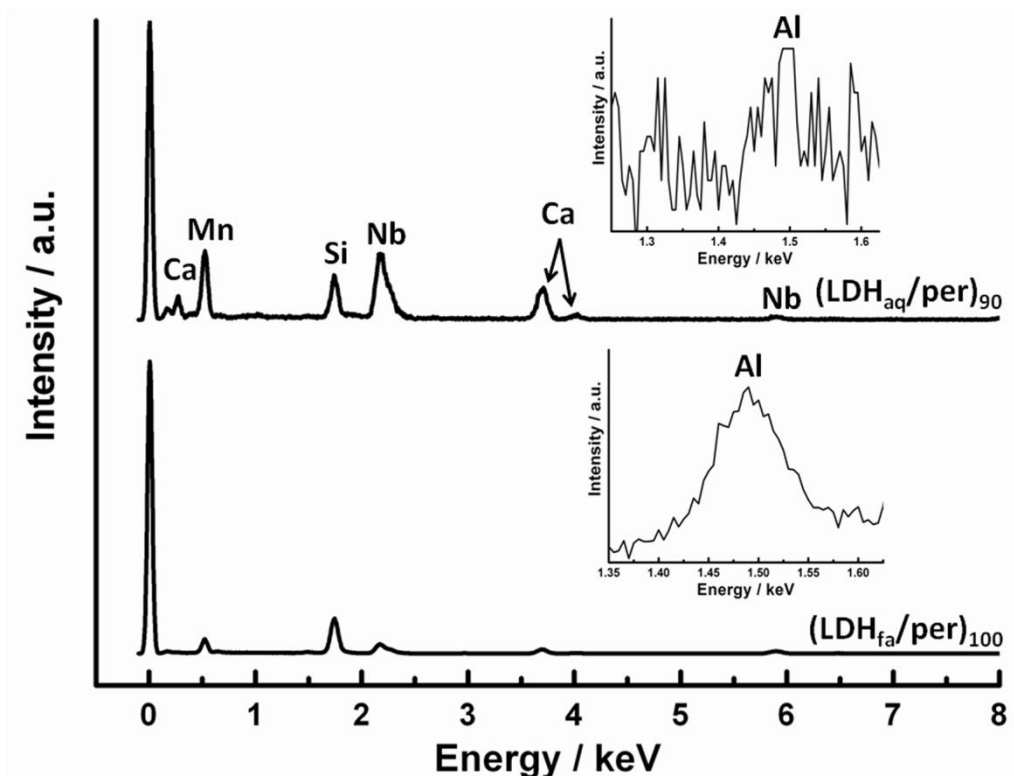


Figure S4.7. EDX spectra of  $(\text{LDH}_{\text{fa}}/\text{per})_{100}$  and  $(\text{LDH}_{\text{aq}}/\text{per})_{90}$ .

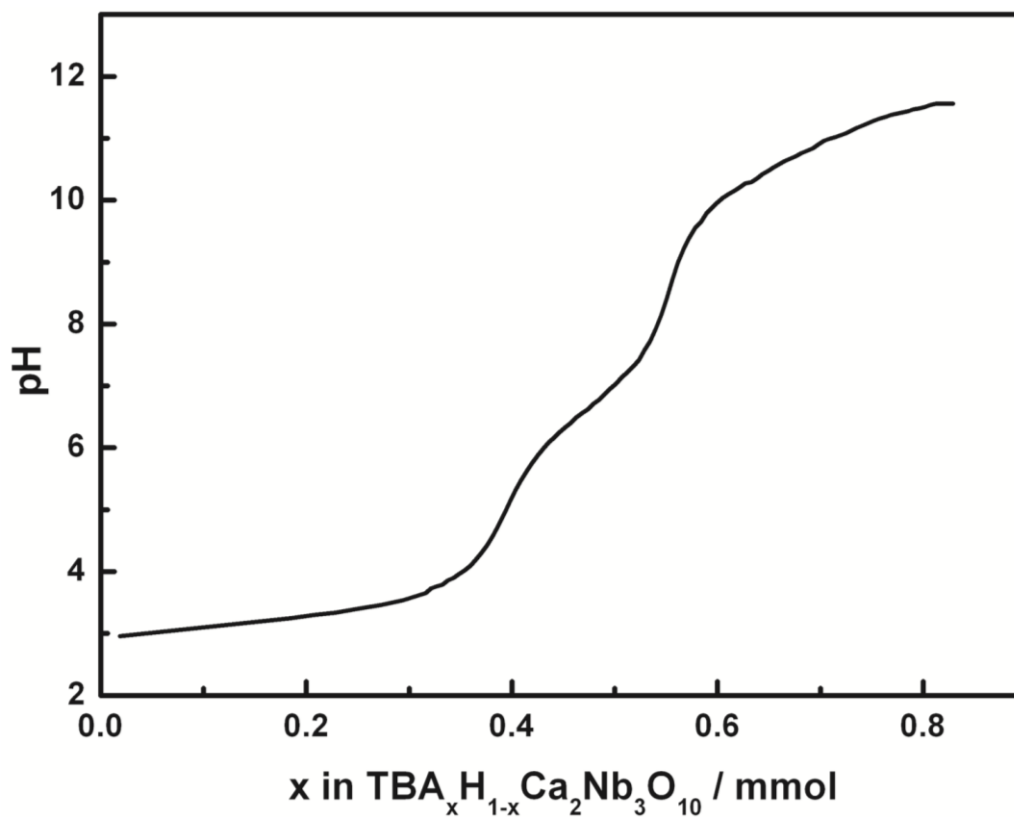


Figure S4.8. HCl titration curve of  $\text{TBA}_x\text{H}_{1-x}\text{Ca}_2\text{Nb}_3\text{O}_{10}$ .

#### 4 LAYER-BY-LAYER ASSEMBLY OF OPPOSITELY CHARGED NANOSHEETS

**Table S4.3.** EDX quantification data for the spectra shown in Figure S7.

Stack/Element (atomic%)	Mn K <sub>α</sub>	Al K <sub>α</sub>	Ca K <sub>α</sub>	Nb L <sub>α</sub>	O K <sub>α</sub>	C K <sub>α</sub>	Si K <sub>α</sub>	Cu K <sub>α</sub>
(LDH <sub>fa</sub> /per) <sub>100</sub>	2.4	0.9	3.9	9.0	45.3	2.4	36.0	0.1
(LDH <sub>aq</sub> /per) <sub>90</sub>	0.6	0.3	6.5	13.0	45.7	25.1	8.4	0.4

**Table S4.4.** Comparison of Nb-Nb and Ca-Ca distances in the perovskite layer found in the bulk materials KCa<sub>2</sub>Nb<sub>3</sub>O<sub>10</sub> and HCa<sub>2</sub>Nb<sub>3</sub>O<sub>10</sub> · 0.5 H<sub>2</sub>O, along with the experimentally obtained values. KCa<sub>2</sub>Nb<sub>3</sub>O<sub>10</sub>, shows a larger distribution of interatomic distances owing to its lower (monoclinic) symmetry.

	KCa <sub>2</sub> Nb <sub>3</sub> O <sub>10</sub>	HCa <sub>2</sub> Nb <sub>3</sub> O <sub>10</sub> · 0.5 H <sub>2</sub> O	Experimental
Nb-Nb <sub>vert</sub>	4.2/4.3 Å	4.2 Å	3.9 ± 0.1 Å
Nb-Nb <sub>horiz</sub>	3.8/3.9 Å	3.9 Å	3.8 ± 0.1 Å
Ca-Ca <sub>vert</sub>	4.1/4.5 Å	4.3 Å	4.5 ± 0.1 Å
Ca-Ca <sub>horiz</sub>	3.5/3.7/4.0/4.3 Å	3.9 Å	4.3 ± 0.1 Å

## 4.2 BIBLIOGRAPHY

### FUNDING SOURCES

This work was supported by the cluster of excellence Nanosystems Initiative Munich (NIM), the Fonds der Chemischen Industrie (FCI) and the Center for Nanoscience (CeNS). Part of the electron microscopy work was performed at the Canadian Centre for Electron Microscopy (CCEM), a Canadian national facility supported by NSERC and McMaster University. G.A.B. is grateful to the NSERC of Canada for partially supporting this work through a Discovery Grant.

### ACKNOWLEDGMENT

We thank Kulpreet S. Viridi for initial microscopy studies, T. Holzmann and A. Schwarze for cross-section TEM sample preparation, C. Minke for SEM/EDX measurements, H. Hartl and M.-L. Schreiber for ICP measurements, R. Eicher for CHNS analysis as well as Stephan Hug and Christine Stefani for additional XRD measurements.

### REFERENCES

- [1] S. W. Keller, H.-N. Kim, T. E. Mallouk, *J. Am. Chem. Soc.* **1994**, *116*, 8817.
- [2] H.-N. Kim, S. W. Keller, T. E. Mallouk, J. Schmitt, G. Decher, *Chem. Mater.* **1997**, *9*, 1414.
- [3] M. Fang, C. H. Kim, G. B. Saupe, H.-N. Kim, C. C. Waraksa, T. Miwa, A. Fujishima, T. E. Mallouk, *Chem. Mater.* **1999**, *11*, 1526.
- [4] R. E. Schaak, T. E. Mallouk, *Chem. Mater.* **2000**, *12*, 2513.
- [5] R. E. Schaak, T. E. Mallouk, *Chem. Mater.* **2000**, *12*, 3427.
- [6] R. E. Schaak, T. E. Mallouk, *Chem. Mater.* **2002**, *14*, 1455.
- [7] T. Sasaki, Y. Ebina, M. Watanabe, G. Decher, *Chemical Communications* **2000**, 2163.
- [8] T. Sasaki, Y. Ebina, T. Tanaka, M. Harada, M. Watanabe, G. Decher, *Chem. Mater.* **2001**, *13*, 4661.
- [9] T. Tanaka, K. Fukuda, Y. Ebina, K. Takada, T. Sasaki, *Adv. Mater.s* **2004**, *16*, 872.
- [10] M. Osada, Y. Ebina, K. Takada, T. Sasaki, *Adv. Mater.* **2006**, *18*, 295.
- [11] K. S. Novoselov, A. K. Geim, S. V. Morozov, D. Jiang, Y. Zhang, S. V. Dubonos, I. V. Grigorieva, A. A. Firsov, *Science* **2004**, *306*, 666.

#### 4 LAYER-BY-LAYER ASSEMBLY OF OPPOSITELY CHARGED NANOSHEETS

- [12] A. K. Geim, K. S. Novoselov, *Nat. Mater.* **2007**, 6, 183.
- [13] A. K. Geim, *Science* **2009**, 324, 1530.
- [14] R. F. Service, *Science* **2009**, 324, 875.
- [15] M. J. Allen, V. C. Tung, R. B. Kaner, *Chem. Rev.* **2010**, 110, 132.
- [16] D. R. Cooper, B. D'Anjou, N. Ghattamaneni, B. Harack, M. Hilke, A. Horth, N. Majlis, M. Massicotte, L. Vandsburger, E. Whiteway, V. Yu, *ISRN Condensed Matter Physics* **2012**, 2012, 56.
- [17] K. S. Novoselov, A. H. C. Neto, *Phys. Scripta* **2012**, T146, 014006.
- [18] L. Li, R. Ma, Y. Ebina, N. Iyi, T. Sasaki, *Chem. Mater.* **2005**, 17, 4386.
- [19] T. Sasaki, M. Watanabe, H. Hashizume, H. Yamada, H. Nakazawa, *J. Am. Chem. Soc.* **1996**, 118, 8329.
- [20] P. Joensen, R. F. Frindt, S. R. Morrison, *Mater. Res. Bull.* **1986**, 21, 457.
- [21] R. Mas-Balleste, C. Gomez-Navarro, J. Gomez-Herrero, F. Zamora, *Nanoscale* **2011**, 3, 20.
- [22] T. Tanaka, S. Nishimoto, Y. Kameshima, M. Miyake, *Mater. Lett.* **2011**, 65, 2315.
- [23] K. Saruwatari, H. Sato, J. Kameda, A. Yamagishi, K. Domen, *Chem. Commun.* **2005**, 1999.
- [24] K. Saruwatari, H. Sato, T. Idei, J. Kameda, A. Yamagishi, A. Takagaki, K. Domen, *J. Phys. Chem. B* **2005**, 109, 12410.
- [25] M. Muramatsu, K. Akatsuka, Y. Ebina, K. Wang, T. Sasaki, T. Ishida, K. Miyake, M.-a. Haga, *Langmuir* **2005**, 21, 6590.
- [26] B.-W. Li, M. Osada, T. C. Ozawa, R. Ma, K. Akatsuka, Y. Ebina, H. Funakubo, S. Ueda, K. Kobayashi, T. Sasaki, *Jpn. J. Appl. Phys.* **2009**, 48, 2009.
- [27] M. Osada, K. Akatsuka, Y. Ebina, H. Funakubo, K. Ono, K. Takada, T. Sasaki, *ACS Nano* **2010**, 4, 5225.
- [28] B.-W. Li, M. Osada, T. C. Ozawa, Y. Ebina, K. Akatsuka, R. Ma, H. Funakubo, T. Sasaki, *ACS Nano* **2010**, 4, 6673.
- [29] B.-W. Li, M. Osada, K. Akatsuka, Y. Ebina, T. C. Ozawa, T. Sasaki, *Jpn. J. Appl. Phys.* **2011**, 50, 09NA10.
- [30] J. L. Gunjekar, T. W. Kim, H. N. Kim, I. Y. Kim, S.-J. Hwang, *J. Am. Chem. Soc.* **2011**, 133, 14998.
- [31] U. Unal, Y. Matsumoto, N. Tanaka, Y. Kimura, N. Tamoto, *J. Phys. Chem. B* **2003**, 107, 12680.

#### 4 LAYER-BY-LAYER ASSEMBLY OF OPPOSITELY CHARGED NANOSHEETS

- [32] U. Unal, Y. Matsumoto, N. Tamoto, M. Koinuma, M. Machida, K. Izawa, *J. Solid State Chem.* **2006**, 179, 33.
- [33] S. Ida, U. Unal, K. Izawa, C. Ogata, T. Inoue, Y. Matsumoto, *Mol. Cryst. Liq. Cryst.* **2007**, 470, 393.
- [34] L. Wang, D. Wang, X. Y. Dong, Z. J. Zhang, X. F. Pei, X. J. Chen, B. Chen, J. Jin, *Chem. Commun.* **2011**, 47, 3556.
- [35] Z. Gao, J. Wang, Z. Li, W. Yang, B. Wang, M. Hou, Y. He, Q. Liu, T. Mann, P. Yang, M. Zhang, L. Liu, *Chem. Mater.* **2011**, 23, 3509.
- [36] J. Huang, R. Ma, Y. Ebina, K. Fukuda, K. Takada, T. Sasaki, *Chem. Mater.* **2010**, 22, 2582.
- [37] J. Han, Y. Dou, M. Wei, D. G. Evans, X. Duan, *Angew. Chem. Int. Ed.* **2010**, 49, 2171.
- [38] P. G. Hoertz, T. E. Mallouk, *Inorg. Chem.* **2005**, 44, 6828.
- [39] L. Li, R. Ma, Y. Ebina, K. Fukuda, K. Takada, T. Sasaki, *J. Am. Chem. Soc.* **2007**, 129, 8000.
- [40] H. Li, L. Deng, G. Zhu, L. Kang, Z.-H. Liu, *Mat. Sci. Eng. B* **2012**, 177, 8.
- [41] X. Zhang, Y. Wang, X. Chen, W. Yang, *Mater. Lett.* **2008**, 62, 1613.
- [42] S. Huang, X. Cen, H. Peng, S. Guo, W. Wang, T. Liu, *J. Phys. Chem. B* **2009**, 113, 15225.
- [43] D. Chen, X. Wang, T. Liu, X. Wang, J. Li, *ACS Appl. Mater. Interfaces* **2010**, 2, 2005.
- [44] E. Coronado, C. Mart -Gastaldo, E. n. Navarro-Moratalla, A. Ribera, S. J. Blundell, P. J. Baker, *Nat. Chem.* **2010**, 2, 1031.
- [45] S. Ida, Y. Sonoda, K. Ikeue, Y. Matsumoto, *Chem. Commun.* **2010**, 46, 877.
- [46] R. Ma, T. Sasaki, *Adv. Mater.* **2010**, 22, 5082.
- [47] T. Hibino, *Chem. Mater.* **2004**, 16, 5482.
- [48] S. Werner, V. W.-h. Lau, S. Hug, V. Duppel, H. Clausen-Schaumann, B. V. Lotsch, *Langmuir* **2013**, 29, 9199.
- [49] M. Dion, M. Ganne, M. Tournoux, *Mater. Res. Bull.* **1981**, 16, 1429.
- [50] Y. Ebina, T. Sasaki, M. Watanabe, *Solid State Ionics* **2002**, 151, 177.
- [51] M. J. Hudson, S. Carlino, D. C. Apperley, *J. Mater. Chem.* **1995**, 5, 323.
- [52] S. Ida, C. Ogata, M. Eguchi, W. J. Youngblood, T. E. Mallouk, Y. Matsumoto, *J. Am. Chem. Soc.* **2008**, 130, 7052.



#### 4 LAYER-BY-LAYER ASSEMBLY OF OPPOSITELY CHARGED NANOSHEETS

- [53] H. Hata, Y. Kobayashi, V. Bojan, W. J. Youngblood, T. E. Mallouk, *Nano Lett.* **2008**, 8, 794.
- [54] T. Tokumitsu, K. Toda, T. Aoyagi, D. Sakuraba, K. Uematsu, M. Sato, *J. Ceramic Soc. Jpn.* **2006**, 114, 795.
- [55] Y. Chen, X. Zhao, H. Ma, S. Ma, G. Huang, Y. Makita, X. Bai, X. Yang, *J. Solid State Chem.* **2008**, 181, 1684.

### 5. SILOXENE

This chapter deals with the characterization, exfoliation and organic modification of the layered compound siloxene, which is obtained from topotactical deintercalation of Zintl phase calcium disilicide. Siloxene has long been known since its discovery of Friedrich Wöhler in 1863,<sup>[1]</sup> however, the structure of this compound has been controversially discussed in the literature ever since. This chapter contains a systematic analytical study of this compound using  $^{29}\text{Si}$  solid-state NMR, IR and Raman spectroscopy in order to examine intramolecular rearrangement reactions of siloxene.

In addition to the structure investigation, bulk siloxene has been modified by liquid-solid hydrosilylation reaction yielding alkyl-siloxene nanosheets, which are soluble in common organic solvents.

## 5.1 STRUCTURE INVESTIGATIONS AND ALKYL-MODIFICATION OF SILOXENE

Stephan Werner, Linus Stegbauer, Viola Duppel, Bettina V. Lotsch

*Parts of this chapter will be published in a peer reviewed scientific journal.*

### ABSTRACT

Two-dimensional materials have come into focus of research recently. Especially the demand for exfoliated semiconducting compounds for use in ultrathin electronic or electrooptic devices is growing rapidly. Siloxene ( $\text{Si}_6\text{H}_3(\text{OH})_3$ ) is a silicon-based semiconductor with a layered structure that is not completely understood yet. Here, we present structural investigations of different siloxene samples using  $^{29}\text{Si}$  solid-state NMR, IR and Raman spectroscopy. In addition, organic modification with hexyl groups and simultaneous exfoliation of siloxene yielding nanosheets which are soluble in organic solvents has been achieved. The nanosheet products have been comprehensively characterized by  $^1\text{H}$  and  $^{13}\text{C}$  1D and 2D solution and solid-state NMR spectroscopy, AFM, TEM, IR and XP spectroscopy.

### 5.1.1 INTRODUCTION

Low-dimensional materials such as 2D nanosheets have attracted much attention during the last years. Owing to their unique properties and potential applications in nanodevices, research has been intensified in this field recently.<sup>[2-4]</sup> Besides graphene,<sup>[5]</sup> metal oxides and perovskites,<sup>[3,6]</sup> layered double hydroxides<sup>[7-9]</sup> and metal chalcogenides<sup>[10-12]</sup> are examples of successfully exfoliated materials. Semiconducting properties of nanosheets are highly desired when it comes to integrating these into electronic circuits. Naturally, therefore, silicon as the prototype material in microelectronics, has come into the focus of 2D research lately. Little work has yet been done in the field of silicon nanosheets (Si-NS). Previously, Nakano *et al.* reported on siloxene ( $\text{Si}_6\text{H}_3(\text{OH})_3$ ) nanosheets which they obtained from a topotactical deintercalation reaction of the Zintl phase compound  $\text{CaSi}_2$  with aqueous HCl, followed by exfoliation of siloxene in aqueous sodium dodecylsulfate solution.<sup>[13]</sup> Siloxene nanosheets are of interest since the parent bulk compound exhibits interesting

## 5 SILOXENE

photoluminescent properties with a green emission maximum at 537 nm. Furthermore, it was shown that this maximum can be blue-shifted upon exfoliation into single sheets.<sup>[13]</sup> The photoluminescent properties of siloxene will be discussed later in this chapter. Siloxene itself has long been known since its discovery in the 19<sup>th</sup> century by Wöhler.<sup>[1]</sup> However, the structure of this compound has been controversially discussed in the literature up to date.<sup>[14-21]</sup> Two possible structures – Wöhler siloxene and Kautsky siloxene (Fig. 5.1 a and b) – have been proposed. Wöhler siloxene consists of Si<sub>6</sub> rings, where either hydrogen or hydroxyl groups are bound to the sp<sup>3</sup>-hybridized Si atoms in an alternating fashion (Fig. 5.1 a). The Si<sub>6</sub> rings are connected to form an infinite 2D honeycomb-type structure analogous to graphene.<sup>[15,17]</sup> In contrast, Kautsky siloxene consists of 2D sheets that are made up of Si<sub>6</sub> rings, which are interconnected by oxygen atoms. In addition, hydrogen is bound to the Si atoms either above or below the plane of the sheet (Fig. 5.1 b).<sup>[14-15,18]</sup> According to the literature the reaction conditions play a crucial role in terms of which of the both isomers is formed. Whilst Weiss et al.<sup>[15]</sup> reported the synthesis of Wöhler siloxene at room temperature, others claimed that the synthesis has to be carried out at 0 °C in order to obtain the same product.<sup>[18]</sup> Furthermore, it is assumed that Wöhler siloxene is metastable and thus rearranges under light irradiation or the presence of oxygen to the more stable Kautsky form.<sup>[22]</sup>

Polysilene (Si<sub>6</sub>H<sub>6</sub>) – also known as layered polysilane<sup>[18]</sup> or silicane<sup>[23]</sup> – is structurally similar to Wöhler siloxene but hydrogen is bound to every Si atom, alternatingly above or below the plane. The synthesis of polysilene is performed at -30 °C, causing the slowing down of the hydrolysis of the silicon hydride network. Due to the sp<sup>3</sup> hybridization of Si, the morphology of the two-dimensional siloxene and polysilene sheets is corrugated<sup>[17,24]</sup> instead of the planar layers in the case of graphene.<sup>[25]</sup> Figure 5.1 a, b and c depict the 2D structures of Wöhler and Kautsky siloxene as well as polysilene, respectively. According to the literature, the 2D silicon backbone of these materials is responsible for their luminescent properties and their band gaps were determined to be 2.3 eV and 2.5 eV for siloxene and polysilene, respectively.<sup>[18]</sup> Even though it is a known phenomenon that different porous silicon and Si:O:H compounds exhibit strong photoluminescence at room temperature, the origin of this effect is still not fully understood.<sup>[16]</sup> Initially it was assumed that the luminescence derives from quantum confinement effects within small crystalline silicon nanoparticles with diameters ≤ 20 Å, leading to charge recombination within these particles with emission of radiation.<sup>[26]</sup> Currently, however, it is assumed that the Si<sub>6</sub> rings in siloxene cause the photoluminescence,<sup>[16,26-27]</sup> which is further enhanced by oxygen

## 5 SILOXENE

insertion into the puckered layers.<sup>[28]</sup> Hence, upon insertion of oxygen into the silicon layers, the electron density at the oxygen is highest, leading to a decrease of electron density in the Si rings and consequently to a widening of the band gap.<sup>[28-29]</sup> This means that upon increasing oxygen content within the layers, the fluorescence undergoes a red-shift down to approximately 1.6 eV.<sup>[29]</sup>

The oxygen free silicon compound polysilene was first exfoliated by doping  $\text{CaSi}_2$  with Mg, followed by soft chemical exfoliation in aqueous propylamine hydrochloride solution.<sup>[30]</sup> Later on, exfoliation of polysilene was achieved by organic modification, e.g. hydrosilylation or Grignard reaction, of the bulk compound and simultaneous delamination of the sheet-like structure.<sup>[31-33]</sup> Nevertheless, due to the high affinity of silicon to oxygen, polysilene compounds are highly sensitive to air and thus all procedures have to be carried out in an inert atmosphere.

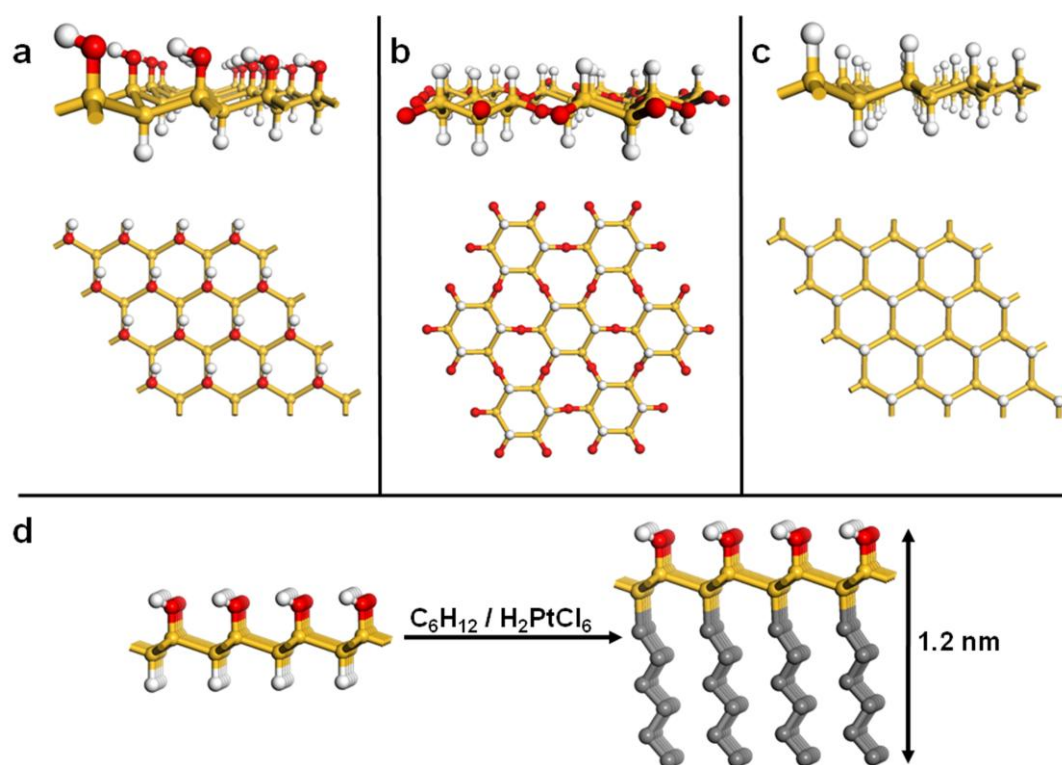


**Fig. 5.1.** (a) Side and top view of (a) Wöhler siloxene ( $\text{Si}_6\text{H}_3(\text{OH})_3$ ), (b) Kautsky siloxene ( $\text{Si}_6\text{H}_6\text{O}_3$ ) and (c) polysilene ( $\text{Si}_6\text{H}_6$ ), showing the corrugated  $\text{Si}_6$ -ring sheet-like structure. (d) Schematic depiction of hexyl functionalization of siloxene. Yellow, red, white and grey spheres represent silicon, oxygen, hydrogen and carbon atoms, respectively. For clarity, hydrogen was omitted in the hexyl groups.

## 5 SILOXENE

It is thus tempting to explore stable 2D silicon compounds such as exfoliated siloxene. To the best of our knowledge, organic functionalization of siloxene compounds has only been carried out on bulk material to yield different alkoxy- and alkylamino-siloxenes without exfoliation into nanosheets.<sup>[15,34-35]</sup> In general, organic functionalization of Si compounds and surfaces can be achieved by different approaches such as hydrosilylation,<sup>[36-37]</sup> self-assembled silane-based monolayers<sup>[38-39]</sup> or covalent grafting of aryldiazonium salts,<sup>[40]</sup> just to name a view, whereas different mechanisms exist for photochemical hydrosilylation according to Buriak.<sup>[36]</sup>

In this work we present the characterization of siloxene, which was prepared and stored under different conditions and annealed to different temperatures up to 400 °C in order to elucidate the structure of the obtained compounds and to investigate the previously postulated rearrangement reaction that oxygen is inserted into the Si<sub>6</sub> rings from axial hydroxyl groups. In order to explore the local structure of these compounds featuring rather low degrees of crystallinity, <sup>29</sup>Si and <sup>1</sup>H solid-state NMR, IR and Raman spectroscopy were applied. Furthermore, a facile chemical modification and simultaneous exfoliation of siloxene into hexyl-siloxene nanosheets is shown (Fig5.1 d). The bulk compound has been modified by a solid-liquid hydrosilylation reaction using H<sub>2</sub>PtCl<sub>6</sub> as catalyst. The resulting nanosheets are soluble in organic solvents, e.g. *n*-hexane, toluene and chloroform. The nanosheet product was analyzed by elemental analysis, <sup>1</sup>H and <sup>13</sup>C liquid NMR, 2D COSY and HMQC NMR, TEM, elemental analysis, IR, AFM and XP spectroscopy.

### 4.1.2 RESULTS AND DISCUSSION

**Structure Investigation.** In order to obtain bulk siloxene, CaSi<sub>2</sub> was immersed in aqueous HCl solution at 0 °C or room temperature as described in the literature and reacted for three and 24 hours, respectively.<sup>[15,18]</sup> Deuterated siloxene was obtained in a similar fashion as siloxene at room temperature by applying 20% deuterated HCl solution. Polysilene was also synthesized similarly but the reaction was carried out at -30 °C in order to suppress hydrolysis of the compound.<sup>[31-32]</sup> All procedures were carried out under Schlenk conditions. To observe the behavior of the rearrangement reaction from Wöhler to Kautsky siloxene the samples were stored under different conditions: ambient atmosphere and light irradiation as well as Ar atmosphere without light irradiation. The siloxene sample that was synthesized at 0 °C was additionally annealed to different temperatures under vacuum for 20 h. The IR spectra of the different products and for comparison that of the starting material CaSi<sub>2</sub> are

## 5 SILOXENE

shown in Figures 5.2 a and b, whereas a close-up of the fingerprint region of  $\text{CaSi}_2$  is shown in Figure S5.4. In Table 5.1 all IR bands of the different samples are listed.

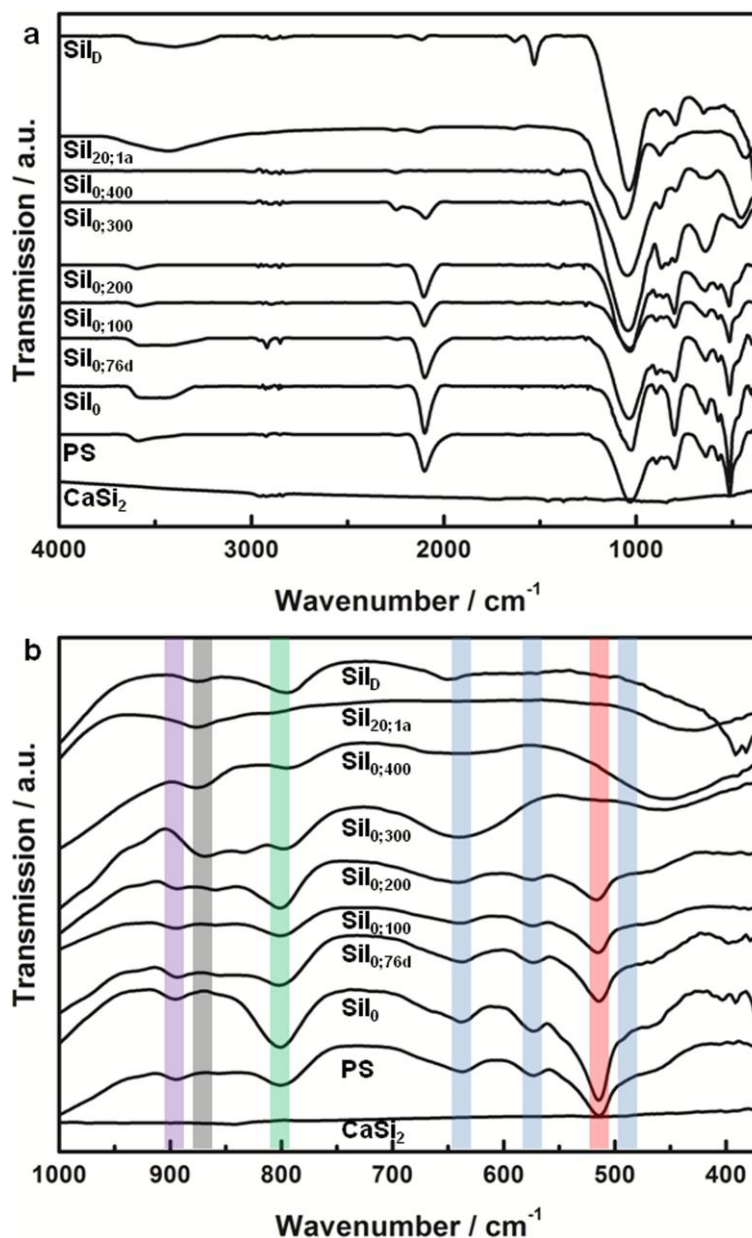


**Fig. 5.2.** (a) IR spectra of different siloxene samples, polysilane and  $\text{CaSi}_2$ . (b) Close-up of the fingerprint area from 370-1000  $\text{cm}^{-1}$  with areas of interest marked in different colors. Purple: H-Si-H, grey: Si-O(H), green: Si-O-Si, blue: Si-H and red: Si-Si bands. The weak bands below 3000  $\text{cm}^{-1}$  and between 1500 and 1200  $\text{cm}^{-1}$  result from grease impurities of the press of the KBr pellet preparation.

## 5 SILOXENE

**Table 5.1.** IR bands of the different characteristic groups in PS and siloxene.

IR band	$\nu / \text{cm}^{-1}$
OH	3600 – 3400 (w);
H-SiO <sub>3</sub>	2250 (w)
Si-H	2100 (s), 640 (m), 575 (m), 470 (w)
Si-O-Si	1165 (w), 1030 (s), 800 (m)
H-Si-H	895 (m)
Si-O(H)	870 (w)
Si-Si	515 (s)
Si-D	1530 (s)
D-Si-D	653 (m)

In the following, the samples are named according to their respective annealing and storage conditions: PS = polysilene; Sil<sub>0</sub> = siloxene synthesized at 0 °C; Sil<sub>20</sub> = siloxene synthesized at 20 °C and stored under ambient conditions, Sil<sub>0;100</sub> = Sil<sub>0</sub> annealed to 100 °C under vacuum, Sil<sub>20;1 a</sub> = Sil<sub>20</sub> stored for one year under ambient conditions and light irradiation, and Sil<sub>D</sub> = siloxene synthesized at 20 °C with 20% deuterated HCl. If not mentioned otherwise, all samples were stored under Ar atmosphere and without light irradiation. In the IR spectra of all siloxene samples, the polysilene and the annealed samples up to 200 °C, an OH stretching band around 3500 cm<sup>-1</sup> is observed. This stretching vibration is intense in Sil<sub>0</sub> and Sil<sub>0;76d</sub> compared to the other samples except for Sil<sub>20;1a</sub>, leading to the assumption that OH groups from Sil<sub>0</sub> rearrange upon annealing into Si-O-Si groups. The lower intensity of the OH stretching vibrations in PS points to a partial depression of the hydrolysis at 0°C. In addition, at 2100 cm<sup>-1</sup> a sharp band in the above mentioned samples and the 300 °C annealed sample indicates a Si-H stretching vibration.<sup>[20]</sup> This band is shifted to 1530 cm<sup>-1</sup> in Sil<sub>D</sub>. In all samples, an additional band at 2250 cm<sup>-1</sup> occurs that points to the formation of H-SiO<sub>3</sub> units<sup>[41]</sup> and a broad and strong band at 1030 cm<sup>-1</sup> is present that derives from asymmetric Si-O-Si stretching.<sup>[42]</sup> In addition, at 1180 cm<sup>-1</sup> in all samples besides PS and Sil<sub>D</sub> a shoulder is visible resulting from asymmetric Si-O-Si stretching in SiO<sub>4</sub> tetrahedra.<sup>[43-44]</sup> The fingerprint area, which is shown in Fig. 5.2b, is of interest for the interpretation of the results, since many important vibrational bands of Si-H and Si-O units occur in this area. Thus, the band at 895 cm<sup>-1</sup> derives from terminal H-Si-H (area marked in purple in



## 5 SILOXENE

Fig. 5.2 b)<sup>[45]</sup> and the bands at 640, 575 as well as the shoulder at 470  $\text{cm}^{-1}$  in PS,  $\text{Si}_0$ ,  $\text{Si}_{0;100}$  and  $\text{Si}_{0;200}$  result from Si-H vibrations (area marked in blue).<sup>[16,20]</sup> Symmetric Si-O-Si stretching<sup>[42]</sup> at 800  $\text{cm}^{-1}$  (area marked in green) and Si-O(H) bending vibration<sup>[46]</sup> at 870  $\text{cm}^{-1}$  (area marked in grey) are observed in all samples. An indication for Si-Si bonds in buckled planar networks is the band at 515  $\text{cm}^{-1}$  that is visible in PS,  $\text{Si}_0$ ,  $\text{Si}_{0;100}$  and  $\text{Si}_{0;200}$ .<sup>[20]</sup> From these data we conclude that the sheet-like structure, which is evidenced by the band at 515  $\text{cm}^{-1}$  (area marked in red), is destroyed by annealing the samples to temperatures above 200 °C, and upon storage under oxygen atmosphere and simultaneous light irradiation. This assumption is substantiated by the finding that the intensity of the Si-H vibrations in the spectra of these samples decrease or the bands completely disappear, and by the presence of a band at 1165  $\text{cm}^{-1}$  pointing to three-dimensional  $\text{SiO}_4$  tetrahedral building units.<sup>[43-44]</sup>

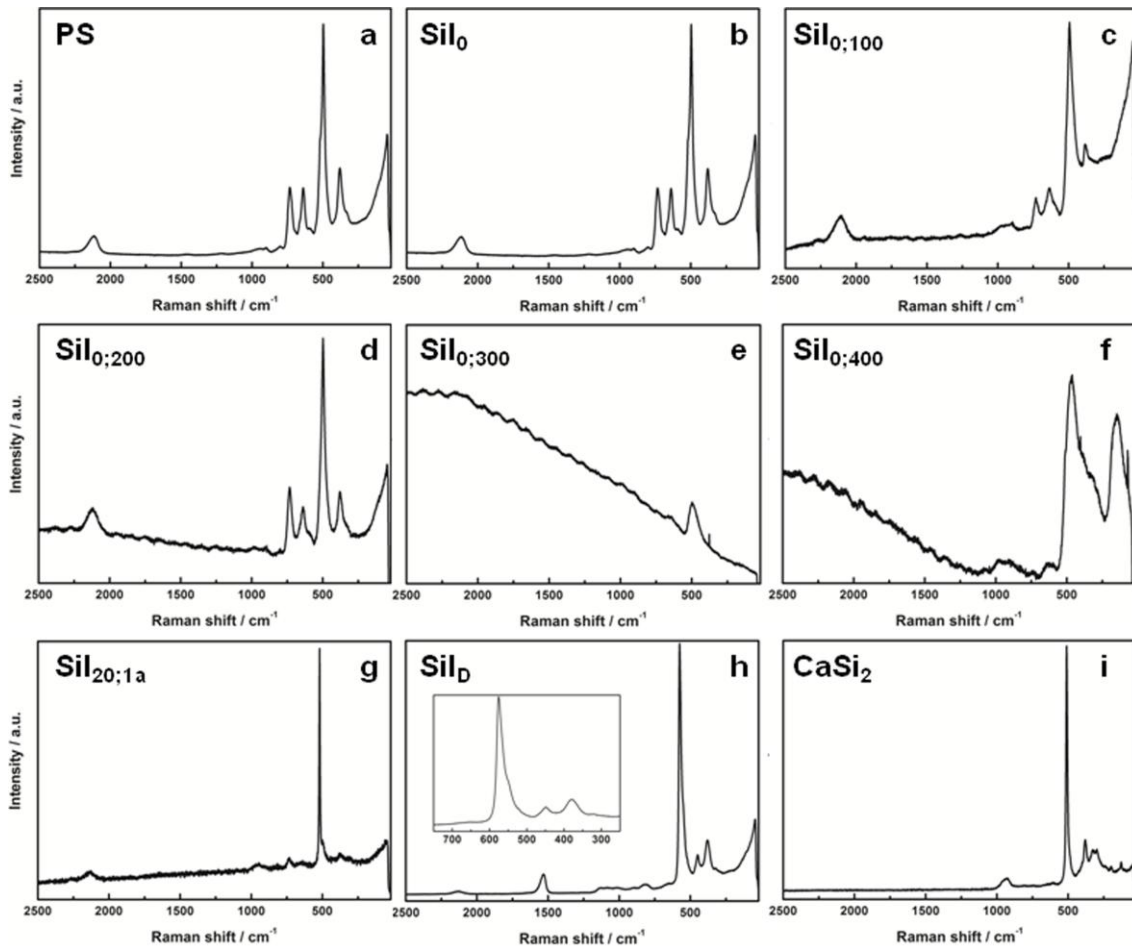


**Fig. 5.3.** (a) Raman spectra of (a) PS, (b)  $\text{Si}_0$ , (c)  $\text{Si}_{0;100}$  (d)  $\text{Si}_{0;200}$  and (e)  $\text{Si}_{0;300}$ , (f)  $\text{Si}_{0;400}$ , (g)  $\text{Si}_{20;1a}$  (h)  $\text{Si}_D$  (inset shows a close-up of the region from 750 – 250  $\text{cm}^{-1}$ ) and (i)  $\text{CaSi}_2$ .

## 5 SILOXENE

In addition, the IR data suggest that PS, which is synthesized at  $-30\text{ }^{\circ}\text{C}$  in order to suppress hydrolysis, is already partially oxidized, as it clearly contains hydroxyl groups and oxygen within the sheet structure. This is consistent with the literature, as also the IR data of PS published from Detlaff-Weglikowska et al.<sup>[18]</sup> and Nakano et al.<sup>[30]</sup> exhibit  $\text{OH}^-$  and Si-O-Si vibrations even after rinsing the product in hydrofluoric acid. The IR spectrum of  $\text{Si}_0\text{D}$  (Fig. 5.2) shows a broad band between  $3500$  and  $3200\text{ cm}^{-1}$  resulting from residual OH groups, while the sharp band at  $1530\text{ cm}^{-1}$  indicates the existence of Si-D groups, which is supported by the fact that the corresponding Si-H band at  $2100\text{ cm}^{-1}$  is weak.<sup>[20]</sup> As expected, the Si-O-Si and Si-O(H) bands at  $1030$  and  $800\text{ cm}^{-1}$  as well as at  $870\text{ cm}^{-1}$ , respectively, remain unaffected by the isotope effect, whereas the band at  $895\text{ cm}^{-1}$  is shifted to  $653\text{ cm}^{-1}$ . In addition a weak band at  $375\text{ cm}^{-1}$  emerges, which results from Si-D vibration.<sup>[21]</sup> Hence, we conclude that the spectrum is in agreement with the literature and that the exchange of isotopes,  $^2\text{H}$  for  $^1\text{H}$ , yields a selective substitution of Si-H by Si-D.

**Table 5.2.** Raman shifts of the different characteristic groups in PS and siloxene

Sample	$\nu / \text{cm}^{-1}$
Si-H	2100 (w); 730 (m); 630 (m), 515 (m)
Si-Si	495 (s); 380 (m)
Si-O-Si	465 (s), 142 (s)
Si-D	1532 (w), 450 (w)

Complementary to the IR measurements, we performed Raman spectroscopy; the spectra of the different compounds can be found in Figure 5.3 and the Raman shifts are listed in Table 5.2. PS,  $\text{Si}_0$ ,  $\text{Si}_{0;100}$  and  $\text{Si}_{0;200}$  show peaks at  $2100$ ,  $730$  and  $640\text{ cm}^{-1}$  resulting from Si-H vibrations.<sup>[20-21]</sup> These become weaker and finally disappear upon annealing or storage in air and light. In addition to the decrease of these peaks and hence the decrease of Si-H groups in the sample, the peaks at  $495$  and  $380\text{ cm}^{-1}$ , which derive from Si-Si bonds in the planes,<sup>[21]</sup> decrease in intensity and become broader. In general, the Raman signal decreases upon annealing, which leads to the observed large signal to noise ratio and sloping background. This is in agreement with the assumption that the layered silicon structure decomposes when annealed to temperatures above  $200\text{ }^{\circ}\text{C}$  in vacuum. Figure 5.3 h shows the Raman spectrum of  $\text{Si}_0\text{D}$ , which is in good agreement with the reported data in the literature.<sup>[20-21]</sup> A signal at  $1532\text{ cm}^{-1}$  and a smaller signal at  $2100\text{ cm}^{-1}$  are found. These

## 5 SILOXENE

result from Si-D and Si-H vibrations, respectively. The peak at  $495\text{ cm}^{-1}$  in hydrogenated siloxene shifts to  $575\text{ cm}^{-1}$  in the deuterated sample. The peak at  $380\text{ cm}^{-1}$  is not shifted in the deuterated samples since it arises from Si-phonons and is thus not affected by the substitution of  $^1\text{H}$  by  $^2\text{H}$ . In contrast, the peak at  $450\text{ cm}^{-1}$  derives from vibrations in Si-D bonds.<sup>[21]</sup>

Solid-state  $^{29}\text{Si}$  NMR spectra of different samples are depicted in Figure 5.4. The spectra shown in Figure 5.4 a-h were recorded in cross polarization mode (CP) at 6 kHz, the spectra in Figure 5.4 j-m were collected as single pulse measurements in order to quantify the relative signal intensities and obtain information about the abundance of the different Si-X groups in the sample. Since the signal at -101 ppm is present in all samples except  $\text{Si}_{0;400}$ , we infer from these data that this signal derives from Si in  $[\text{Si}]_3\text{-Si-[H]}$  groups in polysilene and siloxene, respectively, i.e. Si in oxidation state +1. The chemical shifts are consistent with values of  $[\text{Si}]_3\text{-Si-[H]}$  and  $[\text{Si}]_2\text{-Si-[H]}_2$  groups in porous silicon reported in the literature.<sup>[47]</sup>

The spectra of  $\text{Si}_{20}$ ,  $\text{Si}_{20;30d}$  and  $\text{Si}_{20;1a}$  show additional signals at -72 and -82 ppm that grow in intensity upon storage time.  $\text{Si}_{20;1a}$  exhibits another signal at -112 ppm, which is visible as a shoulder (marked with an arrow) of the signal at -101 ppm and is assigned to an oxidized species with composition close to  $\text{SiO}_2$ .<sup>[19]</sup> Similarly, the spectrum of  $\text{Si}_{0;400}$  shows a broad peak centered between -105 and -112 ppm, which presumably can also be assigned to  $\text{Q}^4$  ( $[\text{SiO}]_4\text{-Si}$ ) groups of formed silicates.<sup>[19,48-49]</sup> Due to the stability of  $\text{SiO}_2$  we attribute the appearance of this phase to the “final” state of the rearrangement and oxidation reactions since it only appears in the spectrum of the sample that was stored for one year in air and light as well as the annealed sample. Still, analysis of samples which have been stored under Ar for one year or longer is required for comparison. However, we assume that the annealed samples will not undergo complete oxidation to  $\text{SiO}_2$  since the oxygen content in all oxidized samples obtained so far is too low for complete oxidation. According to the literature  $[(\text{H}_3\text{Si})\text{O}]_3\text{-Si-[H]}$  groups have chemical shifts at -74.7 ppm and  $[(\text{HO})_3\text{SiO}]_3\text{-Si-[H]}$  groups around -85 ppm.<sup>[47,50]</sup> Hence, we assign the two signals at -72 and -82 ppm that emerge at high reaction temperatures and long storage times to partly oxidized siloxene; i.e. the rearrangement and oxidation reaction takes place already during the synthesis at  $20\text{ }^\circ\text{C}$  and proceeds irrevocably upon storage at least until a certain stage of oxidation of the silicon backbone is reached. Similarly, in the spectrum of  $\text{Si}_{0;400}$  a signal with high intensity occurs at -82 ppm, which can be assigned to  $\text{Q}^2$  phases such as  $[\text{SiO}]_2\text{-Si[OH]}_2$ <sup>[47]</sup> since the IR data shows no existence of hydride phases in this sample. However, upon storage of  $\text{Si}_0$

## 5 SILOXENE

under Ar the rearrangement reaction can be retarded to some extent, as in the spectrum of  $\text{Si}_{0.76\text{d}}$  only a shoulder (marked with an arrow) at -82 ppm can be found. These data suggest that oxidation of the silicon layers does not stop upon formation of the Kautsky isomer, but proceeds until higher oxidized Si species occur, yielding building units like  $[(\text{RO})_3\text{SiO}]_3\text{-Si-H}$ , where  $\text{R} = \text{Si}$  or  $\text{H}$ . Of interest is also the broad signal around -5 ppm in PS that increases in intensity and shifts upfield to -25 ppm in  $\text{Si}_{20;1\text{a}}$ . Because of the low intensity, the broad full width at half maximum (FWHM) and the position of this signal we conclude that it originates from a mixture of different hydroxylated species in siloxene. There are numerous possible compositions of hydroxylated phases in siloxene, such as the suggested prominent phase in Wöhler siloxene,  $[\text{Si}]_3\text{-Si-[OH]}$  and  $[\text{Si}]_2\text{-Si-[OH]}_2$  as well as partially in-plane oxidized species, e.g.  $[\text{Si}][\text{O}]\text{-Si-[OH]}_2$ ,  $[\text{Si}]_2[\text{O}]\text{-Si-[(OH)]}$  and  $[\text{Si}][\text{O}]_2\text{-Si-[OH]}$  structure motifs.

The  $^{29}\text{Si}$  single pulse measurements (Fig. 5.4 j-m) underline the assumption that the peak at -101 ppm derives from  $\text{Si}_3\text{-Si-H}$  groups, since no other peak besides the sharp resonance at -82 ppm, which arises from residual crystalline  $\text{CaSi}_2$  starting material (Fig. S6) or crystalline Si impurities,<sup>[19,47]</sup> can be observed in the as-obtained samples. With the help of the Bruker TopSpin software the CP MAS NMR spectra were fitted in order to obtain relative intensities of the peaks. Hence, the intensity of the signal at -101 ppm relative to the one around -5 ppm decreases by a factor of 25 upon storage and synthesis at room temperature (Fig.S7). The  $^{29}\text{Si}$  CP MAS NMR spectrum of  $\text{Si}_{\text{D}}$  shows the same peaks as the hydrogenated analogue, whereas the intensity of the signal at -101 ppm is decreased by a factor of 4.5 compared to the signal at -5 ppm and the corresponding hydrogenated sample ( $\text{Si}_{20}$ ).

While from the IR data we conclude that  $^1\text{H}$  is substituted by  $> 90\%$   $^2\text{H}$  in Si-H groups, the  $^2\text{H}$  NMR spectrum (Fig. 5.4 i) suggests the existence of only one deuterium position in the sample. Although in principle more than one deuterated moiety is expected in the materials, H substitution for D may preferentially occur at the Si-D/H positions. In addition, the decrease in intensity of the Si-D signal in  $\text{Si}_{\text{D}}$  compared to its analogue  $\text{Si}_{20}$  again suggests that the signal at -101 ppm in the  $^{29}\text{Si}$  NMR spectra indeed results from  $[\text{Si}]_3\text{-Si-[H]}$  groups.

## 5 SILOXENE

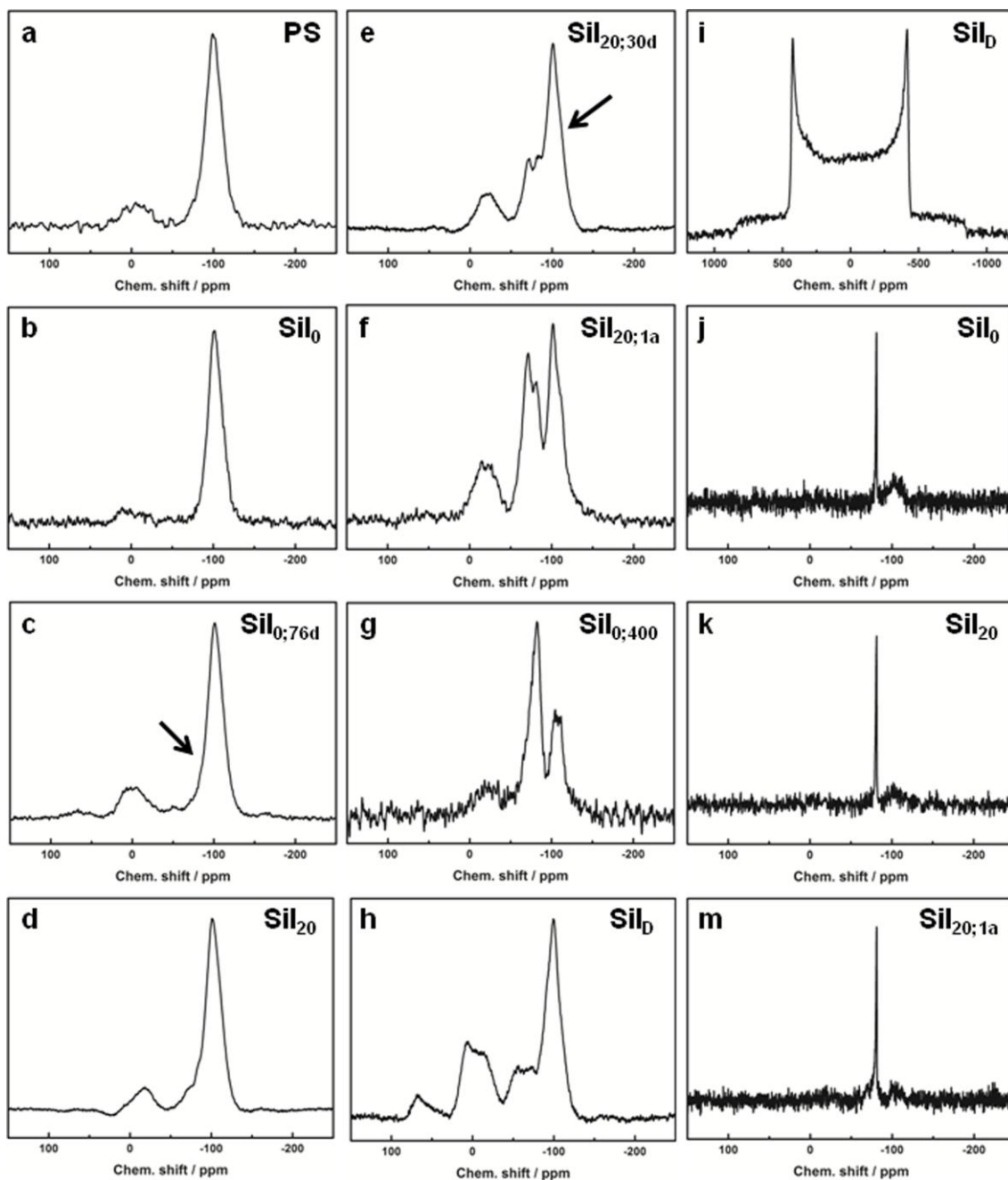


**Fig. 5.4.**  $^{29}\text{Si}$  MAS NMR spectra of (a) PS, (b)  $\text{Si}_0$ , (c)  $\text{Si}_{0;76\text{d}}$ , (d)  $\text{Si}_{20}$ , (e)  $\text{Si}_{20;30\text{d}}$ , (f)  $\text{Si}_{20;1\text{a}}$ , (g)  $\text{Si}_{0;400}$ , (h)  $\text{Si}_D$ , (i)  $\text{Si}_D$ , (j)  $\text{Si}_0$ , (k)  $\text{Si}_{20}$  and (m)  $\text{Si}_{20;1\text{a}}$ . (a)-(h) were recorded with  $^1\text{H}$  -  $^{29}\text{Si}$  cross polarization, (i) is a static  $^2\text{H}$  spectrum and (j)-(m) are single pulse measurements. In all measurements the rotational frequency was 6 kHz and the contact time was 1 ms in CP-MAS measurements.

In summary, we conclude that hydrolysis of the silicon layers cannot be completely suppressed during the synthesis of PS, nor during the synthesis of Siloxene. Thus, hydrolysis inevitably leads to the insertion of oxygen into the layers as suggested by the strong Si-O-Si absorption bands in all IR spectra. Hence, we were not able to obtain pure

## 5 SILOXENE

Wöhler siloxene under the synthesis conditions described. In addition, we observed that Wöhler siloxene rearranges not only into the suggested structure of Kautsky siloxene, but eventually many more X-Si-X building units (X = Si, O or H) are observed with different oxidation states as seen by the different emerging signals in the solid state CP MAS NMR and the Si-O-X (X = Si, H) groups evidenced by IR spectroscopy. This suggests that the isolation of pure bulk Kautsky siloxene is rather difficult, if not impossible. It seems that already during the synthesis, even under inert gas atmosphere, without light irradiation and at temperatures well below 0 °C partial hydrolysis of the sample occurs and, hence, oxygen is inserted into the Si-H bonds as well as into the Si layers. According to the multiple possible oxidation states of Si observed, from our data it does not become clear if oxygen is first inserted into the layers or into the Si-H bond, and whether rearrangement from Wöhler into Kautsky Siloxene indeed takes place or whether Kautsky Siloxene is formed simultaneously with Wöhler Siloxene. However, we note that the presence of Si-OH and Si-O-Si groups is observed already in PS, which points to the rapid insertion of oxygen both into Si-H and Si-Si bonds. In contrast, previous reports agree that firstly hydrolysis leads to Si-OH groups, which then rearrange into the layered structure.<sup>[15,18,28,51]</sup> These studies however, did not systematically investigate the rearrangement reaction by NMR, IR and Raman spectroscopy. Although the exact structure of our siloxene samples cannot be resolved, our data nevertheless suggest that Wöhler siloxene is formed during the synthesis, accompanied by subsequent or even simultaneous rearrangement of this compound into Kautsky siloxene and more highly oxidized species. We observed this for the syntheses at 20 and 0 °C as well as for the synthesis of PS at -30 °C.

**Exfoliation of siloxene.** Bulk siloxene that was synthesized at 20 °C was exfoliated with the help of the organic surfactant sodium dodecylsulfate (SDS). To this end, as-prepared siloxene was dispersed in an aqueous solution of SDS. The AFM images in Fig. 5.5 show siloxene nanosheets with heights of 4.5 nm pointing to a partial delamination of the bulk compound. However, it can be clearly seen that the height profiles of the nanosheets exhibit sharp edges and the lateral dimensions of the sheets range from hundreds of nanometers up to a micrometer. The lateral dimension seems to be affected by the molar ratio of SDS to siloxene. The suspensions from which the image (Fig. 5.5 a) stems has a molar ratio of SDS : Si<sub>6</sub>H<sub>3</sub>(OH)<sub>3</sub> = 1 : 13, yielding rather small nanosheets, whereas the ratio of 1 : 5 (Fig. 5.5 b) yields larger nanosheets up to lateral dimensions of one micrometer. However, the thickness of the nanosheets is not affected by the ratio of surfactant to siloxene.

## 5 SILOXENE

Nevertheless, as can be seen in Fig. 5.5 b, the higher amount of DS not only leads to larger sheets, but also to small particles, presumably also siloxene. Apparently in this case, partial cracking of the layered structure occurs more frequently.

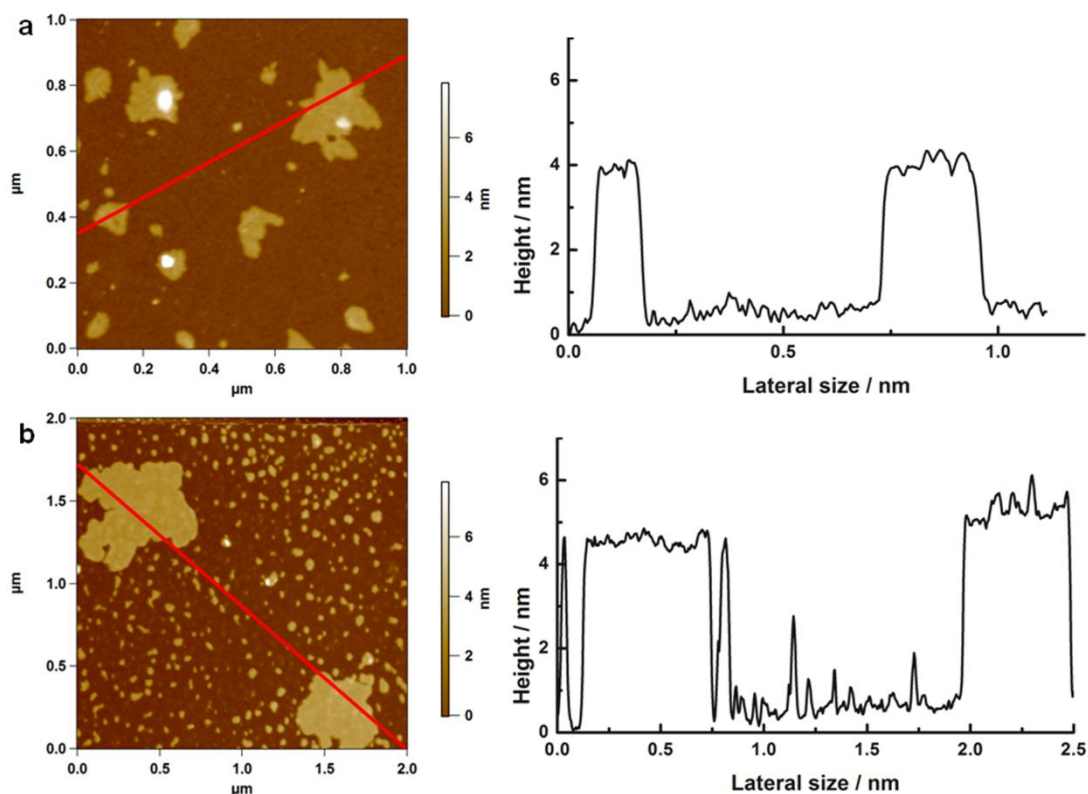


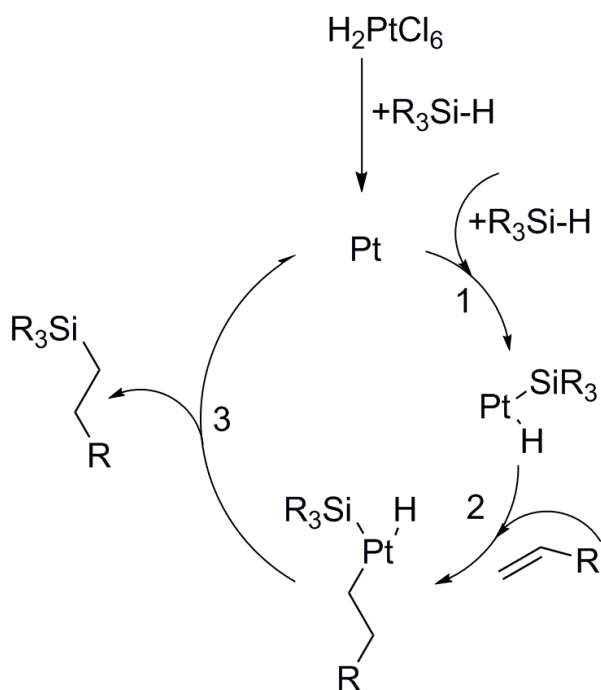
**Fig 5.5.** AFM images with corresponding height profiles of siloxene nanosheets exfoliated at molar ratios of SDS : siloxene (a) 1:13 and (b) 1:5. Height Profiles were taken along the red bar in the images.

The SEM and TEM images of the nanosheets (Fig. S5.8) clearly show the layered structure of the compound. Fan-like (Fig. S5.8 a and c) and plate-like structures (Fig. S5.8 b) as well as thin layers (Fig. S5.8 d) are found in these images. The IR spectrum of centrifuged and dried nanosheets is shown in Fig. S5.9. Obviously the intense band at  $2100\text{ cm}^{-1}$  resulting from Si-H groups disappeared almost completely (marked with a red asterisk), suggesting further oxidation of the compound upon exfoliation. Therefore, the formation of Wöhler or Kautsky siloxene-type nanosheets is unlikely, as the surface Si-H species are easily oxidized to yield predominantly OH-terminated nanosheets. However as the band at  $500\text{ cm}^{-1}$  suggests, the sheet-like character is retained.

## 5 SILOXENE

**Siloxene modification.** The siloxene, which was synthesized at 0 °C for three hours and which resembles a mixture of several modifications, presumably with large amounts of partially oxidized siloxene, was dispersed in toluene.  $\text{H}_2\text{PtCl}_6$  and 1-hexene were added and the suspension was stirred for one day. The resulting hexyl-functionalized siloxene was then separated from residual solids, unreacted siloxene and catalyst, by dissolving the nanosheets in chloroform.

Scheme 5.1 shows the reaction mechanism for a general hydrosilylation reaction using  $\text{H}_2\text{PtCl}_6$  as catalyst, also called “Speier’s catalyst”. The  $\text{Pt}^0$  species is formed by adsorption of the silane to  $\text{H}_2\text{PtCl}_6$ . Subsequently the olefin is added leading to the formation of an intermediate Pt complex with a silyl, hydride and alkyl substituent. In the following elimination of an alkylsilane occurs, which generally follows anti-Markovnikov’s rule.<sup>[52]</sup>



**Scheme 5.1.** Schematic depiction of hydrosilylation using  $\text{H}_2\text{PtCl}_6$  as catalyst. The starting reaction of  $\text{H}_2\text{PtCl}_6$  and  $\text{R}_3\text{Si-H}$  occurs only once, i.e. that in step 1  $\text{R}_3\text{Si-H}$  is not inserted but only in the following reaction circuits.

$^1\text{H}$  and  $^{13}\text{C}$  NMR spectra of hexyl-siloxene are shown in Figures 5.6 a and b, respectively. In Figure 5.6 a, the signal at 1.25 ppm originates from  $\text{CH}_2$  groups and the signal at 0.07 ppm from the  $\text{CH}_2$  group that is attached to the silicon backbone. The signal at 0.85 ppm results from the terminal  $\text{CH}_3$  group of the alkyl group. The remaining peaks



## 5 SILOXENE

originate from impurities, which could not be removed.  $^{13}\text{C}$  NMR underlines these results as the signals at 22.8, 29.8 and 32.1 ppm are assigned to the carbon of the  $\text{CH}_2$  groups, the signal at 1.2 ppm results from the carbon attached to silicon and the signal at 14.2 ppm derives from the  $\text{CH}_3$  carbon. In Table 5.3 the  $^1\text{H}$  and  $^{13}\text{C}$  chemical shifts of *n*-hexane,<sup>[53]</sup> 1-hexene<sup>[54]</sup> and hexyl-siloxene are listed with respect to TMS for comparison. The inset in Figure 5.6 b shows that the olefinic groups have reacted, since the signal of those appears at 114 and 139 ppm. 2D NMR experiments were undertaken in order to confirm the preservation of the intact hexyl group since it shows coupling signals of adjacent  $\text{CH}_x$  groups and a coupling signal of the corresponding  $^1\text{H}$  and  $^{13}\text{C}$  signals in COSY and HMQC measurements, respectively (Figs. 5.7 and 5.8).

**Table 5.3.**  $^1\text{H}$  and  $^{13}\text{C}$  NMR shifts of *n*-hexane, 1-hexene and hexyl-siloxene relative to TMS.

Compound	$^1\text{H}$ shift / ppm	$^{13}\text{C}$ shift / ppm
<i>n</i> -hexane	0.88; 1.26	14.14; 22.70; 31.64
1-hexene	0.90; 1.29; 2.06; 4.92; 4.96; 5.80	13.96; 22.45; 31.53; 33.78; 114.12; 139.20
hexyl-siloxene	0.07; 0.85; 1.24	1.20; 14.21; 22.74; 29.78

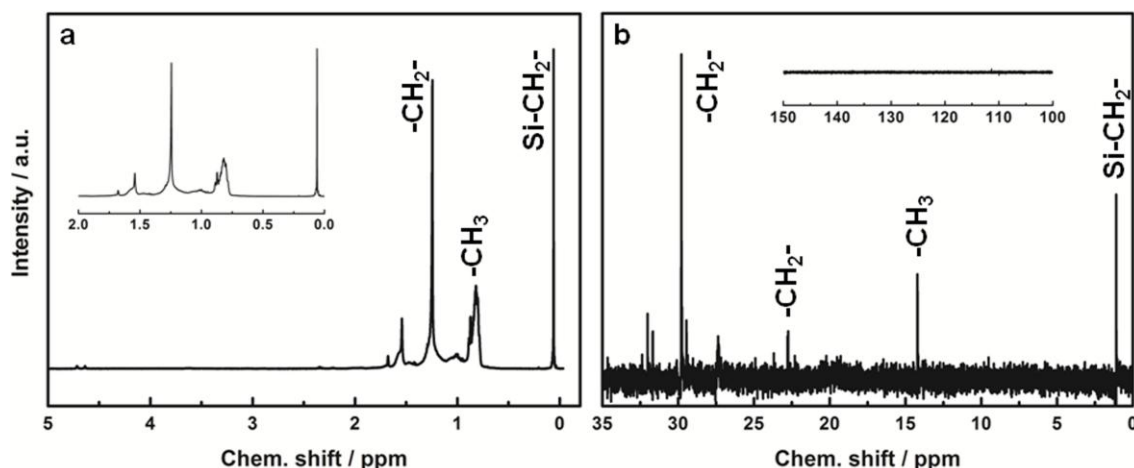


**Fig. 5.6.** (a)  $^1\text{H}$  and (b)  $^{13}\text{C}$  NMR of hexyl-modified siloxene nanosheets collected at 400 kHz in  $\text{CDCl}_3$ . In (a) the inset shows a close-up of the area of 0 - 2 ppm.

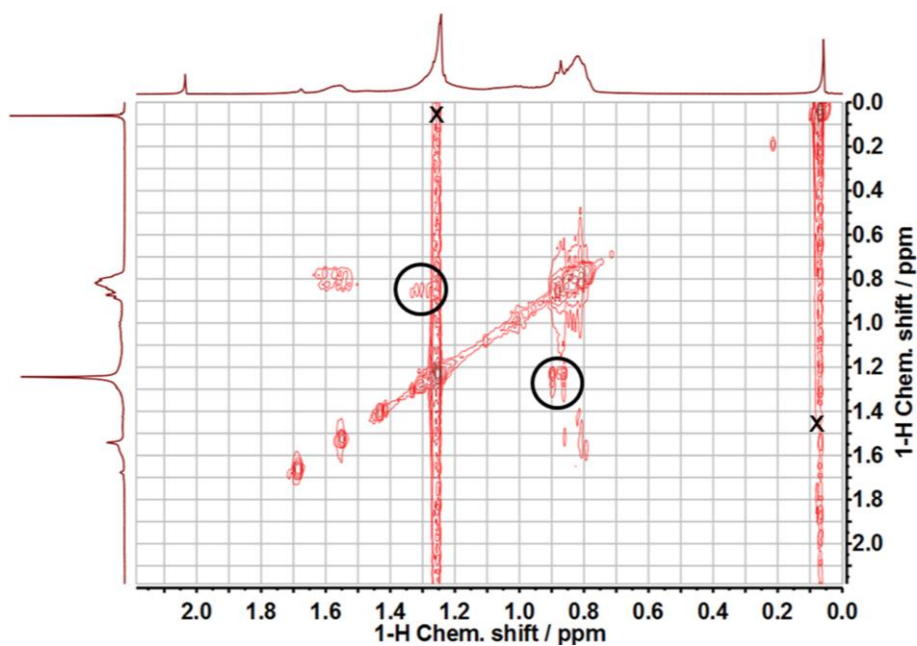


**Fig 5.7.** 2D  $^1\text{H}$  COSY NMR of alkyl-modified siloxene nanosheets. The circles indicate the coupling between  $\text{CH}_3$  and  $\text{CH}_2$  groups of the hexyl group. The crosses indicate the theoretical cross peak position of the  $\text{CH}_2$  group that is attached to the silicon backbone and the adjacent  $\text{CH}_2$  group that disappear in the noise.

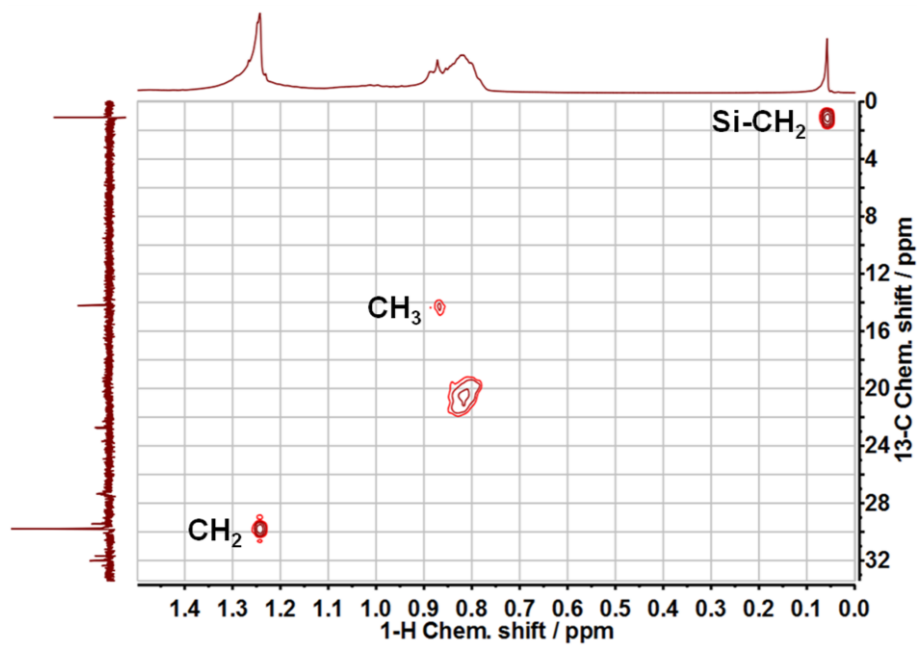


**Fig 5.8.** 2D  $^1\text{H}$  –  $^{13}\text{C}$  HMQC NMR of alkyl-modified siloxene nanosheets. The signal, which is not marked results from impurities.

## 5 SILOXENE

2D COSY NMR (Fig. 5.7) shows the cross peaks, marked with black circles, of the CH<sub>2</sub> groups and the terminal CH<sub>3</sub> group. The coupling between the CH<sub>2</sub> group that is bound to the silicon and the adjacent CH<sub>2</sub> could not be observed due to the low signal to noise ratio. The peaks should appear where the black crosses are located in the diagram. However, in the 2D HMQC NMR spectrum (Fig. 5.8) the cross peak of the CH<sub>2</sub> group attached to the silicon and the <sup>13</sup>C signal from the C-Si carbon can clearly be distinguished. Furthermore, cross-coupling signatures of the CH<sub>3</sub> group and the CH<sub>2</sub> groups are found. These results confirm the preservation of the hexyl group, whereas the formation of a carbon-silicon bond by hydrosilylation is evidenced by the 1D NMR experiments. However, it has to be mentioned that the reaction did not proceed quantitatively. The yield of the hydrosilylation reaction is 9%. This rather low yield is somewhat expected since the exact composition of the starting material is not known, as it presumably exists in different oxidation states. Hence, it is likely that not many Si-H groups, which are necessary for a hydrosilylation reaction, were available. From IR data we infer that 46% of the existing Si-H groups have either reacted or were oxidized during the synthesis.

XP spectroscopy supports the formation of a Si-C bond. Figures 5.9 a, b and c show the XPS survey, C1s and Si2p spectra of the hexyl-modified siloxene, respectively. In the survey spectrum all expected lines such as C1s, Si2s and Si2p and O1s as well as Pt4f, resulting from residual catalyst, can be found. The C1s (Fig. 5.9 b) and Si2p (Fig. 5.9 c) spectra exhibit peaks at 283.1 and 100.7 eV, respectively, which are consistent with values reported in the literature for Si-C bonds.<sup>[55-56]</sup> The existence of fully oxidized silicon species such as SiO<sub>2</sub> and silicates can be excluded, since the binding energies of these compounds occur at 103.3 eV and between 102-103 eV, respectively.<sup>[57]</sup> However, the peak of the Si-C group exhibits a shoulder at higher energies, which points to the partial oxidation of Si by oxygen insertion into the layers. Hence, as expected it is very likely that partially oxidized species such as [Si]<sub>2</sub>[O]-Si-[C<sub>6</sub>H<sub>12</sub>] are present in the sample.<sup>[58]</sup>

Figure 5.10 shows the IR spectra of siloxene **1** and hexyl-modified siloxene **2**. The bands at 2850 – 2955 cm<sup>-1</sup> (–CH<sub>2</sub>– and –CH<sub>3</sub> stretching vibration), at 1454 cm<sup>-1</sup> (–CH<sub>2</sub>– and –CH<sub>3</sub> bending vibration), 1378 cm<sup>-1</sup> (–CH<sub>3</sub> bending vibration) and 720 cm<sup>-1</sup> (–CH<sub>2</sub>– rocking vibration) evidence the presence of alkyl chains in the hexyl-modified sample. In addition, the band at 2100 cm<sup>-1</sup> in **1** resulting from Si-H stretching disappeared almost completely and a band at 1180 cm<sup>-1</sup> appeared in **2** that originates from the Si-C bond. This suggests partial substitution of the Si-H for a Si-C bond. In addition, bands at 1020 cm<sup>-1</sup> and 800 cm<sup>-1</sup> are observed, which result from asymmetric and symmetric Si-O-Si stretching

## 5 SILOXENE

vibrations, respectively, whereas the bands resulting from Si-OH groups disappeared. Hence, we conclude that only structural units of siloxene similar to the Kautsky form have reacted, or that Wöhler rearranges into Kautsky siloxene during the hydrosilylation reaction. Unreacted bulk compounds have been removed by filtration. Elemental analysis yields an experimentally obtained empirical formula of  $\text{Si}_2\text{HO}(\text{C}_6\text{H}_{13})$ . According to the assumption that only Kautsky siloxene has reacted – the theoretical formula for 100% yield would then be  $\text{Si}_2\text{O}(\text{C}_6\text{H}_{13})_2$  – the data indicates the exchange of Si-H for Si- $\text{C}_6\text{H}_{13}$  by 50%. On the background that Wöhler siloxene would have been modified, an exchange of Si-H for Si- $\text{C}_6\text{H}_{13}$  of 100% would have taken place since the empirical formula matches the theoretical one ( $\text{Si}_2(\text{OH})(\text{C}_6\text{H}_{13})$ ).

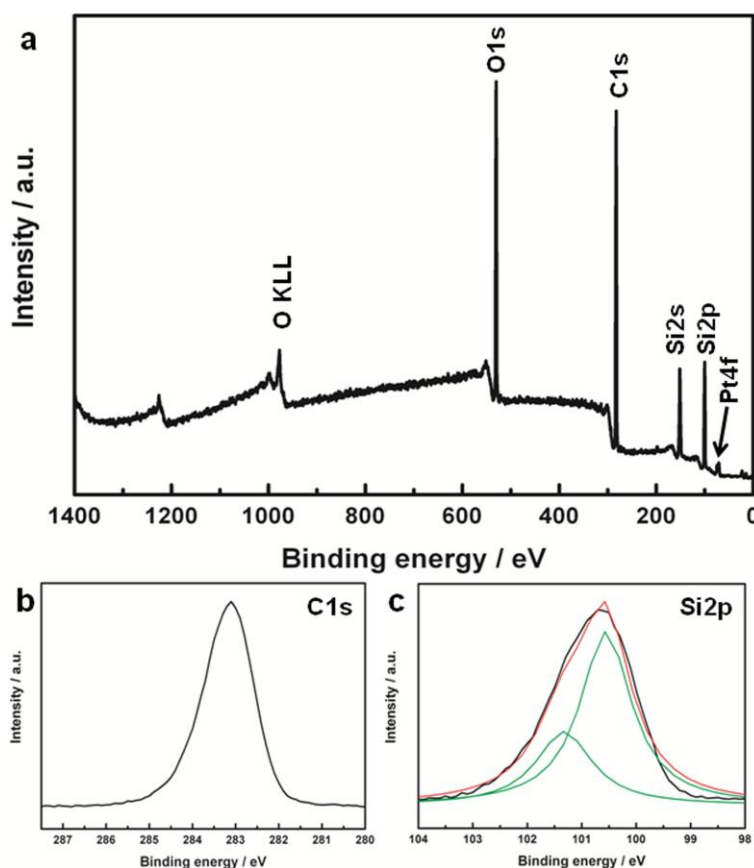


**Fig. 5.9.** (a) XP spectra of alkyl-modified siloxene. (b) and (c) enlargement of the C1s and Si2p peaks, respectively. The green and red curves in (c) resemble deconvolution fits of the Si2p peak.

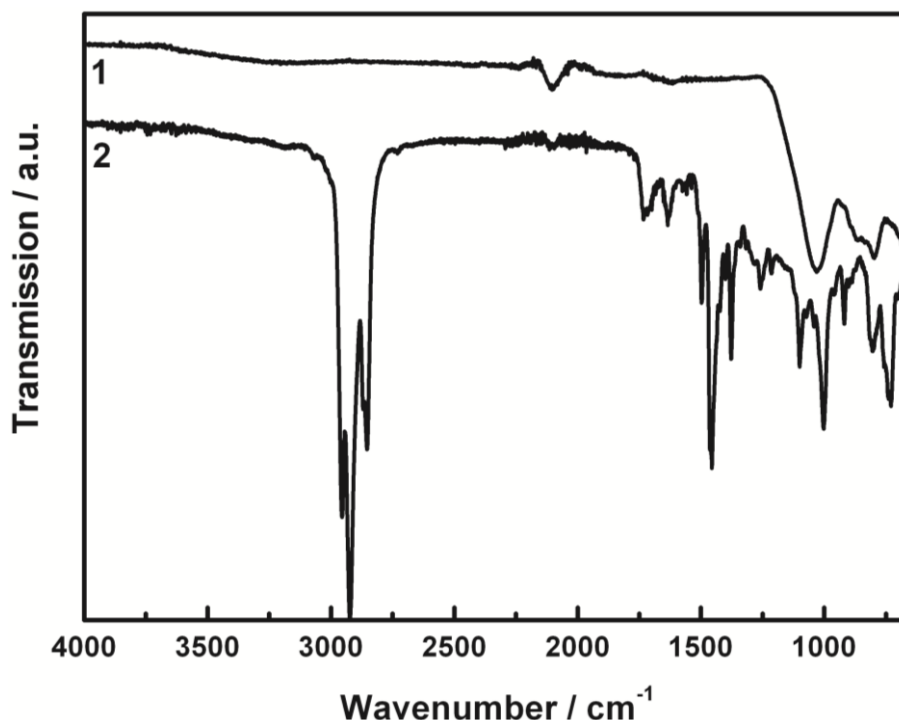


**Fig 5.10.** IR spectra of the starting material siloxene **1** and hexyl-modified siloxene **2**.

The AFM image with its corresponding height profile outlined in Figures 5.11 a and b show that the 2-dimensional structure of the siloxene was retained and nanosheets were indeed obtained. This leads to the assumption that the hydrosilylation took place at intact siloxene rather than decomposition products which likely will not preserve their 2D structure. The height of 1.5 nm fits with the theoretical value of 1.2 nm estimated from the proposed structure in Figure 5.1 c, taking adsorbed solvent molecules and surface water into account. The AFM measurements have been carried out under ambient conditions and, hence, larger heights than the theoretical values are expected.<sup>[59-60]</sup> The sizes of the nanosheets that vary in the range of several hundreds of nanometers, obtained by TEM (Fig. 5.11 c), are consistent with the findings of the lateral dimensions found by AFM. The shape of the edges are rather undefined due to the amorphous character of the sheets, and thus the different termini of this material. EDX analysis yields a composition of Si : O : C = 1 : 2.2 : 1.4. This is an indication that further oxidation of the layers has taken place during the synthesis.

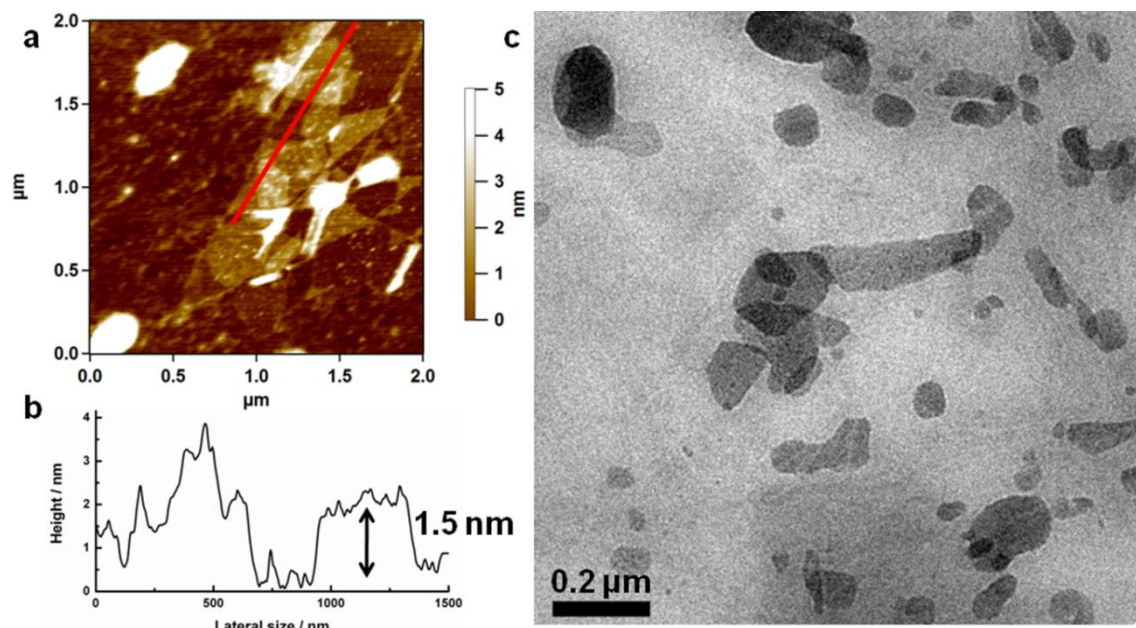


**Fig. 5.11.** (a) AFM image of hexyl-modified siloxene nanosheets, (b) the corresponding height profile taken along the red bar, and (c) TEM image of the nanosheets.

### 5.1.3 CONCLUSION

In summary, we have studied different reaction conditions for the synthesis of polysilane and siloxene in order to elucidate the composition and local structures of the resulting polymeric materials. However, we found complex decomposition pathways already incipient during synthesis, such that the isolation and a detailed understanding of the exact structures of the compounds is challenging, since rearrangement and oxidation reactions occur in all samples under all reaction and work-up conditions that were tested, which cannot be completely prevented or even stopped. However, they can be retarded and probably limited to a significant stage of oxidation through storage of the samples under Ar and light elimination. This was already expected for Wöhler siloxene, which was reported to transform into Kautsky siloxene by rearrangement reactions. However, to the best of our knowledge no such rearrangement process and oxidation reactions were reported for polysilane so far. Our results however show that during synthesis of this compound hydrolysis cannot be totally suppressed, and thus similar reactions as those seen for Wöhler siloxene occur in this compound. In addition, the rearrangement does not stop once Kautsky siloxene is formed, but the Si sheets are oxidized further with oxygen insertion into the Si layers, leading to the destruction of the layers and thus supposedly to three dimensional building units similar to  $\text{SiO}_2$  in air as the final product.<sup>[18]</sup>

## 5 SILOXENE

Moreover, we synthesized an alkyl-modified siloxene with simultaneous exfoliation, yielding well-defined nanosheets with retained layered structures. The nanosheets have been thoroughly characterized and are air and moisture stable, in contrast to previously published<sup>[31-32]</sup> organic-modified silicon-based nanosheets. Thus, they may be used as 2D building blocks for layer-by-layer assemblies to form new tailor-made 3D hybrid structures.<sup>[61-63]</sup> By appending functional groups to the alkyl chains such as amine moieties, the nanosheets can be tuned regarding their polarity, e.g.  $-NH_2$  groups may be protonated to yield positively charged sheets. The polarity of the surface charge of the nanosheets could thus be tuned as desired for future syntheses such as electrostatic layer-by-layer assembly in order to obtain functional materials, since most of the nanosheets reported to date bear a negative layer charge. At the time of this work several attempts to integrate various alkyl and functional groups to the hybrid compound have been undertaken, however, without success. Several different approaches have been tested to integrate functional groups to the siloxene such as catalyst-mediated hydrosilylation, UV and temperature assisted hydrosilylation, self-assembly of silanes, grafting with diazonium salts and Grignard reactions. Table S5.1 contains information about the approaches that have been undertaken. In some syntheses a successful linkage of siloxene to the hexenyl groups was achieved, however, at the expense of the loss of the functional group. The main challenge in this field remains to find appropriate reaction conditions that allow a linkage of siloxene to an organic molecule with retention of the functional groups.

### 5.1.4 SUPPORTING INFORMATION

#### Experimental procedures

**Synthesis of siloxene.** Siloxene was synthesized by topotactical deintercalation of  $CaSi_2$  according to a literature procedure.<sup>[1,18]</sup> In order to observe structural differences of the siloxene samples the synthesis was carried out at different reaction temperatures and times. Generally, 1 g (10 mmol) of  $CaSi_2$  was immersed in an Ar filled flask containing 50 mL 37% HCl. The mixture was reacted either at 0 °C for three hours or at room temperature overnight. The obtained powder was filtrated and washed with  $H_2O$  and dried under vacuum. Furthermore, the samples, which were synthesized at room temperature, were stored under ambient conditions including air and light irradiation to study the rearrangement reaction of the siloxene sample. For the annealing experiments, the siloxene

## 5 SILOXENE

samples, which were synthesized at 0 °C, were annealed in vacuum to 100, 200, 300 or 400 °C for 20 h.

**Exfoliation of siloxene.** 11 mg (0.034 mmol) sodium dodecylsulfate were dissolved in 20 mL deionized H<sub>2</sub>O and 100 mg (0.45 mmol) siloxene was added to the solution. The mixture was shaken for 10 d until a cloudy translucent suspension was obtained. In order to remove possible non-exfoliated particles, the suspension was centrifuged at 5,000 rpm for 10 min; the supernatant suspension was used for further characterization. Nanosheets, which were obtained by higher amounts of DS, were synthesized in the same way but the amount of siloxene used was decreased to 40 mg.

**Synthesis of alkyl-siloxene.** The alkyl-modified siloxene was obtained by starting from the siloxene which was synthesized at 0 °C. The green powder was transformed into alkyl-siloxene nanosheets by solid-liquid hydrosilylation using H<sub>2</sub>PtCl<sub>6</sub> as catalyst. The procedure is as follows: 135 mg (1.6 mmol) 1-hexene were dissolved in 2 mL toluene, 52 mg (0.1 mmol) H<sub>2</sub>PtCl<sub>6</sub> · 6H<sub>2</sub>O and 111 mg (0.5 mmol) of Si<sub>6</sub>H<sub>3</sub>(OH)<sub>3</sub> were added and the suspension was stirred at ambient conditions overnight. The reaction mixture was filtrated and washed with copious amounts of toluene. The solid unreacted residue was removed and the solvent of the filtrate was evaporated yielding a yellowish oily product.

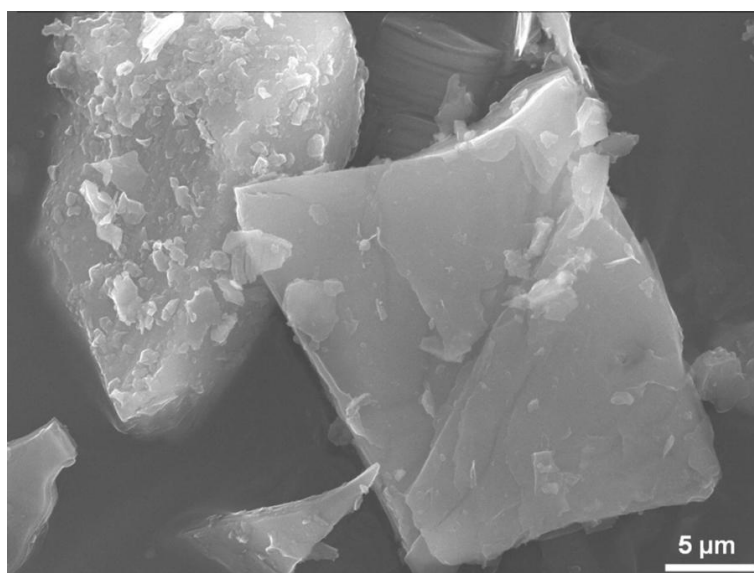
**Characterization.** For AFM and TEM measurements 1 mg of the product was dissolved in 50 mL n-hexane and the solution drop-coated on a Si wafer or on a lacey carbon grid, respectively. The solution was then allowed to evaporate. AFM measurements were carried out in tapping mode using a MFP-3D stand alone AFM (Asylum, Santa Barbara). TEM was performed on a Philips CM 30 ST microscope (Philips, Amsterdam) equipped with a LaB<sub>6</sub> cathode at an acceleration voltage of 300 kV. IR spectroscopy of solid samples were carried out on an IFS 66v/S (Bruker, Madison) spectrometer, organo-modified samples were measured on a Spectrum BXII FT-IR (Perkin Elmer, Waltham) spectrometer. Elemental analysis was performed on an Elementar vario EL (Elementar Analysensysteme, Hanau). Photoluminescence spectra were recorded on an USB 4000 spectrometer (Ocean Optics, Dunedin) using an excitation wavelength of 360 nm. Scanning electron microscopy (SEM) was carried out on a JSM-6500F electron microscope (JEOL Ltd., Tokyo) for morphology analysis of the LDH compounds.



## 5 SILOXENE

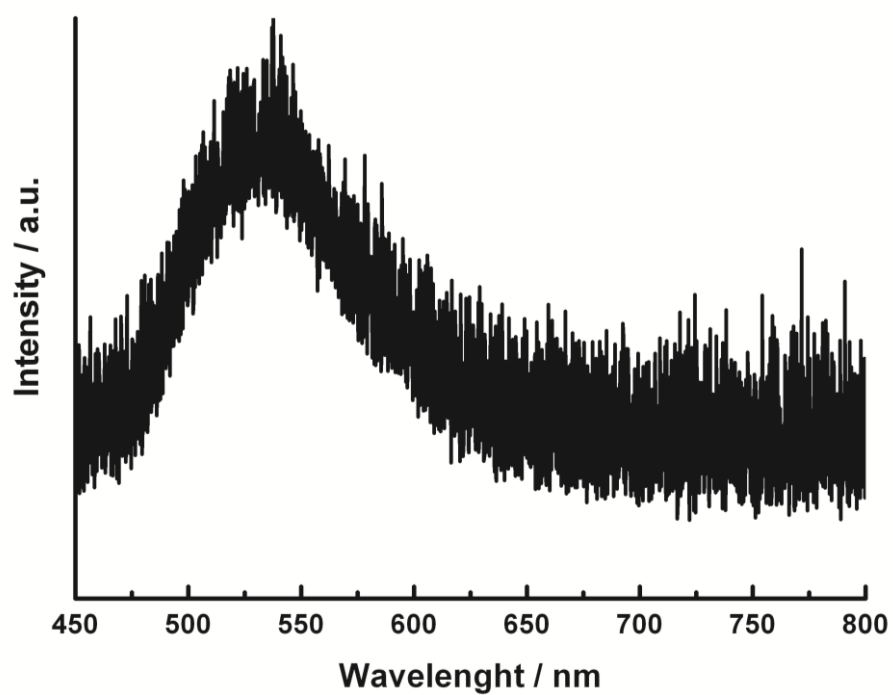
### Observations

The SEM image (Fig. S5.1) displays the plate-like morphology of siloxene. In addition, the PL spectrum of  $\text{Si}_{20}$  (Fig. S5.2) with an emission maximum at 537 nm is in agreement with the literature.<sup>[18]</sup> A photoluminescence maximum at 2.3 eV is reported in the literature that shifts upon annealing to lower energies. A photograph of the annealed samples can be found in Figure S5.3, which shows a color change from green to red at increasing temperature. However, the annealed samples did not show photoluminescence. Similarly, PS and  $\text{Si}_0$ , which is darker than  $\text{Si}_{20}$ , did not show photoluminescence. A possible explanation is the low signal to noise ratio caused by self-absorption of the samples. According to the literature a red-shift of the photoluminescence occurs upon annealing siloxene. Simultaneously, a decrease in intensity results at temperatures above 200 °C.

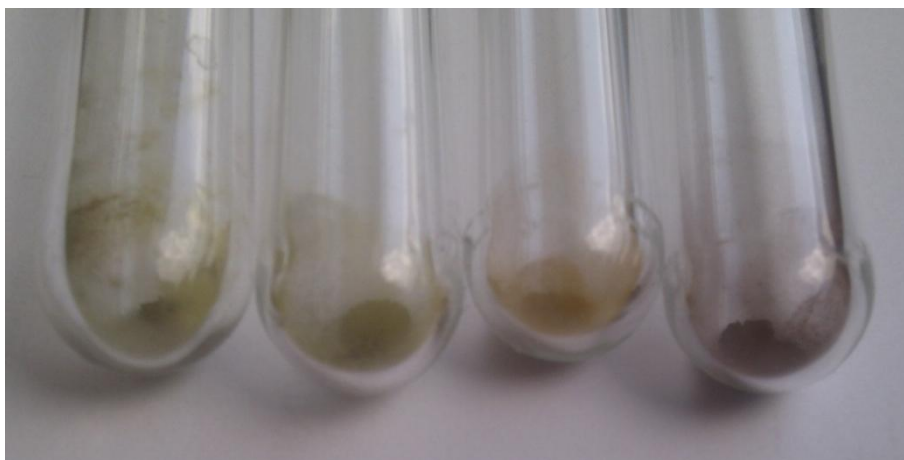


**Fig S5.1** SEM image of  $\text{Si}_6\text{H}_3(\text{OH})_3$ .

## 5 SILOXENE

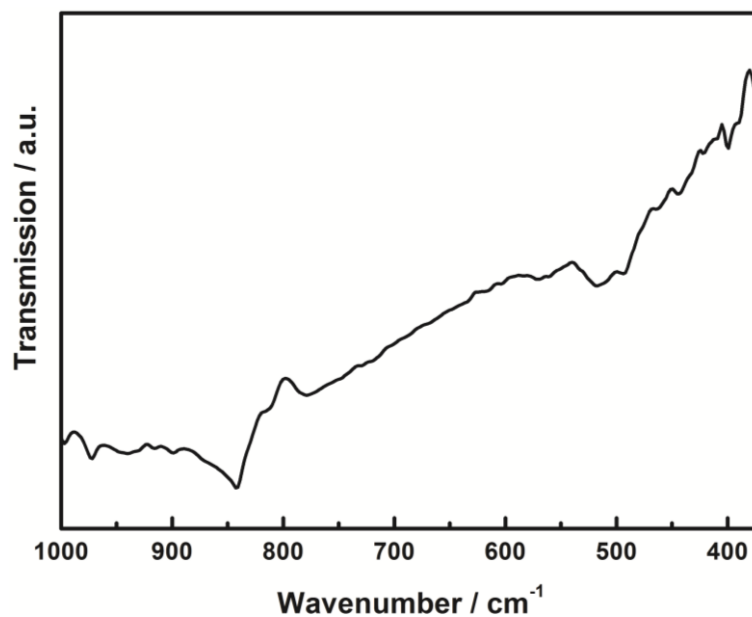


**Fig S5.2** Photoluminescence spectrum of  $\text{Sil}_{20}$ .

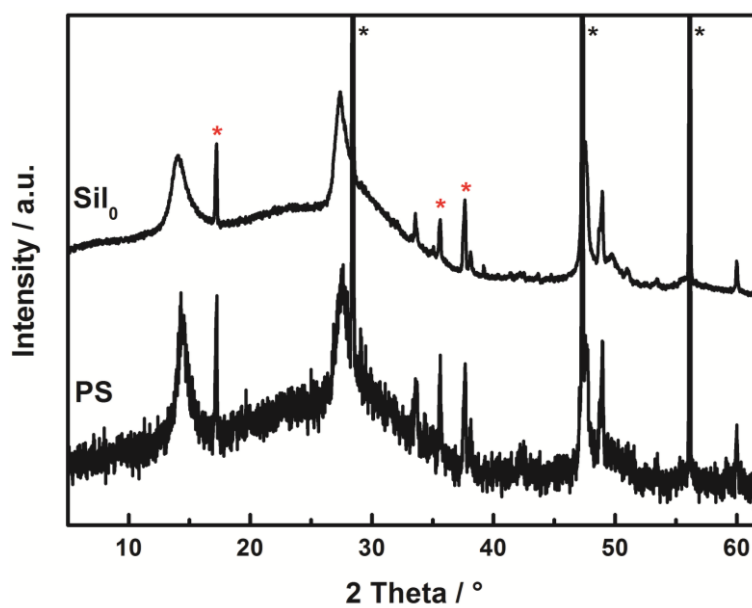


**Fig S5.3** Photograph of the annealed samples in evacuated ampoules showing the color change from green to red. From left to right:  $\text{Sil}_{0;100}$ ,  $\text{Sil}_{0;200}$ ,  $\text{Sil}_{0;300}$ ,  $\text{Sil}_{0;400}$ .

## 5 SILOXENE

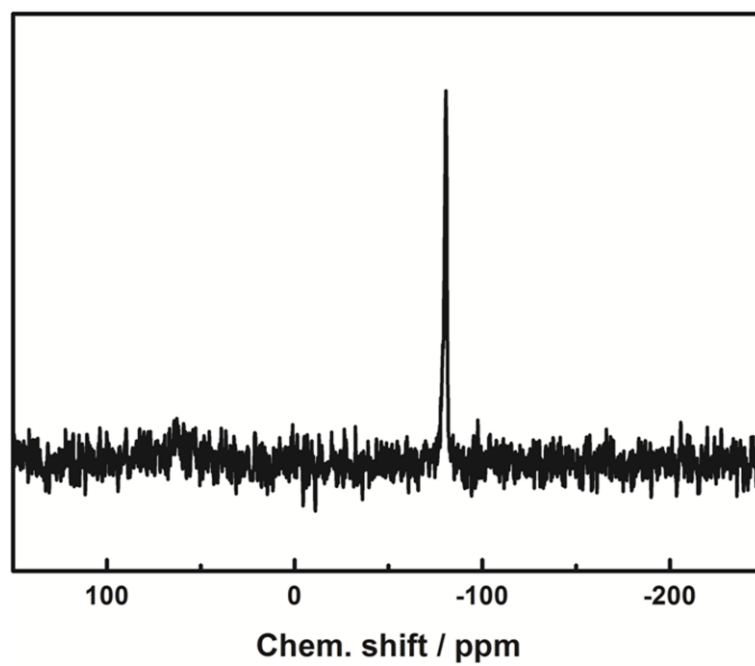


**Fig S5.4** Close-up of the fingerprint area in the IR spectrum of  $\text{CaSi}_2$ . The bands at 515 and 845  $\text{cm}^{-1}$  result from Si-Si bonds and Si-O(H) groups from surface oxidation, respectively.



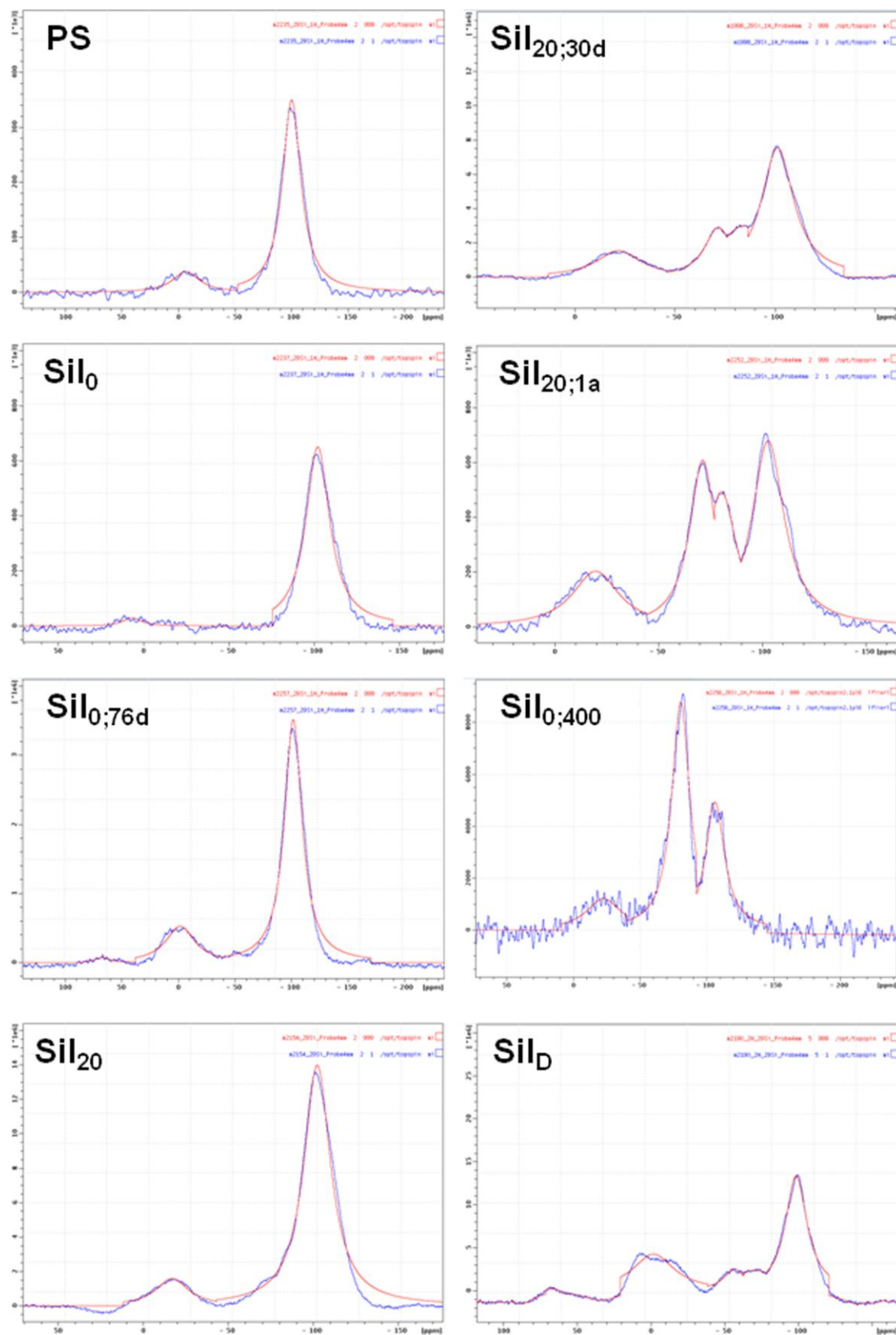
**Fig S5.5** Powder XRD pattern of PS and  $\text{Si}_0$ . The reflections marked with a black and red asterisk result from crystalline Si and residual  $\text{CaSi}_2$  impurities, respectively.

## 5 SILOXENE



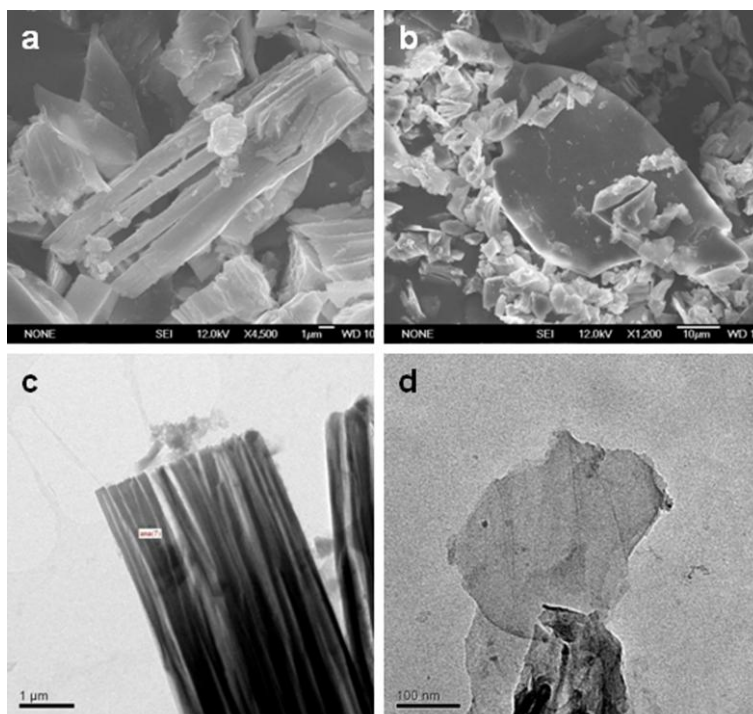
**Fig S5.6**  $^{29}\text{Si}$  ssNMR single pulse measurement of  $\text{CaSi}_2$ .

## 5 SILOXENE

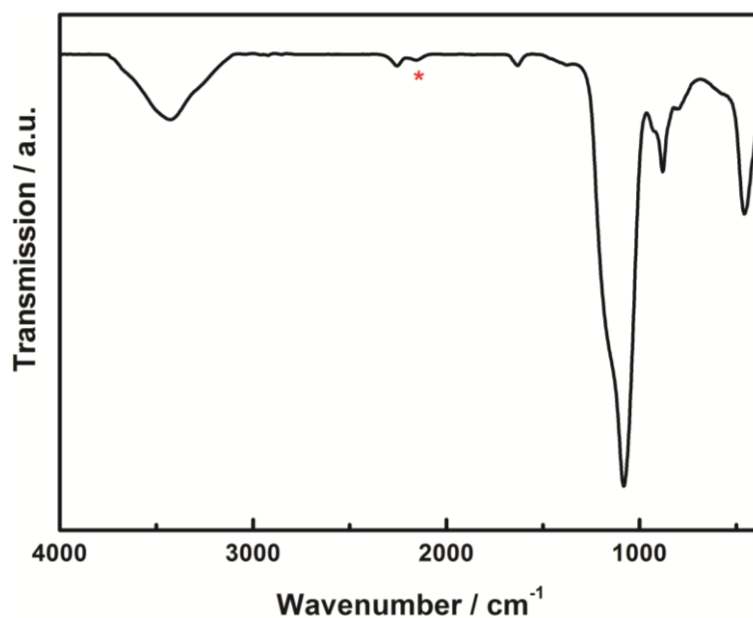


**Fig S5.7**  $^{29}\text{Si}$  CP MAS NMR spectra fitted with a Lorentzian fit in order to quantify the peaks at -101 and -5 ppm using the Bruker TopSpin software.

## 5 SILOXENE



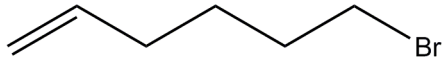
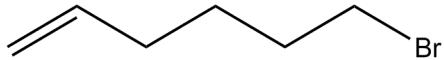
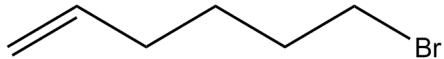
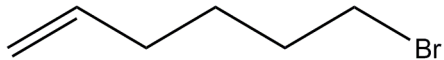
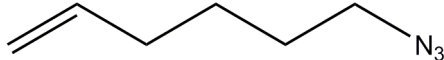
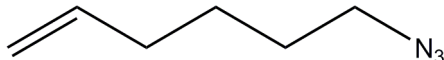
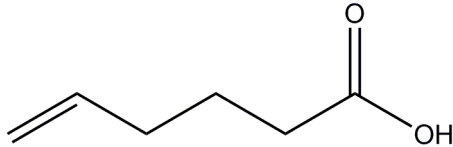
**Fig S5.8** (a) and (b) SEM as well as (c) and (d) TEM micrographs of exfoliated siloxene nanosheets.



**Fig S5.9** IR spectrum of exfoliated siloxene nanosheets. Si-H vibration at  $2100\text{ cm}^{-1}$  is marked with a red asterisk.  $3400$  and  $1630\text{ cm}^{-1}$ : OH bands;  $2250\text{ cm}^{-1}$ : H-SiO<sub>3</sub> units;  $1030$  and  $800\text{ cm}^{-1}$ : Si-O-Si vibrations;  $880\text{ cm}^{-1}$ : Si-O(H) vibration;  $515\text{ cm}^{-1}$ : Si-Si vibration.

## 5 SILOXENE

**Table S5.1** Compilation of different synthetic approaches to integrate functionalized alkyl groups to siloxene.

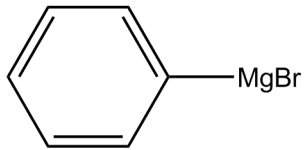
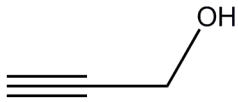
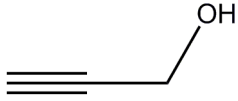
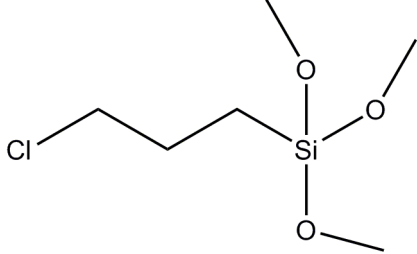
Method	Reagent	Catalyst/Conditions	Solvent	Observation
Hydrosilylation		H <sub>2</sub> PtCl <sub>6</sub>	Toluene	No –CH <sub>2</sub> -Br group visible in the NMR spectra.
Hydrosilylation		H <sub>2</sub> PtCl <sub>6</sub>	THF	No –CH <sub>2</sub> -Br group visible in the NMR spectra.
Hydrosilylation		UV	---	No –CH <sub>2</sub> -Br group visible in the NMR spectra.
Hydrosilylation		180 °C	Mesitylene	No –CH <sub>2</sub> -Br group visible in the NMR spectra.
Hydrosilylation		H <sub>2</sub> PtCl <sub>6</sub>	Toluene	Azide band not visible in IR spectrum.
Hydrosilylation		UV	---	Azide band not visible in IR spectrum.
Hydrosilylation		H <sub>2</sub> PtCl <sub>6</sub>	Toluene	No –CH <sub>2</sub> -COOH group visible in the NMR spectra.

## 5 SILOXENE

Hydrosilylation		$\text{H}_2\text{PtCl}_6$	Toluene	No $-\text{CH}_2-\text{OH}$ group visible in the NMR spectra.
Hydrosilylation		$\text{H}_2\text{PtCl}_6$	Toluene	Amine bands not visible in IR spectrum.
Hydrosilylation		$\text{PtO}_2$	Toluene	Amine bands not visible in IR spectrum.
Hydrosilylation		$\text{PtO}_2$	---	Amine bands not visible in IR spectrum.
Hydrosilylation		UV	---	Amine bands not visible in IR spectrum.
Hydrosilylation		UV	---	No alkyne group visible in the NMR spectra.
Grafting of diazonium salts		---	Acetonitrile	No aromatic peaks visible in the NMR spectra.
Grafting of diazonium salts		---	Acetonitrile	No aromatic peaks visible in the NMR spectra.



## 5 SILOXENE

Grignard reaction		70 °C	Diethyl ether/THF	No aromatic peaks visible in the NMR spectra.
Dehydrogenative addition		Zn(Ac) <sub>2</sub>	THF	No alkyne group visible in the NMR spectra.
Dehydrogenative addition		Zn(2-ethylhexanoate) <sub>2</sub>	THF	No alkyne group visible in the NMR spectra.
Self-assembly of silane		Acetic acid	Toluene	no reaction

## 5.2 BIBLIOGRAPHY

### REFERENCES

- [1] F. Wöhler, *Liebigs Ann. Chem.* **1863**, 127, 257-274.
- [2] S. Z. Butler, S. M. Hollen, L. Cao, Y. Cui, J. A. Gupta, H. R. Gutiérrez, T. F. Heinz, S. S. Hong, J. Huang, A. F. Ismach, E. Johnston-Halperin, M. Kuno, V. V. Plashnitsa, R. D. Robinson, R. S. Ruoff, S. Salahuddin, J. Shan, L. Shi, M. G. Spencer, M. Terrones, W. Windl, J. E. Goldberger, *ACS Nano* **2013**, 7, 2898-2926.
- [3] M. Osada, T. Sasaki, *Adv. Mater.* **2012**, 24, 210-228.
- [4] F. Bonaccorso, A. Lombardo, T. Hasan, Z. Sun, L. Colombo, A. C. Ferrari, *Mater. Today* **2012**, 15, 564-589.
- [5] K. S. Novoselov, A. K. Geim, S. V. Morozov, D. Jiang, Y. Zhang, S. V. Dubonos, I. V. Grigorieva, A. A. Firsov, *Science* **2004**, 306, 666-669.
- [6] M. Osada, T. Sasaki, *J. Mater. Chem.* **2009**, 19, 2503-2511.
- [7] Q. Wang, D. O'Hare, *Chem. Rev.* **2012**, 112, 4124-4155.
- [8] Y. Zhao, B. Li, Q. Wang, W. Gao, C. J. Wang, M. Wei, D. G. Evans, X. Duan, D. O'Hare, *Chem. Sci.* **2014**.
- [9] R. Ma, Z. Liu, L. Li, N. Iyi, T. Sasaki, *J. Mater. Chem.* **2006**, 16, 3809-3813.
- [10] D. D. Vaughn II, R. J. Patel, M. A. Hickner, R. E. Schaak, *J. Am. Chem. Soc.* **2010**, 132, 15170-15172.
- [11] Y. Omomo, T. Sasaki, Wang, M. Watanabe, *J. Am. Chem. Soc.* **2003**, 125, 3568-3575.
- [12] X. Huang, Z. Zeng, H. Zhang, *Chem. Soc. Rev.* **2013**, 42, 1934-1946.
- [13] H. Nakano, M. Ishii, H. Nakamura, *Chem. Commun.* **2005**, 0, 2945-2947.
- [14] H. Kautsky, *Z. anorg. allg. Chem.* **1921**, 117, 209-242.
- [15] A. Weiss, G. Beil, H. Meyer, *Z. Naturforsch. B* **1979**, 34b, 25-30.
- [16] H. D. Fuchs, M. Stutzmann, M. S. Brandt, M. Rosenbauer, J. Weber, A. Breitschwerdt, P. DeÅ;k, M. Cardona, *Phys. Rev. B* **1993**, 48, 8172-8189.
- [17] J. R. Dahn, B. M. Way, E. Fuller, J. S. Tse, *Phys. Rev. B* **1993**, 48, 17872-17877.

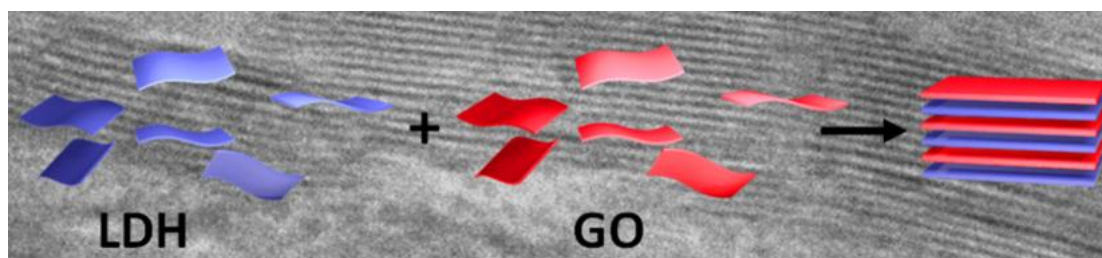
- [18] U. Dettlaff-Weglikowska, W. Hönle, A. Molassioti-Dohms, S. Finkbeiner, J. Weber, *Phys. Rev. B* **1997**, *56*, 13132-13140.
- [19] M. S. Brandt, S. E. Ready, J. B. Boyce, *Appl. Phys. Lett.* **1997**, *70*, 188-190.
- [20] N. Zamanzadeh-Hanebuth, M. S. Brandt, M. Stutzmann, *J. Non-Cryst. Solids* **1998**, *227-230, Part I*, 503-506.
- [21] M. S. Brandt, L. Höppel, N. Zamanzadeh-Hanebuth, G. Vogg, M. Stutzmann, *Phys. Status Solidi B* **1999**, *215*, 409-412.
- [22] E. Hengge, in *Silicium-Chemie, Vol. 9/1*, Springer Berlin Heidelberg, **1967**, pp. 145-164.
- [23] S. Jiang, S. Butler, E. Bianco, O. D. Restrepo, W. Windl, J. E. Goldberger, *Nat. Commun.* **2014**, *5*.
- [24] M. J. S. Spencer, T. Morishita, M. Mikami, I. K. Snook, Y. Sugiyama, H. Nakano, *Phys. Chem. Chem. Phys.* **2011**, *13*, 15418-15422.
- [25] M. J. Allen, V. C. Tung, R. B. Kaner, *Chem. Rev.* **2009**, *110*, 132-145.
- [26] M. S. Brandt, H. D. Fuchs, M. Stutzmann, J. Weber, M. Cardona, *Solid State Commun.* **1992**, *81*, 307-312.
- [27] E. Hengge, K. Pretzer, *Chem. Ber.* **1963**, *96*, 470-477.
- [28] M. P. Gallo, *Zur Chemie von Siloxenen und zur Darstellung von Polysilinen und nanodimensionierten Siliciumteilchen*, Bielefeld, **2004**.
- [29] P. Deák, M. Rosenbauer, M. Stutzmann, J. Weber, M. S. Brandt, *Phys. Rev. Lett.* **1992**, *69*, 2531-2534.
- [30] H. Nakano, T. Mitsuoka, M. Harada, K. Horibuchi, H. Nozaki, N. Takahashi, T. Nonaka, Y. Seno, H. Nakamura, *Angew. Chem. Int. Ed.* **2006**, *45*, 6303-6306.
- [31] H. Nakano, M. Nakano, K. Nakanishi, D. Tanaka, Y. Sugiyama, T. Ikuno, H. Okamoto, T. Ohta, *J. Am. Chem. Soc.* **2012**, *134*, 5452-5455.
- [32] Y. Sugiyama, H. Okamoto, T. Mitsuoka, T. Morikawa, K. Nakanishi, T. Ohta, H. Nakano, *J. Am. Chem. Soc.* **2010**, *132*, 5946-5947.
- [33] H. Okamoto, Y. Kumai, Y. Sugiyama, T. Mitsuoka, K. Nakanishi, T. Ohta, H. Nozaki, S. Yamaguchi, S. Shirai, H. Nakano, *J. Am. Chem. Soc.* **2010**, *132*, 2710-2718.
- [34] H. Kautsky, H. P. Siebel, *Z. anorg. allg. Chem.* **1953**, *273*, 113-123.

- [35] Y. Sugiyama, H. Okamoto, H. Nakano, *Chem. Lett.* **2010**, 39, 938-939.
- [36] J. M. Buriak, *Chem. Rev.* **2002**, 102, 1271-1308.
- [37] J. M. Buriak, *Chem. Mater.* **2013**, 26, 763-772.
- [38] S. J. Schoell, M. Sachsenhauser, A. Oliveros, J. Howgate, M. Stutzmann, M. S. Brandt, C. L. Frewin, S. E. Saddow, I. D. Sharp, *ACS Appl. Mater. Interfaces* **2013**, 5, 1393-1399.
- [39] Y. Wang, J. Cai, H. Rauscher, R. J. Behm, W. A. Goedel, *Chem. Eur. J.* **2005**, 11, 3968-3978.
- [40] M. P. Stewart, F. Maya, D. V. Kosynkin, S. M. Dirk, J. J. Stapleton, C. L. McGuinness, D. L. Allara, J. M. Tour, *J. Am. Chem. Soc.* **2004**, 126, 370-378.
- [41] M. Zacharias, H. Freistedt, F. Stolze, T. P. Drüsedau, M. Rosenbauer, M. Stutzmann, *J. Non-Cryst. Solids* **1993**, 164–166, Part 2, 1089-1092.
- [42] Y. H. Xie, W. L. Wilson, F. M. Ross, J. A. Mucha, E. A. Fitzgerald, J. M. Macaulay, T. D. Harris, *J. Appl. Phys.* **1992**, 71, 2403-2407.
- [43] T. M. Miller, L. Zhao, A. B. Brennan, *J. Appl. Polym. Sci.* **1998**, 68, 947-957.
- [44] E. Ayres, W. L. Vasconcelos, R. L. Oréface, *Mater. Res.* **2007**, 10, 119-125.
- [45] M. Cardona, *Phys. Status Solidi B* **1983**, 118, 463-481.
- [46] M. A. Karakkasides, D. Gournis, D. Petridis, *Clay Miner.* **1999**, 34, 429-438.
- [47] W. K. Chang, M. Y. Liao, K. K. Gleason, *J. Phys. Chem.* **1996**, 100, 19653-19658.
- [48] T. Tsuboi, T. Sakka, Y. H. Ogata, *Phys. Rev. B* **1998**, 58, 13863-13869.
- [49] T. Pietraß, A. Bifone, R. D. Roth, V. P. Koch, A. P. Alivisatos, A. Pines, *J. Non-Cryst. Solids* **1996**, 202, 68-76.
- [50] J. Casanovas, F. Illas, G. Pacchioni, *Chem. Phys. Lett.* **2000**, 326, 523-529.
- [51] E. Z. Kurmaev, S. N. Shamin, D. L. Ederer, U. Dettlaff-Weglikowska, J. r. Weber, *J. Mater. Res.* **1999**, 14, 1235-1237.
- [52] B. Marciniec, *Hydrosilylation* **2009**, 1.
- [53] H. E. Gottlieb, V. Kotlyar, A. Nudelman, *J. Org. Chem.* **1997**, 62, 7512-7515.
- [54] P. A. Couperus, A. D. H. Clague, J. P. C. M. van Dongen, *Org. Magn. Resonance* **1976**, 8, 426-431.
- [55] J. M. Powers, G. A. Somorjai, *Surf. Sci.* **1991**, 244, 39-50.

- [56] I. Kusunoki, Y. Igari, *Appl. Surf. Sci.* **1992**, 59, 95-104.
- [57] J. F. Moulder, W. F. Stickle, P. E. Sobol, K. D. Bomben, *Handbook of X-ray Photoelectron Spectroscopy* **1992**.
- [58] L.-A. O'Hare, B. Parbhoo, S. R. Leadley, *Surf. Interface Anal.* **2004**, 36, 1427-1434.
- [59] S. Ida, C. Ogata, M. Eguchi, W. J. Youngblood, T. E. Mallouk, Y. Matsumoto, *J. Am. Chem. Soc.* **2008**, 130, 7052-7059.
- [60] T. C. Ozawa, K. Fukuda, K. Akatsuka, Y. Ebina, T. Sasaki, *Chem. Mater.* **2007**, 19, 6575-6580.
- [61] C. Ziegler, S. Werner, M. Bugnet, M. Wörsching, V. Duppel, G. A. Botton, C. Scheu, B. V. Lotsch, *Chem. Mater.* **2013**, 25, 4892-4900.
- [62] S. W. Keller, H.-N. Kim, T. E. Mallouk, *J. Am. Chem. Soc.* **1994**, 116, 8817-8818.
- [63] M. Osada, K. Akatsuka, Y. Ebina, H. Funakubo, K. Ono, K. Takada, T. Sasaki, *ACS Nano* **2010**, 4, 5225-5232.

## 6. SUMMARY

### 6.1 LAYERED DOUBLE HYDROXIDES



In order to extend the toolbox of cationically charged nanosheets for the synthesis of lamellar hybrid materials,  $\text{Mn}^{\text{II}}\text{Al}^{\text{III}}$  sulfonate and dodecylsulfate (DS) layered double hydroxides (LDHs) are synthesized and exfoliated into nanosheets. Therefore, the sulfonate LDHs, namely ethylbenzenesulfonate, toluenesulfonate, and naphthalenesulfonate, are synthesized by the typical coprecipitation method. The DS LDH is synthesized *via*  $\text{Mn}^{\text{II}}\text{Al}^{\text{III}}$  chloride LDH as intermediate, followed by anion exchange replacing the chloride by DS. In addition to the exfoliation of the  $\text{Mn}^{\text{II}}\text{Al}^{\text{III}}$  LDHs, the resulting positively charged nanosheets were assembled by flocculation and electrostatic self-assembly (ESD) with graphene oxide (GO) yielding new functional hybrid materials. The flocculated product (GO/LDH), which is subsequently reduced to reduced GO (RGO)/LDH is investigated for potential application as battery material for pseudocapacitors. Especially the material GO/LDH shows promising electrochemical properties, such as enhanced capacitance over the constituent building blocks with good cycle stability for up to 500 charge-discharge cycles. Secondly, the sequential deposition of the LDH nanosheets and GO is achieved by ESD. AFM analysis of the films shows a linear progression of the film thickness for up to

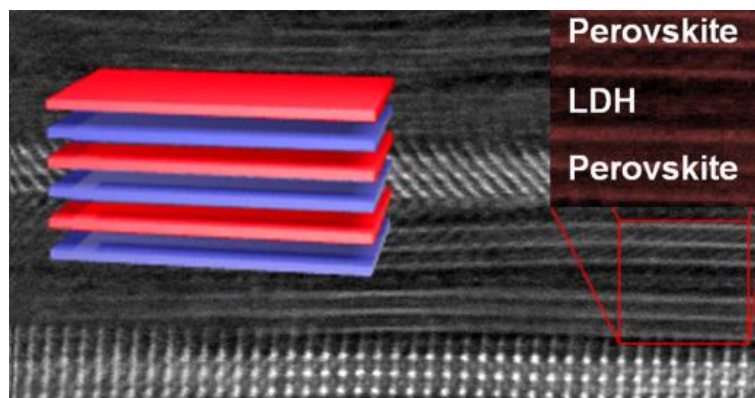
## 6 SUMMARY

100 double layers. The sequential deposition is further confirmed by TEM cross sectional analysis which shows a layered structure of the newly formed composite material.

As second part of this chapter the synthesis and exfoliation of a  $\text{Zn}^{\text{II}}\text{Cr}^{\text{III}}$  DS LDH and subsequent flocculation with  $\text{TBA}_x\text{Ti}_{2-x/4}\text{O}_4$  nanosheets is achieved. The LDH nanosheets are obtained by anion exchange of  $\text{Zn}^{\text{II}}\text{Cr}^{\text{III}}$  nitrate LDH with DS. Sonication of this compound in formamide leads to partial exfoliation of the LDH and nanosheets with heights down to ca. 4.5 nm. The flocculated product shows a significant red shift of the UV-Vis absorption spectra. However, the expected photocatalytic activity in terms of hydrogen evolution and oxygen evolution reaction could not be proven.

Recapitulating, this chapter shows the extension of available cationically charged nanosheets and their combination with oppositely charged nanosheets by flocculation and ESD to form hybrid compounds.

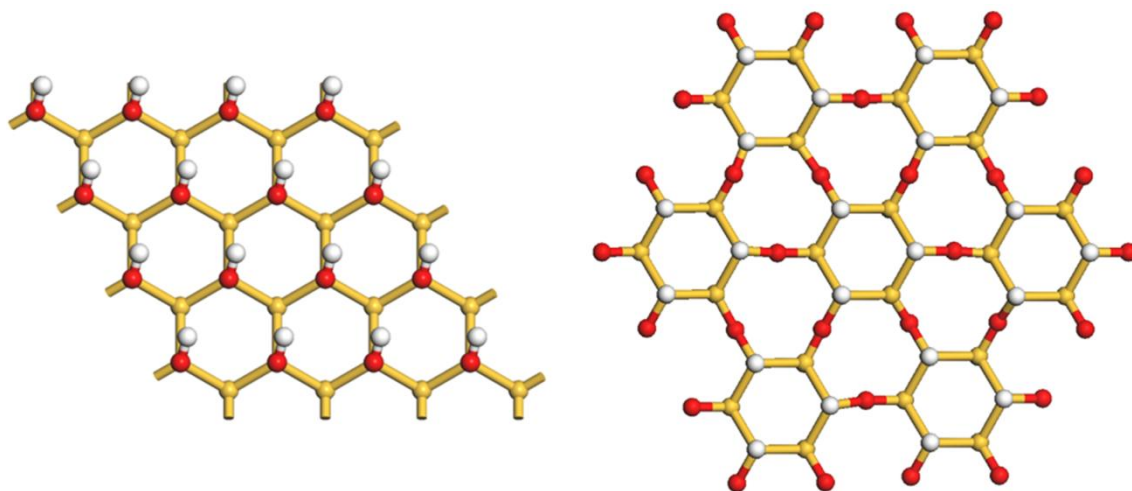
## 6.2 LAYER-BY-LAYER ASSEMBLY OF OPPOSITELY CHARGED NANOSHEETS



Chapter 4 outlines the sequential deposition of cationic  $\text{Mn}_2\text{Al}(\text{OH})_6^+$  and anionic  $\text{Ca}_2\text{Nb}_3\text{O}_{10}^-$  nanosheets and the in-depth analysis of the composition and local structure of the formed multilayer film. The hybrid film is fabricated by a soft chemical synthesis protocol, i.e. sequential electrostatic layer-by-layer (LBL) assembly starting from stable colloidal suspensions of oppositely charged LDH and perovskite nanosheets. The focus of this chapter is on the precise local analysis of the formed stacks by means of (S)TEM, HRTEM, and EEL spectroscopy. The combined analysis of the films reveals the structure of the composite in bulk dimensions and on the molecular scale. Hence, as expected the overall stack contains voids and defects which are likely caused by a combination of imperfections during layer-by-layer fabrication and cross-section sample preparation. Nevertheless, the atomic-scale structure reveals the successful sequential deposition of single LDH and perovskite slabs, confirming the proof of concept that oppositely charged nanosheets can be assembled by soft chemistry forming tailor-made artificial solids that are inaccessible by established high-temperature synthetic routes. In addition, it is shown that the choice of the solvent of the nanosheet suspension heavily affects the composition of the stack. Hence, these results are important for future research in the design of artificial heterostructures, both in terms of confirming the feasibility of sequential layer-by-layer deposition for the assembly of bulk layered solids and with respect to the expected alternating structure, in order to predict possible properties and applications of the formed stacks according to the atomic-level and overall structure and morphology of the samples.



### 6.3 SILOXENE



Siloxene is a compound that has been known for more than 150 years since its discovery by Friedrich Wöhler. However, its exact structure still remains ambiguous. Even if the crystal structure of one modification – Wöhler siloxene (Fig. left) – was reported early on, clear evidence of the second form, Kautsky siloxene (Fig. right), is still elusive. Chapter 5 contains investigations of the structure of siloxene. In detail, it is shown that siloxene presumably does not consist of only two “isomers”, but the compound rearranges and oxidizes into several side products, even upon storage under an inert atmosphere and light exclusion. This assumption is concluded from a systematic study of siloxene based on different synthetic approaches and spectroscopic investigations of the compounds obtained after different storage times and conditions. In addition to siloxene, polysilene, which is based on a layered silicon backbone isostructural to Wöhler siloxene, is studied. According to the literature polysilene consists of puckered silicon layers with only hydrogen bound to the Si atoms. The present study, however, shows that hydrolysis of the samples during the synthesis cannot be completely avoided. Hence, also this compound reveals hydroxyl groups, which inevitably lead to rearrangement and insertion of the oxygen into the layers. The quintessence of this study is that both, siloxene and polysilene, do not consist of single phase materials. In all samples, either from air or from intramolecular hydroxyl groups, oxygen inserts into the layered silicon backbone and gradually destroys the 2D structure. Moreover, this chapter outlines the exfoliation and modification of bulk siloxene. The demand of nanosized semiconducting materials for electronic devices steadily increases and

## 6 SUMMARY

hence, research on the exfoliation of semiconducting layered compounds has intensified over the past years. Siloxene, which is a semiconductor with bandgaps ranging from 1.7 to 2.75 eV, is exfoliated into nanosheets by means of surfactants. In addition, organic functionalization of bulk siloxene leads to spontaneous exfoliation of the compound into single layers. To date, very little has been reported in the field of silicon-based nanosheets. This work therefore contributes to the extension of the toolbox of available van der Waals nanosheets, including organically modified ones, to a semiconducting material containing silicon as a main constituent.

## 7. CONCLUSION AND OUTLOOK

In materials research, the area of 2D materials and their combination to create tailor-made artificial solids has emerged only very recently and is therefore still in its infancy. Thus, it is a major goal to extend the existing toolbox of nanosheets in order to increase the diversity of possible combinations in layer-by-layer (LBL) techniques to built new materials. Of particular interest is the synthesis of cationic single layered materials since LDHs are one class of materials among very few from which those can be obtained. In addition, positively charged nanosheets are still scarce in number compared to their negatively charged counterparts but the existence of cationic nanosheets is a prerequisite for LBL techniques that rely on electrostatic interactions. Moreover, the design of hybrid compounds, either from oppositely charged nanosheets by flocculation and electrostatic self-assembly (ESD) techniques or by the Langmuir-Blodgett (LB) method to combine charged or uncharged nanosheets remains a key challenge in research. This dissertation puts forward the exfoliation of  $\text{Mn}^{\text{II}}\text{Al}^{\text{III}}\text{LDH}$  into cationic nanosheets and the combination of these with negatively charged GO and  $\text{Ca}_2\text{Nb}_3\text{O}_{10}^-$  nanosheets to form new hybrid superstructures. For future work it may be conceived that the variety of nanosheets can still be extended by exfoliation of yet unexfoliated layered van der Waals and ionic solids. In addition, exfoliation processes, especially for cationic layered compounds, have to be improved. As described in chapter 1.2.1, LDHs carry a high surface charge, which makes delamination of the Brucite-type layers difficult. Therefore, new techniques are necessary to overcome the forces between the layers in order to gently exfoliate the materials and thus to generate well defined, micrometer sized nanosheets with sharp edges and smooth surfaces. Another approach to overcome this challenge and produce cationically charged nanosheets is to modify existing nanosheets with organic ligands, e.g. amines, which can be protonated in acidic media to yield positive surface charges. This issue also follows up the synthesis and organic modification that has been shown in chapter 5. In this thesis the modification of

## 7 CONCLUSION AND OUTLOOK

siloxene has been achieved by hydrosilylation attaching hexyl groups to the 2D backbone. This synthesis may be modified to connect functional groups to reverse the polarity of the formed sheets to make nonpolar sheets applicable for ESD. Moreover, the presence of functional groups, e.g. azides, alkynes, amines or carboxylic acids, attached to organic modified sheets is desired in order to apply “click chemistry” to nanosheet research. With the help of this facile chemical instrument the toolbox of functional nanosheets could be enlarged significantly. Since essentially any organic molecule could then be attached to the nanosheets, this method offers new functionalities of 2D materials relevant for sensing, optoelectronics, energy storage and conversion.

Besides research on the development of new types of nanosheets, the combination of these into heterostructures is a big challenge. Owing to the synergism of the properties resulting from the constituent nanosheets, the hybrid materials offer a wide range of applications. To date a major goal is the protection of the environment and therefore the quest for renewable energy sources. From nanosheet building blocks, the synthesis of combined photocatalytic systems for both oxygen and hydrogen evolution reaction is possible in principle. Therefore, the combination of  $\text{Ca}_2\text{Nb}_3\text{O}_{10}^-$  nanosheets, which have been reported to evolve hydrogen from water under light irradiation, and  $\text{Zn}^{\text{II}}\text{Cr}^{\text{III}}$  LDH nanosheets, which according to the literature are applicable for the oxygen evolution reaction (OER) from water, might be interesting. Though, as described above exfoliation of the LDH nanosheets has to be improved in order to obtain single layers and thus to intimately combine the two compounds on the molecular scale and to provide facile charge transfer between them. Efficiency of hybrid materials for photocatalytic applications might be higher for compounds synthesized by flocculation rather than by ESD or the LB technique since the surface area of thin films is smaller than in flocculated samples and surface as well as active site accessibility plays a crucial role in photocatalysis. In order to increase the surface of hybrid compounds a template synthesis could be the choice for a synthetic route which maximizes the accessible surface area. Therefore, as model system the synthesis of inverse opals can be mentioned. For example, polystyrene nanoparticles could be added to the nanosheet suspensions before flocculation starts in order to force a template flocculation around the polymer spheres. By removal of the polystyrene, a highly porous compound would be obtained with tunable porosity depending on the particle size.

Concluding, the research area of 2D materials has been re-opened by the discovery of graphene in 2004. Since then this field has been developing very rapidly including exfoliation of layered compounds into nanosheets and their combination by different

## 7 CONCLUSION AND OUTLOOK

methods to yield hybrid compounds. Still, the resources of layered compounds are not yet exhausted so that the variety of nanosheets can be enlarged. In addition, LBL methods have the potential to form hybrid functional materials that are inaccessible by other synthetic routes. Hence, this field of research is promising concerning the possibilities that can be achieved with low costs and facile soft chemical synthetic approaches, opening new avenues to potential applications of layered hybrid materials as energy conversion systems or electronic devices.

## 8. APPENDIX

### 8.1 LIST OF PUBLICATIONS

Published as part of this thesis:

**Cationically charged Mn<sup>II</sup>Al<sup>III</sup> LDH nanosheets by chemical exfoliation and their use as building blocks in graphene oxide-based materials**

Stephan Werner, Vincent Wing-hei Lau, Stephan Hug, Viola Duppel, Hauke Clausen-Schaumann, Bettina V. Lotsch  
*Langmuir* **2013**, 29, 9199; DOI: 10.1021/la400846w.

**Artificial solids by design: Assembly and Electron Microscopy study of nanosheet-derived heterostructures**

Christian Ziegler,\* Stephan Werner,\* Matthieu Bugnet, Kulpreet Viridi, Matthias Wörsching, Viola Duppel, Gianluigi A. Botton, Christina Scheu, Bettina V. Lotsch  
\*equal contribution  
*Chem. Mater.* **2013**, 25, 4892; DOI: 10.1021/cm402950b.

Published previously:

**Ultrathin 2D Coordination Polymer Nanosheets by Surfactant-Mediated Synthesis**

Sebastian C. Junggeburth, Leo Diehl, Stephan Werner, Viola Duppel, Wilfried Sigle, Bettina V. Lotsch  
*J. Am. Chem. Soc.* 2013, 135, 6157; DOI: 10.1021/ja312567v.